

International Hydrology Programme



Effects of Pollutants on Atmospheric Environment

-The Textbook for Thirteenth IHP Training Course in 2003-

Edited by Yutaka Ishizaka and Toshihiro Kitada

Hydrospheric Atmospheric Research Center, Nagoya University



United Nations Educational Scientific and Cultural Organization

Prepared for the Thirteenth IHP Training Course on Effects of Pollutants on Atmospheric Environment, 7 March-20 March, 2004, Nagoya and Tokyo, Japan

Working Group for IHP Training Course,
Sub-Committee for IHP,
Japan National Commission for UNESCO

Chairperson: Prof. K. Nakamura, Nagoya University

Secretariat:

Mr. S. Sato, Ministry of Education, Culture, Sports, Science and Technology

Ms. M. Ogawa, Ministry of Education, Culture, Sports, Science and Technology

Mr. S. Nagata, Nagoya University

Members:

Prof. K. Takeuchi, Yamanashi University

Prof. Y. Fukushima, Research Institute for Humanity and Nature

Mr. S. Ohtani, Ministry of Land Infrastructure and Transport

Dr. Y. Takemura, Japan Meteorological Agency

Dr. T. Kishii, National Research Institute for Earth Science and Disaster Prevention

Dr. H. Ohno, National Institute for Agro-Environmental Sciences

Prof. Y. Iwasaka, Nagoya University

Prof. T. Kitada, Toyohashi University of Technology

Dr. S. Hatakeyama, National Institute for Environmental Studies

Prof. Y. Ishizaka, Nagoya University

Prof. N. Yoshida, Tokyo Institute of Technology

Prof. M. Nakawo, Research Institute for Humanity and Nature

Prof. E. Nakakita, Kyoto University

Published in 2005 by the Hydrospheric Atmospheric Research Center, Nagoya University and United Nations Educational Scientific and Cultural Organization

Printed by Nagoya University COOP

ISBN: 4-9980619-5-X

Cover: The effect of air pollutants on climate change

Preface

The general aim of the 13th IHP Training Course is to help participants to broaden their basic knowledge of the effect of air-pollutants on the atmospheric environments and climate changes and to develop their skills to solve current global environmental problems. As a part of UNESCO International Hydrological Programme (IHP), the course is held every Japanese fiscal year that starts in April. The first IHP Training Course was held on 1991. From 1991 to 1996, the Training Courses were focused on general hydrology. Later on the Training Courses were focused on various topics of scientific interests such as: snow hydrology (1998), remote sensing (1999), limnology (1999), hydrology related to water management (2000), hydrogen and oxygen isotopes in hydrology (2002), and precipitation and water resources (2003).

The 13th IHP Training Course was held from 7 to 20 March, 2004. Lectures and technical tours were carried out at Hydrospheric Atmospheric Research Center and Graduate School of Environmental Studies, Nagoya University, Nagoya, Japan, Toyohashi University of Technology, Toyohashi, Japan, University of Tokyo, Tokyo, Japan, National Institute for Environmental Studies, Tsukuba, Japan, Earth Observation Research Center, Tokyo, Japan and The Earth Simulator Center, Yokohama, Japan. The participants were from the Asia-Pacific region. The Training Course focused on two major subjects. The first one was related to study the effect of anthropogenic pollutants on atmospheric environments from observational point of view. Fundamental knowledge of monitoring gases, aerosol particles and clouds with aircraft/ground observations and lidar/satellite observations were explored through a series of lectures and practical tours. The second one was related to study the effect of anthropogenic pollutants on atmospheric environment from modeling and simulation point of view. In this sense, participants could get essential and comprehensive idea of planning, managing and solving problems related to air pollutants in their home countries.

The 13th IHP Training Course was successfully completed by contributions from professors, experts and staffs of universities and research institutes led by Prof. K. Nakamura, Prof. Y. Ishizaka and Prof. Y. Iwasaka from Nagoya University, Dr. S. Hatakeyama and Dr. N. Sugimoto from National Institute for Environmental Studies, Prof. H. Fukushima from Tokai University, Prof. T. Kitada and Dr. G. Kurata from Toyohashi University of Technology, and Prof. A. Sumi from University of Tokyo.

The Training Course would not have been possible to be conducted without managing support of Dr. Giuseppe Arduino and his colleagues from UNESCO Jakarta office. The IHP Training Course is under continuous support from the Ministry of Education, Culture, Sports, Science, and Technology of Japan.

16 April, 2005

Kenji Nakamura
Chairperson of Working Group for IHP Training Course
Director, Hydrospheric Atmospheric Research Center,
Nagoya University

Acknowledgements

We would like to express my sincere thanks to all authors for their great contributions to this textbook. This textbook would not have been published without their indispensable efforts. The editing work was done with the help of Mr. T. Takahashi, Hydrospheric Atmospheric Research Center, Nagoya, Japan and Mr. P. Khatri, Graduate School of Environmental Studies, Nagoya University. Thanks are extended to Prof. Kenji Nakamura, the chairperson of the working group of the IHP Training Course and the director of Hydrospheric Atmospheric Research Center.

The supports from Japan National Commission for UNESCO, sub-committee of IHP led by Prof. Takeuchi from Yamanashi University and the working group of IHP Training Course are highly acknowledged. Thanks are also extended to Mr. S. Sato and Ms. M. Ogawa from the Ministry of Education, Culture, Sports, Science and Technology of Japan and Mr. S. Nagata from Nagoya University for sharing their role of secretariat. Local arrangement was accomplished by Ms. T. Mizuno and S.Haga. Last but not least, thanks are also extended to the staffs of Hydrospheric Atmospheric Research Center and Graduate School of Environmental Studies, Nagoya University, Toyohashi University of Technology, Center for Climate System Research, The University of Tokyo, National Institute for Environmental Studies, Earth Observation Research Center, JAXA and The Earth Simulator Center, JAMSTEC for their lectures, local practices and/or scientific tours.

April, 2005

Yutaka Ishizaka and Toshihiro Kitada
Co-Editors

List of the contributors

- Chapter 1 Basics on Transport Processes of Air-Pollutant and their Modeling in the Atmosphere
T. Kitada
- Chapter 2 Basics of Gases, Aerosol Particles and CCN
Y. Ishizaka and M. Adhikari
- Chapter 3 Long-range Transport of Air-Pollutants in the East Asian Pacific Rim Region
S. Hatakeyama
- Chapter 4 Observation of Aerosol Particles in the East Asia using Lidars
N. Sugimoto
- Chapter 5 Observation of Aerosol Particles in the East Asia Using Satellites and Their Radiative Forcing
H. Fukushima
- Chapter 6 Nature and Behaviors of Aerosol Particles in the Atmosphere
Y. Iwasaka
- Chapter 7 Numerical experiments on Effect of Air-Pollutants on Microphysical Properties of Clouds
M. Nishizawa and Y. Ishizaka
- Chapter 8 Comprehensive Modeling of Transport/Chemistry /Deposition, and its Use for Evaluation of the Effect of Air-Pollutants on Air Quality, Water Quality and Ecology
T. Kitada
- Chapter 9 Human Activity and Climate Change
A. Sumi
- Practices Computer Simulation of Transport of Pollutants in the Atmosphere
G. Kurata
- Technical Tours
Remote Sensing Technologies for the Atmospheric Sciences
R. Imasu
Climate in the Past
A. Abe-Ouchi
The Earth Simulator Center, JAMSTEC

Current address of the contributors (alphabetical order)

- A. Abe-Ouchi..... Center for Climate System Research, University of Tokyo
E-mail: abeouchi@ccsr.u-tokyo.ac.jp
- H. Fukushima School of High-Technology for Human Welfare, Tokai University
E-mail: hajime@fksh.fc.u-tokai.ac.jp
- S. Hatakeyama..... Atmospheric Environment Division, National Institute for Environmental Studies
E-mail: hatashir@nies.go.jp
- R. Imasu..... Center for Climate System Research, University of Tokyo
E-mail: imasu@ccsr.u-tokyo.ac.jp
- Y. Ishizaka Hydrospheric Atmospheric Research Center, Nagoya University
E-mail: ishizaka@hyarc.nagoya-u.ac.jp
- Y. Iwasaka Graduate School of Environmental Studies, Nagoya University
E-mail: iwasaka@stelab.nagoya-u.ac.jp
- T. Kitada Department of Ecological Engineering, Toyohashi University of Technology
E-mail: kitada@earth.eco.tut.ac.jp
- G. Kurata Department of Ecological Engineering, Toyohashi University of Technology
E-mail: kurata@eco.tut.ac.jp
- N. Sugimoto..... Atmospheric Environment Division, National Institute for Environmental Studies
E-mail: nsugimoto@nies.go.jp
- A. Sumi Center for Climate System Research, University of Tokyo
E-mail: sumi@ccsr.u-tokyo.ac.jp

Contents

Part I Textbook

1. Basics on Transport Processes of Air-Pollutant and their Modeling in the	
Atmosphere	1
1.1 Basic equations of advection/diffusion/deposition of air-pollutants in the	
Atmosphere	1
1.1.1 Modeling of environmental transport phenomena and role of	
their numerical analysis	1
1.1.2 Atmospheric advection-diffusion equation	2
1.1.3 Boundary condition	7
1.1.4 Qualitative description of air pollutant transport in the atmosphere	8
1.2 Gaussian plume/puff models	24
1.2.1 Analytical solution	24
1.2.2 Statistical model	27
1.2.3 Atmospheric diffusion model for environmental impact assessment	31
References	38
2. Basics of Gases, Aerosol Particles and CCN	39
2·1 Introduction	39
2·2 Sulfur dioxide and sulfate aerosol	40
2·3 Activation of aerosol particles as CCN	41
2·3·1 Activation of soluble particles as CCN	41
2·3·2 Activation of mixed particles as CCN	44
2·4 Some data observed over the East China Sea	46
2·4·1 Vertical distribution of SO₂ concentration	46
2·4·2 Vertical distribution of aerosol particle concentrations	47
2·4·3 Vertical distribution of CCN concentrations	48
References	51
3. Long-range Transport of Air-pollutants in the East Asian Pacific Rim Region	55

3.1 Introduction	55
3.2 Aerial observations of atmospheric pollutants over the seas between Asian continent and Japan – three types of transport from Asia.....	56
3.2.1 High concentration of SO ₂ over the western part of the Sea of Japan.....	56
3.2.2 Three types of transport during winter monsoon period	63
3.3 Transport of high concentration of pollutants from central Eastern China driven by migratory low/high pressure system.....	67
3.3.1 Large scale transport following a migratory low pressure system	68
3.3.2 Large scale transport following a moving high pressure system	71
3.4 Aircraft observation of atmospheric pollutants in a large source area in China.....	75
References	80
 4. Observation of Aerosol Particle in the East Asia using Lidars.....	83
4.1 Introduction	83
4.2 Mie-scattering lidar Instrument.....	84
4.3 Lidar equation	87
4.4 How to look at the lidar data	89
4.4.1 Range-corrected signal intensity and signal depolarization ratio	89
4.4.2 Two-wavelength signal ratio	90
4.4.3 Attenuated backscattering coefficient and extinction coefficient	92
4.5 Observations of Asian dust and air-pollution aerosols with lidars.....	93
4.5.1 Scatterer classification method	94
4.5.2 Estimation of extinction coefficient of dust and air-pollution aerosols	97
4.5.3 Application to validation of chemical transport models.....	99
References	101
 5. Observation of Aerosol Particles in the East Asia using Satellites	103
5.1 Introduction	103
5.2 Principles of satellite observation of aerosol	103

5.3 Satellite sensors for aerosol observation.....	106
5.4 Aerosols seen in satellite image – examples	108
5.4.1 Soot/sulfate and Asian dust aerosols in SeaWiFS aerosol imageries	108
5.4.2 Forest fire smoke aerosol observed by GLI and SeaWiFS.....	108
5.4.3 MODIS standard aerosol products.....	111
5.5. Useful Web Pages and Readings.....	114
References	115
 6. Nature and Behaviors of Aerosol Particles in the Atmosphere.....	117
Abstract	117
6.1 Introduction	118
6.2 Method.....	119
6.3 Results.....	124
6.4 Discussion	129
6.4.1 Atmospheric condition and mixing state of particles.....	129
6.4.2 Diffusion of dust existed in surface atmosphere.....	136
6.5 Conclusions	139
References	141
 7. Effect of Air Pollutants on Microphysical Properties of Clouds	145
7.1 Introduction	145
7.2 Numerical models of meteorological field and cloud physics	145
7.3 Configuration of numerical experiment	146
7.4 Result and Discussion.....	147
7.5 Summary	150
References	150
 8. Numerical Models for Transport of Air-pollutants in the Atmosphere	151
8.1 Finite difference method	151
8.1.1 Basis.....	151
8.1.2 Consistency, convergence and stability	153

8.1.3 Methods for solution of algebraic equations system	156
8.1.4 Iterative method for linear algebraic equations system	157
8. 2 Numerical method for advection/diffusion equation	159
8.2.1 Definition of the equation and its boundary condition	159
8.2.2 Pressure equation for fluid dynamics calculation	163
8.2.3 Errors associated with numerical solution of advection/diffusion equation	166
8.2.4 Explicit methods	168
8.2.5 Implicit method	177
8.2.5 Fractional Steps Method or Alternative Direction Method.....	182
8.2.7 Comparison of various numerical schemes	187
8.3 Finite element method.....	189
8.3.1 Basis.....	189
8.3.2 Finite element formulation based on the method of weighted residuals....	190
8.3.3 FEM (Finite Element Method) equation.....	194
References	199
Appendix	200
9. Climate Change	205
9.1 Introduction	205
9.2 Climate system and its variability	207
9.2.1 Climate system	207
9.2.2 Forcing and response	210
9.2.3 Variability	214
9.2.4 Global Warming.....	215
9.3 Climate models.....	216
9.3.1 Energy Balance Model (EBM).....	216
9.3.2 AGCM an NWP	217
9.3.3 OGCM.....	218
9.3.4 Coupled models	218
9.4 Global warming issue.....	218

9.4.1 Detection	218
9.4.2 Prediction.....	219
9.4.3 Attribution	220
9.5 Summary	221
References	222

Practice

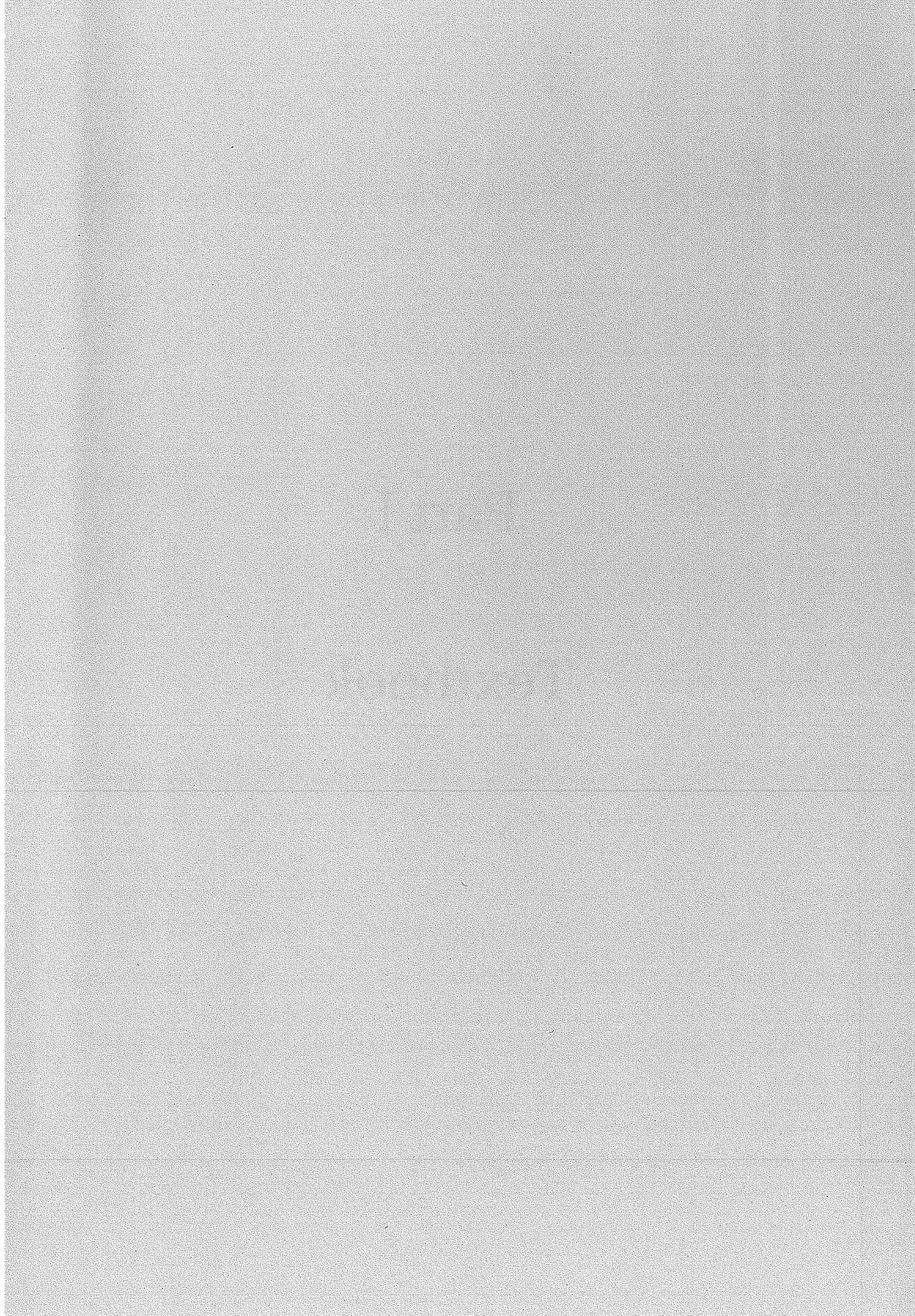
Computer Simulation of Transport of Pollutants in the Atmosphere.....	223
---	-----

Technical Tours

Remote Sensing Technologies of Atmospheric Sciences	235
Climate in the Past.....	245
The Earth Simulation Center	253
Part II Outline of the Training Course in 2004.....	259
Part III Past Activities of the IHP Training Course	265

Part I

Textbook



Chapter 1

Basics on Transport Processes of Air-Pollutant and their Modeling in the Atmosphere

Toshihiro KITADA
Faculty of Engineering,
Toyohashi University of Technology
Toyohashi, JAPAN
e-mail: kitada@earth.eco.tut.ac.jp

1.1 Basic equations of advection/diffusion/deposition of air-pollutants in the atmosphere

1.1.1 Modeling of environmental transport phenomena and role of their numerical analysis

Transport phenomena of momentum, heat, and mass in the atmosphere are often investigated by formulating mathematical model for the phenomena and solving the model equations to analyze, predict, and control the transport phenomena. Characteristics of this approach may be summarized as follows.

- ① We can examine the theoretical knowledge, on which mathematical models have their basis, by comparing the model's solution with field observation and laboratory experiment. As a result, deficiency of the theory might be pointed out.
- ② When we try to investigate how various fundamental processes interact each other and produce the observed phenomenon, only numerical solution of the mathematical model makes it possible. For example, often it is impossible to conduct controlled experiment on natural phenomena, while numerical experiment of the relevant mathematical model can do it.
- ③ Effective design of field observation or laboratory experiment becomes possible by executing the numerical analysis of the fundamental system

(model) in advance.

- ④ Perhaps the discovery of completely new phenomenon might be better carried out by field observation and laboratory experiment. However, mathematical model that was formulated on the basis of the various facts obtained with field observation and/or laboratory experiment still can find the phenomenon which is hidden in the system (model). This may be an important role of the mathematical model and its numerical analysis.
- ⑤ Mathematical models that describe transport phenomena of momentum, (thermal) energy, and mass with nonlinear chemical reactions usually can not be solved analytically, and thus some kind of numerical method is required for their solution. Methods of finite difference, finite element, and spectral method are usually applied for the solution of these partial differential equations.

1.1.2 Atmospheric advection-diffusion equation

Concentration of trace chemical species in environmental fluid such as the atmosphere, the ocean, the lakes, the rivers, etc. can be described by the solution of "advection-diffusion equation". In the atmosphere, for example, the time-varying distributions of the nitrogen oxide and SPM near the roadside, the oxidant on city or regional scale, acidic species on regional to country scale, and carbon dioxide on a terrestrial scale are usually obtained by the equation with the processes of non-linear chemical reactions, mass-transfer term between liquid phase and gas phase etc.

The advection-diffusion equation can be derived by applying "mass-conservation law" and an assumption on diffusional mass flux, as described in the following subsection.

(1) Mass conservation law

Assume a small volume of $\Delta V = \Delta x \Delta y \Delta z$ fixed in the atmosphere as in Fig. 1; then, mass conservation of a concerned trace chemical species in the volume can be written as follows:

$$\begin{aligned} \{\text{rate of temporal change of mass in the volume}\} = & \{\text{mass inflow velocity}\} \\ & - \{\text{mass outflow velocity}\} + \{\text{production or destruction rate of mass}\} \end{aligned} \quad (1)$$

where the "production or destruction rate" stands for the rate of emission source,

or chemical production/destruction.

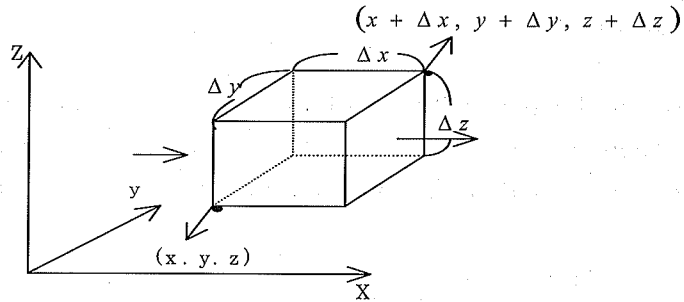


Figure 1. Volume element $\Delta x \Delta y \Delta z$. Arrows parallel to x axis show x -component of mass flux across face at x and $x + \Delta x$ as an example of contribution to the mass balance.

The following variables are used in the derivation of the advection-diffusion equation.

ρ : air density (kmol/m^3), C : concentration of the concerned trace chemical species (dimensionless), $\vec{N} = (N^x, N^y, N^z)$: flux of the species ($\text{kmol}/\text{m}^2 - s$), $\vec{V} = (u, v, w)$: flow velocity (m/s), D : molecular diffusivity in the atmosphere (m^2/s), R : reaction rate ($\text{kmol}/\text{m}^3 - s$), and S : source strength ($\text{kmol}/\text{m}^3 - s$).

Net mass flow rate per unit time, which enters into the volume (ΔV) across the faces perpendicular to the x axis, can be expressed with the term (2).

$$(N^x)_x \Delta y \Delta z - (N^x)_{x+\Delta x} \Delta y \Delta z \quad (2)$$

Similarly, the net mass flows through the other two sets of walls of the volume can be obtained.

Rates of production/destruction in the volume in unit time can be written as the terms (3a) and (3b).

$$R \Delta x \Delta y \Delta z \quad (3a)$$

$$S \Delta x \Delta y \Delta z \quad (3b)$$

In addition, the mass accumulated in ΔV during unit time can be written as Eq.(4).

$$\frac{\partial(\rho C)}{\partial t} \Delta x \Delta y \Delta z \quad (4)$$

After substitution of the terms (2) ~ (4) into Eq. (1), when both sides of the equation are divided through by $\Delta V (= \Delta x \Delta y \Delta z)$ and the limits of $\Delta x, \Delta y, \Delta z \rightarrow 0$ are taken, then the following Eq. (5) can be obtained.

$$\frac{\partial(\rho C)}{\partial t} = - \left(\frac{\partial N^x}{\partial x} + \frac{\partial N^y}{\partial y} + \frac{\partial N^z}{\partial z} \right) + R + S \quad (5)$$

Eq. (5) is a mathematical expression of the mass conservation law. Here, each component of mass flux vector (N^x, N^y, N^z) may be expressed by the sum of an advective (or convective) part and an diffusive part. Thus we may write the x component of the mass flux, N^x , as in Eq.(6).

$$N^x = u \rho C - \rho D \frac{\partial C}{\partial x} \quad (6)$$

By substituting Eq. (6) and similar expressions for N^y and N^z into Eq. (5), an advection-diffusion equation (7) can be obtained.

$$\begin{aligned} \frac{\partial(\rho C)}{\partial t} + \frac{\partial}{\partial x} (u \rho C) + \frac{\partial}{\partial y} (v \rho C) + \frac{\partial}{\partial z} (w \rho C) \\ = \frac{\partial}{\partial x} \left(\rho D \frac{\partial C}{\partial x} \right) + \frac{\partial}{\partial y} \left(\rho D \frac{\partial C}{\partial y} \right) + \frac{\partial}{\partial z} \left(\rho D \frac{\partial C}{\partial z} \right) + R + S \end{aligned} \quad (7)$$

Assuming $\rho \cong \text{constant}$, Eq. (7) can be rewritten as Eq. (8) where the concentration is redefined as $\tilde{C} \equiv \rho C$ ($\tilde{C}: \text{kmol}/\text{m}^3$).

$$\begin{aligned} \frac{\partial \tilde{C}}{\partial t} + \frac{\partial}{\partial x} (u \tilde{C}) + \frac{\partial}{\partial y} (v \tilde{C}) + \frac{\partial}{\partial z} (w \tilde{C}) \\ = \frac{\partial}{\partial x} \left(D \frac{\partial \tilde{C}}{\partial x} \right) + \frac{\partial}{\partial y} \left(D \frac{\partial \tilde{C}}{\partial y} \right) + \frac{\partial}{\partial z} \left(D \frac{\partial \tilde{C}}{\partial z} \right) + R + S \end{aligned} \quad (8)$$

In the same situation, Eq. (7) can also be expressed in a different way as Eq. (9) which is derived by dividing Eq. (7) with $\rho (= \text{const})$.

$$\begin{aligned} \frac{\partial C}{\partial t} + \frac{\partial}{\partial x}(uC) + \frac{\partial}{\partial y}(vC) + \frac{\partial}{\partial z}(wC) \\ = \frac{\partial}{\partial x}\left(D \frac{\partial C}{\partial x}\right) + \frac{\partial}{\partial y}\left(D \frac{\partial C}{\partial y}\right) + \frac{\partial}{\partial z}\left(D \frac{\partial C}{\partial z}\right) + \frac{1}{\rho}(R + S) \end{aligned} \quad (9)$$

By using the continuity equation of $\frac{\partial \rho}{\partial t} + \nabla \cdot (\rho \vec{V}) = 0$ (a complete form) or $\nabla \cdot \vec{V} = 0$ (the continuity equation for homogeneous or heterogeneous incompressible fluid), Eqs. (7) and (9) are further rewritten as Eqs. (10) and (11), respectively.

$$\begin{aligned} \rho \frac{\partial C}{\partial t} + \rho u \frac{\partial C}{\partial x} + \rho v \frac{\partial C}{\partial y} + \rho w \frac{\partial C}{\partial z} \\ = \frac{\partial}{\partial x}\left(\rho D \frac{\partial C}{\partial x}\right) + \frac{\partial}{\partial y}\left(\rho D \frac{\partial C}{\partial y}\right) + \frac{\partial}{\partial z}\left(\rho D \frac{\partial C}{\partial z}\right) + R + S \end{aligned} \quad (10)$$

$$\begin{aligned} \frac{\partial C}{\partial t} + u \frac{\partial C}{\partial x} + v \frac{\partial C}{\partial y} + w \frac{\partial C}{\partial z} \\ = \frac{\partial}{\partial x}\left(D \frac{\partial C}{\partial x}\right) + \frac{\partial}{\partial y}\left(D \frac{\partial C}{\partial y}\right) + \frac{\partial}{\partial z}\left(D \frac{\partial C}{\partial z}\right) + \frac{1}{\rho}(R + S) \end{aligned} \quad (11)$$

Eqs. (7), (8), and (9) are called the “conservation form” of advection-diffusion equation, while Eqs. (10) and (11) the “advection form”.

(2) Turbulent diffusion equation

Atmospheric flow is usually thought to be turbulent, because of large Reynolds number, e.g., $\text{Re} = \frac{V d}{\nu} \approx \frac{2(m/s) \cdot 10(m)}{0.2 \times 10^{-4}(m^2/s)} = 10^6$. Thus we need an

equation to be able to predict averaged concentration under turbulent flow. As an example, let us use Eq. (8) for its derivation. For simplicity, the reaction term R and

the emission term S in Eq. (8) are eliminated. First, let us assume that physical and chemical quantities consist of average value (ensemble average or time-average) and fluctuation from the average; e.g., $C = \bar{C} + C'$, $u = \bar{u} + u'$, etc. Substitute these relations into Eq. (8) and take average on Eq. (8), O.K. Eq. (12) can be obtained; on the averaging procedure, appropriate rule is applied such as

$$\begin{aligned} \overline{u'C'} &= 0, \quad \overline{u\bar{C}} = \bar{u}\bar{C}, \quad \overline{\frac{\partial u'C'}{\partial x}} = \frac{\partial \overline{u'C'}}{\partial x}, \text{ etc.} \\ \frac{\partial \bar{C}}{\partial t} + \frac{\partial(\bar{u}\bar{C})}{\partial x} + \frac{\partial(\bar{v}\bar{C})}{\partial y} + \frac{\partial(\bar{w}\bar{C})}{\partial z} \\ &= D \left(\frac{\partial^2 \bar{C}}{\partial x^2} + \frac{\partial^2 \bar{C}}{\partial y^2} + \frac{\partial^2 \bar{C}}{\partial z^2} \right) - \frac{\partial(\overline{u'C'})}{\partial x} - \frac{\partial(\overline{v'C'})}{\partial y} - \frac{\partial(\overline{w'C'})}{\partial z} \end{aligned} \quad (12)$$

where $\overline{u'C'}$, $\overline{v'C'}$, $\overline{w'C'}$ are called turbulent mass flux. These turbulent fluxes are often treated by using the hypothesis of Boussinesq as Eq. (13).

$$\overline{u'C'} = -K_{xx} \frac{\partial \bar{C}}{\partial x}, \quad \overline{v'C'} = -K_{yy} \frac{\partial \bar{C}}{\partial y}, \quad \overline{w'C'} = -K_{zz} \frac{\partial \bar{C}}{\partial z} \quad (13)$$

where K_{xx} etc. are called turbulent diffusivity or eddy diffusivity.

By substituting the relations of (13) into Eq. (12), Eq. (14) is obtained.

$$\begin{aligned} \frac{\partial \bar{C}}{\partial t} + \frac{\partial(\bar{u}\bar{C})}{\partial x} + \frac{\partial(\bar{v}\bar{C})}{\partial y} + \frac{\partial(\bar{w}\bar{C})}{\partial z} \\ = \frac{\partial}{\partial x} \left(K_{xx} \frac{\partial \bar{C}}{\partial x} \right) + \frac{\partial}{\partial y} \left(K_{yy} \frac{\partial \bar{C}}{\partial y} \right) + \frac{\partial}{\partial z} \left(K_{zz} \frac{\partial \bar{C}}{\partial z} \right) \end{aligned} \quad (14)$$

In Eq. (14), molecular diffusivity "D" is ignored since it is much smaller than the turbulent diffusivity; for example, $D \approx 0.2 \text{ cm}^2 / \text{s}$, while $K_{zz} \approx 0.1 \sim 100 \text{ m}^2 / \text{s}$; thus,

$$K_{xx}, K_{yy}, K_{zz} \gg D$$

Turbulent diffusivity varies with the state of the atmosphere such as wind shear, and thermal stratification, and is, thus, a function of time and spatial position.

Determination of this eddy diffusivity is an important problem. One way for this is to follow Prandtl's theory, so called "mixing length theory". Prandtl (1925) proposed the following model:

(1) Eddy diffusivity is proportional to the product of "turbulent velocity scale" and "turbulent length scale" which is analogy of the molecular diffusivity given by product of "average velocity of molecular motion" and "mean free path of the molecule".

(2) The turbulent length scale (that is, "mixing length") is a function of distance from solid wall, and the turbulent velocity scale is estimated with spatial gradient of velocity multiplied by the length scale.

The Prandtl's concept (1), in particular, is still used to obtain eddy diffusivity. There are several classes of model based on the the Prandtl's concept (1). Like mixing length theory, the model which does not need new differential equation for describing turbulent state is called "0 equation model". The "one equation model" additionally adopts one differential equation for turbulent kinetic energy, k . In this model the turbulent kinetic energy gives information on the "turbulent velocity scale", while the length scale is usually given by a linear function of the height from the ground to a certain height and is given with a fixed constant value above the height. The "two-equation model" solves two additional differential equations for the estimation of the turbulent velocity scale and length scale. There are two famous "two-equation" models; that is, one is $k-\epsilon$ (dissipation rate of turbulent kinetic energy) model, and the other is $k-k_l$ model, where k_l stands for a dependent variable of the product of turbulent kinetic energy and length scale.

Well-known Monin-Obukhov similarity theory for the surface layer can be regarded a "0-equation model".

1.1.3 Boundary condition

Equations (7)~(11) and (14) are non-steady partial differential equations. Hence to determine the solution of the equations requires initial and boundary conditions specified. Three kinds of boundary conditions are possible.

Dirichlet boundary condition specifies concentration on the boundary as Eq. (15).

$$C = C_1 \quad (15)$$

where C_1 can be a function of time and space.

Neumann boundary condition specifies gradient or flux on the boundary as Eq.(16).

$$\frac{\partial C}{\partial n} (= \vec{n} \cdot \nabla C) = f \quad (16)$$

where \vec{n} is the outward unit vector normal to the boundary surface.

Robin boundary condition is given by Eq. (17), and is a mixed form of the Dirichlet and Neumann boundary conditions. Since the first term and the second term on the left-hand side in Eq. (17) can express diffusional mass flux and advective mass flux, respectively, Eq. (17) is useful in atmospheric diffusion calculation.

$$h_1 \frac{\partial C}{\partial n} + h_2 C = h_3 \quad (17)$$

1.1.4 Qualitative description of air pollutant transport in the atmosphere

(1). Structure of the atmosphere

The troposphere is characterised by active convection, which transports various chemical species discharged at the ground into free troposphere. The depth of the troposphere is 15~20 km thick in tropical region, and 8 km thick in high latitudinal area. The interface between stratosphere and troposphere is called tropopause, and because of stable stratification in the stratosphere, the tropopause usually serves as a barrier to the mass exchange between both regions. Fig. 2 shows typical flow structure in the troposphere (i.e., general circulation). In Fig. 2a, three circulations of Hadley Cell, Ferrel Cell, and Polar Cell can be seen on the meridional-vertical plane.

The lowest layer of 1~2 km in depth in the troposphere is atmospheric boundary layer, temperature of which is affected by diurnal variation in temperature at the ground in a day. Furthermore, the lowest 50~100 m from the ground is called surface layer, and can be regarded as constant flux layer in which various fluxes such as momentum, heat, and mass are constant regardless of height. The atmospheric boundary layer and surface layer are most important for air pollution transport. Fig. 3 describes features of the boundary layer.

Fig. 4 shows temporal and spatial scales of various kinds of flow systems in the troposphere. They are related to characteristic air pollution phenomena, which

will be briefly discussed in later subsection.

(2) Effect of wind speed and thermal stratification on mass transport

(i) Wind speed and fluctuation of wind direction

Large wind velocity dilutes pollutant concentration more effectively as shown in Fig. 5. Strong wind generates large wind shear, and hence strong turbulence further enhances pollutant's dispersion.

Fluctuation of wind direction also contributes to dispersion of smoke as in Fig. 6.

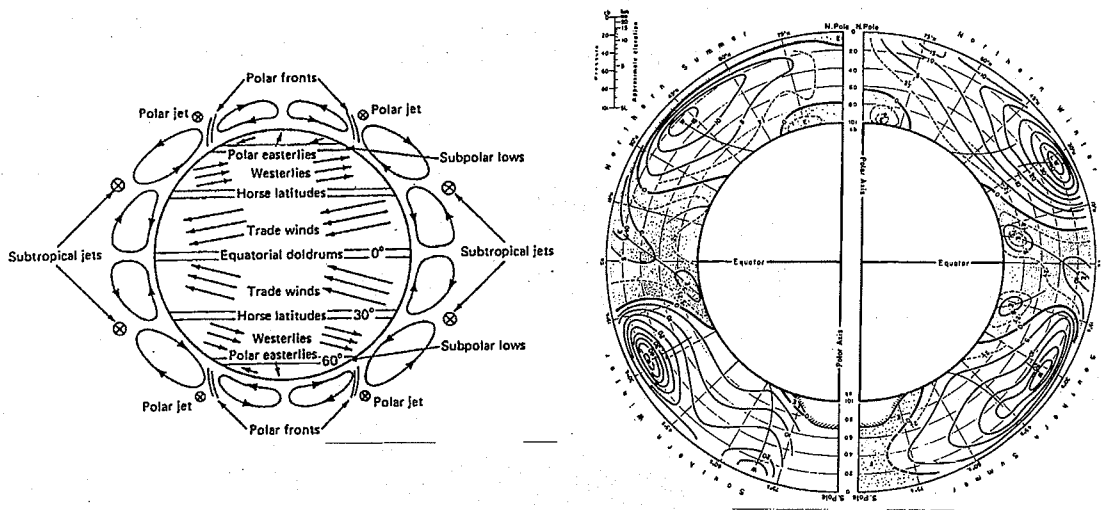


Figure 2. (a) General circulation in the troposphere, and (b) contours of zonal wind in summer of the northern hemisphere (left), and in winter of it (right); positive number shows westerly.

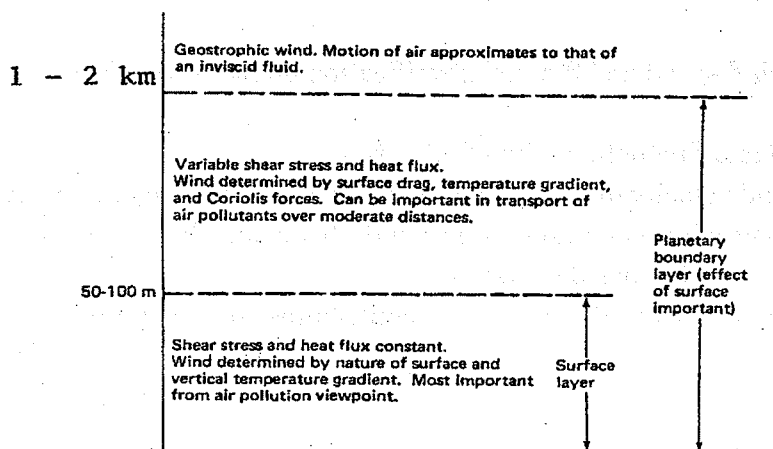


Figure 3. Atmospheric boundary layer and surface layer.

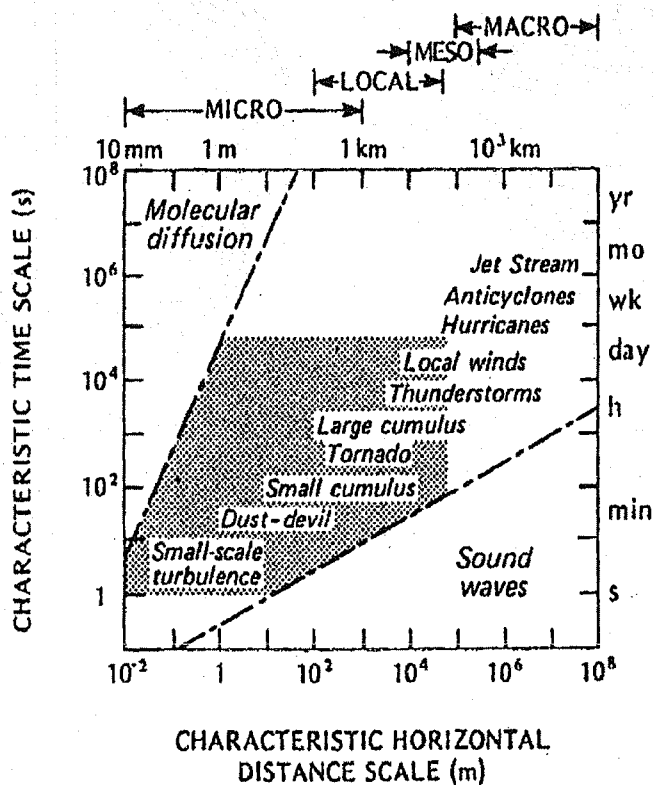


Figure 4. Various phenomena in the troposphere: their temporal and spatial scales (Smagorinsky, 1974).

(ii) Atmospheric stability: thermal stratification.

The atmosphere is thermally stratified. Hence vertical diffusion strongly depends on the stratification. Vertical motion of the airmass occurs almost adiabatically. Thus, when the vertical gradient of the temperature is larger or smaller than the dry-adiabatic lapse rate, the atmosphere is called “unstable” or “stable”, respectively. In the “neutral” state, the temperature gradient is equal to the lapse-rate; the dry-adiabatic lapse rate is about 10 K/km. Under unstable situation, of course, vertical mixing is strong and smoke rapidly disperses. Fig. 7 illustrates how the thermal stratification changes the smoke dispersion. In real situation, vertical gradient of the temperature varies with height, and examples such as “roof” type (Fig. 7d) and “fumigation” type (Fig. 7e) can occur.

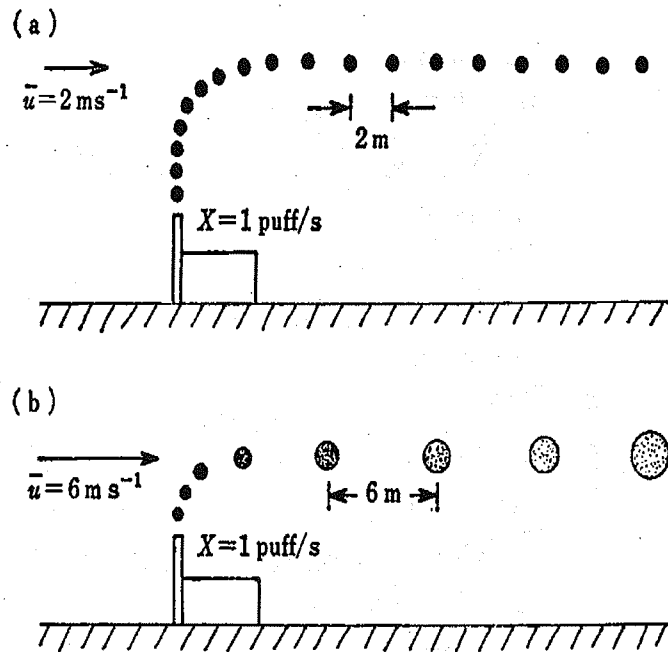


Figure 5. Dilution of smoke due to wind velocity: elongation of smoke (Oke, 1978).

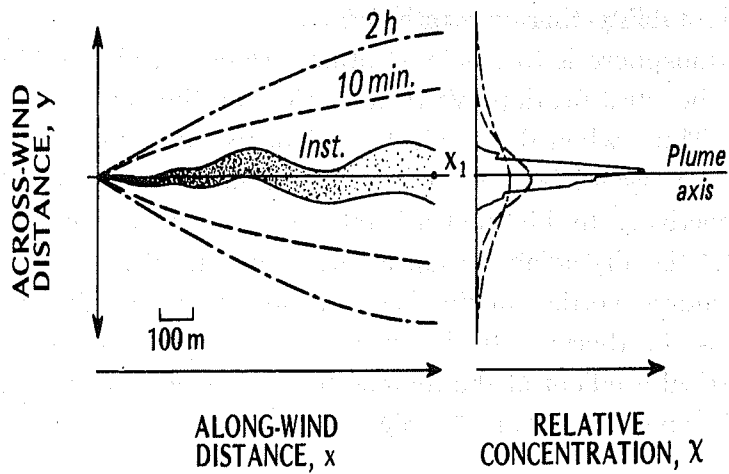


Figure 6. Horizontal spreading of smoke due to the fluctuation of wind direction (Oke, 1978).

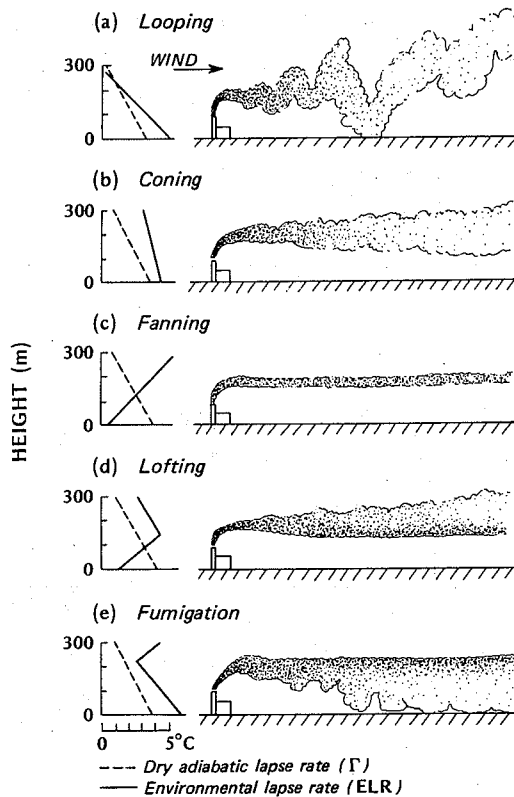


Figure 7. Smoke diffusion under different thermal stratification (Oke, 1978).

In particular, the layer in which the temperature increases with height is called an “inversion” layer, and this layer serves as a barrier for the vertical mass transport. Fig. 8 shows several mechanisms by which the inversion layer is formed aloft; (a) & (b) inversion by downward blowing wind associated with high pressure system, (c) temperature rise by the wind blowing over the mountain, and (d) warming by the downward air motion between clouds. The well known inversion can develop at the surface level because of radiational cooling of the ground during the nighttime, and it is called “surface inversion”. The surface inversion tends to cause severe air pollution since most of the emission sources are located at the ground level. Fig. 9 shows observed diurnal variation of temperature profile in Aichi Pref., Japan. The figure demonstrates development of the “surface inversion” in early morning.

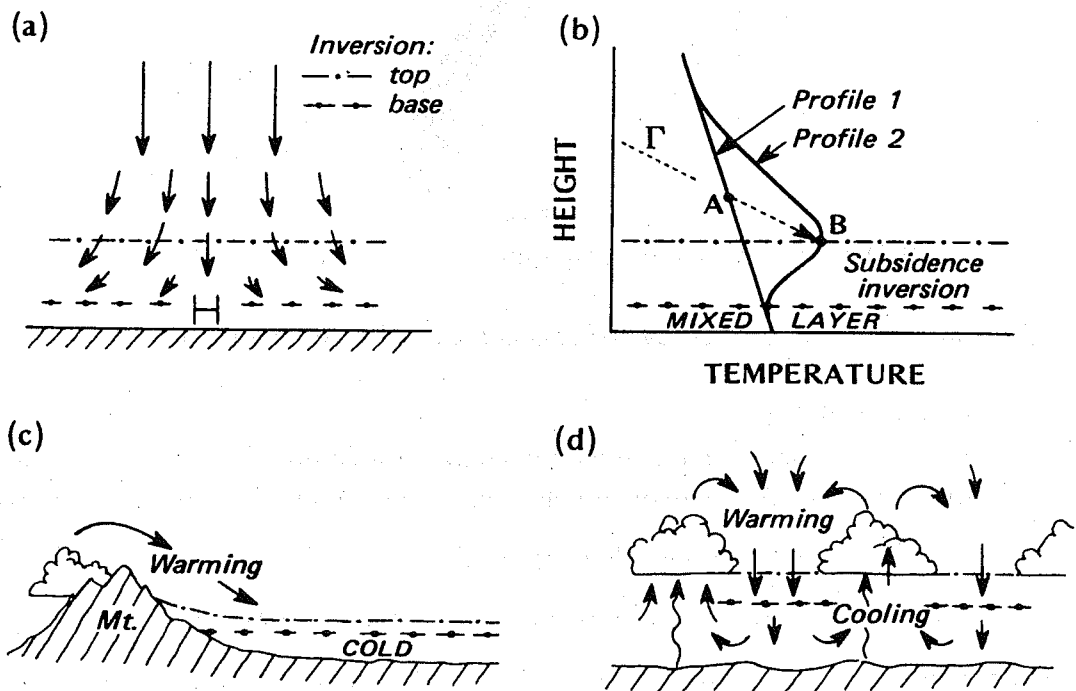


Figure 8. Formation of inversion layer (Oke, 1978)

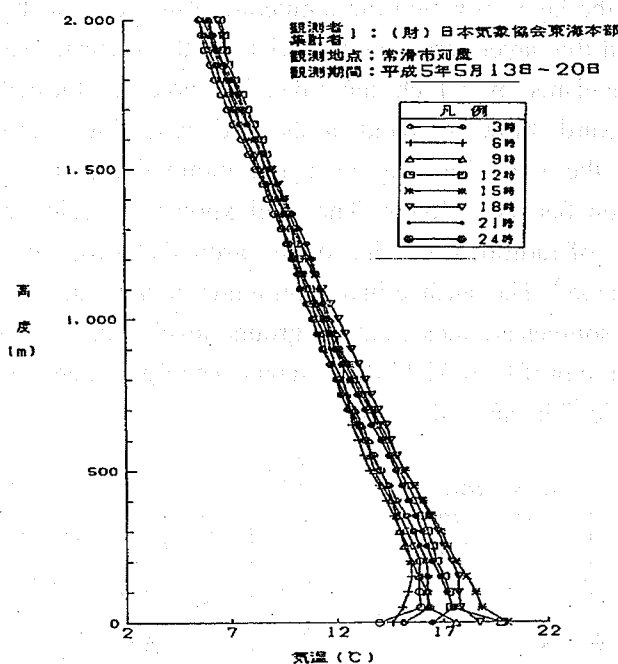


Figure 9. Diurnal variation of temperature profile: May, Aichi Prefecture.

(3) Flow modified and induced by building and small scale topography

(i) Flow around building

Around an obstacle such as building, characteristic flow is formed as shown in Fig. 10. Though the flow can be largely changed depending on Reynolds number, $Re (= Vh_B / \nu)$, and internal Froude number, $Fr (= V / \sqrt{g'h_B})$, the flow in Fig. 10 can be regarded as typical. In these two dimensionless numbers, V is the wind velocity, h_B is the height of the building, ν is the kinematic viscosity of the air, and $g' = (\Delta\theta/\theta)g$ is the gravitational acceleration modified by thermal stratification; θ is, for example, the potential temperature at the ground level in K, and $\Delta\theta$ is the gap of θ between the ground and top of the building.

The flow passing over the building generates positive pressure on the upstream side of the building, and negative pressure on the roof, the side walls and the downstream side of the building; the “positive” and “negative” indicate difference from the reference pressure in the area not-affected by the building.

These pressure fluctuations modify stream lines, generate secondary circulation and separation of the flow, and thus form turbulence as indicated in Fig. 10. As shown in Fig. 10a, when the building is close to a cube and general flow blows normal to the building wall (i.e. 0 incidence angle), the height of the "cavity" zone behind the building is about 1.5 times of the building height (h_B) and the length is about $2.5-3h_B$ from the upstream edge of the building. If the width of the building is large, then the height becomes much larger and the length reaches even $12h_B$. If the building is long for the wind direction or the building is submerged within turbulent shear flow, the flow around the building may reattach to the roof or the side walls of the building. In case of wide and long building, the cavity zone may reach the distance of $7h_B$ from the leeside of the building.

The cavity zone is not enclosed by the stream line starting from the upstream edge of the roof but by the one originating from the wall of upstream side. Thus pollutant can enter into the cavity zone not only by eddy diffusion crossing the streamlines but also by advection along the streamline from the upstream side of the building.

Behind the cavity zone, aerodynamical downwash occurs and the pollutant discharged above the building roof is sometimes brought down to the ground. In addition, wake zone with large turbulence intensity extends over $5-30h_B$. The height of the cavity zone can be decreased by making edges of the building round or installing set-back at the lee side of the roof. In the displacement zone, the flow is accelerated.

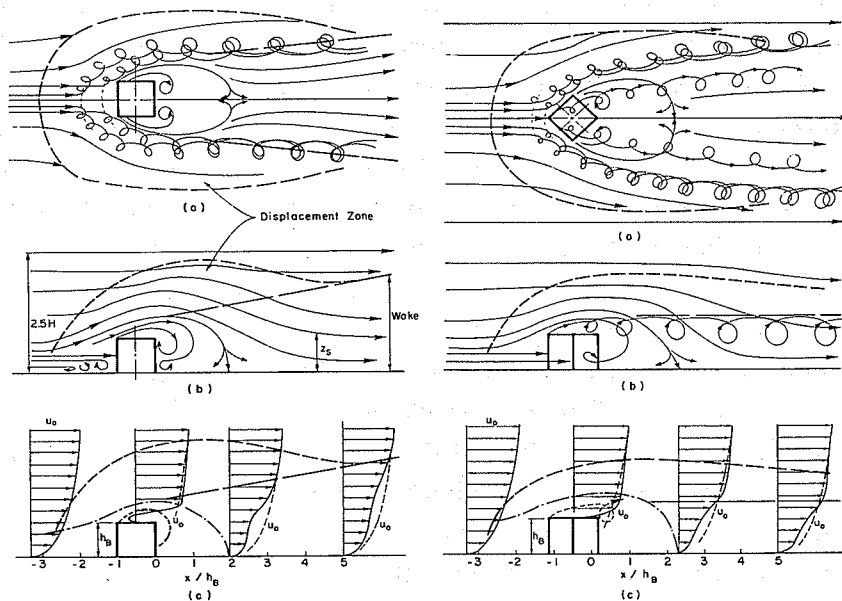


Figure 10(a). Stream lines around a cubical building: 0°orientation (Meroney, 1982).

Figure 10(b). Same as in Fig. 10(a) but for 45°orientation (Meroney, 1982).

(ii) Air quality around road and building

Movement of air pollutant modified by the characteristic flow around the buildings can be predicted by examining the flow field shown in Fig. 10. For example, in so-called "street canyon", ventilation of the polluted air mass in the canyon is controlled by a ratio of $\Delta H / \Delta R$ where ΔR stands for the width of the road and ΔH is the characteristic height of the buildings. As can be seen in Fig. 11a,b, a small ratio of $\Delta H / \Delta R$ leads to better ventilation, and vice versa. When $\Delta H / \Delta R$ is large, the space between the buildings is formed almost by the "cavity zone", and thus the air mass tends to stagnate in the canyon.

Behind a tall building, the cavity zone also traps air pollutant. When the chimney on the building's roof is not tall enough for the ventilation of the pollutant into the displacement zone, the polluted air mass tends to be brought down to the ground and to be accumulated within the vortex (see Fig. 11 c,d). Figs. 12 and 13 show how the pollutant released at various locations in the flow shown in Fig. 10a is dispersed.

(iii) Characteristic flow and pollution transport around slope topography

Small topography such as a slope can also form characteristic wind field and seriously affect air quality. Fig. 14 illustrates a separating flow over the back-slope topography forms a lee eddy and this eddy can trap pollutant released from the chimney located on the slope (Fig. 14a) or can bring down to the ground the pollutant once discharged from a chimney at the foot of the slope (i.e., downwash; Fig. 14b).

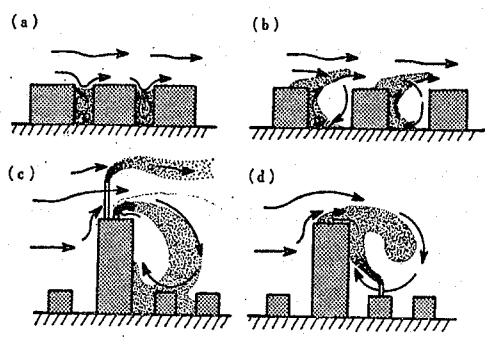


Figure 11. Pollutant dispersion: (a) & (b) street canyon, and (c) & (d) over and behind a tall building (Oke, 1978).

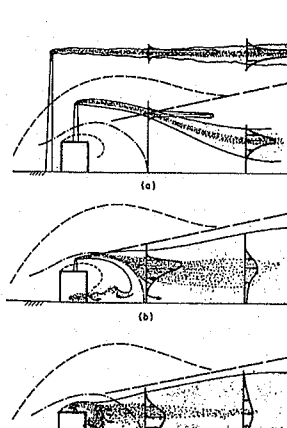


Figure 12. Short stack plume dispersion around a 0° orientation cubical building (Meroney, 1982).

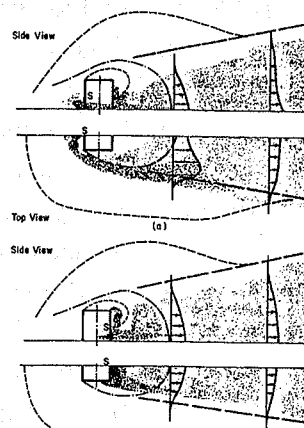


Figure 13. Flush vent exhaust dispersion around a 0° orientation cubical building (Meroney, 1982).

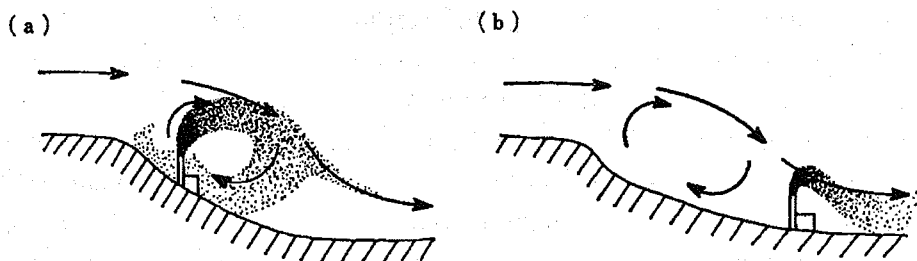


Figure 14. Pollutant transport over slope topography (Oke, 1978).

(4) Pollution transport by local wind: land and sea breeze, etc.

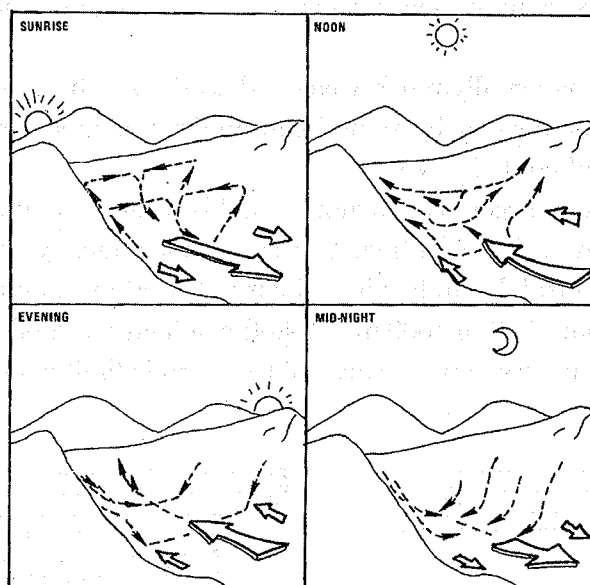
The "Local Winds" described in Fig. 4 represent land/sea breeze, mountain/valley wind, plain-to-plateau wind, and urban-rural wind. They are all formed by differential heating. Their characteristic time and size are one day and 100 km, respectively. These local winds tend to develop under weak synoptic flow condition associated with high pressure system, and they have often circulation on vertical plane.

(i) Mountain/valley wind

In the daytime, ground surface is heated by the solar radiation. When the surface on the slope in valley topography is heated and then the air over the surface is warmed, the temperature of the air is higher than that of air mass at the same altitude but over the plain or valley floor. Then positive buoyancy force tends to act on the air over the slope, and the force accelerates upward motion of the air. At the same time, air mass over the valley floor moves toward the slope to compensate it. In this manner, the valley wind starts in the morning. This mechanism is basically same to that of up-slope wind. In the case of the valley wind, however, its wind speed tends to be larger since air over the valley has larger ratio of its heated surface area to its volume compared with the air over the simple slope and thus the air over the valley is heated more effectively during the daytime. During the nighttime, the air over the slope is cooled from the surface, and thus the reverse wind, i.e. down-slope wind and mountain wind, occurs. In the upper layer over the center of the valley floor, a compensating flow is formed; that is, downward flow during the daytime and upward flow during the nighttime. Figure 1.15 schematically shows diurnal variation of the wind caused by this flow mechanism.

(ii) Land and sea breeze

Land and sea breezes are formed by differential heating between land and sea surfaces. Let us assume that the temperatures over the land and sea surfaces are the same at some time point in the morning. As the solar radiation becomes strong, the air over the land is rapidly warmed and its temperature increases while the temperature over the sea surface is kept rather constant. One reason is that the water has larger heat capacity than the land surface such as soil and buildings, and another reason is that the rate of heat exchange between surface and deeper layers is much faster for sea water than for land.



Valley winds caused by the heating and cooling of the sides of the valley, according to Defant, 1951.

Figure 15. Conceptual map showing diurnal change of mountain and valley wind (Defant, 1951).

The air column over land area, being heated below, expands vertically, while that over sea surface does not. Hence, at the upper layer into which the heated air penetrates from the boundary layer, atmospheric pressure over the land becomes higher than that over the sea, and thus air mass starts to migrate from the land to the sea at the upper layer. By this migration of the air, atmospheric pressure at the surface level becomes higher in turn over the sea than the land, and hence the sea breeze starts. During the daytime when the heating of the land surface is continued, the sea breeze is maintained. In contrast to this, a reverse wind called the land breeze blows from land to sea during the nighttime due to the reverse mechanism. Figure 16 shows this land and sea breeze mechanism schematically. Figure 17 illustrates vertical cross section of the sea and land breezes. The figures also demonstrate that thermal internal boundary layer (plotted with the dashed line) is possibly formed in the daytime and the nighttime. During the daytime, the internal boundary layer develops over the land (Fig. 17a); the atmosphere is unstably stratified below the layer and is neutral or weakly stable above the layer. Similarly, an internal boundary layer appears also in the nighttime (Fig. 17b), when the cooler air mass originated from the land is heated over the warm sea surface. In general,

the nighttime heat flux from the sea surface is not so strong and the internal layer is shallow.

The land breeze is usually much weaker than the sea breeze, since the stably stratified surface layer formed by radiational cooling of land surface suppresses further development of cool air layer.

In realistic cases a larger scale synoptic wind is often superimposed, and these land/sea breezes tend to be modified. In the summertime, typical sea breeze in coastal area of the central Japan has its velocity of $5\sim6\text{ ms}^{-1}$, and the depth of the sea breeze layer is about 500 to 1000 m, while the velocity of land breeze is at most 2 ms^{-1} , the depth is 50 m or so and the area of the wind is limited near the coast.

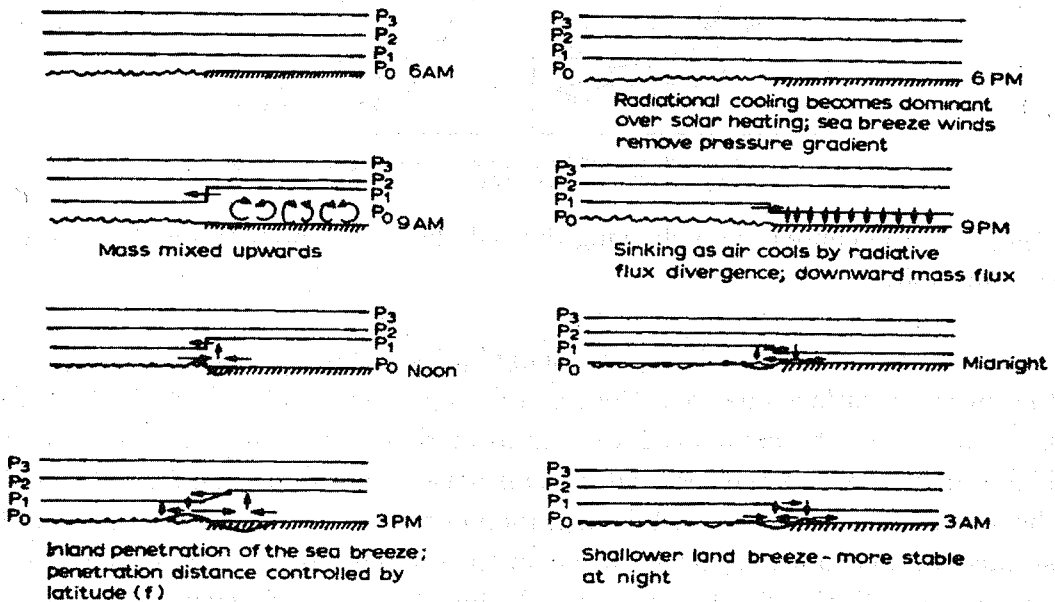


Figure 16. Conceptual map showing mechanism of diurnal variation of land/sea breeze (Pielke, 1982).

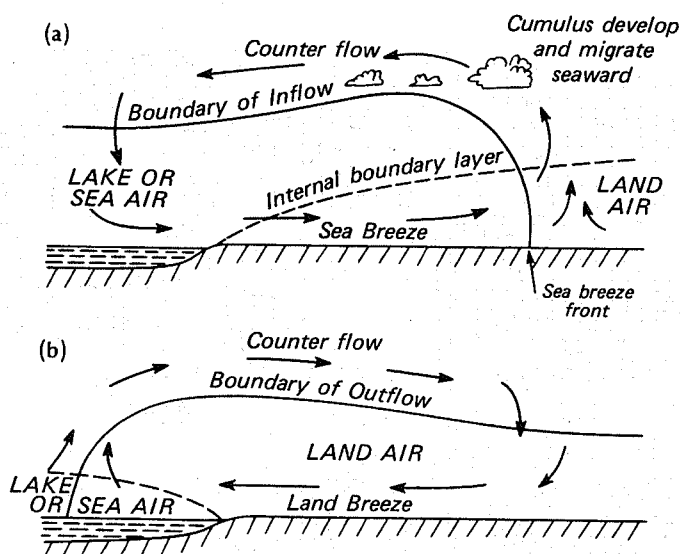


Figure 17. Circulations of (a) sea breeze and (b) land breeze; development of internal boundary layers is also illustrated; during the daytime, the thermal internal layer is formed over the land area, while over the ocean surface during the nighttime (Oke, 1978).

In the thermal internal boundary layer during the daytime (Fig. 17a), so called fumigation phenomena may occur. Figure 19a suggests that the pollutant once discharged from high stack in the coastal area may be incorporated into the internal layer, and be brought down to the ground and trapped within the layer. The sea (and land) breeze can be regarded as a gravity current, which is the flow of heavier (cooler) fluid under lighter (warmer) fluid driven by gravity. Thus the pollutant released into the sea breeze layer moves inlandward with the head of the gravity current (Kitada and Ueda, 1989; Kitada and Kitagawa, 1990). The sea breeze front can give different effect on the transport of the pollutant released into sea breeze layer and that discharged at inland area prior to the arrival of the front. Figure 18a shows temporal development of hypothetical non-buoyant particles emitted in the sea breeze layer, suggesting that these particles eventually catch up with the front and then moves with the front. Thus the frontal air is formed with dirty air mass in which the pollutants from the coastal area are accumulated. In contrast to Fig. 18a Fig. 18b illustrates that the pollutants released in inland area are carried upward at the front and then either stagnate there or migrate to the coastal area in the return flow of the sea breeze (Kitada and Kitagawa, 1989).

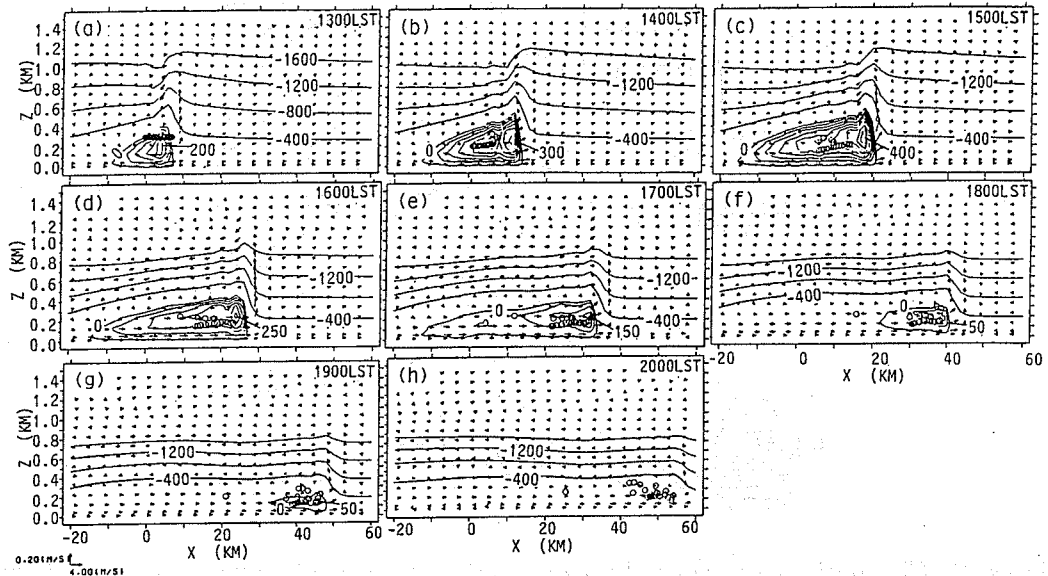


Figure 18a. Temporal development of the hypothetical non-buoyant particles released in the sea breeze layer (Kitada and Kitagawa, 1989).

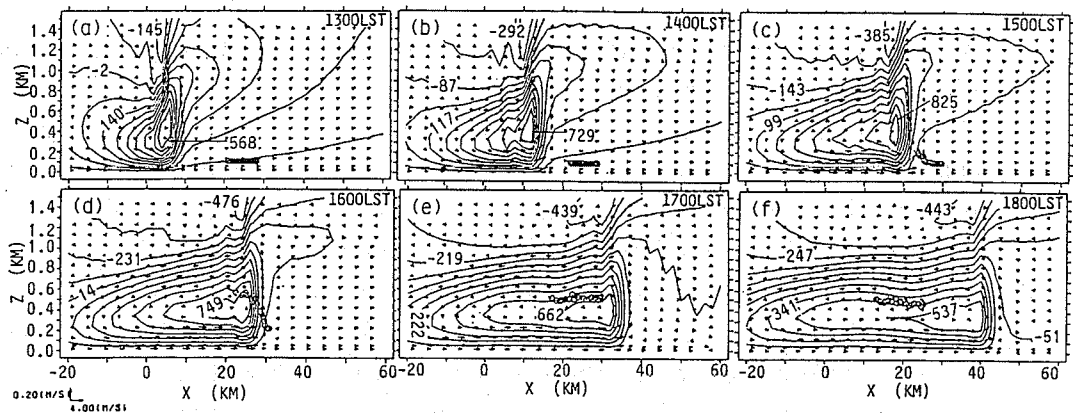


Figure 18b. Same as in Fig. 18a but for the particles released in the inland area prior to the arrival of the sea breeze front (Kitada and Kitagawa, 1989).

Similar phenomena can also occur over the urban area (Fig. 19b), since contrast of urban and rural areas can be the same to that of land and sea. As suggested in Fig. 19a, stably stratified rural air may cap the urban canopy and thus vertical movement of the polluted air over the urban area might be suppressed.

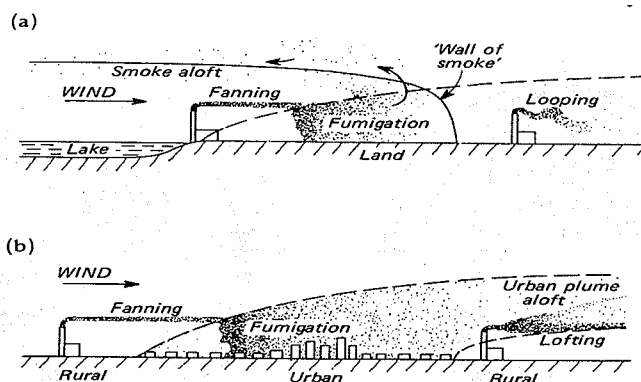
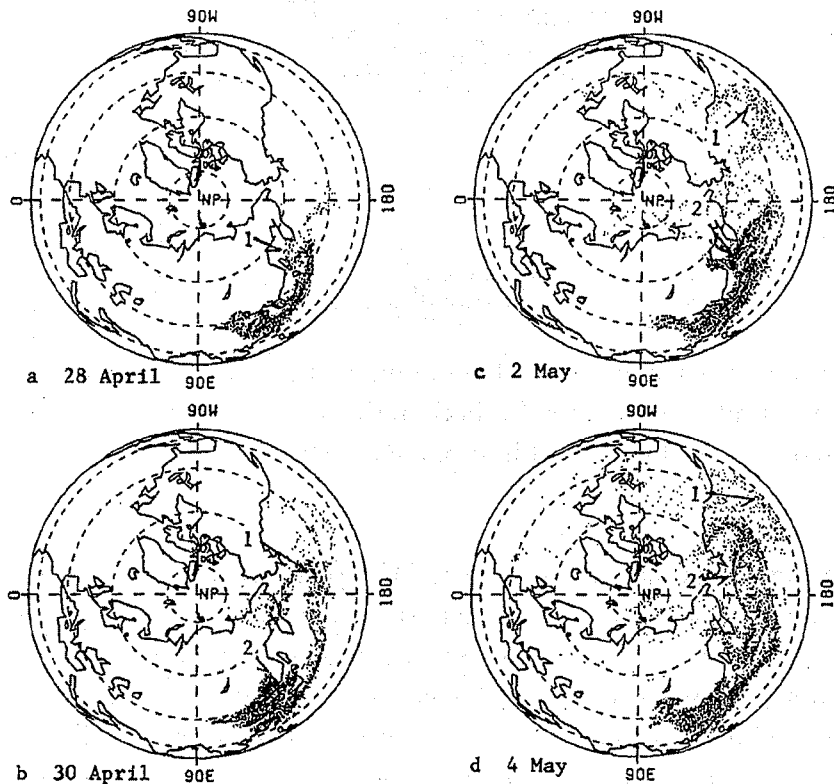


Figure 19. Schematic maps of possible pollutant transport in sea breeze (a) and in the wind from rural to urban area (b) both in the daytime. Similarity in both cases is demonstrated: i.e. development of internal boundary layer (Oke, 1978).

(5) Pollution transport induced by high and low pressure systems

In mid-latitudinal area of the northern hemisphere, periodic passage of high and low pressure systems dominates the weather in synoptic scale particularly in spring and autumn. Associated with this periodic change of pressure systems, large scale mass transport of air pollutants often occurs. For example, a huge amount of air pollutants such as sulfate can be transported toward the Pacific Ocean in East Asia in winter and spring; the pollutants are discharged in China, Korea, Japan, Taiwan, etc., which form one of the largest emission source regions in the world. In East Asia, the long range transport of not only the anthropogenic air pollutants but also natural soil dust "Kosa (yellow sand)" is prominent in these seasons. This long range transport of the yellow sand has long been observed at the remote islands such as Wake islands in the Pacific Ocean.

Figure 20 shows calculated temporal evolution of the transport of hypothetical non-buoyant particles, regarded as sulfur containing pollutants emitted from China in spring (Kitada and Tanaka, 1992). The figure suggests that the pollutants tend to accumulate over the source areas under the high pressure system, and the pollutants are subsequently carried over the Pacific Ocean by the low pressure systems. For example, in the simulated period of about ten days from April 25 to May 4, 1986 the low pressure system passed twice over the area. By the events, the clusters of the particles, depicted with the numbers of "1" and "2", show their characteristic distributions (Fig. 20).



Computed horizontal distribution in case 1, 2 and 3 (see Table 1): at 1200GMT on (a) 28 April, (b) 30 April, (c) 2 May, and (d) 4 May, 1986. Symbols "1" and "2" denote the event number of the particular low pressure systems which passed over East Asia. The simulation was initiated at 1200GMT on 25 April, 1986.

Figure 20. Long range transport of SO_2 and Sulfate associated with high- and low-pressure systems (Kitada & Tanaka, 1992).

1.2 Gaussian plume/puff models

1.2.1 Analytical solution

When $C(x, y, z, t)$ satisfies advection-diffusion equation (i.e., Eq. (7), (8), (9), (10), (11), (14) etc.) with boundary condition such as Eqs. (15), (16), and (17) and initial condition, it is called analytical solution. So far, only limited numbers of

analytical solutions are obtained. Some of the solutions are introduced in the following sub-sections.

(1) Instantaneous point source — Constant diffusivity (Roberts, O.F.T.: The theoretical scattering of smoke in a turbulent atmosphere, Proc. Roy. Soc., A, 104, 640, 1923)

Roberts solved analytical solution of unsteady pure-diffusion equation in infinite 3-D domain for the case of instantaneous discharge of pollutant at $(x, y, z) = (0, 0, 0)$. Isotropic uniformity is assumed on the medium.

$$\frac{\partial C}{\partial t} = K \left(\frac{\partial^2 C}{\partial x^2} + \frac{\partial^2 C}{\partial y^2} + \frac{\partial^2 C}{\partial z^2} \right) \quad (18)$$

$$C \rightarrow \infty \quad \text{as} \quad t \rightarrow 0 \quad \text{at} \quad (x, y, z) = (0, 0, 0)$$

$$C = 0 \quad \text{as} \quad t \rightarrow 0 \quad \text{at} \quad r \neq 0 \quad (r = x^2 + y^2 + z^2)$$

$$C = 0 \quad \text{as} \quad r \rightarrow \infty \quad \text{at} \quad t > 0$$

$$\iiint_{-\infty}^{\infty} C \, dx \, dy \, dz = Q$$

$$\text{Solution: } C = \frac{Q}{8(\pi K t)^{3/2}} \exp \left(-\frac{x^2 + y^2 + z^2}{4 K t} \right) \quad (19)$$

Eq. (19) can be modified so that it allows discharge of the pollutant at an arbitrary point, and also it accommodates migration of pollutant by wind and diffusion with different diffusivity for each direction. For example, when the pollutant discharged at a point P (x_0, y_0, z_0) at time t_0 migrates with constant wind $\vec{V} = (u, v, w)$, Eq. (19) can be rewritten as Eq. (20):

$$C = \frac{Q}{8\{\pi^3(t-t_0)^3 K_x K_y K_z\}^{1/2}} \times \exp \left\{ -\frac{1}{4(t-t_0)} \left[\frac{(x-x_0-ut)^2}{K_x} + \frac{(y-y_0-vt)^2}{K_y} + \frac{(z-z_0-wt)^2}{K_z} \right] \right\} \quad (20)$$

Different diffusivity for different direction shown in Eq. (20) was introduced into

the solution (19) by applying following transformation to Eq. (18); i.e. $(x, y, z) \rightarrow (\xi_1, \xi_2, \xi_3)$:

$$\xi_1 \equiv x\sqrt{K/K_x}, \quad \xi_2 \equiv y\sqrt{K/K_y}, \quad \text{and} \quad \xi_3 \equiv z\sqrt{K/K_z} \quad (21)$$

(2) Continuous point source — Constant diffusivity (Roberts, 1923)

Steady state advection-diffusion equation in 3-D space with constant wind velocity u (Eq. 22) and constant diffusivity was solved by Roberts (1923); the solution is given by Eq. (23).

$$u \frac{\partial C}{\partial x} = K_y \frac{\partial^2 C}{\partial y^2} + K_z \frac{\partial^2 C}{\partial z^2} \quad (22)$$

Emission Q : constant strength ($kmol/s$), and released at the origin.

$$\text{(Solution)} \quad C = \frac{Q}{4\pi x (K_y K_z)^{\frac{1}{2}}} \exp \left[-\frac{u}{4x} \left(\frac{y^2}{K_y} + \frac{z^2}{K_z} \right) \right] \quad (23)$$

(3) Continuous line source — Constant diffusivity (Roberts, 1923)

Steady state advection-diffusion equation in $x - z$ space with constant u and K_z (Eq. 24) was given as Eq. (25) by Roberts (1923).

$$u \frac{\partial C}{\partial x} = K_z \frac{\partial^2 C}{\partial z^2} \quad (24)$$

Emission Q : constant strength ($kmol/m-s$); released at $(x, z) = (0, 0)$.

$$\text{(Solution)} \quad C = \frac{Q}{2(\pi K_z u x)^{\frac{1}{2}}} \exp \left(-\frac{uz^2}{4K_z x} \right) \quad (25)$$

1.2.2 Statistical model

Another algebraic equation model, i.e. "statistical model", can be obtained by considering statistical nature of the concentration distribution in turbulent field. Characteristic of both analytical and statistical models may be summarized as follows:

- { Analytical model: Given by solution of advection-diffusion equation; effect of turbulence can be taken into account through eddy diffusivity.
- Statistical model: Concentration distribution is derived directly from statistical characteristics of turbulent field.

(1) General formulation

For derivation of the statistical models, first the following distribution functions are assumed:

Instantaneous point source:

$$C = A_1 \exp \left[- \left(a |x|^p + b |y|^r + C |z|^s \right) \right] \quad (26)$$

Continuous point source:

$$C = A_2 \exp \left[- \left(b |y|^r + C |z|^s \right) \right] \quad (27)$$

Continuous line source:

$$C = A_3 \exp \left[- C |z|^s \right] \quad (28)$$

Then coefficients of $A_1 \sim A_3$ and $a \sim c$ in Eqs. (26) ~ (28) are tried to be expressed in terms of distribution index " p, r, s ", standard deviation ("smoke width") " $\sigma_x, \sigma_y, \sigma_z$ ", and emission strength Q .

The following relations are used for the above mentioned task:

$$\sigma_x^2 = \frac{\int_{-\infty}^{\infty} x^2 C dx}{\int_{-\infty}^{\infty} C dx}, \sigma_y^2 = \frac{\int_{-\infty}^{\infty} y^2 C dy}{\int_{-\infty}^{\infty} C dy}, \sigma_z^2 = \frac{\int_{-\infty}^{\infty} z^2 C dz}{\int_{-\infty}^{\infty} C dz} \quad (29)$$

$$\iiint_{-\infty}^{\infty} C dx dy dz = Q \text{ (kmol)} \quad \text{for instantaneous point source} \quad (30)$$

$$\iint_{-\infty}^{\infty} uC \, dy \, dz = Q \, (kmol/s) \quad \text{for continuous point source} \quad (31)$$

$$\int_{-\infty}^{\infty} uC \, dz = Q \, (kmol/m-s) \quad \text{for continuous infinite line source} \quad (32)$$

When the parameters in Eqs. (26)~(28) are determined so that they satisfy the relations (29)~(32), the following models are obtained:

Instantaneous point source:

$$C = \frac{Q}{B_1 \sigma_x \sigma_y \sigma_z} \exp \left[- \left\{ \left(\frac{\Gamma(3/p)}{\Gamma(1/p)} \right)^{p/2} \left(\frac{|x|}{\sigma_x} \right)^p + \left(\frac{\Gamma(3/r)}{\Gamma(1/r)} \right)^{r/2} \left(\frac{|y|}{\sigma_y} \right)^r + \left(\frac{\Gamma(3/s)}{\Gamma(1/s)} \right)^{s/2} \left(\frac{|z|}{\sigma_z} \right)^s \right\} \right] \quad (33)$$

Continuous point source:

$$C = \frac{Q}{B_2 \sigma_y \sigma_z} \exp \left[- \left\{ \left(\frac{\Gamma(3/r)}{\Gamma(1/r)} \right)^{r/2} \left(\frac{|y|}{\sigma_y} \right)^r + \left(\frac{\Gamma(3/s)}{\Gamma(1/s)} \right)^{s/2} \left(\frac{|z|}{\sigma_z} \right)^s \right\} \right] \quad (34)$$

Continuous line source:

$$C = \frac{Q}{B_3 \sigma_z} \exp \left[- \left(\frac{\Gamma(3/s)}{\Gamma(1/s)} \right)^{s/2} \left(\frac{|z|}{\sigma_z} \right)^s \right] \quad (35)$$

where B_1 , B_2 , and B_3 are given by the following equations:

$$\frac{1}{B_1} = \frac{prs}{8} \frac{\{\Gamma(3/p)\Gamma(3/r)\Gamma(3/s)\}^{1/2}}{\{\Gamma(1/p)\Gamma(1/r)\Gamma(1/s)\}^{3/2}} \quad (36)$$

$$\frac{1}{B_2} = \frac{rs}{4u} \frac{\{\Gamma(3/r)\Gamma(3/s)\}^{1/2}}{\{\Gamma(1/r)\Gamma(1/s)\}^{3/2}} \quad (37)$$

$$\frac{1}{B_3} = \frac{s}{2u} \frac{\Gamma(3/s)^{1/2}}{\Gamma(1/s)^{3/2}} \quad (38)$$

Here definition of gamma function and its nature are as follows:

$$\Gamma(x) = \int_0^{\infty} e^{-t} t^{x-1} dt \quad (x > 0) \quad , \quad \Gamma(n) = (n-1)! \quad ,$$

$$\Gamma\left(\frac{1}{2}\right) = \sqrt{\pi} \quad , \quad \Gamma\left(\frac{3}{2}\right) = \frac{\sqrt{\pi}}{2}$$

Values of p , r , and s determine type of concentration distribution for x , y , and z directions, respectively; for example, if the value is equal to 2, the distribution becomes "Gaussian". Fig. 21 shows that how the value of "s" changes vertical concentration distribution.

(2) Plume and Puff model

When $p = r = s = 2$ is used, Eqs. (33), (34), and (35) present so-called "puff" and "plume" models. The "puff" and "plume" models are widely used for "Environmental Impact Assessment" in Japan.

(puff; point source)

$$C = \frac{Q}{(2\pi)^{3/2} \sigma_x \sigma_y \sigma_z} \exp \left\{ -\frac{1}{2} \left(\frac{x^2}{\sigma_x^2} + \frac{y^2}{\sigma_y^2} + \frac{z^2}{\sigma_z^2} \right) \right\} \quad (39)$$

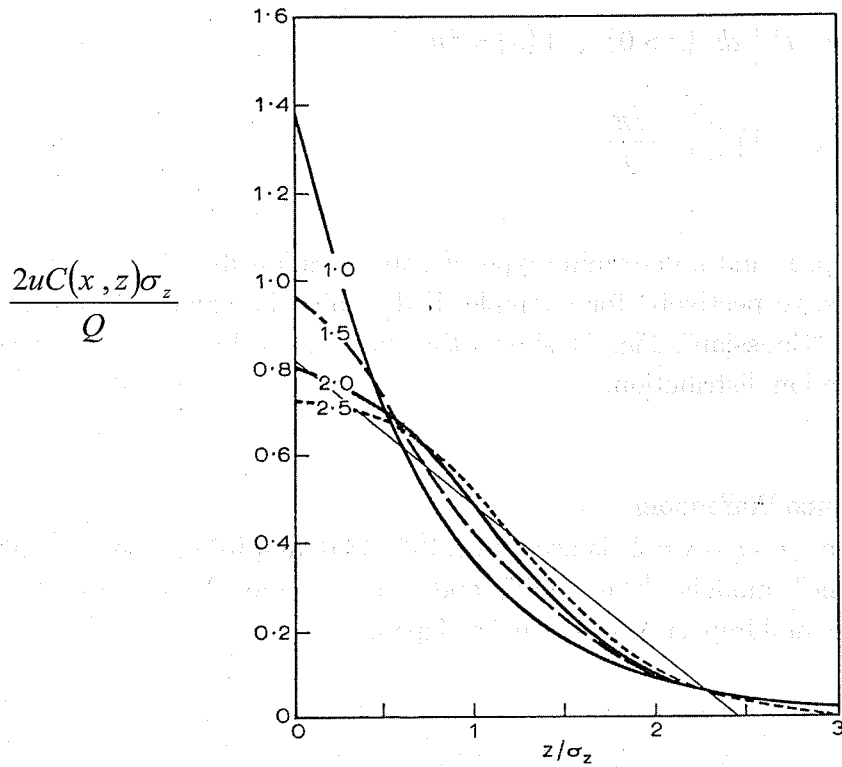


Figure 21. Variation of vertical profiles of concentration for the values of "s"; see Eq. (35); dimensionless vertical height (horizontal axis) vs. dimensionless concentration (vertical axis) (Pasquill, 1974).

(plume; point source)

$$C = \frac{Q}{2\pi u \sigma_y \sigma_z} \exp \left[-\frac{1}{2} \left(\frac{y^2}{\sigma_y^2} + \frac{z^2}{\sigma_z^2} \right) \right] \quad (40)$$

(plume; line source)

$$C = \frac{Q}{(2\pi)^{\frac{1}{2}} u \sigma_z} \exp \left[-\frac{z^2}{2\sigma_z^2} \right] \quad (41)$$

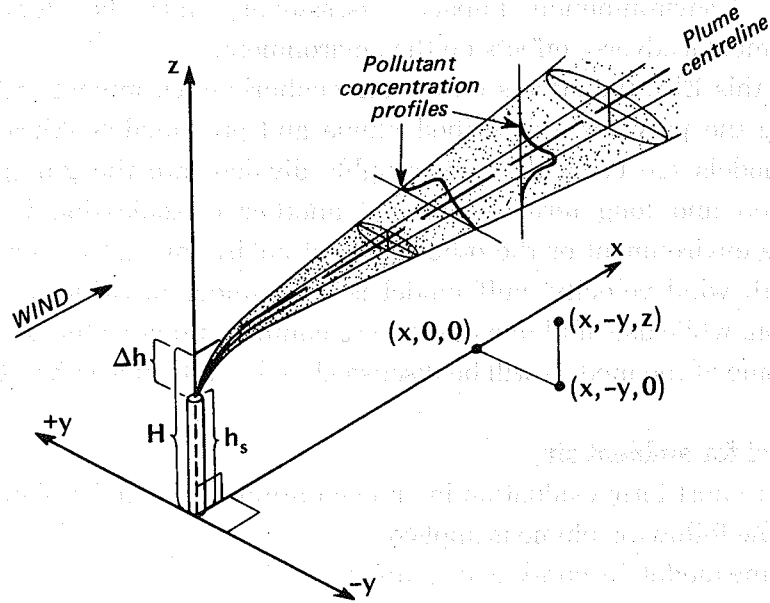


Figure 22. (Turner, 1969).

(3) Modification: Effect of ground, inversion layer, etc.

In the application of the models (39) ~ (41), they can be modified in practical form to accommodate arbitrary location of emission source, effect of the ground and the inversion layer, etc. For example, when emission source is located at a height of H above the ground, and the ground works as a perfect reflection wall, Eq. (41) for a continuous line source can be rewritten as Eq. (42):

$$C = \frac{Q}{(2\pi)^{\frac{1}{2}} u \sigma_z} \left\{ \exp \left[-\frac{(z-H)^2}{2\sigma_z^2} \right] + \exp \left[-\frac{(z+H)^2}{2\sigma_z^2} \right] \right\} \quad (42)$$

In Eq. (42), the effect of the ground as a perfect reflection wall is expressed by adding concentration by a hypothetical emission source located at the depth of H under the ground, i.e. the location of the hypothetical source at $(x, z) = (0, -H)$.

1.2.3 Atmospheric diffusion model for environmental impact assessment

In Japan, when any kinds of development with its scale over certain level are

planned, "Environmental Impact Assessment" must be done to avoid the development's adverse effects on the environment.

In this EIA, the effects on the atmospheric environment are evaluated often by using the previously described plume and puff models. Various variations of these models are used; they are roughly divided into the groups for short time evaluation and long term evaluation; another classification is the models for roadside environment or the other ambient environment. The models applied also vary with wind velocity: puff model is used under no wind or very weak wind condition, while use of plume models is a common practice for normal wind case.

Some of the models will be discussed in the following subsections.

(1) Model for ambient air

For short term evaluation in ambient atmosphere under significant wind ($u > 1 \text{ m/s}$), the following plume is applied:

(Plume model for continuous point source)

$$C(x, y, z) = \frac{Q}{2\pi \cdot u \cdot \sigma_y \cdot \sigma_z} \exp\left(-\frac{y^2}{2\sigma_y^2}\right) \times \left[\exp\left\{-\frac{(z-H)^2}{2\sigma_z^2}\right\} + \exp\left\{-\frac{(z+H)^2}{2\sigma_z^2}\right\} \right] \quad (43)$$

where $C(x, y, z)$: concentration of pollutant at (x, y, z) either in (ppm) for gaseous species or in (mg/m^3) for particulate matter.

Q : emission strength either in ($\text{ml} - \text{pure gas concerned}/\text{s}$) or in (mg/s) for particulate matter.

u : wind velocity in (m/s)

H : height of the emission source above ground in (m)

σ_y, σ_z : width of dispersing cloud for horizontal (y), and vertical (z) directions in (m)

x : down-wind distance from the emission source (m)

y : distance from the x axis in (m)

z : height from the $x-y$ plane in (m)

The plume width of σ_y, σ_z are functions of both down-wind distance from the source and atmospheric stability. They are determined based on empirical relations.

Widely used example of these relations is summarized in Table 21 and Fig. 22.

For short term evaluation in ambient atmosphere in windless situation ($u < 1$ m/s), the following puff model is used:

(Puff model for instantaneous point source)

$$C(x, y, z, t) = \frac{Q}{\sigma_x \sqrt{2\pi}} \cdot \exp \left[-\frac{1}{2} \left(\frac{x}{\sigma_x} \right)^2 \right] \frac{Q}{\sigma_y \sqrt{2\pi}} \cdot \exp \left[-\frac{1}{2} \left(\frac{y}{\sigma_y} \right)^2 \right] \\ \times \left\{ \frac{1}{\sigma_z \sqrt{2\pi}} \cdot \exp \left[-\frac{1}{2} \left(\frac{z-H}{\sigma_z} \right)^2 \right] + \frac{1}{\sigma_z \sqrt{2\pi}} \cdot \exp \left[-\frac{1}{2} \left(\frac{z+H}{\sigma_z} \right)^2 \right] \right\} \quad (44)$$

Eq. (44) is for “instantaneous source”. In practice, continuous point source in windless condition often has to be treated. For this purpose, we can derive a model by replacing Q (g) in Eq. (44) with Qdt (Q in g/s; dt in s), and integrating with respect to time. The resultant equation is given as Eq. (45).

(Puff model for continuous point source)

$$C(x, y, z, T) = \int_0^T \frac{Q}{(2\pi)^{3/2} \cdot \sigma_y^2(t) \cdot \sigma_z(t)} \exp \left\{ -\frac{x^2 + y^2}{2\sigma_y^2(t)} \right\} \\ \times \left[\exp \left\{ -\frac{(z+H)^2}{2\sigma_z^2(t)} \right\} + \exp \left\{ -\frac{(z-H)^2}{2\sigma_z^2(t)} \right\} \right] dt \quad (45)$$

Eq. (45) can be further simplified for application to “roadside” air quality. The “roadside” means area within 100 m from the road. By several numerical experiments in which the time for integration, T , in Eq. (45) was varied, it was clarified that the air quality in the area do not change for $T >$ about 30 min. Thus “ T ” in Eq. (45) can be made to be infinity without loss. Furthermore, the starting time for integration can be chosen t_0 rather than 0, since it takes some time, t_0 , before the pollutant emitted from cars reaches the end of the road width from which the pollutant starts to disperse for outside of the road. By assuming these things, Eq. (45) can be simplified as Eq. (46).

(Puff model for continuous point source near roadside: simplified integral-puff model)

$$C(x, y, z) = \frac{Q}{(2\pi)^{3/2} \cdot \alpha^2 \cdot \gamma} \left\{ \frac{1 - \exp\left(-\frac{l}{t_0^2}\right)}{2l} + \frac{1 - \exp\left(-\frac{m}{t_0^2}\right)}{2m} \right\} \quad (46)$$

where

$$l = \frac{1}{2} \cdot \left\{ \frac{x^2 + y^2}{\alpha^2} + \frac{(z - H)^2}{\gamma^2} \right\}$$

$$m = \frac{1}{2} \cdot \left\{ \frac{x^2 + y^2}{\alpha^2} + \frac{(z + H)^2}{\gamma^2} \right\}$$

t_0 : time for which the puff discharged at the center of the road reaches the end of the road width; initial width of dispersing cloud is determined with this time, in (s)

α, γ : parameters related to cloud width; $\alpha=0.3$, $\gamma=0.18$ (daytime), 0.09 (nighttime) are frequently used.

(2) Width and depth of pollutant cloud: Diffusion parameter

The width of dispersing pollutant cloud, $\sigma_x, \sigma_y, \sigma_z$, in Eqs. (45) and (46) is affected by the turbulence in the atmosphere, and thus determined based on field observation.

The state of turbulence in the atmosphere is often described by "atmospheric stability". Pasquill proposed a method to classify the stability with alphabet from A ~ G: "A" stands for most unstable situation, while "G" is the most stable case; "D" means thermally neutral and this situation usually occurs most frequently in the atmosphere. These stabilities of "A" to "G" are diagnosed by a combination of wind velocity, and solar radiation intensity, or cloudiness.

Table 1 shows σ_y and σ_z in Eq. (44) as functions of the stability and the downwind distance, x. Fig. 23 illustrates these σ_y and σ_z .

In case of no-wind or very low wind velocity, σ_x, σ_y and σ_z in Eq. (45) is expressed as linear function of time, t (s) after the release of pollutant as:

$$\sigma_x = \sigma_y = \alpha \cdot t, \text{ and } \sigma_z = \gamma \cdot t \quad (47)$$

The parameters α and γ in the relation (47) are given in Table 2 as function of the stability and time after the release.

Table 1a. σ_y in Pasquill-Gifford chart : $\sigma_y(x) = \gamma_y \cdot x^{\alpha_y}$

Atmospheric Stability	α_y	γ_y	Down wind distance, $x(m)$
A	0.901	0.426	0~1,000
	0.851	0.602	1,000~
B	0.914	0.282	0~1,000
	0.865	0.396	1,000~
C	0.924	0.1772	0~1,000
	0.885	0.232	1,000~
D	0.929	0.1107	0~1,000
	0.889	0.1467	1,000~
E	0.921	0.0864	0~1,000
	0.897	0.1019	1,000~
F	0.929	0.0554	0~1,000
	0.889	0.0733	1,000~
G	0.921	0.0380	0~1,000
	0.896	0.0452	1,000~

Table 1 b. σ_z in Pasquill-Gifford chart : $\sigma_z(x) = \gamma_z \cdot x^{\alpha_z}$

Atmospheric Stability	α_z	γ_z	Down wind distance, x(m)
A	1.122	0.0800	0~ 300
	1.514	0.00855	300~ 500
	2.109	0.000212	500~
B	0.964	0.1272	0~ 500
	1.094	0.0570	500~
C	0.918	0.1068	0~
D	0.826	0.1046	0~1,000
	0.632	0.400	1,000~10,000
	0.555	0.811	10,000~
E	0.788	0.0928	0~1,000
	0.565	0.433	1,000~10,000
	0.415	1.732	10,000~
F	0.784	0.0621	0~1,000
	0.526	0.370	1,000~10,000
	0.323	2.41	10,000~
G	0.794	0.0373	0~1,000
	0.637	0.1105	1,000~2,000
	0.431	0.529	2,000~10,000
	0.222	2.17	10,000~

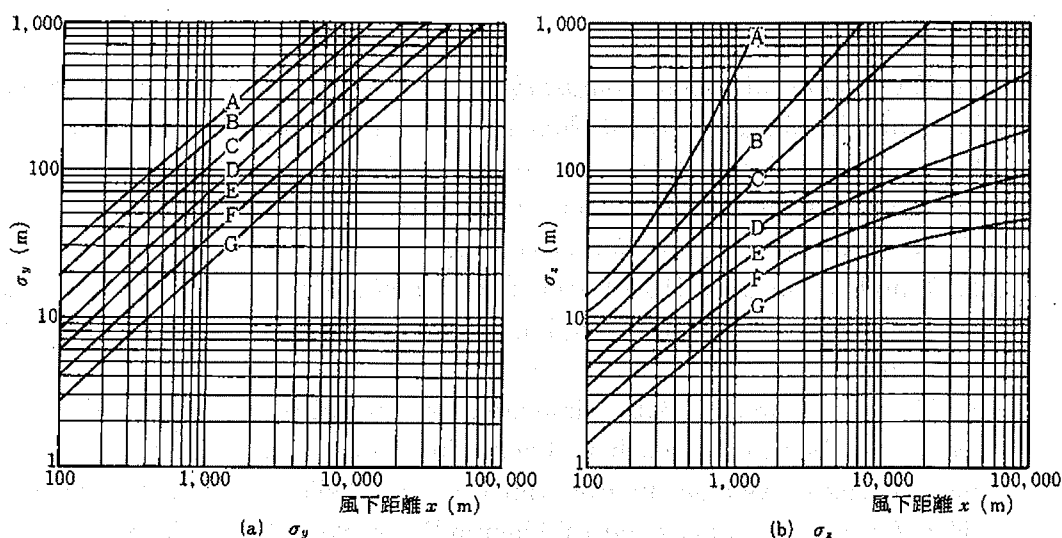


Figure 23. The width of dispersing cloud, σ_y and σ_z as function of atmospheric stability and down-wind distance.

Table 2. The parameters, α and γ , of dispersing cloud under weak wind condition:

$$\sigma_x = \sigma_y = \alpha \cdot t, \text{ and } \sigma_z = \gamma \cdot t$$

(a) No wind ($u \leq 0.4 \text{ m/s}$): α and γ

Atmospheric Stability		α	γ
By Pasquill	By Shir		
A	-3	0.948	0.569
A ~ B	-3 ~ -2	0.859	0.862
B	-2	0.781	0.474
B ~ C	-2 ~ -1	0.702	0.314
C	-1	0.635	0.208
C ~ D	-1 ~ 0	0.542	0.153
D	0	0.470	0.113
E	1	0.439	0.067
F	2	0.439	0.048
G	3	0.439	0.029

(b) Weak wind ($u: 0.5 \sim 0.9 \text{ m/s}$): α and γ

Atmospheric Stability		α	γ
By Pasquill	By Shir		
A	-3	0.748	1.569
A ~ B	-3 ~ -2	0.659	0.862
B	-2	0.581	0.474
B ~ C	-2 ~ -1	0.502	0.314
C	-1	0.435	0.208
C ~ D	-1 ~ 0	0.342	0.153
E	0	0.270	0.113
F	1	0.239	0.067
G	2	0.239	0.048
	3	0.239	0.029

References

- Defant, F. (1957) Local winds, *Compendium in Meteorology*, Atmos. Met.Soc., 655.
- Kitada, T. and E. Kitagawa (1989) Numerical investigation of the role of sea breeze front in air pollution transport: An observation from advecting behavior of fluid particles, In Brasser, L.J. and Mulder, W.C. (eds.) *Man and his Ecosystem*, Elsevier, Amsterdam, The Netherlands, 209-214.
- Kitada, T. and E. Kitagawa (1990) Numerical analysis of the role of sea breeze front on air quality in coastal and inland polluted areas, *Atmos. Environ.*, **24A**, 1545-1559.
- Kitada, T. and K. Tanaka (1992) Simulated semi-global transport of SO_2 and SO_4^- from East Asia to the northern Pacific in spring season: The role of low and high pressure systems, In Han van Dop and Kallos, G. (eds.) *Air Pollution Modeling and Its Application IX*, Plenum Press, New York, 445-454.
- Kitada, T. and H. Ueda (1989) Pollutant dispersion and land/sea breeze circulations, In Cheremisinoff, P.N. (ed.) *Encyclopedia of Environmental Control Technology*, Vol.2, Gulf Pub. Co., 583-630.
- Meroney, R.N. (1982) Turbulent diffusion near buildings, In Plate, E. (ed.) *Engineering Meteorology*, Elsevier, Amsterdam, The Netherlands, 481-525.
- Oke, T.R. (1978) *Boundary Layer Climates*, John Wiley & Sons, New York.
- Pasquill, F. (1974) *Atmospheric Diffusion* 2nd Edition, Ellis Horwood Ltd., Chichester, Sussex, England.
- Pielke, R.A. (1984) *Mesoscale Meteorological Modeling*, Academic Press, Orlando, Florida.
- Prandtl, L. (1925) Über die ausgebildete Turbulenz, *ZAMM (Zeitschrift fuer Angewandte Mathematik und Mechanik)*, **5**, 136.
- Roberts, O.F.T. (1923) The theoretical scattering of smoke in a turbulent atmosphere, *Proc. Roy. Soc.*, **A**, **104**, 640.
- Smagorinsky, J. (1974) Global atmospheric modeling and the numerical simulation of climate, In Hess, W.N. (ed.), *Weather and Climate Modification*, Wiley, New York.

Chapter 2

Basics of Gases, Aerosol Particles and CCN

Yutaka ISHIZAKA and Mandira ADHIKARI

Hydrospheric Atmospheric Research Center

Chikusa-ku, Nagoya 464-8601 JAPAN

Phone: +81-52-789-3485, FAX: +81-52-789-3436

E-mail: ishizaka@hyarc.nagoya-u.ac.jp

mandira43@hotmail.com

2- 1. Introduction

Gases and aerosol particle are drastically increasing in East-Asia region due to rapid industrial development (van Aardenne et al., 1999), biomass and coal burning and increasing number of automobiles (Elliott et al., 1997) in Asia. Thornton et al. (1997) showed that high levels of SO_2 are present in the outflow from Asia and that anthropogenic sources in eastern Asia now dominate the sulfur chemistry not only in the lower troposphere but also in the mid and upper atmosphere over the Pacific Ocean. Few researchers (Akimoto and Narita, 1994; Hatakeyama et al., 1995, 2004) often found high concentrations of SO_2 in the atmosphere over the East China Sea, Yellow Sea and the Sea of Japan under the inflow of anthropogenic pollutants from the Asian continent.

Anthropogenic particles, many of which contain soluble sulfate and nitrate compounds, act often as efficient CCN (Cloud Condensation Nuclei) (e.g. O'Dowd et al., 1999). A thermal analytical study of CCN in some parts of Japan showed that the CCN concentration was highly influenced by anthropogenic inorganic pollutants (Ishizaka and Adhikari, 2003). In the other hand, cloud activities can produce new aerosol particles in the atmosphere (Hegg et al., 1991; Ishizaka et al., 1997; Hudson and Xie, 1999). Aerosol particles produced by cloud activities may increase CCN concentration in the atmosphere. CCN concentrations are usually fewer than 100 cm^{-3} in the maritime atmosphere, while they are 1000 cm^{-3} or more in the polluted atmosphere (e.g. Twomey and Wojciechowski, 1969; Radke and Hobbs, 1976; Ishizaka and Adhikari, 2003; Adhikari et al., 2005). Ishizaka et al. (1995) found that the concentration of CCN activated at 0.5% supersaturation was

as high as 1500 cm^{-3} in the boundary layer over the Southwest Islands area in Japan. CCN either produced by cloud activities or from anthropogenic emission strongly modulate cloud microstructure and radiative properties of clouds (Charlson et al., 1987; Yu, 1996). Increasing CCN concentrations increase cloud droplet concentrations (Fitzgerald and Spyers-Duran, 1973) and limit size of cloud droplet. Large number concentrations of smaller droplets reflect more solar radiation, which enhance cloud albedo (Twomey et al., 1984). Hence, the first indirect forcing of aerosol particles on climate derives from the fact that cloud albedo depends on cloud liquid water path and droplet size (Twomey, 1977; Hobbs, 1993; Vong and Covert, 1998). In other hand, decrease in droplet size reduces efficiency of gravitational collection of droplet and precipitation efficiencies (Young, 1993) thereby extending cloud lifetime and extend (Albrecht, 1989; Liou and Ou, 1989; Radke et al., 1989), which enhance second indirect forcing. Thus the CCN affects global climate through indirect interactions with solar and terrestrial radiation.

In order to basically understand the effect of air pollutants on CCN concentrations, we explain the physical and chemical characteristics of the anthropogenic gases and atmospheric aerosols and some results observed over the East China Sea (Adhikari et al., 2005).

2.2 Sulfur dioxide and sulfate aerosol

Large quantities of sulfur dioxide enter the atmosphere each year from anthropogenic sources, mainly the combustion of fossil fuels and the smelting of metals. SO_2 indisputably ranks as a prominent of pollutant, and it is understandable that research of the past 30 yr dealing with atmospheric sulfur has concentrated on such problems as the dispersal of SO_2 from power station and urban centers, its conversion to sulfuric acid, the formation of sulfate aerosols, and the deposition of sulfate and SO_2 at the ground surface.

Atmospheric gas-phase reactions may lead to the formation of condensable products, which subsequently associate with the atmospheric aerosol. The best known reaction of this is the oxidation of SO_2 to H_2SO_4 and its neutralization by ammonia to form sulfate salts. Condensation may either cause the formation of new particles in the Aitken range (homogeneous nucleation) or deposit material onto preexisting particles (heterogeneous nucleation). Gas-to-particle conversion one usually starts with air freed from particles by filtration. The development of the particle size spectrum then goes through three successive stages, dominated by

nucleation, coagulation, and heterogeneous condensation, in that order. In the atmosphere, all three processes take place concurrently. The generation of new particles then requires conditions that allow the growth of molecular clusters by condensation in the face of competition from heterogeneous condensation.

Pathways for the oxidation of SO_2 in the atmosphere are complex and have not yet been fully delineated. The reactions occur in the gas phase, in fog and cloud droplets, and on the surface of aerosol particles. Refer the textbook of Warneck (1988) about some of the reaction processes of SO_2 and other gases in the atmosphere.

2.3. Activation of aerosol particles as CCN

The classical laboratory experiments demonstrated that, in particle-free air, water vapor condenses (by homogeneous nucleation) to form droplets only if the supersaturation is several hundred percents. By contrast, in the presence of aerosol particles water droplets form (by heterogeneous nucleation) at supersaturation of about 2% or less. Aerosol particles, which are capable of initiating drop formation at the observed low supersaturations are called cloud condensation nuclei (CCN). All aerosol particles are eventually able to initiate drops provided that the supersaturation of the water vapor in their environment is high enough. Read the textbooks of Mason (1971) and Pruppacher and Klett (1997) in more detail about nucleation and condensation of droplets on aerosol particles.

2.3.1 Activation of soluble particles as CCN

The nucleation of water drops by water-soluble particles by the mass and chemistry of the water-soluble component. The equilibrium vapor pressure p_r over the surface of a droplet of pure water of radius r exceeds that over a plane water surface at the same temperature p_∞ as expressed by

$$\ln p_r/p_\infty = 2\sigma_{LV}M/\rho_L RTr \quad (1)$$

Thus a drop introduced in to a just saturated atmosphere will evaporate; a droplet can't persist, much less grow, unless the environment is supersaturated by

an amount required by (1). If, however, a droplet is formed on a wholly or partially soluble nucleus, the equilibrium vapor pressure at its surface is reduced by an amount depending on the nature and concentration of the solute, which means that condensation will be able to set in at a lower supersaturation than on an insoluble particle of the same size. Köhler (1936) first derived an expression for the equilibrium vapor pressure at the surface of a solution droplet. A modified version has since been used rather uncritically in the literature.

We shall consider a solution droplet, radius r , at the surface of which the vapor pressure is p'_r , to be in equilibrium with an atmosphere in contact with a plane water surface whose equilibrium vapor pressure is p_∞ . If an elemental mass dm of water is transferred from the droplet to the plane water surface, the resulting decrease in the free energy of the solution will be

$$\Delta G = \sigma' dA - P dV = \frac{2\sigma' dm}{r\rho_L'} - \frac{P dm}{\rho_L'} \quad (2)$$

where $dA (= 8\pi r dr)$ and dV are the changes in the surface area and the volume of the droplet, σ' , ρ_L' and P are respectively the surface tension, density, and osmotic pressure of the solution. Alternatively, the decrease of free energy is given by the work gained in evaporating the mass dm of water at pressure p'_r , expanding the vapor to the lower pressure p_∞ and condensing it at pressure p_∞ , the whole process being carried out reversibly and isothermally.

When the solution droplet is in equilibrium with the surrounding atmosphere, with its surface temperature equal to that of the air, p'_r must equal the partial pressure of the water vapor, so $H/100 = p'_r/p_\infty$, where H is the relative humidity of the air. Thus the condition for equilibrium becomes

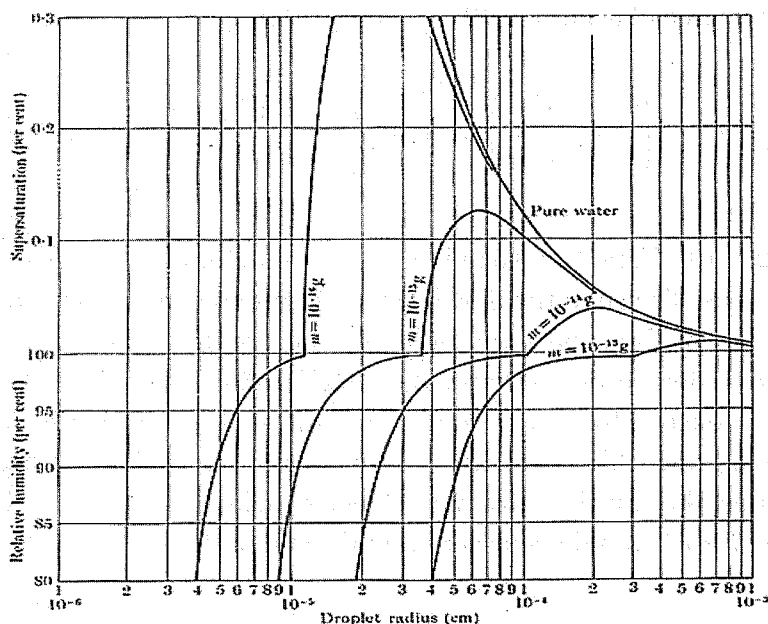


Figure 1. The equilibrium relative humidity (or supersaturation) as a function of droplet radius for solution droplets containing the indicated masses of sodium chloride.

$$\frac{H}{100} = \left(\exp \frac{2\sigma' M}{\rho'_L R T r} \right) \left\{ 1 + \frac{imM}{W \frac{4}{3} \pi r^3 \rho'_L - m} \right\}^{-(\rho_L / \rho'_L)} \quad (3)$$

an equation which can be used to calculate the radius of drops in equilibrium with an atmosphere of a given relative humidity. Specimen equilibrium curves for NaCl nuclei of different masses are plotted in Fig. 1. When a nucleus droplet reaches equilibrium with an atmosphere of 100% relative humidity, the depression of the equilibrium vapor pressure due to the presence of the dissolved solute is equal and opposite to the elevation caused by the curvature of the droplet surface. At higher values of the relative humidity, the equilibrium radius of the nucleus droplet increases, until a critical value of the supersaturation is reached corresponding to the maximum of the relevant curve in Fig 1. At this stage, the solution is so dilute

that, to a high degree of accuracy, (3) may be written

$$\frac{H}{100} = e^{B/r} \left(1 - \frac{C}{r^3} \right) \approx 1 + \frac{B}{r} - \frac{C}{r^3}, \quad (4)$$

where $B = 3.2 \times 10^5/T$ and $C = 8.6 \text{ m/W}$ are constants for a given temperature and a particular nucleus. The condition for the curve to attain a maximum, corresponding to critical values of the supersaturation (S_c) and droplet radius (r_c), is $dH/dr = 0$ hence, to a high degree of accuracy, $r_c^3 = 3C/B$ and $S_c/100 = 1 + (4B^3/27C)^{1/2}$. If a nucleus droplet exceed the critical radius and the supersaturation is maintained, it will continue to grow with a decrease of free energy to form a water droplet. Under these conditions, the transition from a nucleus droplet ($r_c > r$) to a fully developed cloud droplet ($r > r_c$) would occur very rapidly, and in theory, the drop would grow without limit.

2.3.2 Activation of mixed particles as CCN

Junge (1950) found from the observations that some aerosol particles consisted of an insoluble core surrounded with a thin coat of hygroscopic substance. He called such particles as "mixed nuclei". At humidity above 70 %, the mixed nuclei would react to changes in humidity in much the same way as wholly soluble nuclei of equivalent size, but at humidity below about 70%, the solution coat would shrink, the particles becoming almost wholly solid. In a later investigation, Junge and McLare (1971) considered the theoretical background for the process of condensation on natural aerosol. A size distribution $n(r)$ is assumed for particles, which at low relative humidity have a dry radius of r . They further have a composition such that the fraction of soluble matter is

$$\varepsilon = \frac{\text{Volume of soluble matter}}{\text{total volume of dry particle}}, \quad (5)$$

where ε can vary from 0 to 1, from completely insoluble (but wettable) particles to completely soluble particles, respectively. The concept of mixed particles includes the possibility that ε is a function of radius, $\varepsilon(r)$, and that for given r this $\varepsilon(r)$ is

an average of actual values which scatter around the average with a radius-dependent standard deviation.

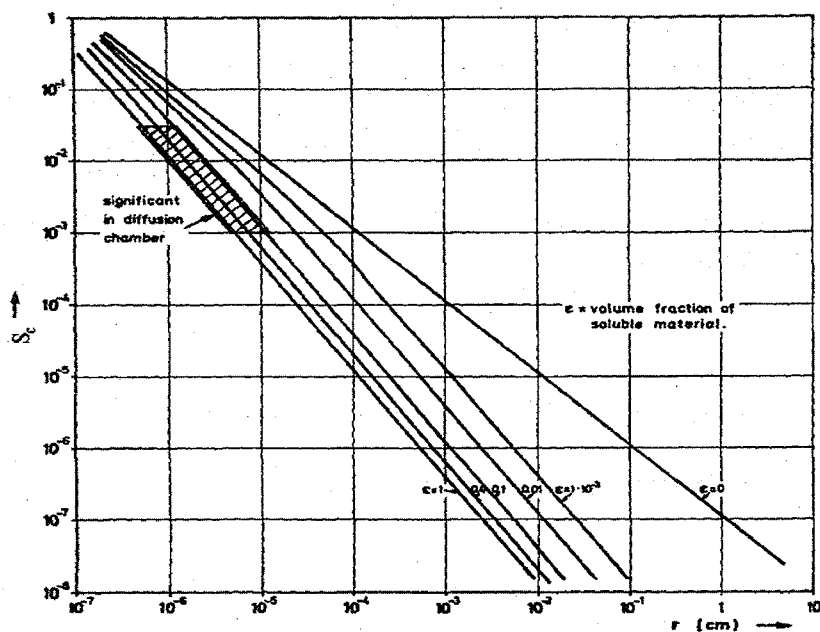


Figure 2. Critical supersaturation-dry radius relationship for particles of various compositions. The area of significance for diffusion chamber measurement of normal aerosols is shaded.

With increasing humidity the radius of the particles increases with absorption of water, first in a reversible manner and then, as a critical radius r_c is reached at a particular supersaturation S_c , spontaneously to a very large size. The critical radius occurs at the maximum of the Köhler curve relating droplet vapor pressure deviations from bulk water, due to curvature and solution effects, to droplet radius.

Beginning with the relationship for the vapor pressure of a droplet as a function of radius and solute concentration, expressions of the following form, relating the critical radius r_c to supersaturation S_c , dry radius r , and composition ϵ , can be derived:

$$S_c = \frac{a}{r_c} + \frac{a^2}{2r_c^2} + \frac{a^3}{6r_c^3} - X - \frac{aX}{r_c} - \frac{a^2X}{2r_c^2},$$

$$n^6 - f(r_c)n^3 + 4 = 0 \quad (6)$$

where $n = r_c/r$, $X = b \varepsilon r^3 / (r_c \rho' - r^3 \rho_d)$, $a = 2 \sigma M / (\rho_w RT)$, $b = i M \rho_s / M_s$, i = van't Hoff factor, M_s = molecular weight of soluble salt, ρ_w = density of water, ρ_s = density of soluble part of nucleus, ρ' = density of solution droplet with any insoluble material included, ρ_d = density of original dry nucleating particles.

The numerical solutions are plotted in Fig. 2 as a family of curves (each of a particular ε) relating r to S_c .

2.4. Some data observed over the East China Sea

2.4.1 Vertical distribution of SO₂ concentration

Figure 3 shows vertical profile of SO₂ concentration observed in April 2001 over the sea near the Southwest Islands area in Japan. The concentration was as low as 0.3 ppb in the boundary layer and almost constant above the boundary layer on 18 April. On the other hand, SO₂ concentration was 2 ppb near the surface and sharply increased to 10 ppb (beyond the scale limit) near the top of the boundary layer on 26 April. On 28 April the concentration was about 5 ppb near the surface, which decreased with increasing altitude. On 23 April, SO₂ concentration was about 1 ppb near the surface and decreased slowly to top of the boundary layer. The influence of pollutants on SO₂ and aerosol particle concentrations was not observed above the boundary layer. Similar results were also reported by Hatakeyama et al. (1995), Raga and Jonas (1995) and others. Based on the concentration of aerosol particles and SO₂ and back trajectory the atmosphere on 18 April was considered as clean (marine) atmosphere and that on the other days were considered as polluted (continental) atmosphere.

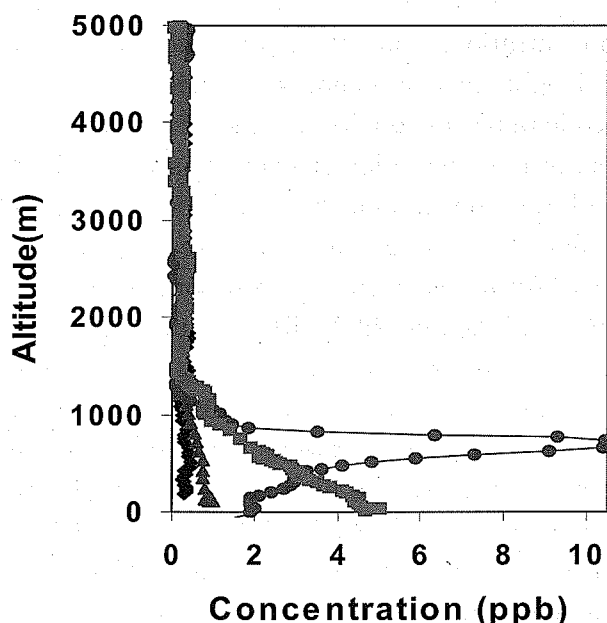


Figure 3. Vertical distribution of SO_2 concentration on clear days over the sea near the Southwest Islands area in Japan (Diamond shape: 18 April 2001, Triangle: 23 April, Circle: 26 April, Diamond: 28 April)

2.4.2 Vertical distribution of aerosol particle concentrations

In order to characterize the distributions of aerosol particles, vertical measurements were performed on clear days (18, 23, 26 and 28 April, 2001) over the ocean near the Southwest Islands of Japan. The observational data showed that the total aerosol concentrations ($d > 0.003 \mu\text{m}$, not shown) were more than 3000 cm^{-3} on 23 and 28 April. The concentrations were $\sim 6000 \text{ cm}^{-3}$ near the sea surface and they increased drastically to $\sim 30000 \text{ cm}^{-3}$ near the top of the boundary layer on 26 April. In order to distinguish the clean atmosphere from the polluted one, vertical distributions of concentrations of nuclei mode particles (NP, $0.12 > d > 0.01 \mu\text{m}$), fine particles (FP, $1.01 > d > 0.12 \mu\text{m}$) and coarse particles (CP, $3.11 > d > 1.01 \mu\text{m}$) are plotted in Figures 4a, b and c, respectively. It was generally seen that the NP and FP concentrations were high in the boundary layer and low above the boundary layer. The NP concentrations varied from 1200 to 3600 cm^{-3} near the surface on 23, 26 and 28 April. The concentrations were as high as $\sim 17000 \text{ cm}^{-3}$ near the top of the

boundary layer on 26 April. The TSI data was not available on 18 April. The vertical profiles of FP concentrations on 18 April showed a slight decrease in concentrations with height, in agreement with those presented by Hudson and Frisbie (1991) for the clean marine environments off the coast of California. On the other hand, FP concentrations were lower near the sea surface and increased to a maximum at 200 m altitude on 26 and 28 April. The concentrations were almost constant in the boundary layer on 23 April. The peak concentrations of FP were less than 500 cm^{-3} on 18 April but peak concentrations were 2 to 4 times as high as those on the other days (23, 26 and 28 April). In contrast, CP peak concentrations were $\sim 30 \text{ cm}^{-3}$ on 18 April and less than 2 cm^{-3} on 23, 26 and 28 April. The vertical distributions of aerosol particle above the boundary layer was different from those in the boundary layer. The NP concentrations were low and almost constant with height in all the observation days. The high concentration of FP was observed at higher altitude between 3 and 4 km on 28 April. The CP concentration was comparatively low on 23, 26 and 28 April whereas it was high on 18 April above the boundary layer. It was found that relative humidity was about 50% at 3-4 km on 28 April and as high as 70% above the boundary layer on 18 April. The high relative humidity indicates that coagulation and/or condensation processes were the possible cause of high concentrations of aerosol particle in the free troposphere on 18 and 28 April. From the vertical profile it is considered that there were a little effect of air pollutants on aerosol concentrations in the free troposphere, however, the effect of air pollutants on aerosol particles concentrations was novel in the boundary layer over the East China Sea.

2.4.3 Vertical distribution of CCN concentrations

Vertical profiles of CCN at 0.3% supersaturation are plotted in Figure 5 to examine the effects of pollutants on CCN concentration. CCN concentrations in the boundary layer were low (120 cm^{-3}) on 18 April and very high (about

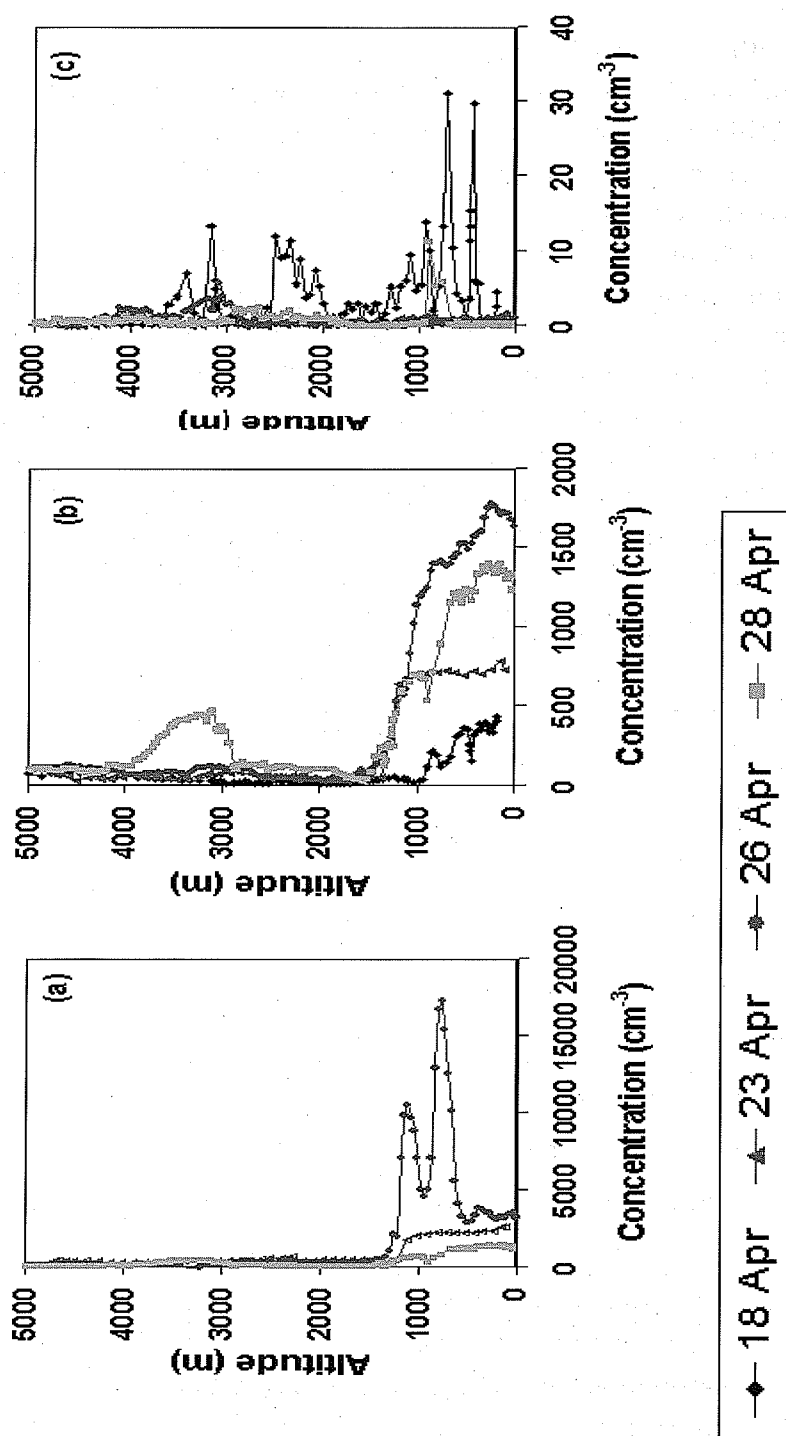


Figure 4. Vertical distributions of (a) Nuclei mode (NP, $0.12 > d > 0.01 \mu\text{m}$) (b) Fine (FP, $1.05 > d > 0.12 \mu\text{m}$) and (c) Coarse (CP, $3.11 > d > 1.05 \mu\text{m}$) particles concentrations observed over the sea on clear days.

$750\text{--}2200\text{ cm}^{-3}$) on the other observation days. Above the boundary layer CCN concentrations were low and almost similar in all observation days except on 28 April at 3–4 km altitude. Although there were two peaks of very high concentrations of CN on 26 April, no peaks were observed in CCN profiles (Figure 5). There were marked differences in the shape of the vertical distributions of CCN concentrations and CN concentrations although vertical distributions of CCN and fine particle concentrations were comparable to each other. The possible cause of this is difference in size ranges. According to Köhler equation the NaCl particles larger than $0.05\text{ }\mu\text{m}$ in diameter (dry) will be activated as CCN at 0.3% SS. However, the CN concentrations include the particles smaller than $0.05\text{ }\mu\text{m}$ in diameter. CCN concentrations on 23 and 26 April were about 3–5 times those on 18 April. On the other hand, CCN concentrations on 28 April were nearly 10 times those on 18 April although the FP concentrations on 28 April were nearly 3 times those on 18 April. This shows that air pollutants increase the contribution of aerosol particle concentrations and hence CCN concentration over the East China Sea.

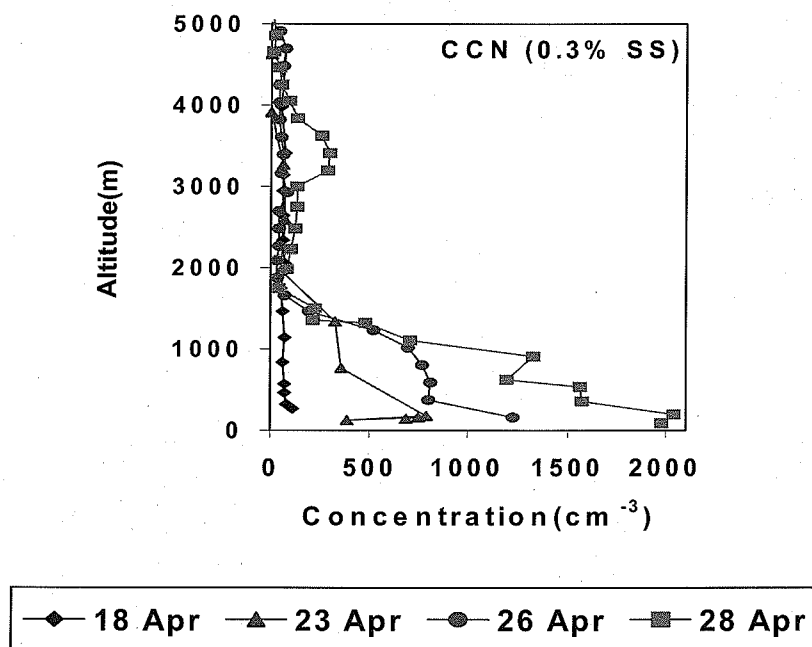


Figure 5. Vertical distribution of CCN activated at 0.3% supersaturation (SS) on clear days.

References

- Adhikari, M., Y. Ishizaka, H. Minda, R. Kazaoka, J. B. Jenson, J. Gras and T. Nakajima, 2005: Vertical distribution of cloud condensation nuclei concentrations and their effect on microphysical properties of clouds over the sea near the southwest islands of Japan. *J. Geophys. Res.* **110**, D10203, doi:10.1029/2004JD004758
- Akimoto, H. and H. Narita, 1994: Distribution of SO₂, NO_x and CO₂ emission from fuel combustion and industrial activities in Asia with 1° x 1° resolution. *Atmos. Environ., Part A*, **28**, 213-225.
- Albrecht, B., 1989: Aerosols, cloud microphysics and fractional cloudiness. *Science*, **245**, 1227-1230.
- Charlson, R. J., J. E. Lovelock, M. O. Andrea and S. G. Warren, 1987: Oceanic phytoplankton, atmospheric sulfur, cloud albedo and climate. *Nature*, **326**, 655-661.
- Elliott, S., M. Shen, D. R. Blake, R. Lu, A. G. Russell, C. Y. J. Kao, G. E. Streit, X. P. Zhao, E. I. McCreary, F. S. Rowland, M. J. Brown and R. P. Turco, 1997: Atmospheric effects of the emerging main land Chinese transportation system at and beyond the regional scale. *J. Atmos. Chem.*, **27**, 31-70.
- Fitzgerald, J. W., and P. A. Spyers-Duran, 1973: Changes in cloud nucleus Concentration and cloud droplet size distribution associated with pollution from St. Louis. *J. Appl. Meteorol.*, **12**, 511-516.
- Hatakeyama, S., A. Takami, F. Sakamaki, H. Mukai, N. Sugimoto and A. Shimizu, 2004: Aerial measurement of air pollutant and aerosols during 20-22 March 2001 over the East China Sea. *J. Geophys. Res.*, **109**, D13304, doi:10.1029/2003jd004271.
- Hatakeyama, S., K. Murano, H. Bandow, F. Sakamaki, M. Yamato, S. Tanaka and H. Akimoto, 1995: The 1991 PEACAMPOT aircraft observation of ozone, NO_x and SO₂ over the East China Sea, the Yellow Sea, and the Sea of Japan. *J. Geophys. Res.*, **100**, 23143-23151.
- Hegg, D. A., L. F. Radke and P. V. Hobbs, 1991: Measurements of Aitkin nuclei and cloud condensation nuclei in the marine atmosphere and their relation to the DMS-Cloud-Climate hypothesis. *J. Geophys. Res.*, **96**, 18727-18733.
- Hobbs, P. V., 1993: Aerosol cloud interactions, in *Aerosol-Cloud-Climate Interactions*, edited by P. V. Hobbs, Academic, San Diego, Calif. p.33-37

- Hudson, J. G. and P. R. Frisbie, 1991: Cloud condensation nuclei near marine stratus. *J. Geophys. Res.*, **96**, 20795-20808.
- Hudson, J. G. and Y. Xie, 1999: Vertical distributions of cloud condensation nuclei spectra over the summertime northeast Pacific and Atlantic Oceans. *J. Geophys. Res.*, **104**, 30219-30229.
- Ishizaka, Y., Y. Kurahashi and H. Tsuruta, 1995: Microphysical properties of winter stratiform clouds over the Southwest Islands area in Japan. *J. Meteorol. Soc. Japan*, **73**, 1137-1151.
- Ishizaka, Y., J. Li and G.W. Qian, 1997: Aircraft observation of cloud effect on aerosol particles over the Northwest Pacific Ocean, *Proceeding of Inter. Symposium on Atmospheric Chemistry and Future Global Environment* (November 11-13 at Nagoya), p.405-408.
- Ishizaka, Y. and M. Adhikari, 2003: Composition of cloud condensation nuclei. *J. Geophys. Res.*, **108**, D4, 4138, doi:10.1029/2002JD002085.
- Junge, C. and E. McLaren 1971: Relationship of cloud nuclei spectra to aerosol size distribution and composition. *J. Atmos. Sci.*, **28**, 382-390.
- Kato, N. and H. Akimoto, 1992: Anthropogenic emissions of SO₂ and NO_x in Asia: Emission inventories. *Atmos. Environ.*, **26A**, 2997-3017.
- Köhler, H., 1936: The nucleus and the growth of hygroscopic droplets. *Trans. Faraday Soc.*, **32**, 1152-1162.
- Liou, Kuo-Nan and Szu-Cheng Ou, 1989: The role of cloud microphysical processes in climate: An assessment from a one-dimensional perspective. *J. Geophys. Res.*, **94**, 8599-8607.
- O'Dowd, C. D., J. A. Lowe, M. H. Smith, and A. D. Kaye, 1999: The relative importance of nss-sulphate and sea-salt aerosol to the marine CCN population: an improved multi-component aerosol-cloud droplet parameterization. *Quart. J. Roy. Meteorol. Soc.*, **125**, 1295-1313.
- Pruppacher, H. R. and J. D. Klett, 1997: *Microphysics of clouds and precipitation*. Kluwer, Dordrecht, p.287-308.
- Radke, L. F., and P. V. Hobbs, 1969: Measurement of cloud condensation nuclei, light scattering coefficient, sodium containing particles, and Aitken nuclei in the Olympic Mountains of Washington. *J. Atmos. Sci.*, **26**, 281-288.
- Radke, L. F., J. A. Coskley, Jr., and M. D. King, 1989: Direct and remote sensing observations of the effects of ships on clouds. *Science*, **24**, 1146-1149.
- Raga, G. B. and P. R. Jonas, 1995: Vertical distribution of aerosol particles and CCN in clear air around the British Isles. *Atmos. Environ.*, **29**, 673-684.
- Thornton, D. C., A. R. Bandy, B. W. Blomquist, R. W. Talbot and J. E. Dibb, 1997:

- Transport of sulfur dioxide from the Asian Pacific rim to the North Pacific troposphere. *J. Geophys. Res.*, **102**, 28489-28499.
- Twomey, S. and T. A. Wojciechowski, 1969: Observations of the geographical variations of cloud nuclei. *J. Atmos. Sci.*, **26**, 684-688.
- Twomey, S., 1977: Influence of pollution on the short-wave albedo of cloud. *J. Atmos. Sci.*, **34**, 1149-1152.
- Twomey, S. A. M. Piepgrass and T. L. Wolfe, 1984: An assessment of the impact of pollution on global cloud albedo. *Tellus*, **36B**, 356-366.
- Young, K. C., 1993: *Microphysical Processes In Clouds*, Oxford Univ. Press, New York.
- Yu, S., 1996: CCN-cloud-climate hypothesis: chemical role. In: Kulmala, M., Wagner, P.E. (Eds.), *Nucleation and Atmospheric Aerosols*, Pergamon, pp. 915-918.
- van Aardenne, J. A., G. R. Carmichael, H. Levy II, D. Streets and L. Hordijk, 1999: Anthropogenic NO_x emissions in Asia in the period 1999-2020. *Atmos. Environ.*, **33**, 633-646.
- Vong, R. J. and D. S. Covert, 1998: Simultaneous observations of Aerosol and Cloud Droplet Size Spectra in Marine Stratocumulus. *J. Atmos. Sci.*, **55**, 2180-2192.
- Warneck, P., 1988: *Chemistry of the natural atmosphere*, Academic Press, Inc. (London) LTD, p.484-542.

Chapter 3

Long-range Transport of Air-pollutants in the East Asian Pacific Rim Region

S. HATAKEYAMA

Atmospheric Environment Division

National Institute for Environmental Studies

Tsukuba, JAPAN

e-mail: hatashir@nies.go.jp

3.1. Introduction

The Pacific coast of East Asia, like Europe and North America, is a region in which human activities impose a heavy load on the atmosphere. Air pollutants released from this region are known to affect not only the Asian continent but also a large area of the Pacific. Moreover, emissions of SO_2 and NO_x , which have been decreasing or at least remaining steady since 1980 in Western Europe and North America, are still growing in Asia and will likely continue to do so in this century. Although the rate of SO_2 emission in China has been generally decreasing (Streets et al., 2001), the total amount of SO_2 emitted is still large. Luo (2001) reported that emission of SO_2 from industrial sectors increased in 2001. Thus, the emission of SO_2 in East Asia will continue to significantly affect the atmospheric environment of this area.

In East Asia, transport of air pollutants is closely related to transport of yellow sand dust. Yellow sand dust is a good indication of transport of air masses from inland China. In contrast, anthropogenic pollutants are transported mainly from heavily industrialized coastal regions. Mizohata and Ito (1995) reported that SO_4^{2-} was mostly distributed on the surface layer of yellow sand dust particles. This means that sulfates, or their precursor, SO_2 , were trapped on the surface of yellow sand particles during transport. Therefore, it is very important to analyze the spatial distribution of not only gaseous species but also particulate species in order to clarify the large scale transport of pollutants from the Asian continent.

In this chapter, transport patterns of air pollutants from East Asia during

winter monsoon period will be described first. Three types of transport patterns were found. Then, large scale transport of pollutants following moving low/high pressure systems from central area of China will be explained. Most of data were obtained by the aerial observation experiments around Japan. Finally, aerial observation over China will be described.

3.2 Aerial observations of atmospheric pollutants over the seas between Asian continent and Japan – three types of transport from Asia

3.2.1 High concentration of SO_2 over the western part of the Sea of Japan

(1) High concentration of SO_2 over the western part of the Sea of Japan observed in 1992

Measurements of atmospheric pollutants on an aircraft were made on November 8, 10, 11, and 12, 1992. Flight areas were south of Cheju island (Korea) over East China Sea between $32^\circ 15'N$, $127^\circ E$ (Point C) and $31^\circ 05'N$, $126^\circ 20'E$ (Point D) and west of Oki islands over Sea of Japan between $35^\circ 20'N$, $132^\circ 30'E$ (Point B) and $36^\circ 40'N$, $132^\circ 30'E$ (Point A).

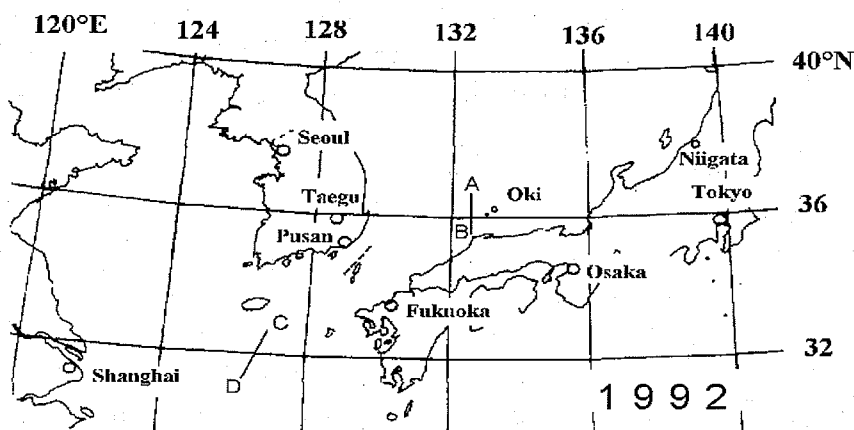


Figure 1. Flight plans of the 1992 experiments

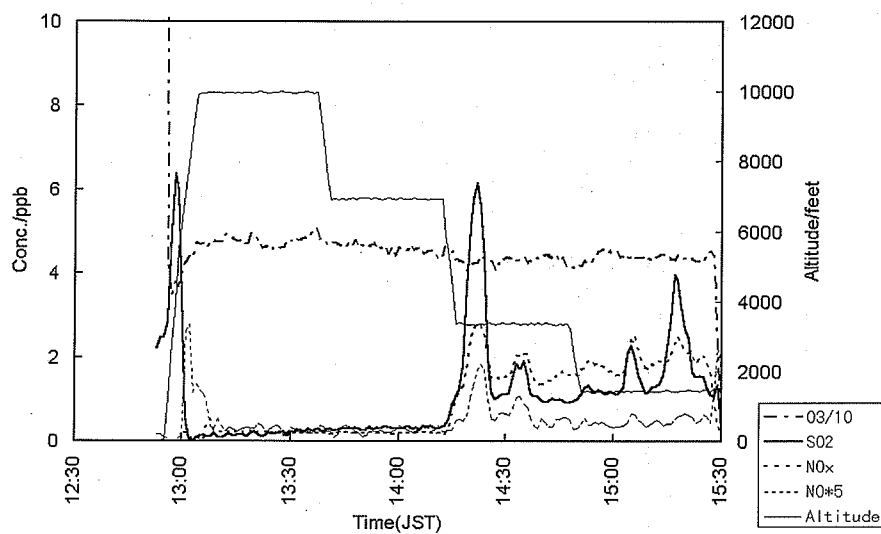


Figure 2. Concentration profiles of SO_2 , NO_x , and ozone on Nov. 11, 1992.

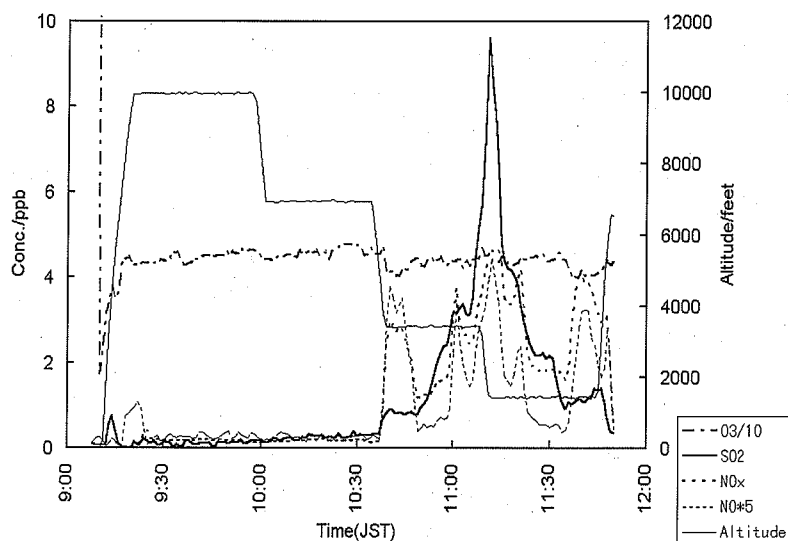


Figure 3. Concentration profiles of SO_2 , NO_x , and ozone on Nov. 12, 1992.

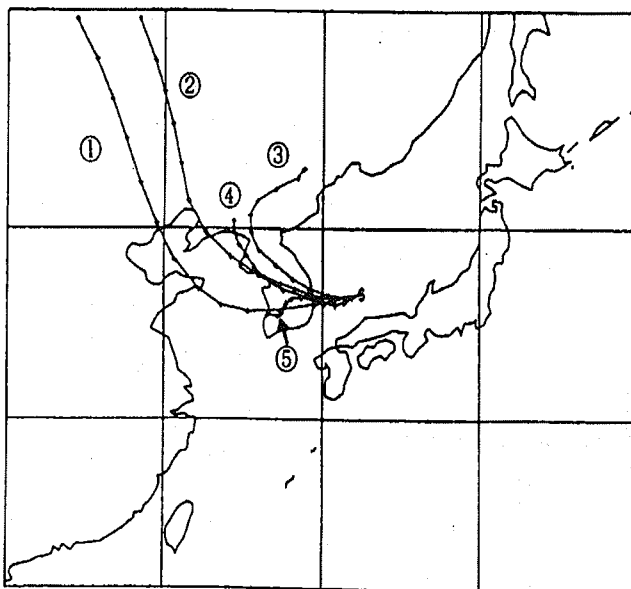


Figure 4. Back trajectory of air mass reaching point A at 11:10 am on Nov. 12, 1992. ① 800 hPa, ② 850 hPa, ③ 900 hPa, ④ 950 hPa, and ⑤ 1000 hPa.

Figure 1 shows the flight courses of the experiments in November, 1992. In this section only the results obtained on the course over the western part of Sea of Japan is described, *i.e.*, north of Honshu and west of Oki islands between point B and point A as depicted in Fig. 1. Figures 2 and 3 show the concentration of SO_2 , NO_x , and O_3 along with flight altitude on Nov. 11 and 12. Since the weather conditions were generally mild on both Nov. 11 and 12, the air covering this area seemed very uniform. The concentration of ozone did not show clear dependence on the altitude, although average concentration of upper layer (average 46.9 and 45.2 ppb for Nov. 11 and 12, respectively) was, as expected, higher than that of lower layer (average 43.5 and 43.3 ppb for Nov. 11 and 12, respectively).

On the other hand the concentration profile of SO_2 and NO_x showed a remarkable feature. At higher altitudes (7000 and 10000 feet) SO_2 and NO_x were both very low. Namely, SO_2 was average 0.24 and 0.18 ppb on Nov. 11 and 12, respectively. NO_x was average 0.21 and 0.18 ppb on Nov. 11 and 12, respectively. At lower altitudes (3500 and 1500 feet) average SO_2 and NO_x concentrations were 1.78 and 1.82 ppb, respectively, on Nov. 11 and 2.62 and 2.71 ppb, respectively, on Nov. 12.

Moreover very clear difference in the profile of SO_2 concentration was observed depending on wind direction, particularly at lower altitudes. On Nov. 11 south wind blew. High concentration of SO_2 up to 6 ppb was found near point B at lower altitudes (3500 and 1500 feet) as shown in Fig. 2. A clear symmetrical pattern was observed in concentration profile of SO_2 and NO_x , having A as a mirror surface. Since the peaks of SO_2 in Fig. 2 are very narrow, it can be thought to be the results of local emission in Japan. In contrast, a very high and broad peak of SO_2 was observed on Nov. 12 as shown in Fig. 3 around point A with maximum concentration of 9.6 ppb. The peak was also symmetrical around point A. There is no local source around point A. Wind blew from west or northwest. It clearly indicates the transport of pollutants from East Asian continent including the Korean Peninsula.

This contention was supported by the calculation of back trajectory. Figure 4 shows the back trajectory of the air mass reaching point A on Nov. 12. Starting point of the calculation is Nov. 9. Trajectories calculated for all the altitudes pass through China and/or

Korea. Concentration of SO_2 at higher altitudes was very low and high concentration of SO_2 was observed only at lower altitudes. It suggests that the impact of the emission in Korea is larger in this case. Highly industrialized areas in Korea are in the upstream of the air mass trajectory. The concentration of NO_x was also very high around point A. It should also suggest a short distance transport from Korea, since the lifetime of NO_x is short. However, the NO_x/SO_2 ratio at point A and that at point B were very different as can be clearly seen in Fig. 3. It indicates that the origins of the air mass around both the points were different each other.

In 1992, concentrations of SO_2 in large cities of Korea were still very high. Therefore, our consideration as above was quite plausible. After 1992 the concentration of SO_2 in Korea came down quickly. Fig. 5 shows the change of the concentration of SO_2 in large cities of Korea from 1990 to 2000. Annual average concentration of SO_2 in Seoul was higher than 30 ppb in 1992, but it came down to less than 10 ppb in 2000. Therefore, we thought that such high concentration of SO_2 as mentioned above should not be observed now. However, in a recent experiment we made aerial observations over the western part of the Sea of Japan near Busan, and we found relatively high concentration of SO_2 .

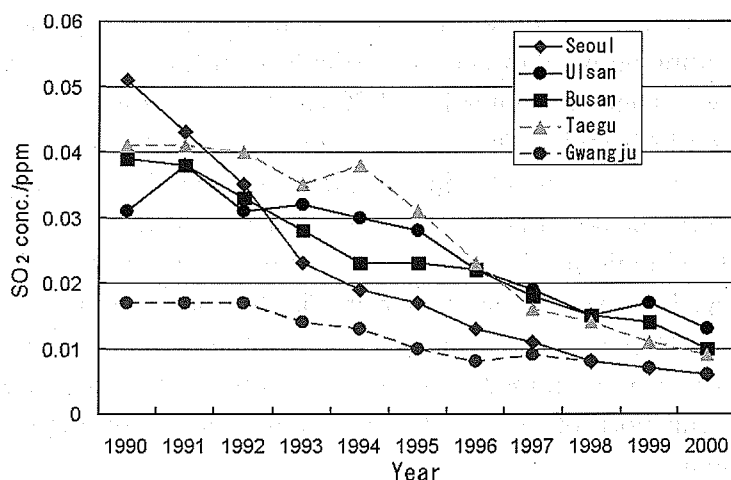


Figure 5. Annual average of SO₂ in large cities of Korea

(2) High concentration of SO₂ over the western part of the Sea of Japan observed in 2002

Aerial observation was carried out in January 2002 by setting Nagoya as the base of the aircraft. Gulfstream II (max. cruising velocity is 933km/hr and max. altitude 13,700m) was used for the experiments. Total 13 flights were made for aerial observation of atmospheric pollutants. Among many flights results of flight Nos. 2, 4, and 6 are described here. Those flights were a round trip to north Kyushu area (Fl#2), one-way trip to Niigata via north Kyushu (Fl#4), and one-way trip to Kagoshima (Fl#6)) (Fig. 6).

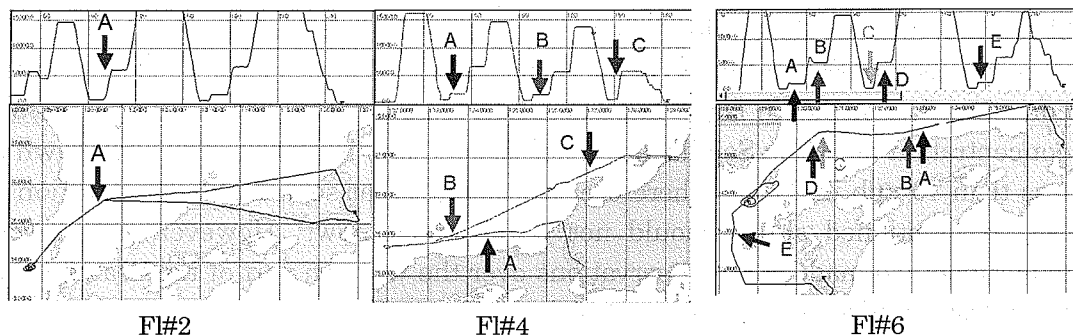


Figure 6. Observation flight routes over the Sea of Japan (Flight Nos. 2, 4, and 6)

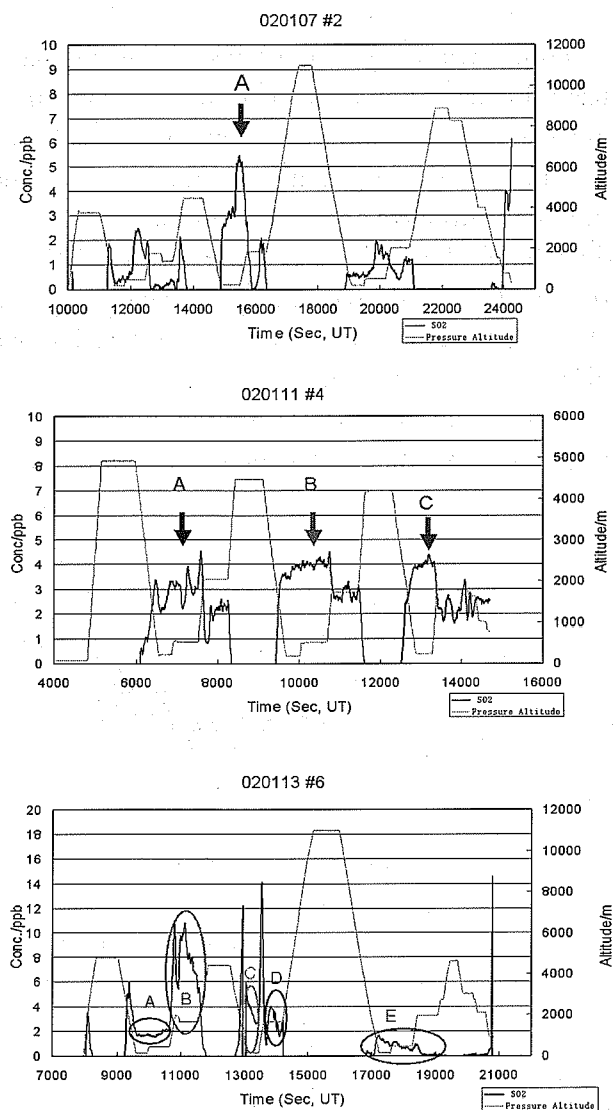


Figure 7. SO₂ measured in Fl#2, Fl#4, and Fl#6 below 4,000m.

SO₂ was monitored continuously on board with TECO Model 43S pulse fluorescence SO₂ monitor. Unfortunately, however, the instrument could be used only below 4,000m of altitude. Other gaseous species such as O₃, NO_y, CO, CO₂, and HC's were also monitored.

Data of SO₂ at the altitudes lower than 4,000 m were analyzed (Fig. 7). In most cases, SO₂ showed a good correlation with CO. That means anthropogenic emission source affects the atmospheric environment of the area observed by the

aircraft.

The highest concentration (~ 5 ppb) was recorded at the point A of Fl#2, which is near Busan, Korea. For Fl#4, correlation between SO_2 and CO was good (Fig. 8). That suggests that the points A, B, and C of Fl#4 are covered with a large uniform air mass. Back trajectory analyses starting from the points A, B, and C were very similar, which supports above contention.

On the other hand, for Fl#6 the correlation of SO_2 against CO showed dependence on the location as shown in Fig. 9. That means the air mass caught at B, D, and E had different origin. Back trajectories starting from points B, D, and E of Fl#6 supported this contention well.

Thus, the concentration of SO_2 near a large city of Korea is still high, but it is much lower than we found in 1992. The environmental situation has been quickly improved in these 10 years.

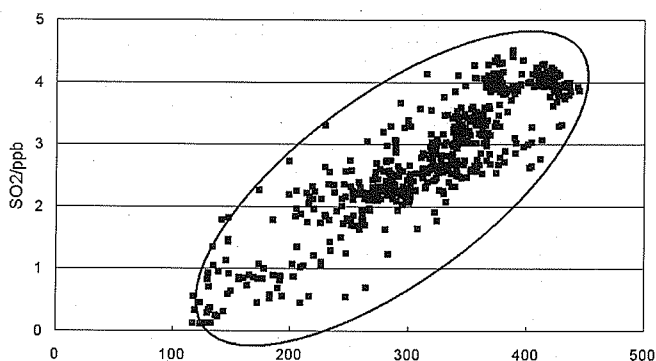


Figure 8. SO_2 - CO correlation in Fl#4.

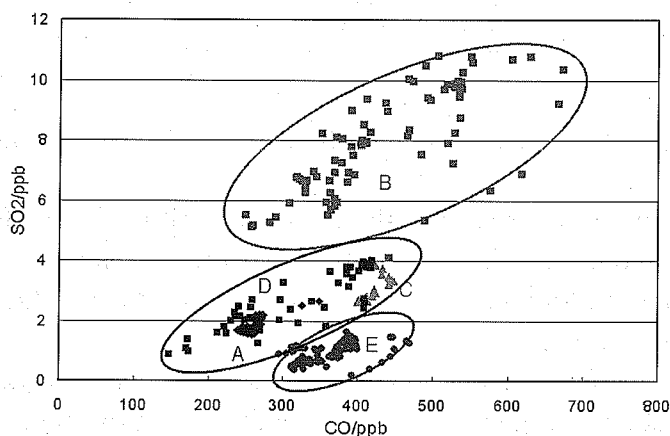


Figure 9. SO_2 - CO correlation in Fl#6.

3.2.2 Three types of transport during winter monsoon period

In this section, the vertical distributions of SO₂ and nss-sulfate aerosols are discussed to elucidate the pattern of transport of sulfur-containing atmospheric pollutants on the basis of the results of our aerial observation experiments.

Experiments to measure the vertical distribution of SO₂ were carried out in November 1992, March 1994, December 1994, and November 1995 (Figs. 10 and 11). Each observation flight consisted of 3 or 4 level flights of about 30 min. Altitudes were usually set approximately 500, 1000, 2000, and 3000 m, whereas other altitudes were sometimes chosen to avoid clouds. In the seasons chosen for the experiments (from November to March) northwest winds prevail throughout Japan (East Asian winter monsoon).

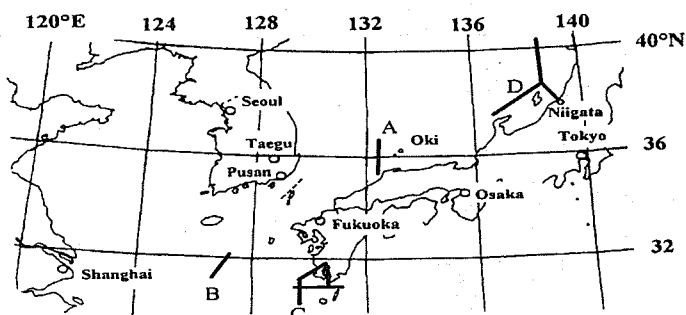


Figure 10. Flight plans of the missions in Nov. 1992 (A and B), Dec. 1994 (C) and Nov. 1995 (D).

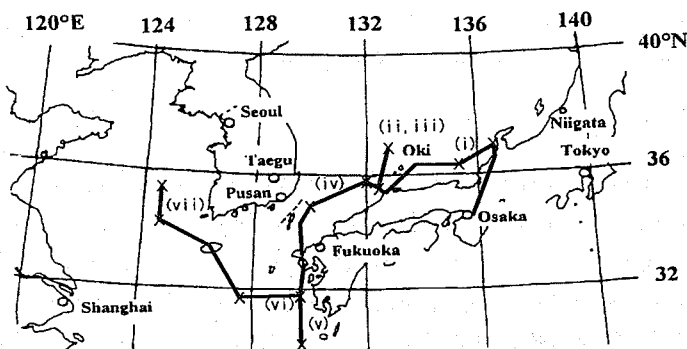


Figure 11. Flight plans of the Mar. 1994 mission.

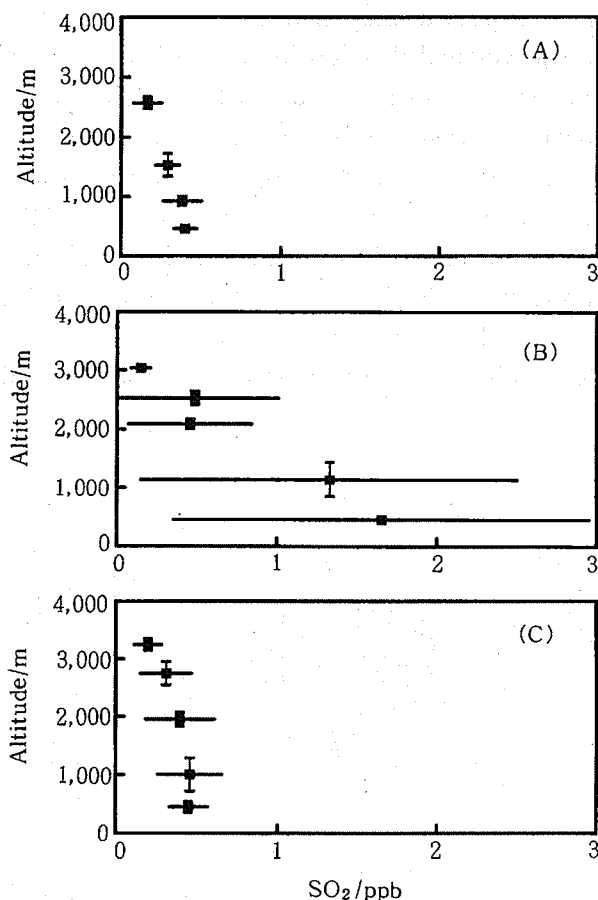


Figure 12. Vertical distribution of SO_2 (A): over the East China Sea near Yakushima; (B): over the Sea of Japan between Japan and Korea; (C): over the northern part of the Sea of Japan. Closed squares show average concentration of SO_2 . Vertical and horizontal bars show one standard deviation of altitude and concentration, respectively.

The highest concentration of SO_2 observed in these experiments was 9.6 ppb observed within the marine boundary layer (~ 500 m) west of the Oki Islands over the Sea of Japan as described in the previous section. The average SO_2 concentrations were 0.9 and 0.4 ppb at altitudes of less than and greater than 2000 m, respectively. The SO_2 distribution profile exhibits altitude dependence, in contrast to that observed in the background marine air (Georgii, and Meixner, 1980). However, the SO_2 change with changing altitude is steeper than has been observed in continental air (Georgii, and Meixner, 1980; Jaeschke et al., 1976;

Varhelyi, 1978). Thus, it can be said that the atmosphere over the seas between Japan and the Asian continent has a character intermediate between those of continental polluted air and background clean air. The vertical distribution of SO_2 differs depending on the area of observation. Over the western part of the Sea of Japan between Korea and Japan, the vertical distribution has a gentler slope (Fig. 12 (B)). On the other hand the vertical distributions of SO_2 over the East China Sea at west of Yaku Island or over the northern part of the Sea of Japan (Fig. 12(A) and 4(C)) are similar to that observed over the Atlantic Ocean (Georgii, and Meixner, 1980), although the average concentration was slightly higher. These results can be explained as follows.

(1) The high concentration of SO_2 observed over the western part of the Sea of Japan must be due to the impact of emissions in Korea, as shown in previous section.

(2) Over the East China Sea to the west of Yakushima the concentration of SO_2 was low, whereas the concentration of SO_4^{2-} was relatively high. An $\text{SO}_4^{2-}/\text{SO}_2$ molar ratio of more than 1.5 was only observed near this area (Fig. 13). The air mass sampled on Dec. 19, 1994 (Fig. 14) came from the northern part of China and passed over the Yellow Sea (Fig. 15). Transport of air from a large industrialized region of northern China to the area sampled during this flight took 2 days or more. If we adopt a conversion rate of 0.02 h^{-1} for $\text{SO}_2 \rightarrow \text{SO}_4^{2-}$ oxidation during long-range transport (Seinfeld, 1986), then the $\text{SO}_4^{2-}/\text{SO}_2$ ratio would have become 1.6 after 48 h of transport, in good agreement with the observed value.

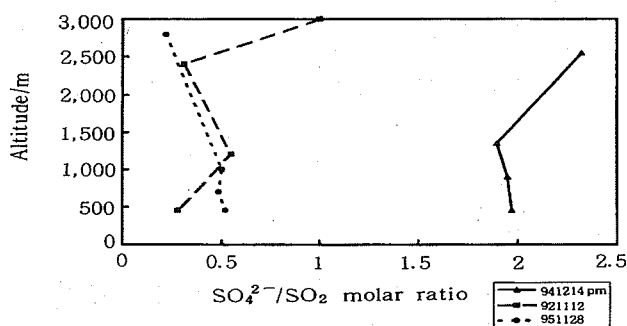


Figure 13. Typical vertical distribution of $\text{SO}_4^{2-}/\text{SO}_2$ over the East China Sea near Yakushima (triangle and thick line), over the Sea of Japan between Japan and Korea (square and broken line), and over the northern part of the Sea of Japan (circle and dotted line).

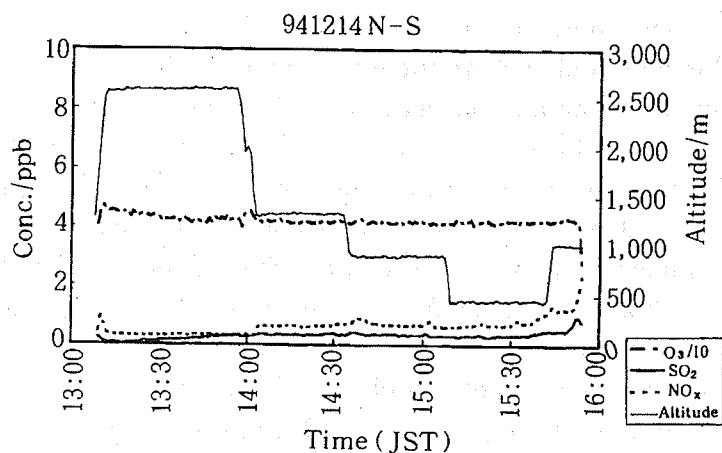


Figure 14. Flight altitude and SO_2 concentrations observed in the experiment of Dec. 14, 1994.

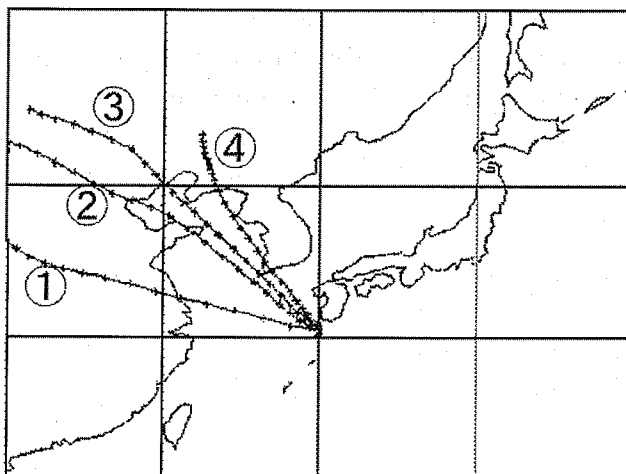


Figure 15. Back trajectories of the air mass reaching to the west of Yakushima at 2 pm on Dec. 14, 1994. (1) 800 hPa, (2) 850 hPa, (3) 900 hPa, and (4) 950 hPa. The interval of the plotts (depicted by "x") is 3 hours.

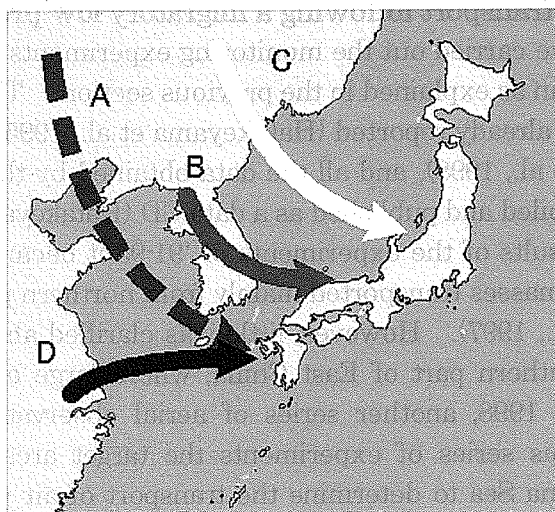


Figure 16. Three types of air mass trajectories reaching Japan from the Asian continent.

(3) Over the northern part of the Sea of Japan, both SO_2 and nss-sulfate were low. Back trajectories reveal that the air masses came from the northern part of Asian continent and that they did not pass over industrialized areas in either Korea or China when northwest winds prevailed. These air masses seem to exhibit characteristics very similar to those of the background continental atmosphere of Asia.

Air masses transported from the Asian continent to Japan in winter can be divided into 3 types: (A) air masses moving from northern China to Kyushu or west of Kyushu, which pass over the Yellow Sea, (B) air masses passing over Korean Peninsula and reaching western Japan, and (C) air masses originating in north Asia which move to eastern Japan, and do not pass over areas with large emissions of atmospheric pollutants. These 3 types of air mass trajectories are schematically shown in Fig. 16. The characteristics of these air masses are: (A) low SO_2 , high $\text{SO}_4^{2-}/\text{SO}_2$ ratio, (B) high SO_2 , low $\text{SO}_4^{2-}/\text{SO}_2$, and (C) low SO_2 , low SO_4^{2-} . Transport pattern (D) will be explained in next section.

3.3 Transport of high concentration of pollutants from central Eastern China driven by migratory low/high pressure system

3.3.1 Large scale transport following a migratory low pressure system

Since 1991 we carried out the monitoring experiments over the seas between East Asia and Japan as explained in the previous section. The results of the 5-year project have been already reported (Hatakeyama et al., 1995a,b; Hatakeyama et al., 1997; Watanabe et al., 1998), and all the data obtained by these observations have already been compiled and published as a data CD (Hatakeyama, 1998).

From the results of the experiments of '91-95 it became clear that there are three types of air masses transported mainly from northern part of Asian Continent (Hatakeyama et al., 1997). However, little was clarified about the transport from the central or southern part of East China, where large emission sources exist. From FY 1996 to 1998, another series of aerial observation experiments were conducted. In this series of experiments the target area was confined to the northern East China Sea to determine the transport of air pollutants from central Eastern China. Samples were taken in almost the same area every year as shown in Fig. 17.

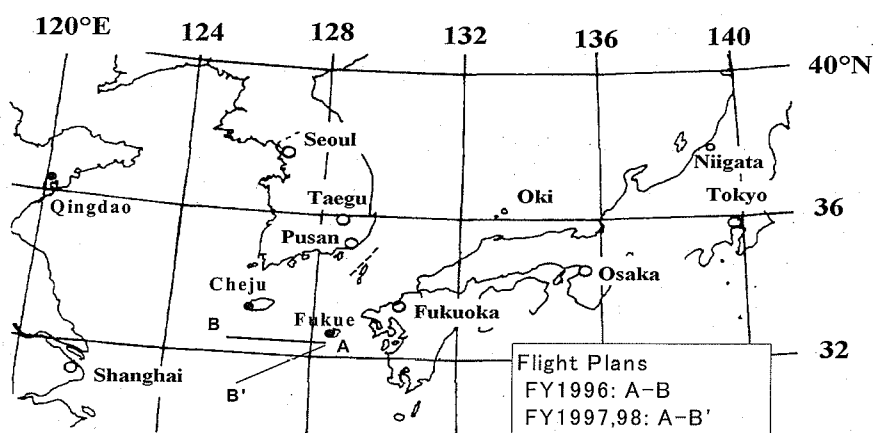


Figure 17. Flight plans for the experiments of FY 1996-1998.

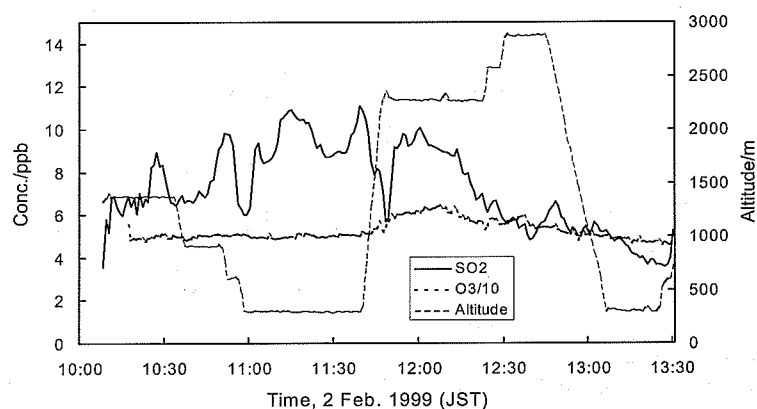


Figure 18. Altitude of measurements and concentrations of SO₂ and ozone measured on Feb. 2, 1999.

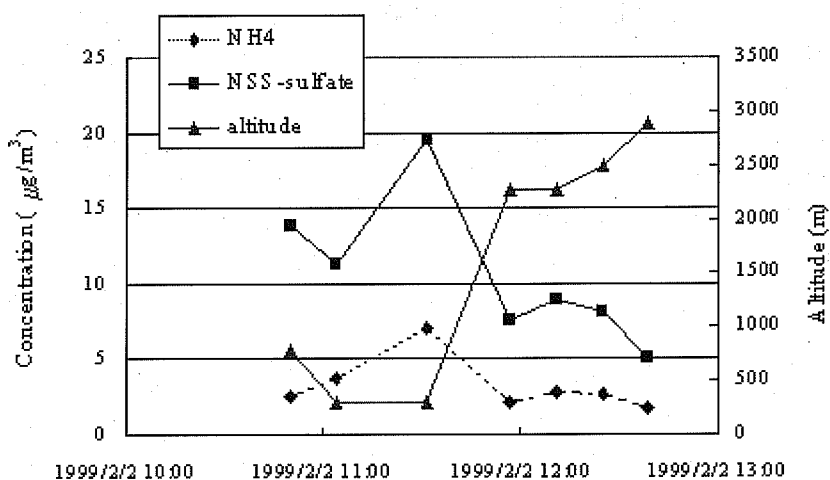


Figure 19. Altitude of measurements and concentrations of SO₂ and ozone on Feb. 4, 1999.

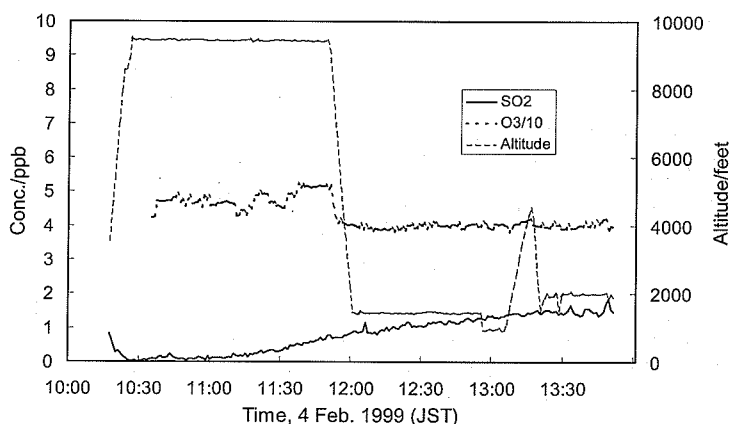


Figure 20. Profiles of sulfate and ammonium on Feb. 2, 1999.

Figure 18 and Figure 19 show a clear contrast: SO_2 concentration was much higher on Feb. 2, 1999 than on Feb. 4, 1999. On Feb. 2, SO_2 was high not only at low altitude (~ 300 m) but also at high altitude (~ 2300 m). NO_x , aldehydes, gaseous HCl, and gaseous HNO_3 showed very similar variations (data not shown). Sulfate and ammonium also showed similar variations (Fig. 20).

Thus, it can be said that the air sampled on that day was highly polluted and well mixed. The vertical distribution of the PAN/ NO_y ratio also clearly showed the mixing of air. On Feb. 4 and 6, the ratio showed a remarkable difference between upper and lower altitudes. In contrast, it showed little dependence on altitude on Feb. 2, which indicates that the air was thoroughly mixed within the lower troposphere.

A low-pressure system originating near Taiwan passed over this area very quickly on Feb. 1 1999, and the weather was very windy on Feb. 2. The system moved along the southern coast of Japan to reach the northwest Pacific; it would have caused mixing. Uno et al. (1998) pointed out that just such a weather pattern should cause a large-scale, long-range transport of polluted air. The results of Feb. 2 support this contention very well.

We have already shown 3 patterns of air masses transported from East Asia as depicted in the section 2.2. In addition to those three types of paths, we found one more path for the long-range transport of an air mass from Asia. This other path ((D) in Fig. 16) is from central Eastern China (around Shanghai) via the northern East China Sea to Japan. The results of our observations gave a clear support to the model predictions. (Hatakeyama, 2000; Hatakeyama, 2001)

3.3.2 Large scale transport following a moving high pressure system

Aircraft observation was also carried out in March 2001. In this campaign ozone, NO_x, and SO₂ were monitored continuously on board. PAN was collected in U-tubes immersed in pulverized dry ice and analyzed later with ECD-GC. Inorganic aerosols were collected on Teflon tape-filter by use of a high-volume tape sampler and the ionic chemical compositions were analyzed with ion chromatography. Aerosol mass concentrations (PM_{2.5} and PM₁₀) were monitored with a simple aerosol mass monitor.

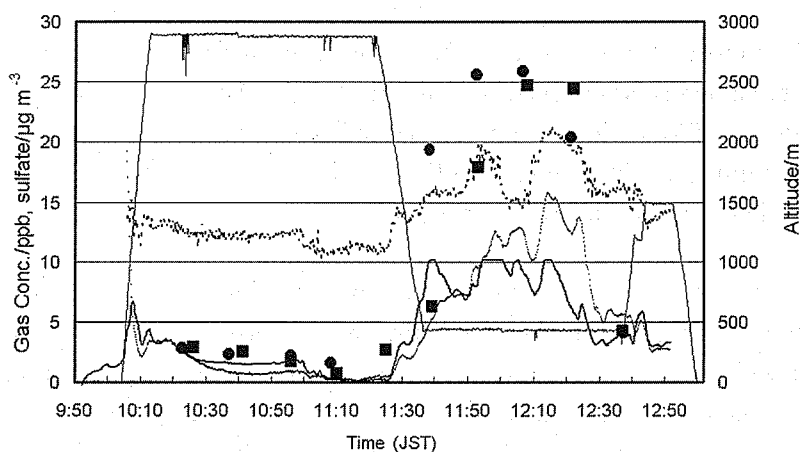


Figure 21. Gaseous pollutants observed over the East China Sea on March 21, 2001. Thick solid line: SO₂; dashed line: O₃; dotted line: NO_x; thin solid line: altitude (right ordinate). Filled circles: nss-sulfate in $\mu\text{g m}^{-3}$ (left ordinate); filled squares: PAN.

Observed area was above the East China Sea between Fukue Island, Nagasaki Pref., Japan and the south of Cheju Island, Korea. Flight plans are just the same as A-B' in Fig. 17. The airplane made two level flights at the altitude of ~3000 m and ~500m for about one hour, respectively.

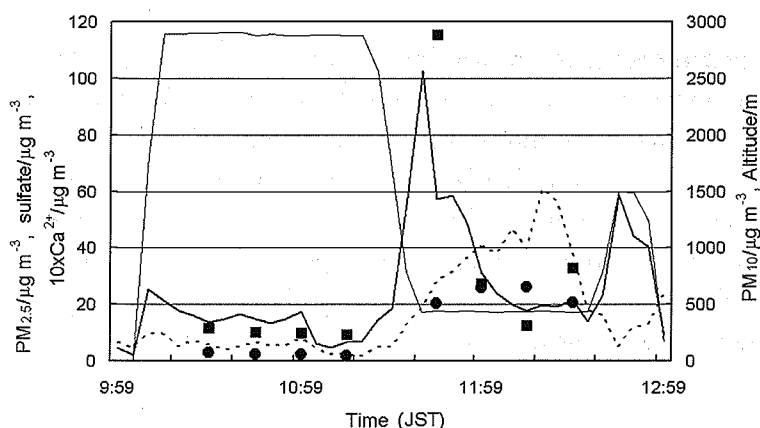


Figure 22. Aerosol mass concentrations and concentrations of sulfate and calcium ions in aerosols observed over the East China Sea on March 21, 2001. Thick solid line: PM_{10} (right ordinate); dashed line: $PM_{2.5}$ (left ordinate); thin solid line: altitude (right ordinate); filled circles: nss-sulfate in $\mu\text{g m}^{-3}$ (left ordinate); filled squares: Ca^{2+} (left ordinate).

On March 21, 2001, air was not mixed well under a high-pressure system. Polluted air mass should be restricted within lower altitude. Figure 21 shows the variation of gaseous species observed on March 21. High concentration of SO_2 (>10 ppb) was observed at low altitude. NO_y , PAN, and sulfate were also high. In contrary, the concentrations of those species were low at higher altitude. Weather pattern before the observation was as follows. A cold front passed over the Korean Peninsula on 20 March and after that a high-pressure system extended from the central China toward the northern East China Sea. Polluted air mass should be pushed out from the central China to the observation area. This result is in marked contrast to our previous results mentioned in the section 3.1.

On March 21, 2001, transport of yellow sand particles was clearly observed. Volume concentrations of aerosols and concentrations of ionic species on March 21 were very interesting. As shown in Fig. 22, the volume concentration of coarse particles (PM_{10}) was high near Cheju Island (turning point of the flight), whereas that of fine particles ($PM_{2.5}$) was high near Kyushu Island. The concentration of Ca^{2+} followed PM_{10} and the concentration of sulfate followed $PM_{2.5}$. That means that the coarse particles are mainly soil dust (yellow sand) and fine particles contains much anthropogenic pollutants.

Back trajectory analyses also located the regional source of the air masses. The trajectories at 500 and 3000 m passed over the Shanghai area (Figs. 23 and 24).

The delayed arrival of the coarse particles on March 21 is related to the different origins of the fine and coarse particles.

The coarse particles (mainly soil dust) originated from Inner Mongolia or the northwest desert area of China, whereas the fine particles (mainly anthropogenic sulfate) originated from the greatly industrialized Shanghai area. In the present case, the source of the coarse particles was upwind, whereas the source of the fine particles was downwind. Similar results were reported by Uematsu et al. (2002). They found that yellow sand dust arrived about 12 h after anthropogenic aerosols at ground level in Nagasaki. In their study, the first peak was broad and corresponded to fine particles rich in sulfur. The second peak was sharp and corresponded to coarse particles rich in mineral components such as Si and Al. Our results on March 21 were quite similar to the results of Uematsu et al.

On March 22 both the peaks of PM_{10} and $PM_{2.5}$ appeared near Kyushu Island. Lidar measurement of aerosol particles at Nagasaki showed that highly depolarized particles (non-spherical particles such as dusts) did not reach the ground level on March 21, but they came down to the ground level on March 22. This fact agrees well with our results.

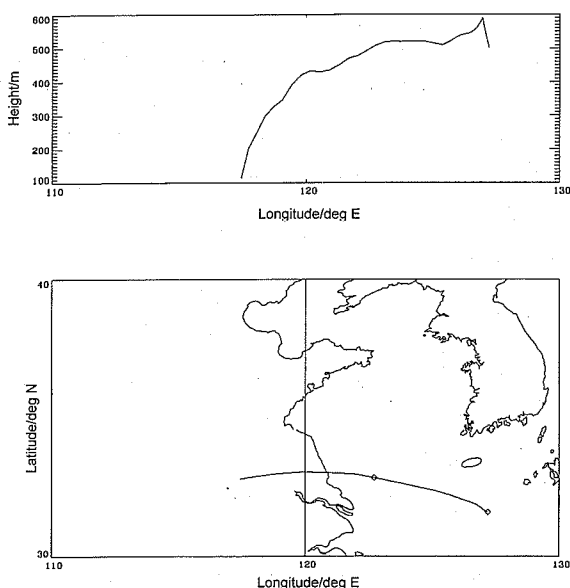


Figure 23. Back trajectory of the air mass at 500 m asl at noon JST on March 21, 2001.

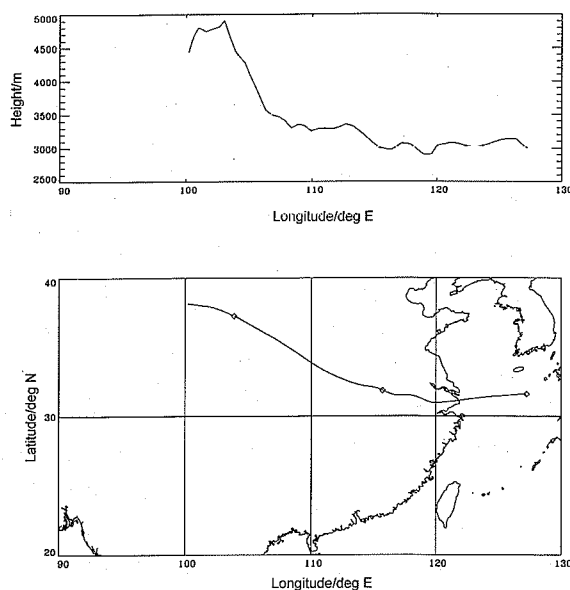


Figure 24. Back trajectory of the air mass at 3000 m asl at noon JST on March 21, 2001.

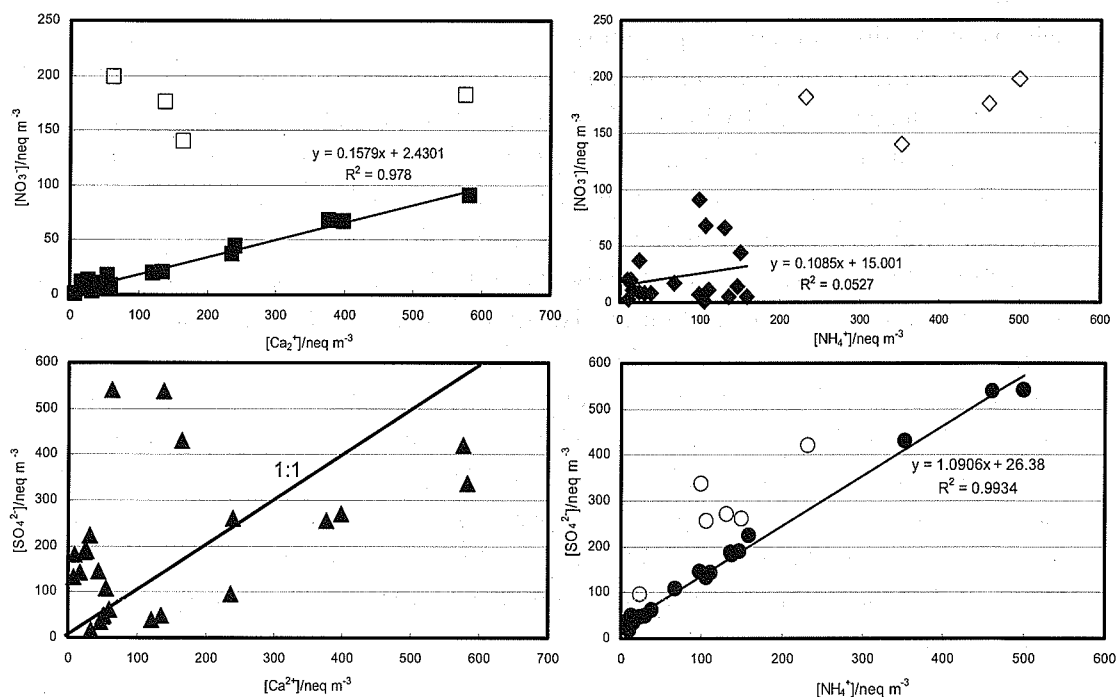


Figure 25. NO_3^- and SO_4^{2-} shown as functions of Ca^{2+} and NH_4^+ . (a) $\text{NO}_3^-:\text{Ca}^{2+}$, (b) $\text{NO}_3^-:\text{NH}_4^+$, (c) $\text{SO}_4^{2-}:\text{Ca}^{2+}$, (d) $\text{SO}_4^{2-}:\text{NH}_4^+$.

A very good linear correlation between nitrate and calcium was obtained (filled squares in Fig. 25a) when we neglected the data obtained at 400 m (open squares) on March 21. Calcium was present in large excess, a result quite similar to the result reported by Jordan et al. (2003). Nitrate usually exists in a coarse mode in aerosols in relatively clean air (Shimohara et al., 2001; Song and Carmichael, 2001; Jordan et al., 2003), because gaseous nitric acid quickly deposits on pre-existing large particles. The filled squares in Fig. 25a deviate greatly from the linear correlation. The samples corresponding to the squares were collected in a highly polluted air mass. In such a case, nitrate must be able to exist in excess of calcium and seems to exist in fine particles, too.

In contrast, no linear correlation between nitrate and ammonium was obtained (Fig. 25b). If we include the 4 open diamonds, the correlation improves. The samples corresponding to the 4 diamonds were also collected at an altitude of 400 m on March 21, in a highly polluted air mass. This result suggests that gaseous nitric acid can be neutralized by ammonia in highly polluted air. In cleaner air,

nitric acid should be mainly adsorbed on the surface of coarse particles, as discussed above. Jordan suggested that the apparent linear correlation they found between NO_3^- and NH_4^+ might be coincidental. Kim and Park (2001) reported that NH_4^+ existed mostly in fine particles irrespective of the presence of dust, which can cause weak correlation between nitrate and ammonium.

No clear correlation was observed between sulfate and calcium (Fig. 25c). Sometimes sulfate was present in excess and sometimes not. The same situation was observed by Jordan et al. (2003).

In contrast, an excellent linear correlation between sulfate and ammonium was obtained when we excluded the 6 open circles in Fig. 25d. The correlation factor was greater than 0.99, and the slope was quite close to unity. Therefore, sulfate is well neutralized by ammonium. The excluded data have calcium concentrations greater than $4 \mu\text{g m}^{-3}$. As described in the introduction, yellow sand dust has a sulfate layer on its surface. Thus, if gaseous SO_2 is adsorbed on the surface of dust particles and oxidized to sulfate, less ammonia is needed to neutralize free sulfuric acid in the gas phase, which can explain the lower content of ammonium in particles containing a very high concentration of calcium. Jordan et al. (2003) showed that sulfate existed in excess of ammonium. This result agrees with our results, at least for samples with a high concentration of calcium.

Kim and Park (2001) analyzed aerosol samples collected in Taejeon, Korea, during both Kosa and non-Kosa periods. They reported a $\text{NH}_4^+/\text{SO}_4^{2-}$ ratio of about 0.6 during the Kosa period and ratios of 1.2 and 0.9 for non-dust days. The former value is close to the ratio for the 6 samples with high calcium concentration, whereas the latter values are in good agreement with our data.

3.4 Aircraft observation of atmospheric pollutants in a large source area in China

In order to clarify the atmospheric environment in northeast Asian region it is necessary to monitor air pollutants in China, Japan and Korea. For this purpose LTP (Long-range Trans-boundary Air Pollutants) working group was organized among Japan, China, and Korea. Collaborative experiments have been performed among those countries. In this section aircraft observations carried out in China for the first time as a cooperative research between China and Japan under the auspices of the LTP project is explained. Experiments were carried out in March 2002.

The experiment was carried out by setting Dalian (Liaoning Province) as the base of the aircraft. A biplane with a single engine, Yun-5, (max. cruising velocity

is ca. 180 km/h) was used for experiments. Two round trips to Dandong (flight levels were 500, 1000, 2000, and 3000 m), one round trip to Jinzhou (500 and 1000 m), one round trip to Qingdao (500 and 1000 m), and one one-way trip to Qingdao (1000m) were made. Fig. 26 is the flight plans over Bohai.

Ozone, NO_x , and SO_2 were monitored continuously on board. A high volume sampler, an Andersen sampler, and a sampler for PM_{10} and 2.5 (APS-3310A) were also set up on board.



Figure 26. Flight plans over Bohai in the aerial experiments in March, 2002.

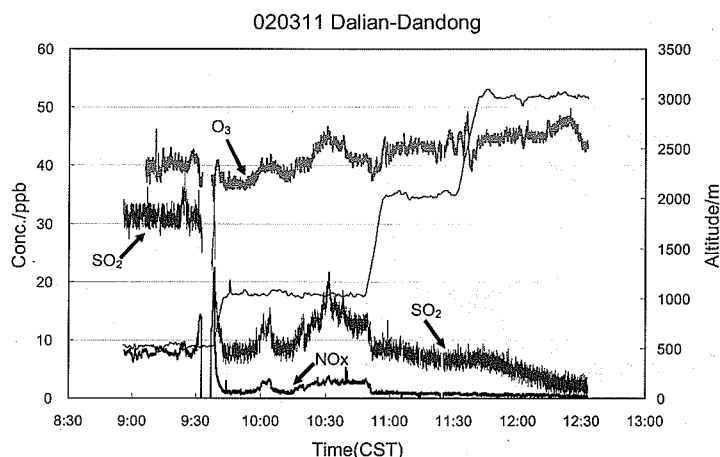


Figure 27. Variation of gaseous pollutants during the flight to Dandong from Dalian on March 11, 2002.

Fig. 27 shows the variation of gaseous pollutants observed during the flight to Dandong from Dalian on March 11, 2002. The area of observation was covered by a high-pressure system on this day. Therefore, highly polluted air mass was thought to be confined to lower altitude. In fact, concentrations of SO_2 and NO_x were more than 30 ppb and more than 10 ppb, respectively, at the altitude of 500 m. In contrast, the concentrations of those species at higher altitudes were lower. Same situation was observed during the flight to Qingdao on the same day. At the altitude of 500 m SO_2 was very high (up to 60 ppb) and NO_x was higher than 10 ppb. At 1000m both species showed lower concentrations.

On the way to Qingdao on March 19, 2002 SO_2 , NO_x , and O_3 were low over the sea, but they showed increasing trend when the airplane approached to Qingdao as shown in Fig. 28.

Correlation between O_3 and NO_x showed a unique feature. As shown in Fig. 29, O_3 and NO_x showed very good correlation over Bohai. It implies that there was an aged air mass reached over Bohai. On the other hand, NO_x showed no correlation to O_3 or even negative correlation on Shantong Peninsula as circled in Fig. 29. That indicates a strong influence of local emission sources near Qingdao.

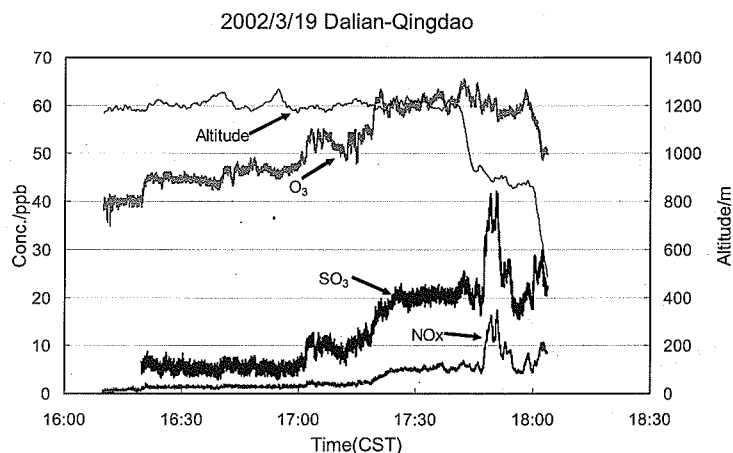


Figure 28. Variation of gaseous pollutants during the flight to Qingdao from Dalian on March 19, 2002.

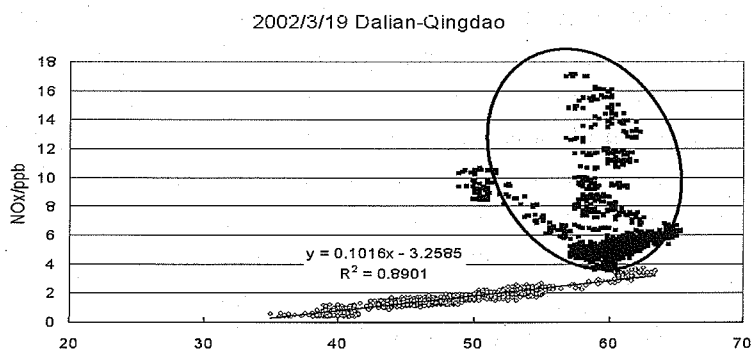


Figure 29. O₃-NO_x correlation for the flight to Qingdao from Dalian on March 19, 2002.

Aerosol data showed high concentrations of sulfate and ammonium. The concentrations of those two chemical species are always nearly the same. It can be concluded that the acidic species are mostly neutralized over Bohai area. Concentrations of most ionic species such as sulfates, nitrates, and ammonium were all rich in fine particles as shown in Fig. 30.

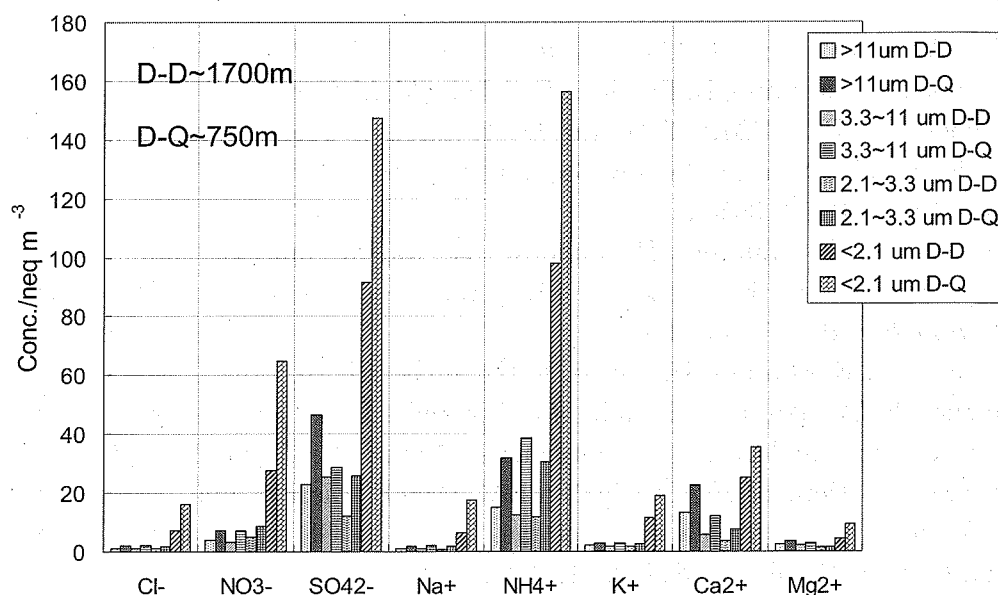


Figure 30. Concentration of ionic species in aerosols collected by means of an Andersen sampler on Mar. 11, 2002.

References

- Georgii, H.W. and Meixner, F.X.; *J. Geophys. Res.*, **85**, 7433-7438 (1980).
- Hatakeyama S., K. Murano, H. Bandow, F. Sakamaki, M. Yamato, S. Tanaka, and H. Akimoto; '91 PEACAMPOT Aircraft Observation of Ozone, NO_x, and SO₂ over the East China Sea, the Yellow Sea, and the Sea of Japan, *J. Geophys. Res.*, **100**, 23143-23151 (1995a).
- Hatakeyama, S., K. Murano, H. Bandow, H. Mukai, and H. Akimoto; High Concentration of SO₂ Observed Over the Sea of Japan, *Terres. Atmos. Oceanic Sci.*, **6**, 403-408 (1995b).
- Hatakeyama, S., K. Murano, H. Mukai, F. Sakamaki, H. Bandow, I. Watanabe, M. Yamato, S. Tanaka, and H. Akimoto; SO₂ and sulfate aerosols over the seas between Japan and the Asian Continent, *J. Aerosol Res. Jpn.*, **12**, 91-95 (1997).
- Hatakeyama, S.; Data of IGAC/APARE/PEACAMPOT Aircraft and Ground-based Observations, '91-'95 Collective Volume, Center for Global Environ. Res., Nat'l Inst. Environ. Studies, CGER-D014(CD)-'98 (1998).
- Hatakeyama, S. eds.; Data of IGAC/APARE/PEACAMPOT II Aircraft and Ground-based Observations, '96-'98 Collective Volume, Center for Global Environ. Res., Nat'l Inst. Environ. Studies, CGER-D026(CD)-'2000 (2000).
- Hatakeyama, S., K. Murano, F. Sakamaki, H. Mukai, H. Bandow, and Y. Komazaki; Transport of atmospheric pollutants from East Asia, *Water, Air, and Soil Pollution*, **130**, 373-378 (2001).
- Jaeschke, W., Schmitt, R., and Georgii, H.W.; *Geophys. Res. Lett.*, **9**, 517-519 (1976).
- Jordan, C. E., J. E. Dibb, B. E. Anderson, and H. E. Fuelberg, Uptake of nitrate and sulfate on dust aerosols during TRACE-P, *J. Geophys. Res.*, **108** (D20), 8817, doi:10.1029/2002JD003101, 2003.
- Kim, B.-G. and S.-U. Park, Transport and evolution of a winter-time Yellow sand observed in Korea, *Atmos. Environ.*, **35**, 3191-3201, 2001.
- Luo, Y.; SO₂ control countermeasures and strategies during "the 9th Five-year Plan" and "the 10th Five-year Plan" period in China, *Proceedings of the 1st Joint Workshop on the Long-range Transboundary Air Pollutants in Northeast Asia*, Aug. 24, 2001, Incheon, Korea, pp. 3-8, 2001.
- Mizohata, A., and N. Ito; Chemical modification of Kosa particles, *J. Aerosol Res. Jpn.*, **10**, 127-134, 1995.
- Seinfeld, J.H.; "Atmospheric Chemistry and Physics of Air Pollution", p.196-197, John Wiley & Sons, New York (1986).

- Shimohara, T., O. Oishi, A. Utsunomiya, H. Mukai, S. Hatakeyama, E.-S. Jang, I. Uno, and K. Murano, Characterization of atmospheric pollutants at two sites in northern Kyushu, Japan – chemical form, and chemical reaction, *Atmos. Environ.*, **35**, 667-681, 2001.
- Song, C. H. and G. R. Carmichael, Gas-particle partitioning of nitric acid modulated by alkaline aerosol, *J. Atmos. Chem.*, **40**, 1-22, 2001.
- Streets, D., N. Y. Tsai, H. Akimoto, and K. Oka; Trends in emissions of acidifying species in Asia, 1985–1997, *Water, Air, Soil Pollution*, **130**, 187–192, 2001.
- Uematsu, M., A. Yoshikawa, H. Muraki, K. Arao, and I. Uno; Transport of mineral and anthropogenic aerosols during a Kosa event over East Asia, *J. Geophys. Res.*, **107** (D7), 10.1029/2001JD000333 (2002).
- Uno, I., T. Ohara, and K. Murano; Simulated acidic aerosol long-range transport and deposition over East Asia – Role of synoptic scale weather systems, in *Air Pollution Modeling and Its Application*, vol. 22, edited by S. E. Gryning and N. Chaumerliac, pp. 185-193, Plenum, New York, 1998.
- Varhelyi, G.,; *Tellus*, **30**, 1494-1502 (1978).

Chapter 4

Observation of Aerosol Particle in the East Asia using Lidars

Nobuo SUGIMOTO

Atmospheric Environment Division

National Institute for Environmental Studies

e-mail: nsugimoto@nies.go.jp

4.1 Introduction

Laser Radars (or Lidars) are useful tools for measuring atmospheric aerosols. The spatial distribution of mineral dust and air-pollution aerosols, and the structure of the atmosphere such as the atmospheric boundary layer can be observed with lidars. Lidars are instruments similar to radar. They utilize light generated by lasers instead of radio wave. Radio wave and light are both electro-magnetic waves, but wavelengths of them are very different. A typical wavelength of lidars is about 500 nanometers, on the other hand wavelength of meteorological radars is about centimeters. Because the wavelength of lidars is very short, they can detect the scattering of very small particles such as atmospheric aerosols. Meteorological radars with a wavelength of centimeters can measure rain droplets having size of about millimeters but cannot detect cloud particles with several to several tens micrometers. A cloud profiling radar with a wavelength of millimeters can detect cloud particles but cannot detect aerosols. A lidar with a wavelength of 500 nanometers can measure aerosols having a size of about 0.1 micrometers and larger. The scattering of light by a particle having a size comparable to the wavelength is called Mie scattering, taking the name of Mie who established the scattering theory. So lidars for aerosol measurement often called as Mie-scattering lidar.

Various lidar methods have been developed for measuring not only aerosols but also air pollution gasses and meteorological parameters (Measures, 1984). In this paper, however, we focus on Mie-scattering lidars for measuring aerosols, because the method is most established and practically applicable to atmospheric environment monitoring. We describe Mie-scattering lidar instruments, data

analysis methods and applications to mineral dust and air-pollution monitoring. We also discuss the definition of data products, which are useful for studies and monitoring of the atmospheric environment.

In the following sections, we describe outline of Mie-scattering lidar instrument and the measurement principle. We then explain the signals obtained with the lidars and how to look at the data. Also, we describe an application to Asian dust measurements.

4. 2 Mie-scattering lidar Instrument

The concept of the Mie scattering lidar measurement of aerosols is illustrated in Fig.1. In the measurement, a laser pulse is transmitted to the atmosphere and scattered by aerosols. The backscattered light is collected by a telescope and detected as a function of time. The delay time corresponds to the range where the laser pulse was scattered, and the intensity is proportional to the aerosol density; the density profile of aerosols is thus measured.

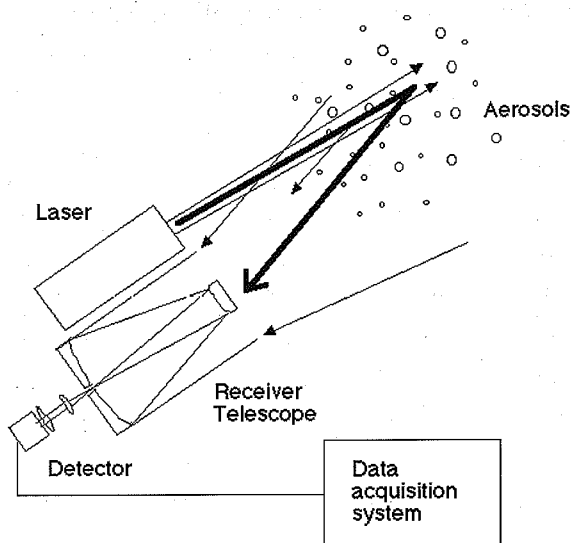


Figure 1. Concept of Mie scattering lidar

A pulsed Nd:YAG laser, a solid-state laser using Neodymium doped Yttrium Aluminum Garnet as a laser media, is widely used as a light source in Mie-scattering lidars. A Nd:YAG laser generates laser light at 1064 nm. Using a second harmonics generator (SHG), laser light at 532 nm is generated. Both of these wavelengths can be used as a light source for Mie-scattering lidars. The pulse duration of a pulsed

Nd:YAG laser using a Q-switch is typically 10 ns. This corresponds to a spatial length of 3 meters. So we can imagine that a column of laser light with a length of 3 meters flies into the sky with a speed of light. If we assume that a scatterer is located at a range of R , the scattered light returns to the receiver at a time delay of $2R/c$, where c is the speed of light and $2R$ corresponds to the round-trip path length. The receiver consists of a telescope for collecting scattered light and a detector. The detector converts the light signal into the electrical signal. Usually, photomultiplier tubes are used at a visible wavelength, and avalanche photodiodes (APDs) are used at a near-infrared wavelength. The waveform of the electrical signal is recorded with a transient recorder as a function of time after laser pulse is transmitted.

In the actual atmosphere, aerosols are distributed continuously, and there is also scattering (Rayleigh scattering) from atmospheric molecules. So the lidar signal looks like that illustrated in Fig. 2. The plot of signal intensity as a function of time, as illustrated in Fig. 2, is sometimes called as "A-scope" from the tradition of the radar community.

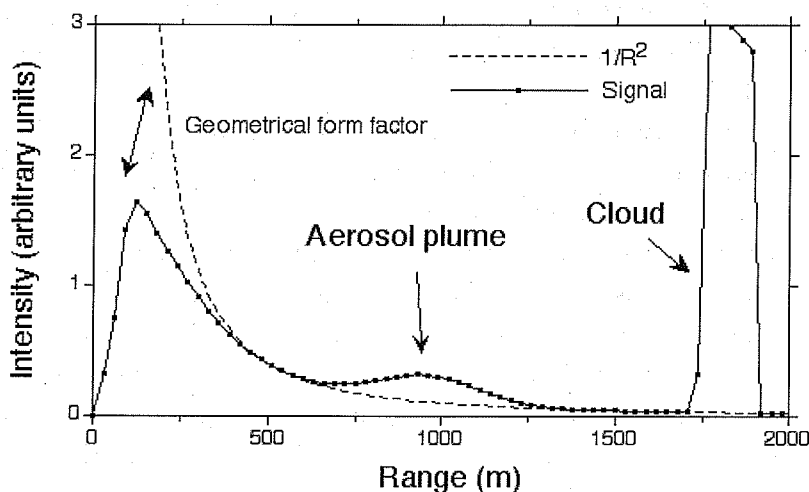


Figure 2. Conceptual lidar return signal.

The lidar signal decreases with range proportional to inverse R square ($1/R^2$), because the scattered light diverges spherically. In Fig. 2, it can be seen that there is a plume of scatterer at a range of 1 km. When the lidar is pointed vertically, range corresponds to height. At the near range, the signal intensity is small, because the transmitted laser beam is not within the telescope field of view. This factor is called

as the geometrical form factor. It is also sometimes called as overlap function or $Y(R)$ function. Clouds generally have very large scattering intensity as illustrated in Fig. 2.

The range resolution of the lidar measurement is limited by the pulse length of the laser. If the pulse temporal width, τ , is 10 nanosecond, the spatial resolution, ΔR , is 1.5 meters. $\Delta R = c \cdot \tau / 2$. The factor of 2 comes because the round-trip path length is twice of the range. In practice, the range resolution is determined by the bandwidth of receiver electronics and sampling interval of the transient recorder (the speed of the analog-to-digital converter). The maximum range of the measurement is determined by the memory length of the transient recorder. If it has 2000 segments with 50 nanosecond sampling rate, it can record a waveform of a length of 100 microseconds. This corresponds to the range of 15 km.

The sensitivity of a lidar is generally determined by the transmitted laser energy and the receiver telescope diameter. Also, the accuracy of transient recorder and characteristics of the detector are important factors determining the sensitivity or signal-to-noise ratio. Optimal size, however, is dependent on the applications of the lidar. For example, in the stratospheric observations, a laser with high power and a large telescope are used to collect very weak scattered light. Large lasers and telescopes are not necessary in the lidars for monitoring mineral dust and air pollution.

An additional function of Mie-scattering lidar is the depolarization measurement utilizing the change in polarization of light by the scattering. In the depolarization measurement, we transmit linearly polarized laser and receive the scattered light with two polarization components separately (parallel and perpendicular to the transmitted polarization direction). If the scatterer is spherical, polarization is conserved. Consequently, only the parallel component is observed. However, the actual aerosols are not necessarily spherical. If it is nonspherical, perpendicular component appears. We define the depolarization ratio as a ratio of perpendicular component to parallel component (P_r/P_l). (Note: Another definition, $P_r/(P_r+P_l)$, is sometimes also used.) The depolarization ratio is a good index of nonsphericity of the scatterer. Usually, depolarization ratio of air pollution aerosols is not large (less than 10%), but that of Asian dust is large (more than 10%). We may consequently characterize aerosols using depolarization ratio (Murayama et al., 1999). As to clouds, water clouds has low depolarization ratio, but ice clouds has large depolarization ratio. The lidars having depolarization measurement function are called as polarization lidar or dual-polarization lidar.

Another additional function of Mie-scattering lidars is multi-wavelength

measurement. Scattering intensity (backscattering coefficient) is dependent on the laser wavelength. Generally, wavelength dependence is larger for smaller particle. The wavelength dependence consequently contains information on particle size of the scatterers.

4.3 Lidar equation

The equation so called lidar equation describes the signals measured with lidars. The lidar equation is the fundamental of all lidar methods. Equation (1) is a simplified form of the lidar equation.

$$P(R) = P_0 \eta_0 Y(R) \frac{ct_p}{2} A_R \frac{\beta(R)}{R^2} \exp[-2 \int_0^R \alpha(r) dr] \quad (1)$$

where $P(R)$ is signal intensity from a range of R , P_0 is transmitted laser power, η_0 is overall efficiency of lidar optics (including reflectivity of mirrors and transmittance of filters, etc.). $Y(R)$ is the geometrical form factor of the transmitter and receiver system (see Section 4.2). c is the speed of light, t_p is the laser pulse temporal width, A_R is receiver aperture area. $\beta(R)$ is backscattering coefficient and $\alpha(r)$ is extinction coefficient. The unit for $P(R)$ and P_0 is Watt. The unit for $\beta(R)$ is $\text{m}^{-1}\text{str}^{-1}$. It is defined as the coefficient for scattering per unit length into unit solid angle. This quantity consequently represents the overall scattering including aerosols and molecules in the volume. The unit for $\alpha(R)$ is m^{-1} . This quantity represents the extinction of the light in the scatterer.

The quantity that is to be derived from the Mie-scattering lidar measurement is the backscattering coefficient $\beta(R)$ or the extinction coefficient $\alpha(R)$. The quantity observed in the measurement is $P(R)$. $Y(R)$ and other constants are known for the lidar system. Consequently, solving the lidar equation to obtain $\beta(R)$ or $\alpha(R)$ is the task of the data analysis. However, as can be seen in Eq.(1), there are two unknowns, $\beta(R)$ and $\alpha(R)$, in the single equation. So it is mathematically not possible to solve the equation. Therefore we need to make some assumptions to solve the equation.

Various data analysis methods were studied for the Mie-scattering lidar data analysis. At present, commonly used methods are Fernald's (Fernald, 1984) and Klett's (Klett, 1981) methods. Both make an assumption on the relationship between $\beta(R)$ and $\alpha(R)$. In the Fernald's method, the scattering of aerosols and

the scattering of molecules are treated separately. $\beta(R)$ and $\alpha(R)$ are written as $\beta(R) = \beta_1(R) + \beta_2(R)$ and $\alpha(R) = \alpha_1(R) + \alpha_2(R)$, where subscript 1 indicates Mie scattering of aerosols and subscript 2 indicates Rayleigh scattering of molecules. The linear relationship is assumed between $\beta_i(R)$ and $\alpha_i(R)$, as follows.

$$\alpha_i = S_i \beta_i, \quad (2)$$

where $i = 1$ is for aerosols, and $i = 2$ is for molecules. S_2 is known from the Rayleigh scattering theory to be $8\pi/3$. S_1 is dependent on aerosol types (aerosol size distribution and complex refractive index). S_1 is commonly called as the lidar ratio or extinction-to-backscatter coefficient. S_1 is the important parameter that needs to be specified in the data analysis.

With the assumption of the lidar ratio, the lidar equation can be written as an integral equation with a single unknown parameter. The equation can be solved with boundary values at the far range. The method is sometimes called as “backward inversion”. At the boundary, we need to give β_1 value. At the far end where aerosol density is small, we may put $\beta_1=0$. It is also possible to give a boundary condition at the near field to perform “forward inversion”. However, the error of the inversion result is larger in the forward inversion method.

In the Klett's method, Mie and Rayleigh scattering components are not separately treated. Generally speaking, Klett's method works well to obtain extinction coefficient profile where aerosol density is very high (optically thick). On the other hand Fernald's method works well where aerosol density is not very high (optically thin). In the Fernald's method, the error in the backscattering coefficient is not very sensitive to the assumption of S_1 where the aerosol density is not high. When optically thick, the error is smaller in the extinction coefficient. It should be noted that the conversion between $\beta_1(R)$ and $\alpha_1(R)$ is directly dependent on the assumption of S_1 . Typical values of S_1 at 532 nm are 50 for urban air pollution aerosols, 40-60 for Asian dust, and 20 for maritime aerosols. It is fortunate that the values for air pollution aerosols and Asian dust are close. (Ansmann et al., 1992; Liu et al., 2002)

Though we did not define the polarization in the lidar equation in the above discussion, we may extend the expression including the polarization by defining two backscatter coefficients separately for the two polarization components that are parallel and perpendicular to the laser polarization direction. The extinction

term is common to both polarization components. Consequently, we can use the total signal for deriving $\beta = \beta_l + \beta_r$, where subscripts l and r represent parallel and perpendicular, and then use the signal depolarization ratio for deriving the aerosol depolarization ratio, ADR, which is defined by $ADR = \beta_r / \beta_l$.

4.4 How to look at the lidar data

4.4.1 Range-corrected signal intensity and signal depolarization ratio

In the case of the NIES Compact Mie-scattering lidar, the measured quantities are the signal intensity and the signal depolarization ratio. The signal intensity at 1064 nm is also measured in the two-wavelength system. In this section, we describe what can be seen in the quick-look indications of the NIES Compact Mie-scattering lidar and in the analyzed data.

In the quick-look indications we display the range-corrected signal intensity and the signal depolarization ratio. An example is shown in Fig. 3. In this example, time-height indication is shown up to a height of 10 km for a five-day period. The range-corrected signal intensity is defined by $R^2P(R)$, where $P(R)$ is signal intensity. From the lidar equation this quantity is written as follow.

$$P(R)R^2 = c_{\text{system}} \beta(R) \exp[-2 \int_0^R \alpha(r) dr] \quad (3)$$

This quantity is approximately proportional to $\beta(R)$ when the extinction term is small. There are ambiguity in the system constant, for example the transmittance of the window on the roof, we indicate the range-corrected signal intensity in arbitrary units. The purpose of the indication is not only for the quick look of the observed atmosphere but also for checking the performance of the lidar system.

Signal depolarization ratio (SDR) is defined as the ratio of the perpendicular polarization component in the signal to the parallel component. It is called signal depolarization ratio to distinguish from the aerosol depolarization ratio (ADR), which is defined for aerosol scattering. (Browell et al., 1990) The ADR is a good indication of the nonsphericity of aerosols. The SDR includes the contribution of the Rayleigh scattering of atmospheric molecules and different from the ADR. However, the difference between SDR and ADR is not large where aerosol density is relatively high.

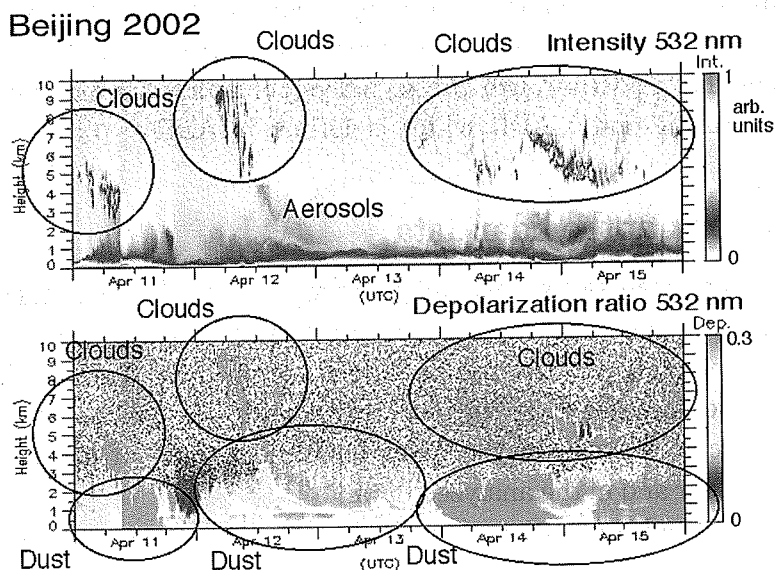


Figure 3. Example of THI of range-corrected signal intensity and signal depolarization ratio.

In the upper panel of Fig. 3, we can observe profiles of aerosols and clouds. Generally speaking, scattering of clouds is much higher than scattering of aerosols at the same altitude. So we can distinguish clouds from aerosols. Also clouds and aerosols can be distinguished from the temporal scale of the variations. Generally, clouds changes much more rapidly than aerosols. From the lower panel of Fig. 3, we can see the nonsphericity of the scatterers. As to clouds, water droplets in water clouds are spherical, so they have small depolarization ratio. On the other hand, ice crystals in ice clouds are not spherical and have large depolarization ratio. However, ice crystals sometimes are aligned in the clouds. In such situations, low depolarization ratio is observed. As to aerosols, air pollution aerosols and sea salt droplets are close to sphere and have low depolarization ratio. Mineral dust such as Asian dust has large depolarization ratio (more than 10%). In the lower panel of Fig. 3, we can see that all of the clouds are ice clouds and the aerosols are mostly dust.

4.4.2 Two-wavelength signal ratio

In the two-wavelength NIES lidar, we obtain signals also at 1064 nm. We indicate also the ratio of the signal intensities at 1064 nm to 532 nm in the quick-look display. Fig. 4 shows an example. The wavelength ratio, $P(1064)/P(532)$, is close to 1 if the diameter of scatterer is very large such as in the water cloud

droplet case (diameter is $\sim 10 \mu\text{m}$ or larger). This is because the wavelength dependence of scattering is small for large particles. Aerosols have smaller values of the wavelength ratio (~ 0.1 to ~ 1.2). Generally the ratio is larger for larger particle.

In the lowest panel of Fig. 4, it can be seen that clouds have large $P(1064)/P(532)$ values. It can be also seen that aerosols at the top of the atmospheric boundary layer (the layer from the ground to $\sim 2 \text{ km}$ in Fig 4) have larger wavelength ratio values. This is probably due to that relative humidity is high near the top of boundary layer and diameter of aerosols is larger.

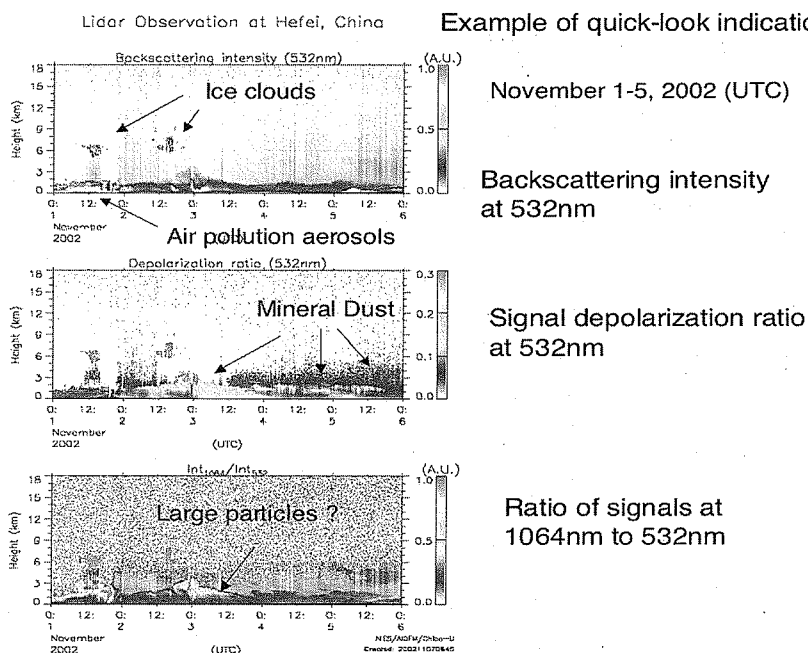


Figure 4. Example of THI of range-corrected signal intensity (532nm), signal depolarization ratio (532 nm) and the ratio of signals at 1064 nm to 532 nm.

In the above discussion, we assumed that $P(1064)/P(532)$ is nearly equal to $\beta(1064)/\beta(532)$. This approximation is valid if the extinction term of the lidar equation is small. However, we need to take care when density of optically absorptive aerosols is high. Fig. 5 shows an example of a forest fire aerosol case observed in Fukue, Japan and Suwon, Korea. In this example, $P(1064)/P(532)$ becomes larger as the height increases. This is because the extinction at 532 nm is larger than extinction at 1064 nm. The signal at 532 nm decreases much faster than that at 1064 nm. Consequently, the ratio $P(1064)/P(532)$ increases with height. To

describe $\beta(1064)/\beta(532)$ quantitatively, we require analysis using inversion methods. The quick-look indication of $P(1064)/P(532)$ is, however, useful to know the situation like the forest fire case. The similar profiles of the wavelength ratio are observed also in heavy air pollution cases.

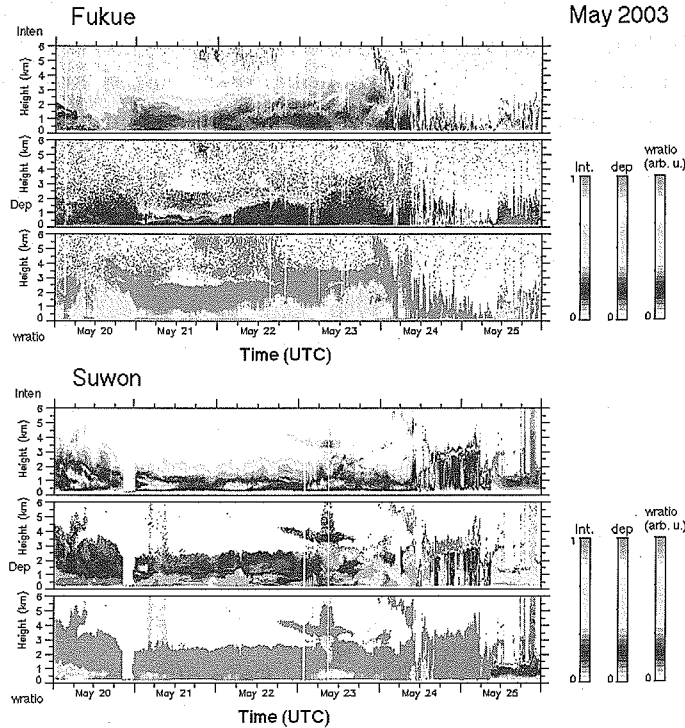


Figure 5. THI of range-corrected signal intensity (532nm), signal depolarization ratio (532 nm) and the ratio of signals at 1064 nm to 532 nm in the heavy Russian forest fire aerosol case.

4.4.3 Attenuated backscattering coefficient and extinction coefficient

Fig. 6 shows an example of the attenuated backscattering coefficient and extinction coefficient for the same data. Extinction coefficient was derived with the Fernald's inversion method with the lidar ratio assumption ($S1=50$). Attenuated backscattering coefficient is same as the range-corrected signal except that it is calibrated at the near range. It is called attenuated backscattering coefficient because the attenuation of the lidar signal is not corrected. The calibration of the backscattering coefficient at the near range is done using the backscattering coefficient (extinction coefficient) obtained by the Fernald's inversion method.

The extinction coefficient is more quantitative because the attenuation is corrected by the inversion method. However, there is a disadvantage that the inversion method is not applicable to the data having strong cloud scattering. In fact, in the lower panel of Fig. 6, some data are missing due to this problem. On the other hand, we can obtain attenuated backscattering profiles even if the profile has clouds. But the backscattering coefficient is underestimated above dense aerosol layers because of the attenuation. Also, it contains the contribution of molecular scattering. We should consequently use these two quantities depending on the purposes. For example, in the aerosol transport analysis, we can use the attenuated backscattering coefficient not to lose transport features under clouds. In the quantitative comparison with the models and climatology of aerosol distribution, we should use the extinction coefficient profiles. We can further apply a method using depolarization ratio to separate contributions of mineral dust and air-pollution aerosols as described in Section 5.

4.5 Observations of Asian dust and air-pollution aerosols with lidars

The National Institute for Environmental Studies conducts continuous observations with a network of Mie-scattering lidars in the East Asia region in cooperation with Universities and other research institutes. Current observation locations are as follows. Tsukuba (36.05N, 140.12E), Nagasaki (Nagasaki University)(32.78N, 129.86E), Amami-Oshima (28.44N, 129.70E), Miyakojima (24.7N, 125.3E), Fukue (32.63N, 128.83E), Sapporo (Hokkaido University)(43.06N, 141.33E), Toyama (Toyama Prefectural Environmental Science Research Center)(36.7N, 137.1E), Suwon, Korea (Kyun Hee University)(37.14N, 127.04E), Beijing (Sino-Japan Friendship Center for Environmental Protection) (39.90N, 117.16E), Hefei (Anhui Institute of Optics and Fine Mechanics) (31.90N, 117.16E), and Sri Samrong, Thailand (17.15N, 99.95E). We conduct studies of Asian dust and anthropogenic aerosols using the network observation data.

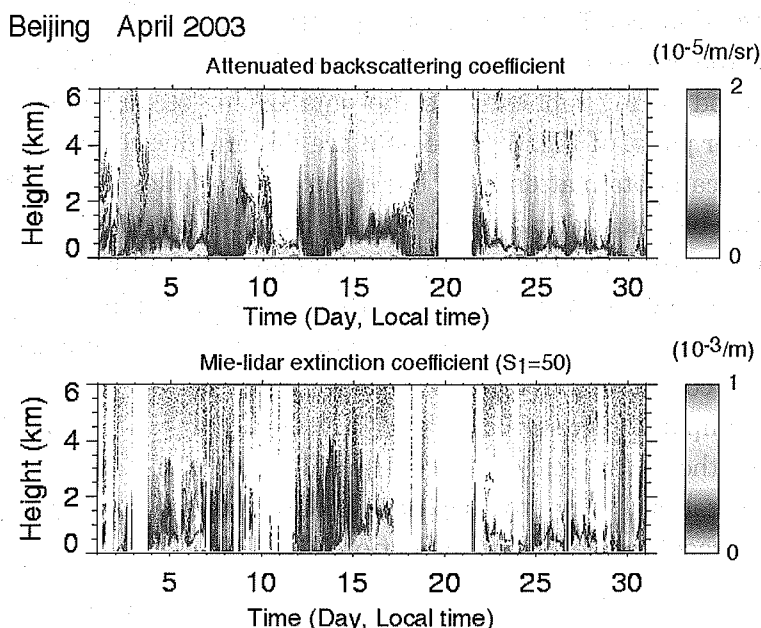


Figure 6. Attenuated backscattering coefficient and extinction coefficient

In this section, we describe the methods for applying lidar data to the studies on Asian dust and air-pollution phenomena. Firstly, in Section 4.5.1, we introduce a simple method for classifying the scatterer observed with the lidars. We classify the scatterers using the scattering intensity and the depolarization ratio, into four categories, mineral dust, spherical aerosols, water clouds, and ice clouds. This method is very simple and useful for statistical analysis of Asian dust phenomena. In Section 4.5.2, we introduce a more quantitative method for estimating the contribution of mineral dust and spherical aerosols in the scattering. With this method, we can estimate the extinction coefficients of mineral dust and other spherical aerosols (mostly air-pollution aerosols) separately. This method is useful quantitative analysis of aerosol distributions and for validation of chemical transport models. We show examples of the comparison with a model in Section 5.3.

4.5.1 Scatterer classification method

In the Mie-scattering lidar with the polarization measurement function, we obtain backscattering intensity and depolarization ratio. We can characterize the scatterers using these two parameters (Shimizu et al., 2004). The simplest method is the method described in this section. Fig. 7 illustrates the concept of the method.

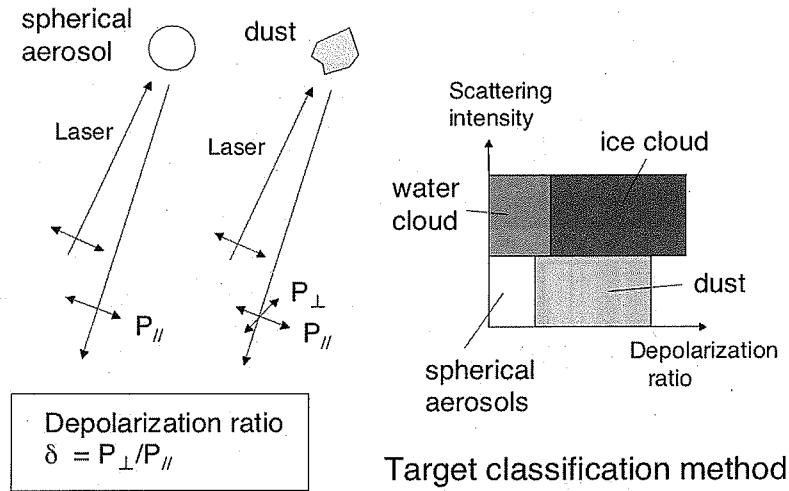


Figure 7. Simple target classification method.

We assume threshold values in the range-corrected signal intensity and the depolarization ratio to classify the scatterers into four categories, namely water cloud, ice cloud, spherical aerosols, and mineral dust. Clouds have generally high scattering intensity. We can distinguish clouds and aerosols with a suitable threshold value of the range-corrected signal intensity. Water clouds and ice clouds are classified with a threshold value of the depolarization ratio. Also, mineral dust and spherical aerosols are classified using a threshold of the depolarization ratio. The threshold value of the range-corrected signal intensity is determined suitably for each data set by looking at the result. We use threshold values of the depolarization ratio of 15% for classifying ice and water clouds and 10% for classifying mineral dust and spherical aerosols. The method can be applied to each height of the lidar signal profiles. Fig.8 shows an example of the result of the scatterer classification with the method. In the figure, time-height indication of classified result is shown for three locations for April 2001. The orange-colored parts in the figure indicate mineral dust. As seen in the figure, in Beijing the frequency that mineral dust is observed is very high in April. In Japan (Nagasaki, Tsukuba), the frequency is much lower. It can be also seen that the vertical distribution characteristics is different in Beijing and in Nagasaki and Tsukuba.

April 2001

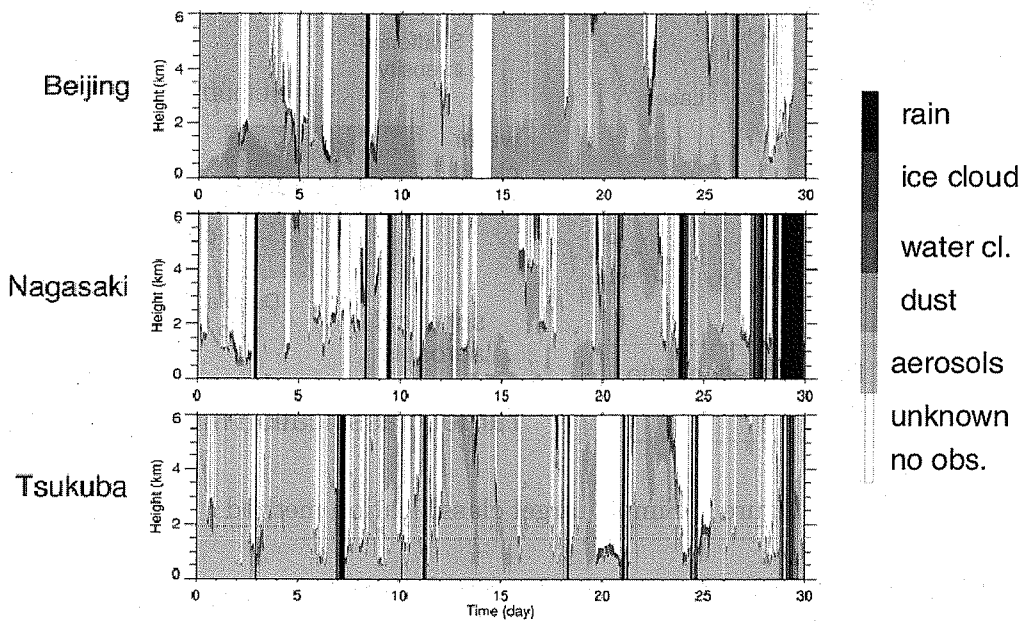


Figure 8. Target classification THI for Beijing, Nagasaki, and Tsukuba (April 2001).

The statistical characteristics are shown in Fig. 9. The panels of Fig. 9 show the frequency of the classified categories for each height, at three locations in March, April and May 2001. We can study the characteristics of dust vertical distribution and seasonal and year-to-year changes using this analysis method.

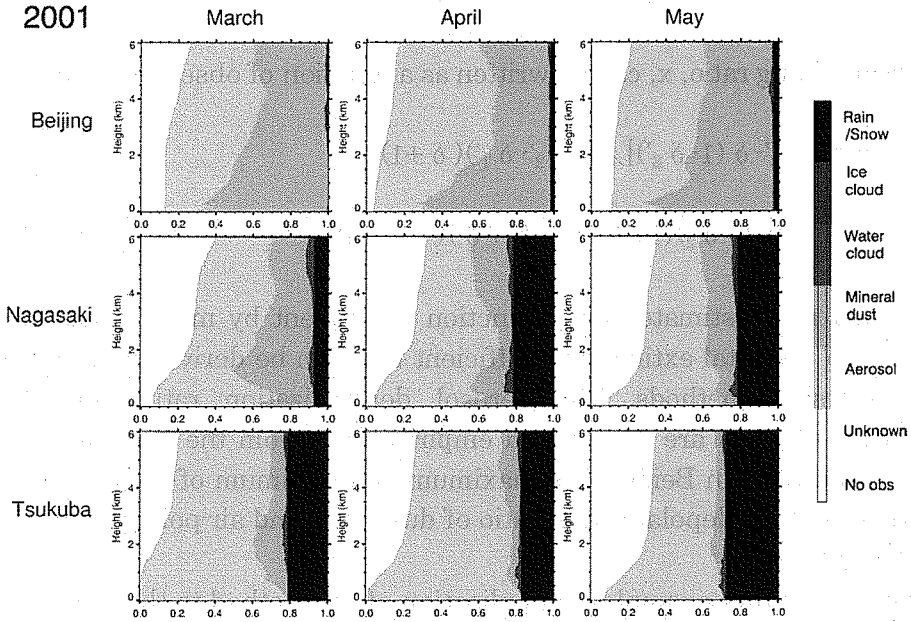


Figure 9. Frequency of the categories for each height.

4.5.2 Estimation of extinction coefficient of dust and air-pollution aerosols

In this section, we describe more quantitative method for estimating contribution of dust aerosols in the total backscattering. (Shimizu et al., 2003; Sugimoto et al., 2003) In this method, we consider an external mixture of two types of aerosols having aerosol depolarization ratio of δ_1 and δ_2 . Here, we define depolarization ratio, δ_i , as $\delta_i = P_{ir}/P_{il}$, where P_{il} and P_{ir} are aerosol backscattering intensity of the parallel and perpendicular polarization components. We also define $\delta_i' = P_{ir}/(P_{ir} + P_{il})$. We should note that these parameters are functions of height, though it is not indicated explicitly for simplicity. The backscattering intensity from the mixture can be written as follows for each polarization component.

$$P_r = [x \delta_1' + (1-x) \delta_2']P \quad (4)$$

$$P_l = [x (1 - \delta_1') + (1-x) (1 - \delta_2')]P \quad (5)$$

where x is the optically effective mixing ratio of type 1 aerosol and $P = P_{ir} + P_{il}$. Observed aerosol depolarization ratio, δ , can be written as

$$\delta = P_r/P_l = [x \delta_1' + (1-x) \delta_2'] / [x (1-\delta_1') + (1-x) (1-\delta_2')]. \quad (6)$$

The optical mixing ratio, x , can be written as a function of observed δ as follows.

$$\begin{aligned} x &= [\delta_2' - \delta (1-\delta_2')] / [(\delta_2' - \delta_1')(\delta + 1)] \\ &= [(\delta - \delta_2)(1 + \delta_1)] / [(1 + \delta)(\delta_1 - \delta_2)]. \end{aligned} \quad (7)$$

We can now estimate dust extinction coefficient by multiplying the mixing ratio, $x(z)$, to the total extinction coefficient that can be derived with Fernald's or Klett's inversion methods. The aerosol depolarization ratios for dust and air-pollution aerosols are determined empirically. From the statistics of aerosol depolarization ratio in Beijing, the maximum and minimum of depolarization ratio that corresponds to depolarization ratio of dust, δ_1 , and air-pollution aerosol, δ_2 , were 0.35 and 0.05.

Figure 10 shows examples of application of the method to the range-corrected intensity.

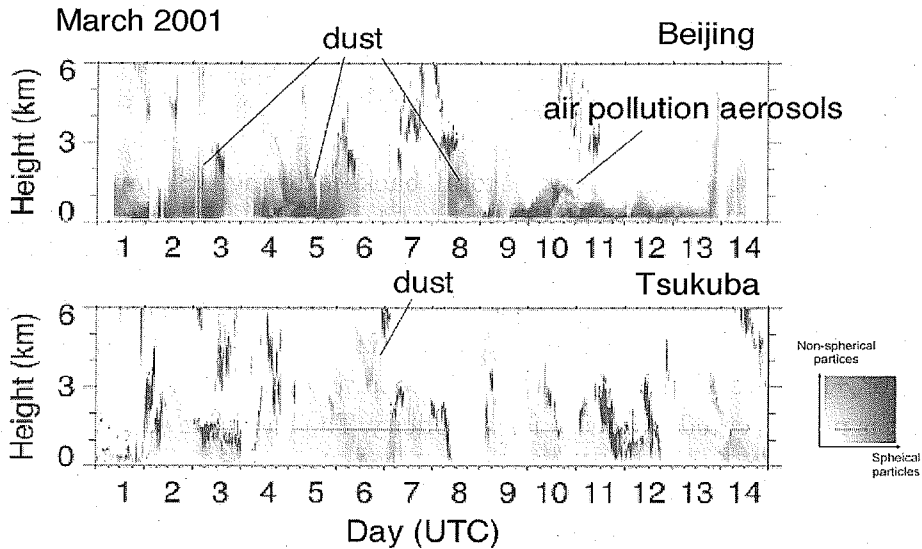


Figure 10. Distributions of dust and spherical (air-pollution) aerosols in Beijing and Tsukuba estimated with the method.

Here, we used signal depolarization ratio instead of aerosol depolarization ratio. This approximation is applicable when aerosol scattering is sufficiently higher than

molecular scattering. In Fig. 10, dust and air-pollution (spherical) aerosol are colored in red and blue and the density of colors indicates density of aerosols. The plumes of dust and air pollution were separated clearly. Clouds are not removed in this indication. Ice clouds and water clouds are indicated in red and blue. We can also apply the method to extinction coefficient profile inverted with Fernald's method.

4.5.3 Application to validation of chemical transport models

The method for estimating extinction coefficient of dust and air-pollution aerosols is useful for validating chemical transport models. We describe here an example of comparison with the Chemical Weather Forecast System (CFORS) developed by Itsushi Uno with Kyushu University. The CFORS is a regional-scale chemical transport model based on the Regional Atmospheric Modeling System (RAMS). It calculates mineral dust and chemical species such as SO_2 /Sulfate, black carbon, organic carbon. Mineral dust emissions are calculated from surface wind velocity. Chemical species are calculated based on the emission inventory data. Such a chemical transport model is essentially important to understand Asian dust phenomena and air pollution phenomena as a whole in the regional scale.

Fig. 11 shows examples of two-dimensional distributions of Asian dust and sulfate aerosols calculated by CFORS. (Uno et al., 2003) Actually, CFORS predicts three-dimensional distributions with three-hour resolution up to three days after. The Horizontal resolution is 80 km x 80 km, and vertically 23 levels are considered. The densities indicated in the figure are those for the ground level.

An example of comparison with the lidar observation is shown in Fig. 12. The time-height indications of the extinction coefficients of dust and spherical aerosols (mostly air-pollution aerosols) are compared with density time-height indications of dust and sulfate calculated with the CFORS. It can be seen that major features of dust and air pollution aerosol distribution pattern observed with the lidar are reproduced well by the CFORS.

Validation of the models and also using lidar data as inputs for the models are very important application of the lidar observations. From the lidar observations, the extinction coefficient profiles for dust and other spherical aerosols can be derived with a reasonable accuracy. As can be seen in this example, continuous data with lidars are very useful for validating chemical transport models.

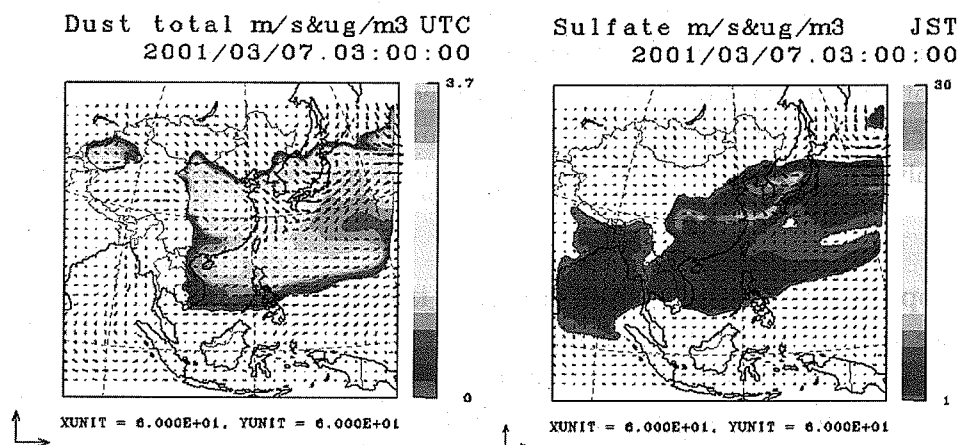


Figure 11. Distribution of dust and sulfate calculated by the CFORS.

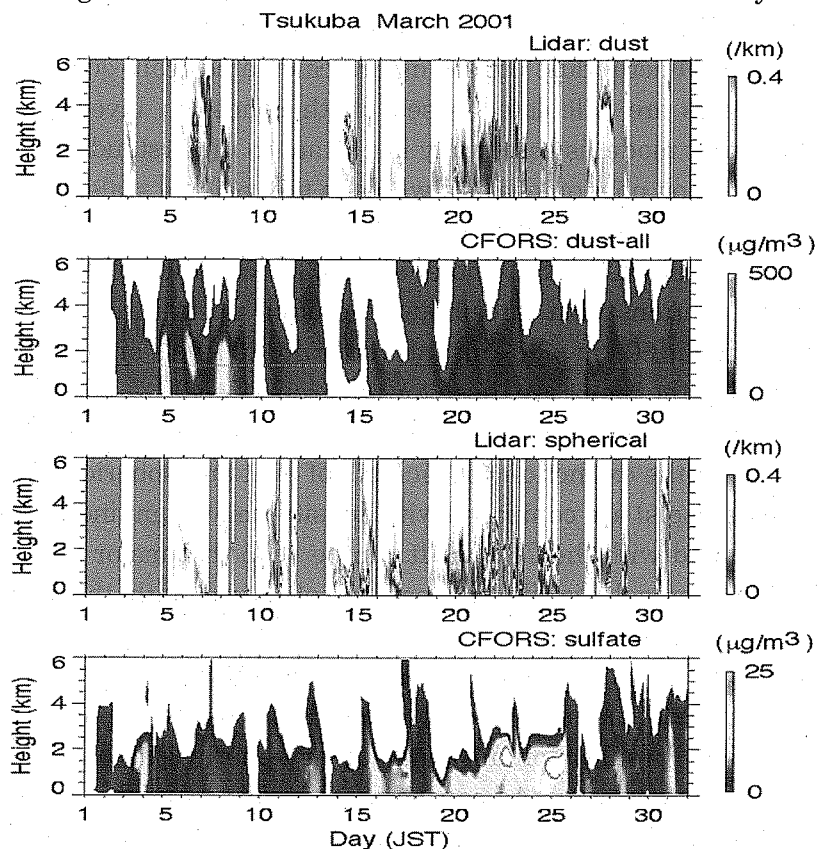


Figure 12. Comparison of lidar derived extinction coefficients of dust and spherical aerosols and those calculated by the CFORS.

References

- Ansmann, A., M. Riebesell, U. Wandinger, C. Weitkamp, E. Voss, W. Lahmann, and W. Mischealis, Combined Raman elastic-backscatter LIDAR for vertical profiling of moisture, aerosol extinction, backscatter, and LIDAR ratio, *Appl. Phys.*, **B55**, 18-28, 1992.
- Browell, E. V., C. F. Butler, S. Ismail, P. A. Robinette, A. F. Carter, N. S. Higdon, O. B. Toon, M.R. Schoeber, and A. F. Tuck, Airborne lidar observations in the wintertime Arctic stratosphere: Polar stratosphere clouds, *Geophys. Res. Lett.*, **17**, 385-388, 1990.
- Fernald, F. G., Analysis of atmospheric lidar observations: Some comments, *Appl. Opt.*, **23**, 659-653, 1984.
- Klett, J. D., Stable analytical inversion solution for processing lidar returns, *Appl. Opt.*, **20**, 211-220, 1981.
- Liu, Z., N. Sugimoto, and T. Murayama, Extinction-to-backscatter ratio of Asian dust observed by high-spectral-resolution lidar and Raman lidar, *Applied Optics*, **41**, 2760-2767, 2002.
- Measures, R.M., *Laser Remote Sensing*, John Wiley & Sons., 1984.
- Murayama, T., H. Okamoto, N. Kaneyasu, H. Kamataki, and K. Miura, Application of lidar depolarization measurement in the atmospheric boundary layer: Effects of dust and sea-salt particles, *J. Geophys. Res.*, **104**, 31,781-31,792, 1999.
- Shimizu, A., N. Sugimoto, I. Matsui, K. Arao, I. Uno, T. Murayama, N. Kagawa, K. Aoki, A. Uchiyama, and A. Yamazaki, Continuous observations of Asian dust and other aerosols by polarization lidar in China and Japan during ACE-Asia, *J. Geophys. Res.*, **109**, D19S17, doi:10.1029/2002JD003253, 2004.
- Sugimoto, N., Uno, I., Nishikawa, M., Shimizu, A., Matsui, I., Dong, X., Chen, Y., Quan, H. Record, Heavy Asian Dust in Beijing in 2002: Observations and Model Analysis of Recent Events, *Geophys. Res. Lett.*, **30**, 12, 1640, doi:10.1029/2002GL016349, 2003.
- Uno, I., G. R. Carmichael, D. G. Streets, Y. Tang, J. J. Yienger, S. Satake, Z. Wang, J.-H. Woo, S. Guttikunda, M. Uematsu, K. Matsumoto, H. Tanimoto, K. Yoshioka, and T. Iida, Regional chemical weather forecasting using CFORS: Analysis of surface observations at Japan island stations during the ACE-Asia experiment, *J. Geophys. Res.*, **108(D23)**, 8636, doi:10.1029/2002JD003252, 2003.

Chapter 5

Observation of Aerosol Particles in the East Asia using Satellites

H. Fukushima
School of High-Technology for Human Welfare
Tokai University
E-mail: hajime@fksh.fc.u-tokai.ac.jp

5.1 Introduction

Satellite is an efficient and valuable vehicle to observe aerosol because it gives regional to global scale aerosol information with repeated opportunities. Although the accuracy of satellite measurement of aerosol properties may not be as good as that of ground or in situ measurement, we would not be able to assess the regional or global impact of aerosol on climate system without satellite observation (Kaufman *et al.*, 2002). At current stage, we can retrieve following information about aerosols over the ocean and, with some limitations, over the land: (1) “aerosol amount”, typically as aerosol optical thickness (AOT or τ_A), (2) particle size, and (3) “type of aerosol”. The effort toward determination of degree of aerosol absorption, which is a good index for anthropogenic or mineral dust aerosol species, is still undergoing although algorithms under development are quite promising. In this chapter, basic principles of satellite aerosol observation are presented followed by description of typical satellite instruments used for aerosol observation. Some of the recent algorithms for aerosol observation are then presented together with examples of satellite retrievals of various aerosols.

5.2 Principles of satellite observation of aerosol

Satellite sensor, or space-borne imaging spectroradiometer, measures radiance L that emerges from instantaneous viewing direction. This can be converted into satellite-observed “total” reflectance R_T defined as

$$R_T(\tau_A, \omega_0; \mu, \mu_0, \phi) = \frac{\pi L}{\mu_0 F_0} \quad (1)$$

where τ_A is the aerosol optical thickness, ω_0 the aerosol single scattering albedo (probability of a photon to be scattered by the particle), μ and μ_0 the

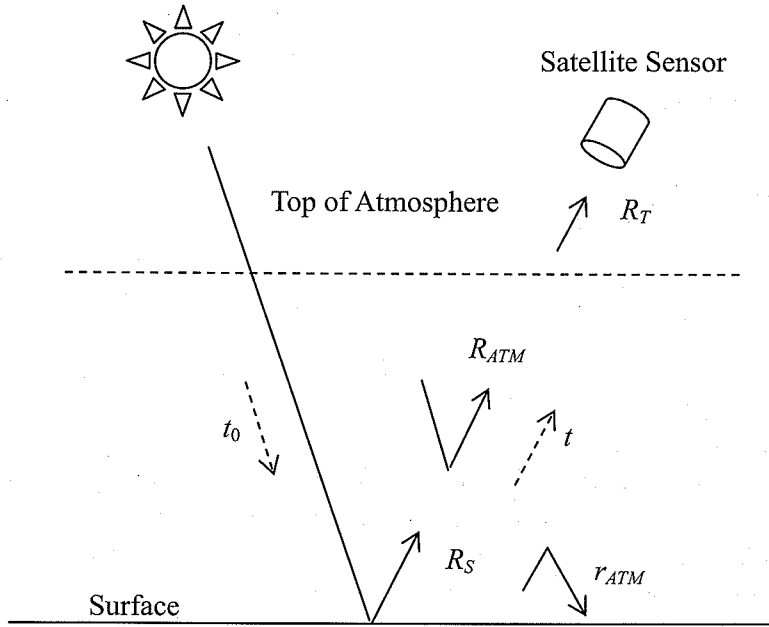


Figure 1. Schematic picture of satellite-observed reflectance and its components.

cosine of the satellite and solar zenith angle, respectively, ϕ the cosine of the relative azimuth between sun and the satellite, and F_0 the extraterrestrial solar irradiance. Note that R_T is implicitly a function of atmospheric pressure and that R_T is spectrally dependent (a function of wavelength) because τ_A , ω_0 and F_0 are wavelength dependent.

This reflectance can be decomposed into several components as illustrated in Figure 1 for cloud-free and vertically homogeneous earth-atmosphere system over a Lambertian surface of reflectance R_S (see King *et al.*, 1999).

$$R_T(\tau_A, \omega_0; \mu, \mu_0, \phi) = R_{ATM}(\tau_A, \omega_0; \mu, \mu_0, \phi) + \frac{t t_0 R_S}{1 - r_{ATM}(\tau_A, \omega_0) R_S} \quad (2)$$

In this expression, R_{ATM} is the reflectance due to atmospheric scattering, t the atmospheric transmittance between the surface and the satellite, and t_0 the same but between the sun and the surface. The term r_{ATM} , or the spherical

albedo, is atmospheric reflectance against upwelling light at the earth surface. When R_S and τ_A are not too high, R_T can be further simplified as follows.

$$R_T(\tau_A, \omega_0; \mu, \mu_0, \phi) = R_R + R_A + t t_0 R_S \quad (3)$$

where R_R is the reflectance due to the scattering of gas molecules, and R_A is the same but due to the scattering of aerosol particles that possibly includes interaction with gas molecules. The molecular scattering is often called as "Rayleigh scattering" whose magnitude is strongly dependent on wavelength (R_R is proportional to the inverse of λ^4). R_R is theoretically predicted if μ , μ_0 , ϕ and the atmospheric pressure are given. Aerosol reflectance R_A is also spectrally dependent but its dependency is generally weak and is variable depending on τ_A and ω_0 that are in turn dependent on the amount of aerosol, the size distribution, and chemical/physical composition of the aerosol. If τ_A is not too large, ($\tau_A < 0.3$ as a guideline), the single scattering approximation holds and R_R is expressed as follows.

$$R_A = \frac{\omega_0 P \tau_A}{4 \mu \mu_0} \quad (4)$$

This helps understanding the relation between basic aerosol optical properties and aerosol reflectance. P is aerosol scattering phase function, which determines the direction of photon after it hits the aerosol particle. This function is also dependent on physical properties of aerosol.

In addition to ω_0 , P , and τ_A , another important parameter that reflects the characteristics of the aerosol is Angstrom exponent α defined by:

$$\frac{\tau_A(\lambda_1)}{\tau_A(\lambda_0)} = \left(\frac{\lambda_1}{\lambda_0} \right)^{-\alpha},$$

or equivalently

$$\alpha(\lambda_1, \lambda_0) = \frac{\log\{\tau_A(\lambda_1)/\tau_A(\lambda_0)\}}{\log(\lambda_1/\lambda_0)} \quad (5)$$

From the Mie theory, if the particle size is small ($r \ll 1 \mu m$), α becomes high ($\alpha > 1$) while α is around 1 if particle is large.

Since the transmittance t , t_0 (and r_{ATM} in (2)) is also a function of τ_A and ω_0 it is quite possible to infer aerosol optical thickness and single scattering albedo from the satellite reflectance R_T based on (2) or (3), provided that we know (or assume) the surface reflectance R_s . Of course this necessitates our knowledge that links actual aerosols to the theoretical properties of aerosols. This is usually done by radiative transfer simulations assuming a set of appropriate model aerosols, such as defined in Shettle and Fenn (1979). Most of current satellite algorithms use precalculated “look up tables” of aerosol reflectance (or total reflectance) that are produced by radiative transfer simulations with various aerosol models under different scan geometry (namely μ , μ_0 , and ϕ). The nature of these algorithms is “to find a best fit model that explains what satellite observed”.

5.3 Satellite sensors for aerosol observation

Table 1 summarizes most popular satellite-borne sensors that are used for aerosol observation. They cover mostly visible spectrum (400-700nm) with some extension to ultra-violet (UV) or near-infrared to short wave-infrared region. It is also possible to use thermal infrared band ($3.7 \mu\text{m}$ or longer wavelength) to estimate the aerosol absorption effect in thermal radiation of the surface, which may enable us to derive aerosol properties. Those techniques will be found elsewhere (in Kaufman 1999, for example).

Sea Wide Field-of-view Sensor (SeaWiFS) was originally designed for ocean color observation but is also suitable for aerosol observation because of its wide dynamic range (does not saturate against bright target like desert, cloud, or ice/snow) and low signal- to-noise (S/N) ratio. It is also very well calibrated throughout the mission. Since the original mission was ocean color observation, and the water-reflectance signal is generally weak but highly variable, accurate correction of atmospheric effect, including that of aerosol, is required (Gordon and Wang, 1994). Hence, the standard product includes “aerosol optical thickness (AOT)” and “Angstrom exponent” imageries which are also useful for aerosol observation.

Total Ozone Mapping System (TOMS) is an instrument originally designed to measure columnar ozone amount daily and globally. It observes earth reflectance in ultraviolet channels some of which can be used for aerosol observation.

Moderate Resolution Imaging Spectroradiometer (MODIS) is a 36-band imager designed for global observation of land, ocean, and atmosphere. The first MODIS instrument is aboard the Terra spacecraft, which was launched in December 1999, while the second MODIS was launched in 2002 aboard the Aqua spacecraft.

Table 1. Satellite-borne imaging spectrometer used for aerosol observation.

Sensor	Spatial resolution	Observation bands*
OrbviewII/SeaWiFS (97-)	1.1 km	6 VIS, 2 NIR
EarthProbe/TOMS (96-)	26 km	5 UV
Terra/MODIS (99-)	250 m	1 VIS, 1 NIR
Aqua/MODIS (02-)	500m	2 VIS, 2 SWIR
	1km	7VIS, 5NIR, 2 SWIR, 16TIR
ADEOS-II/GLI (02-03)	250m	3 VIS, 1 NIR, 2 SWIR
	1km	1 UV, 12 VIS, 6 NIR, 4 SWIR, 7 TIR
ADEOS/POLDER (96-97)		5 VIS (2 POL),
ADEOS-II/POLDER (02-03)	7 km	4 NIR (1 POL) (13ML)
Terra/MISR (99-)	1km or 250m	3VIS, 1NIR (9ML)

* UV: ultraviolet bands (300-400 nm), VIS: visible (400-700 nm), NIR: near-infrared (700-1000 nm), SWIR: shortwave infrared (1-3 μ m), TIR: thermal infrared (3-12 μ m), POL: polarization band, ML: multi-look.

Global Imager (GLI) is also a 36-band imaging spectrometer but with slightly different band allocation (especially ultraviolet bands are quite unique) and has a "tilt" mechanism to reduce sun-glitter contamination on aerosol and ocean color observation. The instrument was aboard ADEOS-II satellite, which was launched in December 2002 to initiate its routine observation in April 2003. Unfortunately, due to a sudden failure of solar battery system, the entire ADEOS-II mission was terminated in October 2003.

Polarization and Directionality of Earth's Reflectance (POLDER) is a unique instrument in observing polarization of backscattered light from the earth surface/atmosphere. While so-called Rayleigh scatterance from the gas molecules may be strongly polarized, aerosol particles have different polarization characteristics and polarization observation is sometimes very useful for aerosol observation. Another unique feature of POLDER is "multi-look" capability: it can observe each pixel location as many as 14 times from different directions. From that multi-look data, one can obtain some information of

scattering phase function (P in equation (4)), which is also useful information about aerosol type. Multi-angle Imaging Spectro Radiometer (MISR) also observes earth surface from 9 different scan geometry, with much higher spatial resolution (250m at best, for local observation).

5.4. Aerosols seen in satellite image – examples

5.4.1 Soot/sulfate and Asian dust aerosols in SeaWiFS aerosol imageries

Figure 2 demonstrates a case where sub-micron particles dominate the aerosol. In north Japan Sea in the satellite scene, there is a moderately turbid air mass (marked “A”) whose AOT is around 0.3 (image (a)). The air mass is also characterized by high Angstrom exponent of about 1.5 (image (b)), implying that small, sub-micron particles prevail in the air mass. Although it is not shown here, the standard ocean color atmospheric correction, which assumes non-absorptive aerosol models, retrieved negative water reflectance, suggesting the air mass contains black carbon particles.

Figure 3 shows an example of Asian dust aerosol, which consists of soil particles originate from Chinese desert area. A huge low depression located in north-eastern China (around “A” in image (a)) was moving east with enormous amount of dust, as also visualized in TOMS Aerosol Index (AI) image shown in image (d) (Herman *et al.*, 1997). Where the thinner dust aerosol is present (location “B”), the AOT is moderately high (about 0.3), while the Angstrom exponent is 0.5-0.8, which could be interpreted as coarse mode (super-micron) dust particles mixed with sub-micron particles.

5.4.2 Forest fire smoke aerosol observed by GLI and SeaWiFS

Forest fire produces carbonaceous particles which is mostly small in size and weakly or moderately absorptive. Since absorptive effect is more easily detected in shorter wavelength bands, some algorithms use “blue” bands or near-UV bands. Holler *et al.* (2004) proposed an algorithm that uses 380 and 400 nm bands of GLI. The algorithm is based on a relation between the reflectance of GLI channel 1 and the reflectance ratio between channel 1 and 2, which is obtained by radiative transfer simulations (see Figure 4) under various scan geometries, surface reflectance, and aerosol models with different absorption. By looking-up a set of tables which carry these relations, and assuming or knowing ground reflectance at these two bands, one can estimate the AOT and the aerosol single scattering albedo pixel-wise.

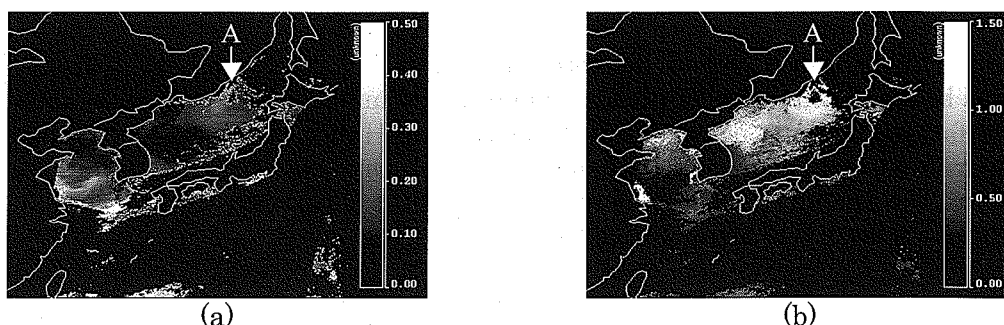


Figure 2. Sub-micron particle dominated air mass seen in SeaWiFS images of (a) Aerosol optical thickness (AOT) and (b) Angstrom exponent, observed on April 3, 2001. The air mass in the north Japan sea (marked as A), has AOT of 0.2~0.3 which indicate that it is moderately hazy. Its relatively high Angstrom exponent implies that small, sub-micron particles dominate this air mass.

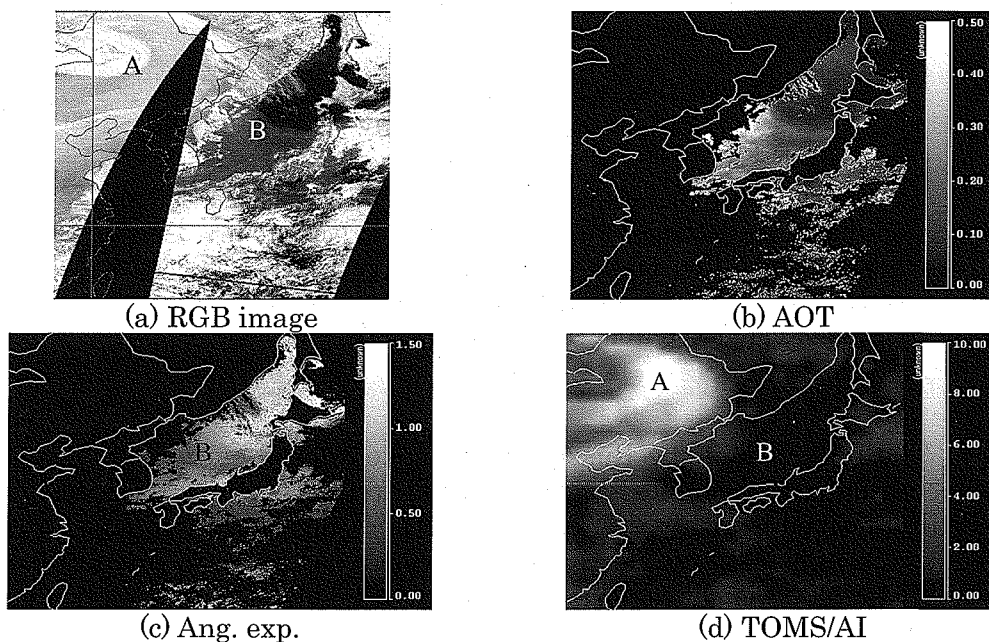


Figure 3. Dust air mass observed in SeaWiFS imagery on April 7, 2001. On that day, a huge, well-developed low depression was moving east toward Japan, conveying enormous amount of soil particles (around "A" in image (a)). On the outer rim of the air mass, the Angstrom exponent is relatively low, meaning that the air mass is dominated by the large, coarse soil particles (images (b) and (c)). TOMS Aerosol Index (image (d)) depicts the spatial distribution of the mineral particles.

There was a large scale forest fire in spring 2003 in Siberia, Russia. Many fires broke out in different places and produced much smoke aerosol which covers the far-east regions from March through June. Holler *et al.* (2004) applied their algorithm to GLI scenes of that smoke aerosol. One example is shown in Figure 5, where the smoke-rich aerosols are seen in north Japan Sea (A) and in mid-Japan Sea (B), where AOT is more than 2.0.

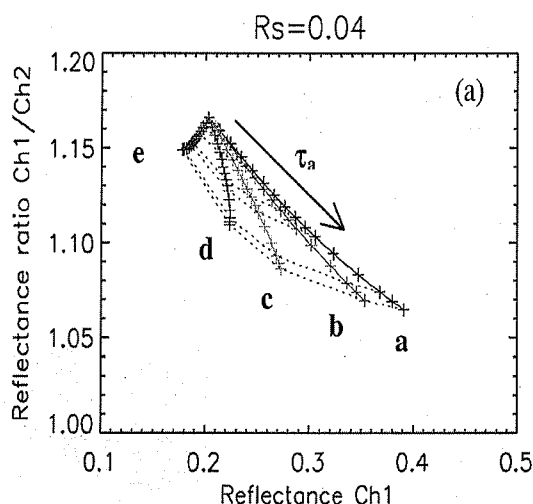


Figure 4. Example of the relation between GLI channel 1 (380 nm band) and channel 2 (400 nm band) derived from radiative transfer simulation under particular scan geometry with model aerosols from “a (non-absorptive)” through “e (most absorptive)” cases. Reproduced from Holler *et al.* (2004).

The influence of the Russian fire smoke aerosol over longer period can also be visualized by compositing a series of satellite images. In figures 6 and 7, SeaWiFS-derived monthly averages of AOT and Angstrom exponent for May in 2001, 2003, and 2004, respectively, are shown. As seen in image (b) in the figures, May 2003 is characterized by its high mean AOT and high Angstrom exponent compared to other years. Interestingly, the other two cases are also characterized in similar way, but differently at the same time, as relatively low AOT with moderately high Angstrom exponent (May, 2001) or moderately high AOT and markedly high Angstrom exponent along the Japanese islands. This is a good example to learn about inter-annual variability of aerosol properties.

5.4.3 MODIS standard aerosol products

Using two instruments, one aboard Terra with the equatorial crossing time (ECT) at 10:30 a.m., the other aboard Aqua with ECT at 1:30 p.m., the MODIS atmosphere project routinely provides daily and monthly aerosol products. There are two algorithms, one for aerosol over land, the other for aerosol over ocean. The output of the two are merged into one output product. Both algorithms basically use 500 m spatial resolution data but the nominal spatial resolution of final product is 10 km. This is because of securing high data quality in the sense they use 20 x 20 pixels to determine the representative value for that area.

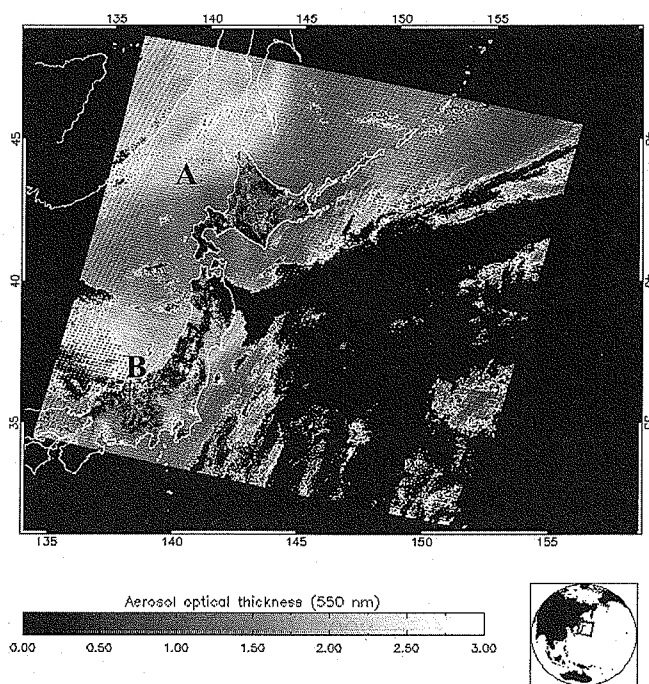


Figure 5. GLI-derived image of estimated AOT for smoke aerosol over land and ocean. Observation made in June 5, 2003. Siberian fire smoke aerosol prevails in north Japan Sea (A) and in mid Japan Sea (B). Reproduced from Holler *et al.* (2004).

The land algorithm uses 0.47, 0.66, and 2.13 μm bands to estimate AOT over land area whose ground reflectance at 2.13 μm band ($R_s(2.13)$) is less than

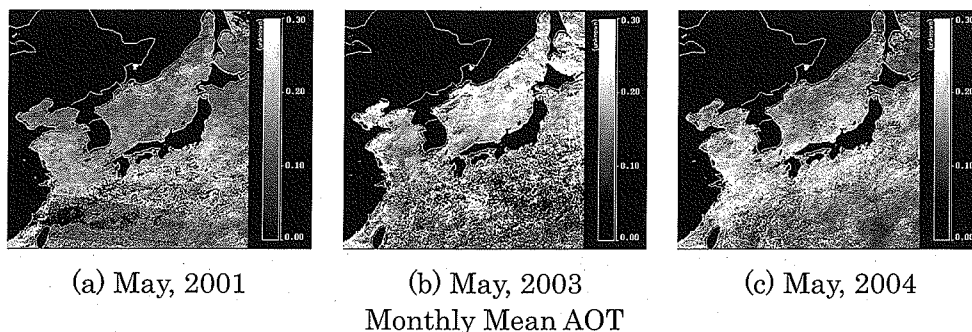


Figure 6. SeaWiFS-derived monthly mean AOT of May in the years 2001, 2003 and 2004. Note that the average AOT in 2003 (image (b)) is obviously high compared to other years. The difference is more significant in higher latitude area, reflecting the Siberian forest fires occurred in April-June 2003.

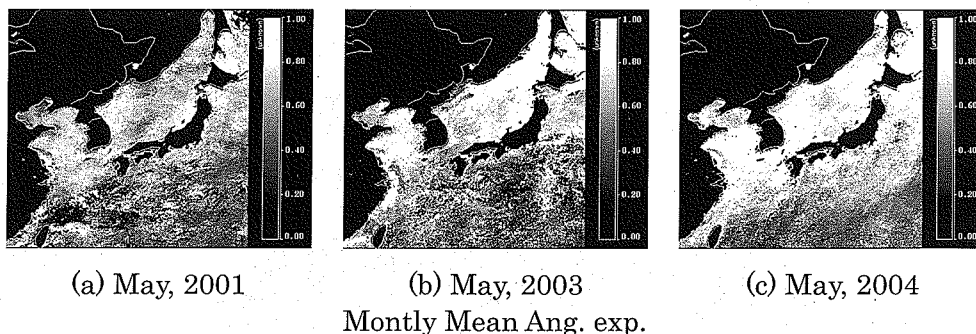
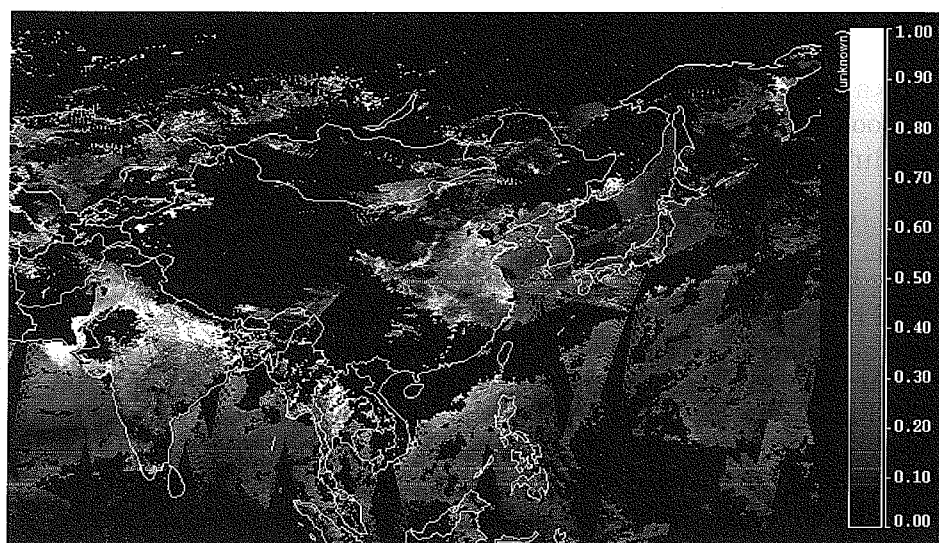


Figure 7. SeaWiFS-derived monthly mean Angstrom exponent in May 2001, 2003 and 2004 corresponding to Figure 6.4. In spring 2001 (image (a)), the average exponent is relatively low, being affected by Asian dust aerosol. While high exponent in 2003 (image (b)) corresponds to the Siberian fire smoke aerosol, similar “high” exponent in May 2004 is supposed due to sub-micron anthropogenic aerosols from the Asian continent.

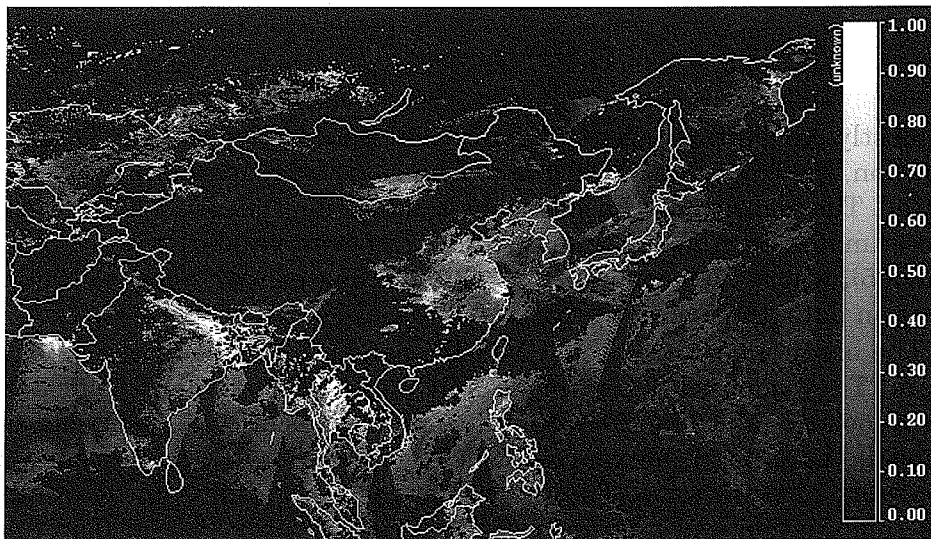
0.25 (mostly vegetation area). As for the information about aerosol size distribution, the fraction of AOT due to fine mode (sub-micron) particles is also estimated. The algorithm is based on the assumption that $R_s(0.47)$ and $R_s(0.66)$ can be estimated from $R_s(2.13)$. According to a recent validation work by Remer *et al.* (2005), where they compared satellite-estimates with about 6,000 ground observation data, the average error of AOT is $\Delta \tau_A = \pm 0.05 \pm 0.15 \tau_A$.

The ocean algorithm uses 6 MODIS bands that range from 0.55 mm to 2.13 mm. They adopted 4 fine mode and 5 coarse mode aerosol models and prepared look-up tables for 20 different combinations of model aerosols, one for fine model, the other from coarse models, via radiative transfer simulations with varying mixture ratio. The essence of the algorithm is to determine the aerosol combination and mixture ratio to estimate total AOT at 0.55 mm and fraction of the fine mode aerosol, as well as aerosol effective radius. The estimation errors for AOT and the effective radius are reported to be $\Delta \tau_A = \pm 0.03 \pm 0.05 \tau_A$ and 25% respectively (Remer *et al.*, 2005).

Figure 8 shows a set of MODIS-derived aerosol images of Asia for April 8, 2004. These images were composed from Terra/MODIS and Aqua/MODIS level 2 data. Similar daily/monthly level 3 images will be available at the MODIS Atmosphere home page. Other examples of monitoring global and local anthropogenic aerosols will be found in Chu *et al.* (2003).



(a) MODIS total AOT



(b) MODIS AOT for small part.

Figure 8. MODIS-derived composite image of aerosol optical thickness (AOT) for April 8, 2004 over Asia. (a) Total AOT imagery synthesized from Terra/MODIS and Aqua/MODIS Level 2 data. (b) Fractional AOT of submicron particles. It can be noted that the aerosols in north-east India, in Indo-china Peninsula, and in east China coastal area are characterized by small particles.

5.5. Useful Web Pages and Readings

Nowadays, most satellite data and their relevant information as well as software tools are available via Internet. Table 2 lists some of the useful web site regarding aerosol remote sensing.

Table 2. Web pages of satellite data and related information.

Satellite Instrument	URL address
SeaWiFS Project	http://oceancolor.gsfc.nasa.gov/SeaWiFS/
TOMS Home Page	http://jwocky.gsfc.nasa.gov/
MODIS Atmosphere	http://modis-atmos.gsfc.nasa.gov/index.html
Products	http://modis-atmos.gsfc.nasa.gov/MOD04_L2/format.html
Viewing Software	http://modis-atmos.gsfc.nasa.gov/MOD04_L2/tools.html
ADEOS-II/GLI	http://suzaku.eorc.jaxa.jp/GLI/index.html
POLDER Home Page	http://smsc.cnes.fr/POLDER/
Terra/MISR	http://www-misr.jpl.nasa.gov/index.html

References

- Chu, D. A., Y. J. Kaufman, G. Zibordi, J. D. Chen, J. Mao, C. Li, and B. N. Holben (2003), Global monitoring of air pollution over land from the Earth Observing System-Terra Moderate Resolution Imaging Spectroradiometer (MODIS), *J. Geophys. Res.*, 108(D21), 4661, doi:10.1029/2002JD003179.
- Gordon, H. R. and Wang, M. (1994), Retrieval of water-leaving radiance and aerosol optical thickness over the oceans with SeaWiFS: A preliminary algorithm, *Appl. Opt.* 33, pp. 443-452.
- Herman, J. R., Bhartia, P. K., Torres, O., Hsu, C., Seftor, C. and Celarier, E. (1997), Global distribution of UV-absorbing aerosols from Nimbus 7/TOMS data, *J. Geophys. Res.* 102(D14), 16,911-16,922.
- Holler, R., Higurashi, A., Aoki, K. and Fukushima, H. (2004), Remote sensing of large-scale boreal forest fire aerosol in Eastern Asia from ADEOS-2/GLI during spring 2003, *Proc. SPIE*. 5571, pp. 312-321.
- Kaufman, Y. J., D. Tanre, and O. Boucher (2002), A satellite view of aerosols in the climate system, *Nature*, 419, 215- 223.
- King, M. D., Y. Kaufman, D. Tanre, and T. Nakajima (1999), Remote sensing of tropospheric aerosols from space: Past, present, and future, *Bull. Am. Meteorol. Soc.*, 11, 2229-2259.
- Remer, L. A., Kaufman, Y. J., Tanré, D., Mattoo, S., Chu, D. A., Martins, J. V., Li, R.-R., Ichoku, C., Levy, R. C., Kleidman, R. G., Eck, T. F., Vermote, E. and Holben, B. N. (2005), The MODIS Aerosol Algorithm, Products and Validation, *J. Atmos. Sci.*, 62, 947-973.
- Shettle E. P. and R. W. Fenn (1979), Models for the aerosols of the lower atmosphere and the effects of humidity variations on their optical properties, *AFGL-TR-79-0214*, U.S. Air Force Geophysics Laboratory, 675, 94pp.

Chapter 6

Nature and Behaviors of Aerosol Particles in the Atmosphere

Y. IWASAKA

Graduate School of Environmental Sciences,

Nagoya University

Nagoya, JAPAN

e-mail: iwasaka@stelab.nagoya-u.ac.jp

Abstract

Behavior of atmospheric aerosols in eastern Asia, especially in the free troposphere, are discussed on the basis of the field measurements made at Dunhuang (40°00'N, 94°30'E), China. The morphology and chemical elements of aerosol were analyzed concerning with particulate collected in the free troposphere in August of 2002 and March of 2003 at Dunhuang, China.

Electron microscopic experiments of the particles directly showed that dust particles were major constituents of coarse mode particles in spring time in the free troposphere over the Taklamakan desert.

Si-rich particles and Ca-rich particles were typical types of those dust particles, and the values of [number concentration of Ca-rich particles]/[number concentration of Si-rich particles] showed large difference between spring and summer: about 0.3 in spring, 2003 and about 1.0 in summer, 2002 in height of 3-5km above the sea level. It is likely that situation of the ground surface and strength of vertical mixing are potential factors causing the difference. Lidar measurements made near the balloon-launching site in Dunhuang, and confirms results obtained in the balloon-borne measurements.

It is, comparing chemical compositions of the particles with those of particles collected over the Japan, strongly suggested that chemical modifications of particles occurred during long-range transport in the free troposphere.

Analysis of wind systems showed that combination of predominating westerly

in the free troposphere and surface wind strongly controlled by geographical structure of the Tarim basin was important process characterizing long-range transport KOSA particles originating in the Taklamakan desert.

Keywords: dust particle, chemical composition, desert areas in china, balloon-borne measurements, Electron microscopic experiment

6.1 Introduction

Asian dust particles (KOSA particles, KOSA literally means yellow sand in Japanese), according to recent many investigations, make important contribution to changes in regional and/or global climate and environment since particles can scatter and/or absorb solar radiation (Sokolik and Toon, 1996; Tegen et al., 1996), act as chemical reaction site (Dentener et al., 1996; Zhang and Iwasaka, 2001; Trochkin et al., 2003a) and play as cloud condensation nuclei or ice nuclei (Levin et al., 1996; Sassen, 2002; DeMott et al., 2003) in the atmosphere. Long-range transport of KOSA particles and chemical-physical transform of KOSA particles during transport, therefore, becomes a matter of great concern and many campaigns such as ACE-Asia including various type of field observations have been conducted (Huebert et al., 2003).

Many lidar measurements made in Japan showed that long-range transport of KOSA particles was extremely active in the free troposphere over East Asia and west Pacific regions in spring (Iwasaka et al., 1988; Kwon et al., 1997; Sakai et al., 2000; Murayama et al., 2001), and Taklamakan desert has been suggested as possible one of strong sources of KOSA particles.

Some investigators, on the basis of lidar measurements, suggested that weak KOSA events which were so small that we could not detect near the ground, in addition to severe KOSA events, made possible contribution of geochemical cycle of minerals (Iwasaka et al., 1988; Kwon et al., 1997). Aircraft-borne measurements also confirmed effect of weak KOSA events on chemical composition of particulate matter in the free troposphere over Japan (Mori et al., 1999). More recently weak KOSA events were suggested even in summer when few effects of Kosa on atmospheric aerosols over Japan and Pacific ocean have been believed since Pacific high covered west Pacific region and westerly wind largely (Matsuki et al., 2002, 2003; Trochkin et al., 2002).

Analysis of trajectories of air masses indicated the possibility that westerly becomes extremely weak in the lower troposphere in summer over the

eastern-north Asian regions but not in the upper troposphere (Matsuki et al., 2003). Iwasaka et al. (2003) showed, on the basis of field observations including lidar and balloon-borne measurements at Dunhuang (40°00'N, 94°30'E), China, wind system and geographical feature of Taklamakan desert areas as important factor controlling weak KOSA events. However, very few observations have been made concerning with free tropospheric KOSA particles over particle source areas and integration of observations is desired.

We made electron-microscopic experiments of the particles collected in the free troposphere over Dunhuang (40°00'N, 94°30'E), China in March, 2003 (spring) following the balloon-borne measurements made in August, 2002 (summer). Here particle mixing states, chemical compositions, wind systems controlling particle transport were discussed on the basis of comparison with those field measurements which were made in different season; summer and spring.

6. 2 Method

Aerosol particles were directly collected with balloon-borne aerosol sampler in the free troposphere over Dunhuang, China (40°00'N, 94°30'E), on March 24, 2003 and August 29, 2002. The Dunhuang city, about 1200 m above the sea level, is located in the east side of the Taklamakan desert which is one of important sources of Kosa particles. Many investigators believe that air-masses including mineral dust derived from Taklamakan desert are frequently passed the free troposphere over Dunhuang. However, the states of aerosol in the free troposphere are little information. Therefore, this observational site is a considered to be effective place to investigate the feature of individual Kosa particles on the initial state of long-range transport.

Table 1 shows data of balloon-borne sampling and weather conditions during the measurement. We made it possible to collect particles in the three different layers of 3-5km, 5-7km, and 7-9km above sea level, using balloon-borne sampler containing three low-volume impactors (LVI) each with two stages. Aerosol particles were collected, to make single particle observation with an electron microscope, on carbon-coated nitrocellulose (collodion) films supported by Ni grids set on each stages of two-stage LVI. The jet diameters of the first and second stages of the impactor are 1.3 mm and 0.4 mm, respectively. The efficiency of 50% aerodynamical cut-off diameter under the flow rate of 1.8l min⁻¹ and standard atmospheric conditions (1013 hPa, 20°C) are evaluated to be 1.36 μm and 0.10 μm, respectively.

CHAPTER 6

We individually examined the shape, size, and elemental composition of the particles with coarse mode ($d > 1\mu\text{m}$) which is recognized as typically size of Kosa particles, collected in the first stage of impactor considering that most of Kosa particles were in the coarse mode range. The scanning electron microscope (SEM; Hitachi, S-3000N) and energy dispersive X-ray analyzer

Table 1. Sampling and weather condition. a) 2003/3/24, b) 2002/8/29.

a)

Date	Time (hh:mm, GMT)	Altitude (km) (above sea level)	Ascending speed (m/min)	Sampling Time	Wind		Weather
					Direction	Speed (m/s)	
24-Mar-03	01:43-01:52	below 3km	237	—	WSW	6.5	Fine
	01:52-02:00	3~5km	286	7.75min	W	11.6	
	02:00-02:07	5~7km	286	7.75min	WNW-W	16.8	
	02:07-02:13	7~9km	318	6.5min	WNW	18.6	

b)

Date	Time (hh:mm, GMT)	Altitude (km) (above sea level)	Ascending speed (m/min)	Sampling Time	Wind		Weather
					Direction	Speed (m/s)	
29-Aug-02	03:31-03:31	below 3.2km	290	—	ENE	6.6	Fine
	03:31-03:37	3.2~5.2km	332	6min	NNE-WNW	5	
	03:37-03:42	5.2~6.9km	320	5.25min	NW	9.2	
	03:42-03:45	6.9~8.0km	374	3min	NNW-WNW	14.3	

(EDX; Horiba, EMAX-500) were used here. The X-ray spectrum of a particle was obtained through a ultra thin window (UTW) detector with a counting time of 50 seconds and was generated from a square covering the particle which was irradiated the electron beam at a 20 kV accelerating voltage. It should be noted, although the EDX is able to quantitatively detect the relative weight and atom ratios of elements ($Z \geq 5$) in a single particle, that the current method is incapable of calculating relative weight ratios of carbon, nitrogen, oxygen and nickel owing to the inclusion of film or grid. The diameter of a particle was evaluated by the arithmetical mean of long width and the orthogonal width.

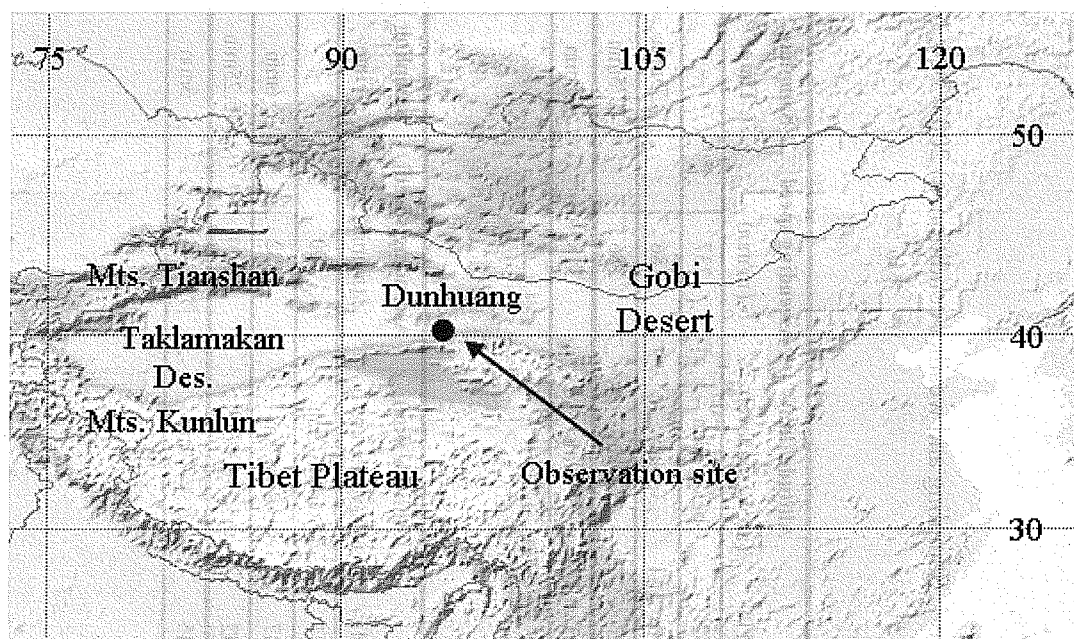


Figure 1. Observation site, Dunhuang, China ($45^{\circ}00'N$, $94^{\circ}30'E$).

The balloon-train is schematically shown in Fig. 2. The balloon-borne sampler used here was already specified by Iwasaka et al. (2003), and only the sampling operation system was changed to the system which is automatically controlled by signals from the Global Positioning System (GPS) data. On-off of valves of air flow system was operated from the command of pressure sensor on

the basis of GPS signals. Distance between balloon launching and landing position of the sampler was about 48km for the measurement of March 24, 2003 (Fig. 3 (a)). Sampler landed on the desert area was able to be immediately recovered about two hours after sampling. Therefore, it made possible to avoid effect of contamination from surrounding air. After samples were recovered, each grid was kept in a plastic capsule, which was then sealed in a plastic bag together with paper-packaged silica gel. Electron microscopic experiment of those particulate materials was performed in Japan (Nagoya University).

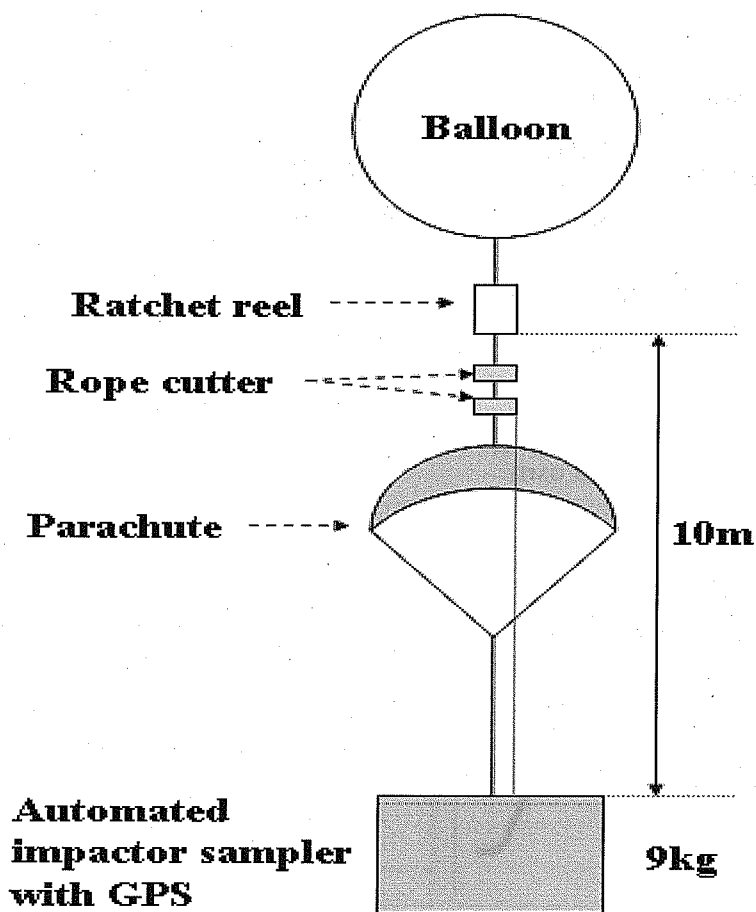


Figure 2. Balloon train used for aerosol collection; March 24, 2003 and August 29, 2002, Dunhuang China.

6.3 Results

As shown in Table 1 and Fig. 2, the wind, during the measurement of spring (March 24, 2003), blown mainly from west, and was stronger, especially in the free troposphere, as compared with summer case (August 29, 2002). The visibility was very long and the weather clear, and its condition was similar to the case of summer observation. The ascending rate of balloon was about 300 m min^{-1} .

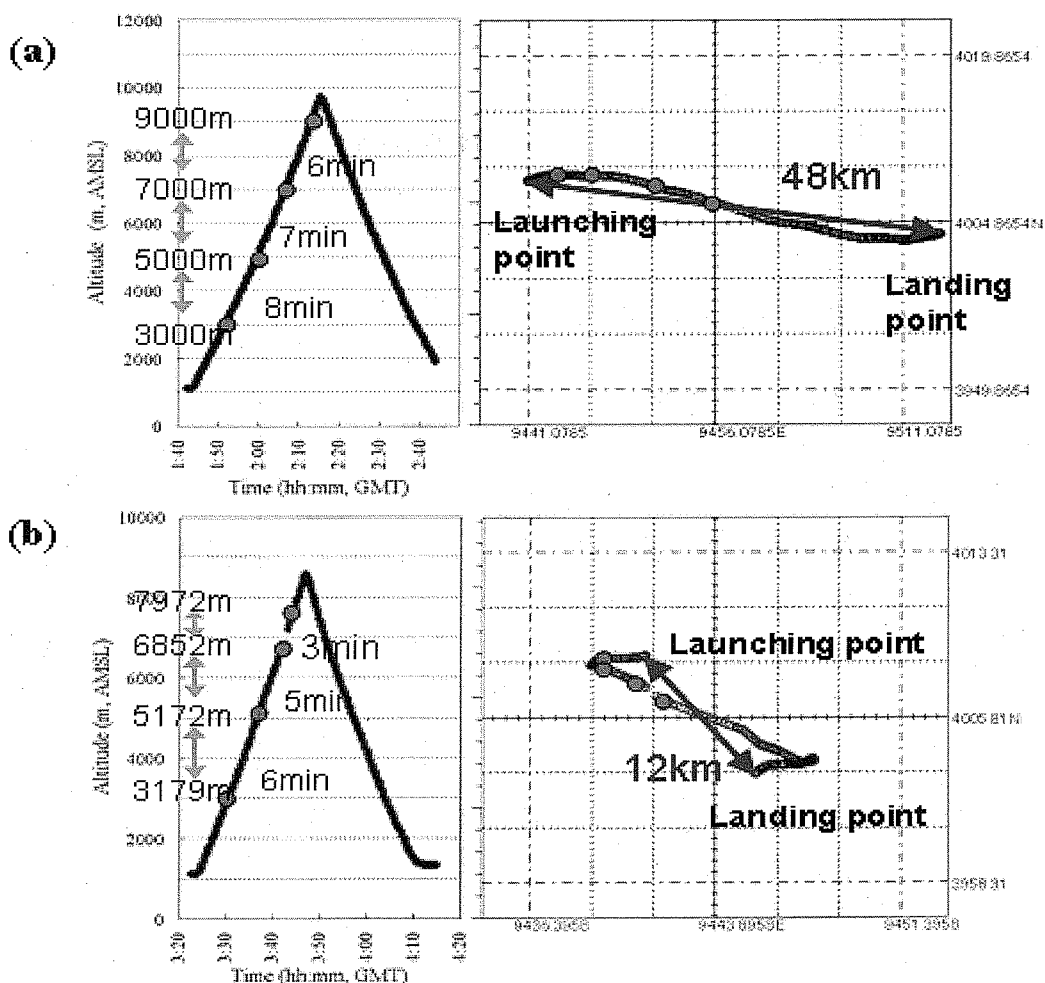


Figure 3. Tracks of the balloon-borne sampler deduced by Global Positioning System (GPS) data. (a) March 24, 2003, and (b) August 29, 2002.

The graph in Fig. 4 illustrates the relative weight ratios on elements detected from individual particles. The horizontal axis corresponds to each particle: total number of coarse mode ($d > 1 \mu\text{m}$) particles collected in 3-5km was 298 and that in 5-7km was 48. As described below, the mixing state of particles collected in both 3-5km and 5-7km heights were very similar. Main particles in both layers were clay mineral such as aluminosilicate which mostly contain Si and Al, Mg, K or Fe in a single particle. Appearance ratio of particles which Si detected was 92.5% in 3-5km and 93% in 5-7km of all analyzed particles. Si-dominant particles, containing Si more than 80% in weight ratio of all detected element from analyzed single particle, were account for 13.7% in 3-5km and 12.5% in 5-7km of total Si-containing particles. Moreover, abundance ratio of particles with Si of between 30% and 80% by relative weight of detected elements indicates 65.8% in 3-5km and 70% in 5-7km.

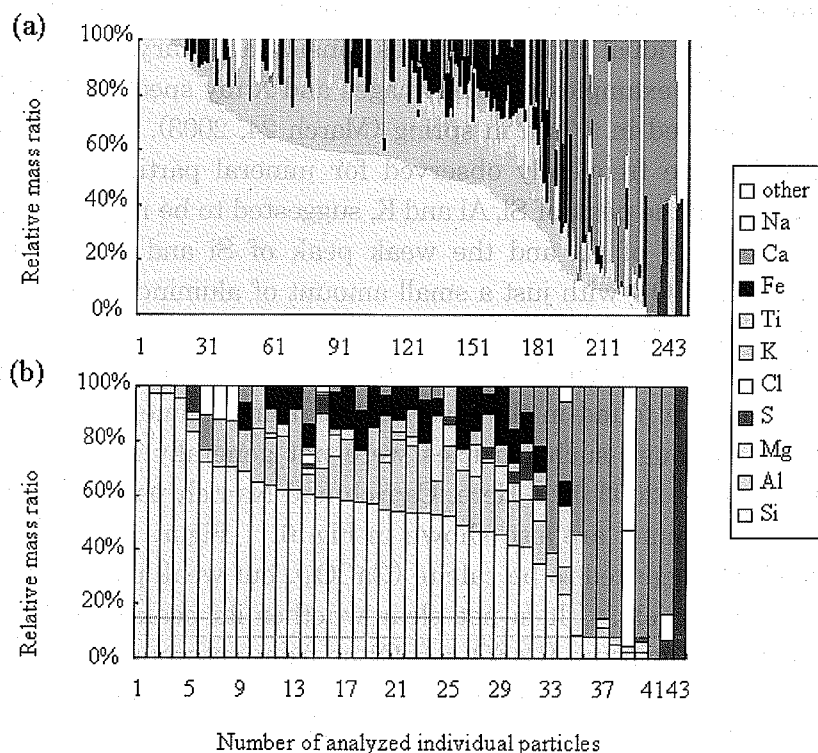


Figure 4. Relative mass ratio on the basis of single particle analysis.
(a) March 24, 2003, and (b) August 29, 2002.

Combinations of chemical elements of the particles collected during the balloon-borne measurements appear in Table 2. Combinations of particles are given on the basis of the quantitative results of EDX analysis by following relation according to Okada and Kai (1995):

Weight ratio of element X, $P(X)$ is

$$P(X) = X / (Na + Mg + Al + Si + S + Cl + K + Ca + Ti + Mn + Fe)$$

The “X-rich” particle in Table 2 is defined as threshold values of $P(X) > 65\%$. Major component of mineral particles was Si-rich particles in the spring. Si-rich and Ca-rich particles were, respectively, about 70% and 20% of total coarse particles collected in both 3–5 km and 5–7 km heights (Table 2). It was suggested that the type of particles existed in free troposphere over source area of Kosa was mostly mineral particles. On the other hand, the type of particles in summer in 3–5 km heights was also mainly mineral particles. However, it should be emphasized that the compositions of individual mineral particles considerably vary.

Figure 5 shows typical examples of SEM images and X-ray spectra of Si-rich and Ca-rich particles collected in 3–7 km in spring (March 24, 2003). Those had irregular shapes which were frequently observed for mineral particles. X-ray spectrum of Fig. 5(a) shows the peak of Si, Al and K, suggested to be mica, and that of Fig. 5(b) shows the peak of Ca and the weak peak of Si and Al, which is suggested to be calcite ($CaCO_3$) with just a small amount of aluminosilicate. In the case of the spring, the abundance ratios of Ca-rich and Si-rich particles were mostly the same, which was 36% and 38%, respectively. It is worth to note that particles containing Na were found in the layer of 3–5 km in summer observation (Iwasaka et al., 2003), although such particles were not generally found on the ground air (Trochkin et al., 2003b). Here, Ca-rich and Na-rich particles which were often found in the summer are also shown in Fig. 6. Figure 6(c) shows a Ca-rich particle, which is suggested to be calcite ($CaCO_3$), but weak peak of sulfur was also detected from particle. It is not clear whether its peak was derived from mineral origin such as gypsum ($CaSO_4 \cdot H_2O$) or from anthropogenic origin. Na-rich particle shown in Fig. 6(d) seems to be thenardite (Na_2SO_4). The existence of these particles, i.e. Ca-rich particle and Na-rich particle, were supported that saline soils in saline lands around the desert areas in Xinjian, China contain significant amount of sulfate salt (Yabuki, et al., 1997). The shape of Ca-rich particles was different from the spring. In summer case, Ca-rich particles with round shape were frequently found, and it is thought that changes of number of those Ca-rich particles contribute to the abundance ratio of Ca-rich particles

when few dust storms occur. However the sources of Ca-rich particles with round shape were still unknown.

Table 2. Collected particles larger than $1.0\ \mu\text{m}$ in diameter.

Type of Particles	2003/3/24 3-5km		2003/3/24 5-7km		2002/8/29 3-5km	
	number	%	number	%	number	%
Al-rich	0		0		0	
Si-rich	187	73.6	32	74.4	16	35.6
Si-dominant	58		9		10	
Si+Al	81		15		3	
Si+Mg	4		2		0	
Si+Fe(+Al)	25		3		3	
others	19		3		0	
Ca-rich	51	20.1	9	20.9	17	37.8
Ca-dominant	31		6		14	
Ca+Si	3		1		0	
Ca+Mg	7		1		1	
Ca+S	6		0		0	
others	4		1		1	
Fe-rich	5	2.0	0		0	
Fe-dominant	3		0		0	
others	2		0		0	
Ti-rich	2	0.8	0	0.0	0	
Ti-dominant	2		0		0	
Na-rich	6	2.4	1	2.3	5	11.1
Na-dominant	0		0		2	
Na+Cl	3		1		0	
Na+S	2		0		1	
others	1		0		2	
Cl-rich	1	0.4	0		0	
Cl+Na	1		0		0	
S-rich	1	0.4	1	2.3	5	11.1
S-dominant	1		1		5	
Others	1	0.4	0	0.0	2	4.4
Total	254	100	43	100	45	100
Ca-rich/Si-rich	0.27		0.28		1.06	
Si-rich+Ca-rich, %	93.7		95.3		73.3	

Figure 7 shows the ratios of number concentration of Ca-rich particles to that of Si-rich particles. The value of [number concentration of Ca-rich particles]/[number concentration of Si-rich particles] in the range of 3-5km and

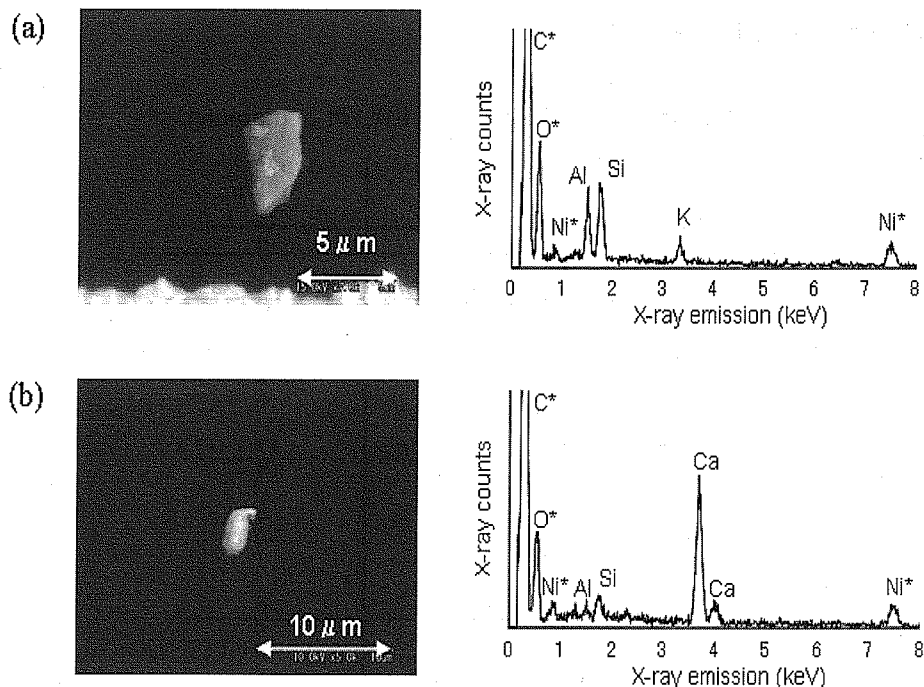


Figure 5. Typical example of electron micrographs and X-ray spectra of particles collected in 3-5km in spring (March 24, 2003). Particle (a) and (b) are Si-rich particle and Ca-rich particle, respectively. The Ni* peak is due to the Ni contained in grid used for the collection surface.

5-7km altitude in spring is considerably similar (Fig. 7(a)). The ratio is much higher, concerning with the distribution in 3-5km altitude in summer, than that in spring (Fig. 7 (b)). Comparison values in 3-5km and those in 5-7km showed also similar feature in spring.

Although the number of coarse particles collected in the 1st stage was clearly decreased with increasing of altitude, mineral particles were dominant in coarse particles at any height. Figure 8 shows vertical distributions of particle number concentration which is sized at diameter > 0.3μm, 0.5μm, 0.8μm, 1.2μm, and 3.6μm, on the basis of measurements with a balloon-borne Optical Particle Counter (OPC; SIGMA TEC) made at Dunhuang corresponding to the particle collection with this balloon-borne impactor, in spring and summer seasons. It is also clear from the OPC observation that the particle number concentration decreases with increasing

of altitude. The peak of the particle number concentration around 8km altitude in 17 August, 2001 was found. It is suggested that the high concentration of particle is due to thin cloud layer. By comparison between the OPC data in spring and winter above 3km altitude, the particle number concentration of larger than 1.2 μ m in spring were much higher than that in summer.

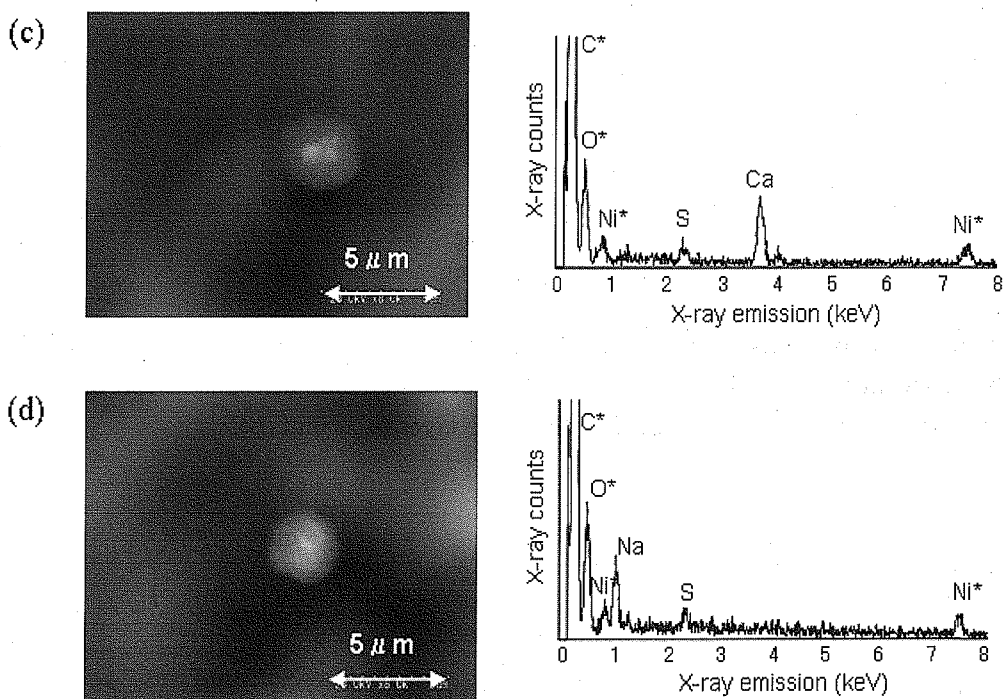


Figure 6. Typical example of electron micrographs and X-ray spectra of particles collected in 3-5km in summer (August 29, 2002). Particles (c) and (d) are Ca-rich particle and Na-rich particle, respectively. The Ni* peak is due to the Ni contained in grid used for the collection surface.

6.4 Discussion

6.4.1 Atmospheric condition and mixing state of particles

Figure 9 shows potential temperature distributions in spring (April 30, 2002 and March 24, 2003) and in summer (August 17, 2001 and August 27,

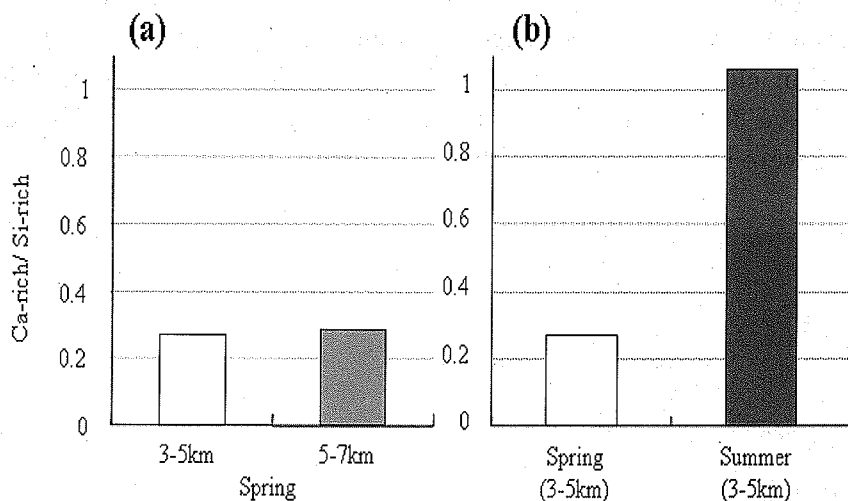


Figure 7. Comparisons of the value of [number concentration of Ca-rich particles]/[number concentration of Si-rich particles] between 3-5km and 5-7km in spring (a), and between spring time and summer time of the same layer of 3-5km (b).

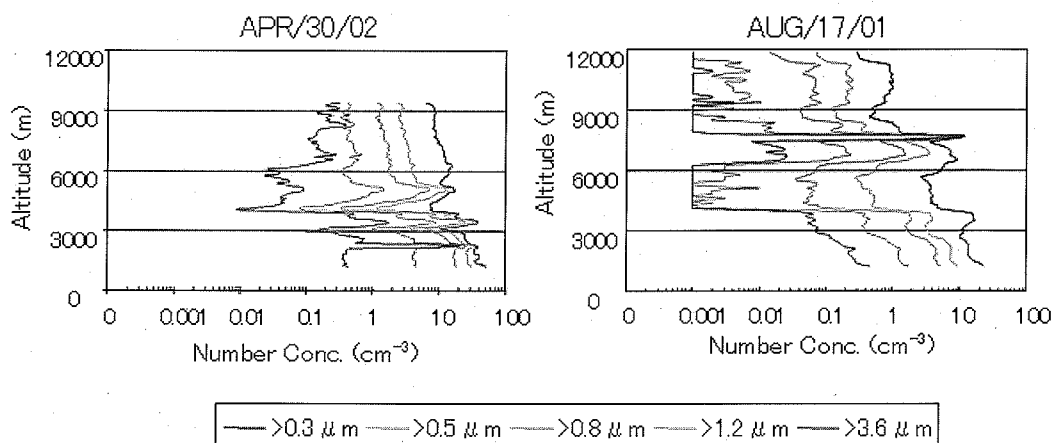


Figure 8. Aerosol number concentration and diameter observed with a balloon-borne optical particle counter in spring (April 30, 2002) and summer (August 17, 2001) at Dunhuang, China. Particle sizing was made at particle diameter = 0.3, 0.5, 0.8, 1.2, and 3.6 μm.

2002) in Dunhuang, which were obtained with radio sonde (VAISALA,

RS80-18E) during the measurements with the balloon-borne OPC. It is, from the gradient of potential temperature, suggested that the height of top of mixing layers in spring and summer were about 2.5-3km and 4km altitude, respectively (Fig. 9).

Vertical distributions of particle number concentration with $0.3-0.8\mu\text{m}$ (fine particle) and those of particles with $D > 1.2\mu\text{m}$ (coarse particle) are compared in Fig. 10, in which curves are averaged by running mean of about 300m interval. It was suggested that the cloud like structure with high relative humidity and high aerosol concentration layer existed at around 7.7km altitude in August 17, 2001 and at around 2.3km altitude in April 30, 2002 (Figs. 8 and 10). Concentrations of coarse particles in the boundary mixing layer in spring were several times higher than that in summer. Similarly, concentrations of coarse particles in the free troposphere in spring were one order of magnitude higher than that in summer (on August 17, 2001). Although the concentration of coarse particles between 4km and 6km altitudes in August 27, 2002 was as high as that in spring cases, this high concentration was suggested to be the dust layer by lidar measurement (Iwasaka et al., 2003). The free troposphere in spring over the Taklamakan Desert is dustier than that in summer owing to high concentration of dust particles. The high concentrations of dust in the free troposphere in spring is also supported from the fact that frequencies of dust outbreaks in the Taklamakan desert in spring, on the basis of routine surface meteorological reports, are higher than that in summer (Merrill et al., 1898).

Figure 11 shows isentropic backward trajectories of air-masses for three days. The calculation was performed with the software provided by NOAA (HYSPLIT transport and dispersion model) to see the history of air-masses on March 24, 2003 and August 29, 2002. The air-masses of 3-5km and 5-7km in March 24, 2003 came through the free troposphere over the Taklamakan desert, and reached over Dunhuang. On the other hand, the air-mass of 3-5km in August 29, 2002 were transported through north part of the Tianshang Mountains. This difference certainly causes interesting difference in mixing state of particles, as described in detail later.

Figure 12 shows the wind vectors at 850 hPa at 1200 (GMT) on March 23 and at 0000 (GMT) on March 24, 2003. It is indicated that the wind of the north side of the Mts. Tianshan and the south side of the Mts. Altai just entered the Tarim Basin as inhaled. The winds entered the Tarim Basin converged

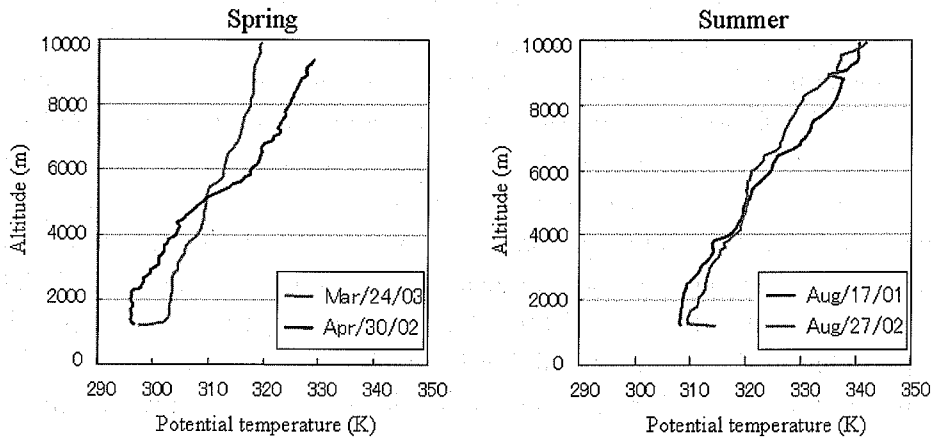


Figure 9. Potential temperature distributions in spring (April 30, 2002; March 24, 2003) and in summer (August 17, 2001; August 27, 2002).

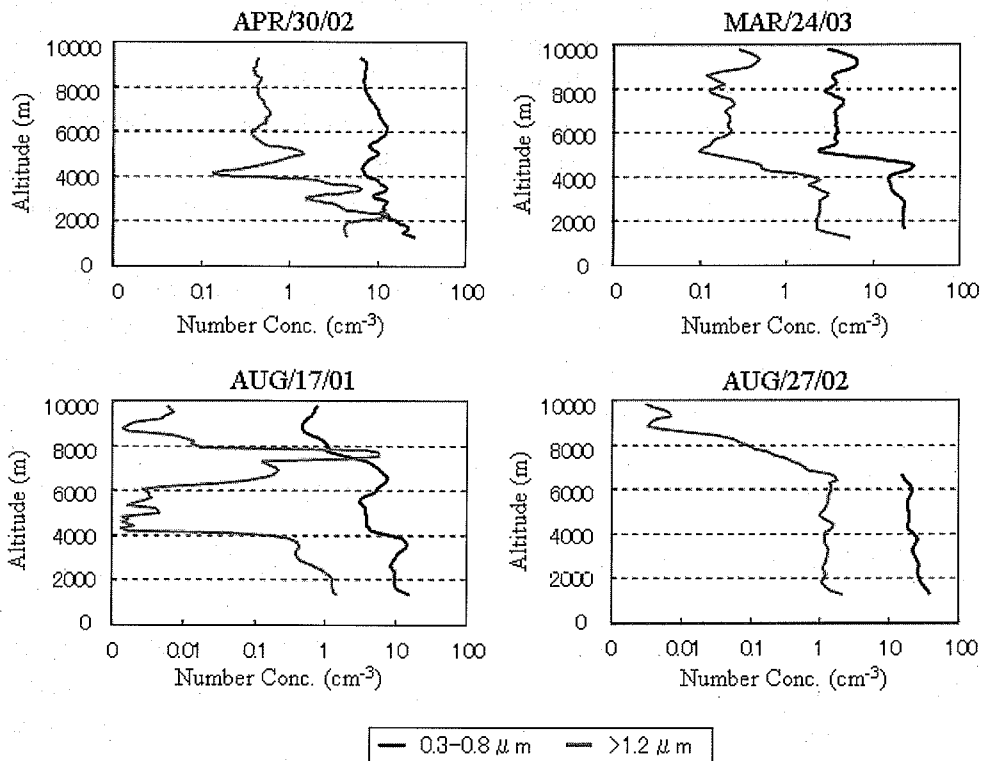


Figure 10. Vertical distributions of aerosol number concentration of coarse particle ($d > 1 \mu\text{m}$) and fine particle ($0.3 < d < 0.8 \mu\text{m}$). The profiles are due to the about 300 m interval running mean.

around the south-west part of the Tarimu Basin. This agreed with the wind system in the Tarim Basin which was reported on the basis of the moving directions of sand dunes in the Taklamakan Desert by Sun et al. (2001). In contrast, the Gobi Desert were mainly affected by westerly or north-westerly winds, and it is suggested, from the wind vectors at 850 hPa, that the air-masses originated from Gobi Desert were directory transported to easterly direction through lower altitude. The place of Dunhuang was located on just turning point of the wind direction in boundary layer. The wind mostly corresponded with the pressure system over the Tibet Plateau except around the Mts. Kunlun and the Mts. Qilian. In this region the wind is prevented by the high mountains, so that the wind direction was changed into westerly.

Figure 13 shows the upper-level chart of 500 hPa at 1200 (GMT) on March 23, 2003. It is suggested, from this chart, that the prevailing winds were westerlies at 500 hPa over the Tarimu Basin and Dunhuang area, although the wind over these regions were mainly easterly or north-east winds at surface of 850 hPa. Owing to the geographical condition that the north, west, and south of the Taklamakan Desert are surrounded by high mountains (average elevation > 5000m), dust at an elevation lower than 5000m cannot easily move out of this desert (Sun et al., 2001). The balloon-borne observation on March 24, 2003 indicated also effect of westerlies in the free troposphere, although the easterly wind prevailed in the lower altitude. It is likely that dust particles lifted to higher than 5000m were transported the long-range distance, and we can recognize the dust collected in the free troposphere over Dunhuang as the particles without chemical-physical transformations caused on dust particle surface during the long-range transport in the atmosphere.

As mentioned in results, the similarity of chemical compositions of dust particles in the layers of 3-5km and 5-7km in spring, which were mainly composed of Si-rich particles as shown in Fig. 4, was found. It is suggested that the dust lifted to the free troposphere in the source area were well mixed, although some very stable layers were sometimes found in the free troposphere over observational site, for example around 4km, 5.5km, 6.8km altitude in March 24, 2003. In other words, once the dust lifted to the free troposphere, even if stable layers appear after that the effect of the appearance of stable layer can be hardly detected in the dust particle distribution, the mixed state remains.

The mixing state of dust particles in the free troposphere in summer was significantly different from that in spring, and the appearance ratio of Ca-rich

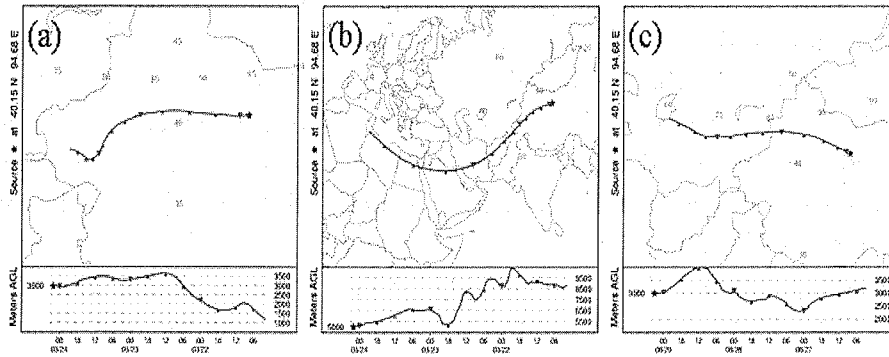


Figure 11. Three-day backward trajectories of air-masses which were observed at 3000m above the ground level (a) and 5000m above the ground level (b) on April 24, 2003, and at 3000m above the ground level on August 29, 2003 (c) at Dunhuang, China (on isentropic surface). These trajectories were analyzed with the HYSPLIT model provided from NOAA Air Resources Laboratory's web server.

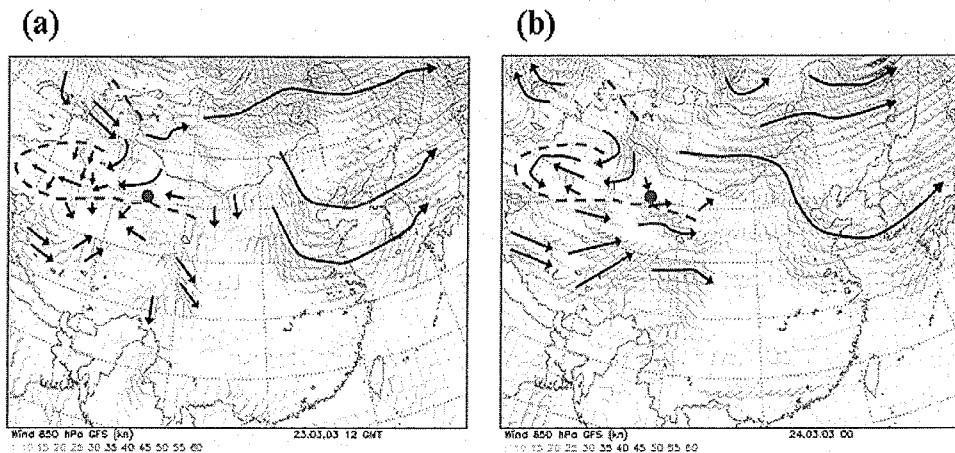


Figure 12. Wind vectors at 850 hPa at 1200 (GMT) on March 23 and at 0000 (GMT) on March 24, 2003. Arrows (\uparrow) show predominant wind, and the filled circle indicates the observational site, Dunhuang (45°00'N, 94°30'E). Broken lines show mountain ranges around the Taklamakan Desert.

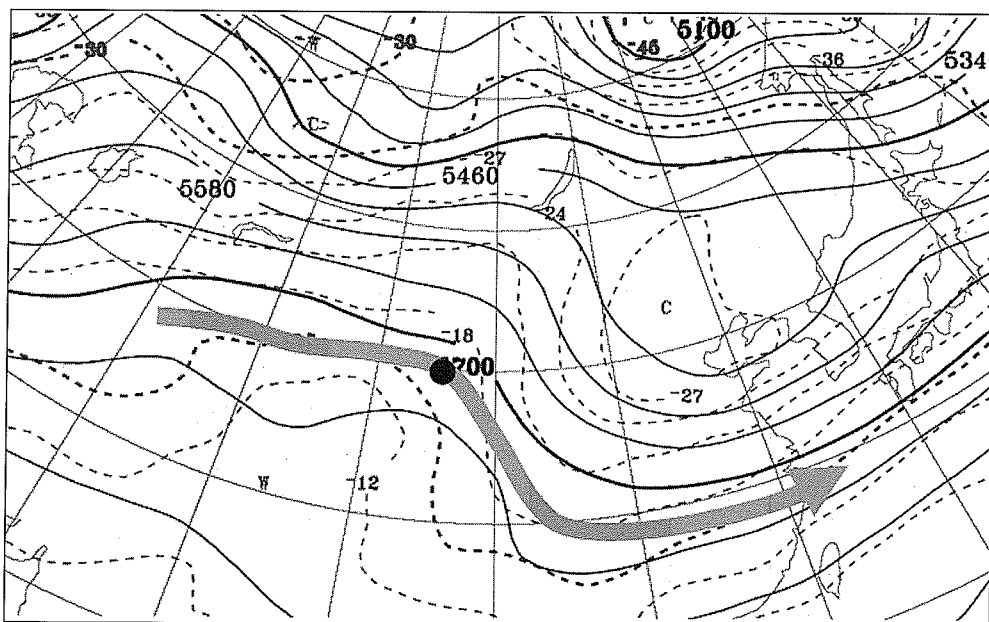


Figure 13. Wind on 500 hPa surface at 1200 (GMT) on March 23, 2003. An arrow (\uparrow) shows direction of predominant wind, and filled circle indicates the observational site, Dunhuang ($45^{\circ}00'N$, $94^{\circ}30'E$).

particles in summer was considerably high (Fig. 7 and Table 2). One possible explanation is the difference in the history of the air-masses; the air-mass was transported through the north side of the Tianshang Mountains in summer but not in spring (Fig. 11). Yabuki et al. (2003) has reported that air borne particles collected in the Tianshan Mountain contain considerable amount of evaporate. Another possibility is that concentration of dust particles in summer is relatively low, comparing with the spring cases (Figs. 8 and 10). Figure 14 shows the diagram to compare values of [number concentration of Ca-rich particles]/[number concentration of Si-rich particles] of particles collected in the surface atmosphere in spring (on April 29, 2002; March 25, 2003) and summer (on August 17; August 18, 2001; August 26, 2002) in Dunhuang (for details on April 29, 2002; August 17, 2001; August 18, 2002, Trochkin et al., 2003). Weather conditions were fine and calm during observations except for April 29, 2002 (dust storm). Interestingly, the ratio of Ca-rich/Si-rich particles in summer was also much higher (0.72) than that in spring (0.35). Ca-rich particles had round shape as shown in Fig. 6 (c) when the relative appearance ratio was high. It is possible to suggest, although the

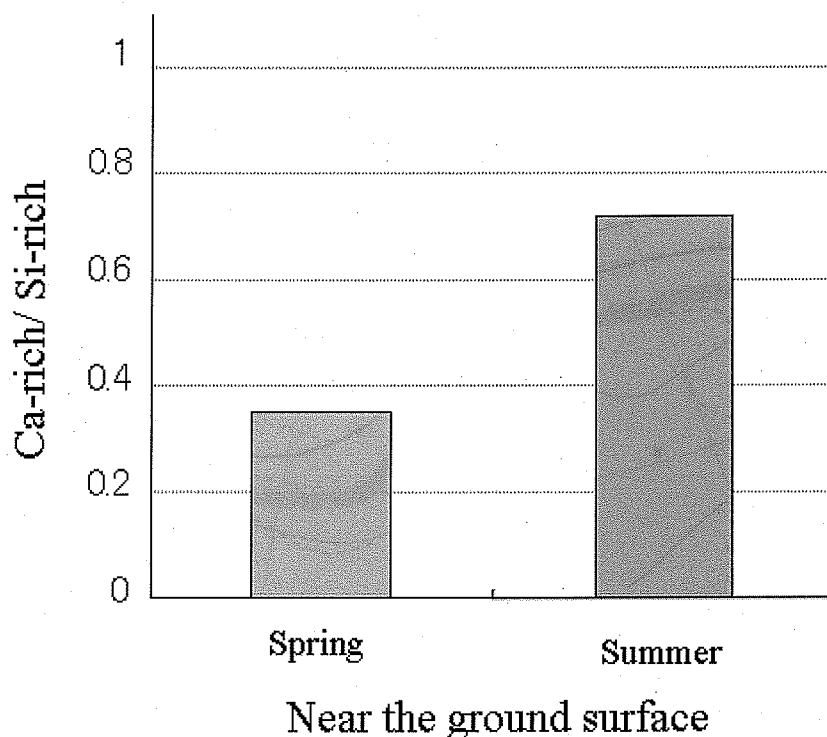


Figure 14. Comparison of the values of [number concentration of Ca-rich particles]/[number concentrations of Si-rich particles] collected in the surface atmosphere in spring and summer in Dunhuang. The data used in this graph are the results on the basis of the sampling in spring (on April 29, 2002; March 25, 2003) and summer (on August 17, 2001; August 18, 2001; August 26, 2002).

origin of Ca-rich particles with round shape is hardly possible to be identified only from, that the ratio of Ca-rich particles relatively increase when the concentration of coarse particles, i.e. dust particle, is low such as summer cases. It is likely that situation of the ground surface and strength of vertical mixing are potential factors causing the difference of chemical mixing state.

6.4.2 Diffusion of dust existed in surface atmosphere

Figure 15 shows appearance frequencies on Si-, Ca-, Na- and Fe-rich particles of three cases; i) the results of particles collected in 3-5km altitude

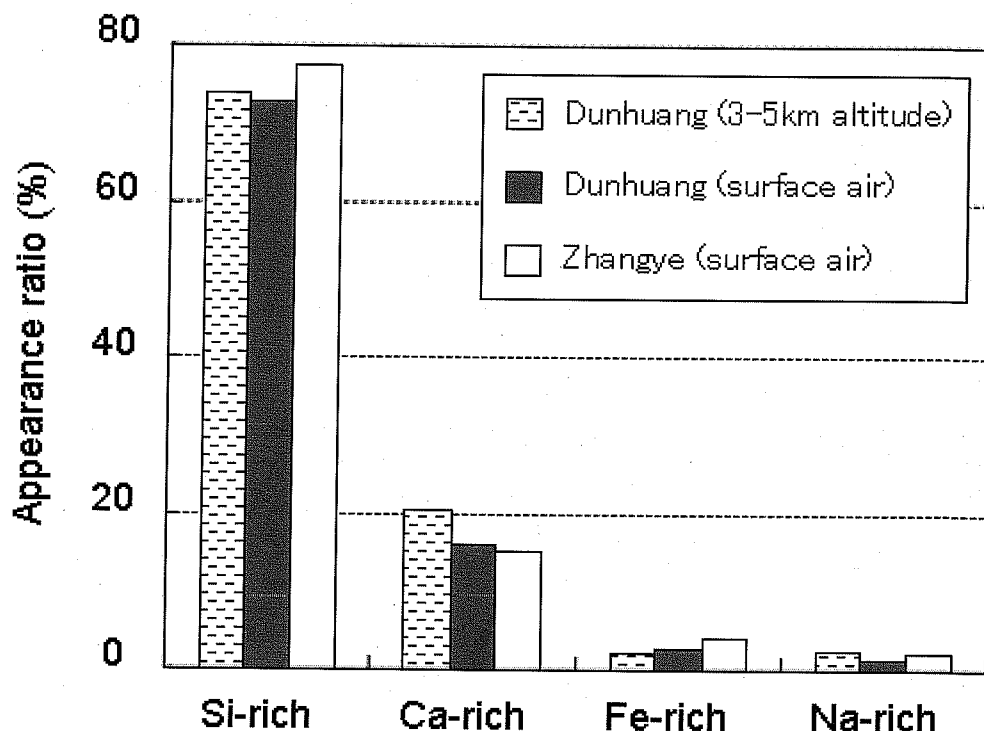


Figure 15. Appearance frequencies on Si-rich, Ca-rich, Na-rich, and Fe-rich particles of the three case; i) the results of particles collected in 3-5km altitude over Dunhuang (on March 24, 2003), ii) those near ground surface during dust-storm periods in Dunhuang (on April 29, 2002), and iii) those near ground surface strong wind or dust-storm in Zhangye (on March 13, 1990; April 27, 1991; May 7, 1991). The data of chemical composition of dust is from samples taken at Zhangye (Okada and Kai, 1995).

over Dunhuang (on March 24, 2003), ii) those near ground surface during dust-storm periods in Dunhuang (on April 29, 2002) (Trochkin et al., 2003b), and iii) those near ground surface during strong winds or dust-storm in Zhangye (39°52'N, 100°23'E) (on March 13, 1990; April 27, 1991; May 7, 1991) (Okada and Kai, 1995). It should be noted here that the value of Zhangye measurements is based on the analysis of the particles with size of 0.1 μ m-6 μ m (Okada and Kai, 1995).

Interestingly, the appearance frequencies of these rich particles in the free troposphere and near surface atmosphere during dust-storm period in

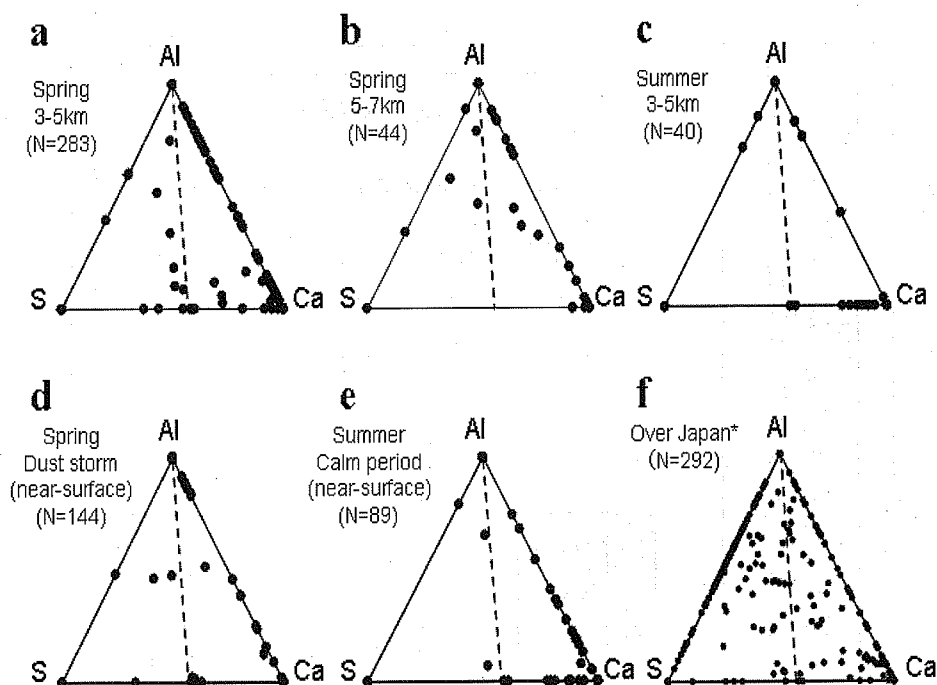


Figure 16. Relative weight ratios of Al, S and Ca for mineral particles. Those particles were collected in 3-5 km altitude over Dunhuang on March 24, 2003 (a), those in 5-7 km altitude over Dunhuang on March 24, 2003 (b), those in 3-5 km altitude over Dunhuang on August 29 (c), those in the surface atmosphere at Dunhuang on April 29, 2002 (d), those in the surface atmosphere at Dunhuang (e), and those in the free troposphere over Japan (f). The graph (f) is from Trochkin et al. (2003).

Dunhuang were mostly the same with particles collected during dust-storm or strong winds, although the Zhangye station is located in about 500km east from observational station in Dunhuang. The appearance ratios of Si-rich particles and Ca-rich particles collected in the free troposphere in spring or near ground under stormy condition were significantly different from the ratios in very calm and fine weather in summer. The types of detected particles in the free troposphere in spring were significantly similar to the values obtained in Dunhuang and Zhangye during dust-storm period. This is highly suggestive because particles collected over Dunhuang can be considered to show typical mixing state of mineral particles

during dust-storm period in source regions.

Relative weight ratios of Al, S, and Ca for the mineral particles are shown in Fig. 16. The dashed line shows the weight ratio of S/Ca for gypsum ($=0.8$) in scattering diagram. If there are many plots on right of the dashed line, it can be assumed that little uptake of SO_x on mineral particles is occurred. Most of dust particles over Dunhuang in spring and summer, from relative weight ratios of S to Ca in Fig. 16, indicated the value of lower than 0.8. The ratios of S to Ca for dust particles collected in the surface atmosphere in Dunhuang also indicated the value of lower than 0.8 (Trochkin et al., 2003b). Moreover, dust particles collected in the surface atmosphere in Zhangye indicated the similar result (Okada and Kai, et al., 1995)

The fact that uptake of SO_x on the dust particles were hardly occurred over the source area is of considerable effective to discuss the modification during long-range transportation. Trochkin et al. (2003a) has pointed out, from comparison with dust particles collected over Japan and near the ground surface, that approximately 40-45% of mineral particles mixed internally with sulfate during their transport in the troposphere. The results obtained here can confirm that dust particles are considerably modified during transportation in the free troposphere over urban areas in China, Korea, and Japan.

6.5 Conclusions

Dust particles collected in the spring free troposphere over the Taklamakan Desert with balloon-borne impactor suggest followings:

(1) Electron microscopic experiments directly showed that mineral dust particles were major constituents of coarse mode particles in spring and summer in the free troposphere over the Taklamakan Desert. This suggests that in the free troposphere over the Taklamakan Desert dust particles is constantly existed, although the number concentrations of dust particles was higher in spring than that in summer.

(2) Analysis of wind systems showed that combination of predominating westerly in the free troposphere and surface wind strongly controlled by geographical structure of the Tarim basin was important process characterizing transport processes of KOSA particles originating in the Taklamakan desert. Dunhuang was located at just turning point of the wind direction in relatively low altitude such as in the boundary layer.

(3) The values of [number concentration of Ca-rich particles]/ [number concentration of Si-rich particles] in the layers of 3-5km and 5-7km altitude in spring is considerably similar. It is likely that once the dust lifted to the free troposphere, even if stable layers appear after that the effect of the appearance of stable layer can be hardly detected in the dust particle distribution, the mixed state remains.

(4) The mixing state of dust particles, especially the appearance ratio of Ca-rich particles, in the free troposphere were of significantly difference between spring and summer, although Si-rich particles and Ca-rich particles were typical types of those dust particles. On the other hand, the ratio of Ca-rich /Si-rich particles of dust collected near the ground surface in Dunhuang and Zhangye during dusty period were very similar to free tropospheric dust. It is likely that the ratio of Ca-rich particles relatively increase when the concentration of dust is low, and situation of the ground surface and strength of vertical mixing are potential factors causing the difference.

The results obtained in this study provide very useful information to discuss the modification of Asian dust-storm particles during long-range transportation, the transport system of KOSA particle, and the radiative effects. For further understandings of the spatial and seasonal distribution of dust particles and chemical composition on individual those dust particles originated from the Taklamakan Desert, field measurements on individual particle composition over the desert and wind systems of the free troposphere in the north-west China are desired.

Acknowledgements. This investigation was supported by Japan Ministry of Education, Culture, Sports, Science and Technology (Grant-in-Aid for Specially Promoted Research, 10144104), and Japan Society for the Promotion of Science (Inter-Research Centers Cooperative Program, Stratospheric Physics and Chemistry Based on Balloon-borne Measurements of Atmospheric Ozone, Aerosols, and Others). Staff members of DunHuang City Meteorological Bureau gave us kind and helpful technical support during balloon-borne measurements.

References

- DeMott, P.J., Sassen, K., Poellot, M.R., Baumgardner, D., Rogers, D.C., Brooks, S.D., Prenni, A.J. and Kreidenweis, S.M.: 2003, 'African dust aerosols as atmospheric ice nuclei', *Geophys. Res. Lett.*, **30**, Art. No. 1732.
- Dentener, F.J., Carmichael, G.R., Zhang, Y., Lelieveld, J. and Crutzen P.J.: 1996, 'Role of mineral aerosol as a reactive surface in the global troposphere', *J. Geophys. Res.*, **101**, 22869-22889.
- Huebert, B.J., Bates, T., Russell, P.B., Shi, G.-Y., Kim, Y.J., Kawamura, K., Carmichael, G. and Nakajima, T.: 2003, 'An overview of ACE-Asia: Strategies for quantifying the relationships between Asian aerosols and their climatic impacts', *J. Geophys. Res.*, **108**, Art. No. 8633.
- Iwasaka, Y., Yamato, M., Imasu, R. and Ono A.: 1988, 'Transport of Asian dust (KOSA) particles: importance of weak KOSA events on the geochemical cycle of soil particles', *Tellus*, **40B**, 494-503.
- Iwasaka, Y., Shi, G.-Y., Yamada, M., Matsuki, A., Trochkin, D., Kim, Y.-S., Zhang, D., Nagatani, T., Shibata, T., Nagatani, M., Nakata, H., Shen, Z., Li, G. and Chen, B.: 2003, 'Importance of dust particles in the free troposphere over the Taklamakan Desert: Electron microscopic experiments of particles collected with a balloon-borne particle impactor at Dunhuang, China', *J. Geophys. Res.*, **108**, Art. No. 8644.
- Levin, Z., Ganor, E. and Gladstein, V.: 1996, 'The effects of desert particles coated with sulfate on rain formation in the eastern Mediterranean', *J. Appl. Meteorol.*, **35**, 1511-1523.
- Kwon, S.-A., Iwasaka, Y., Shibata, T. and Sakai, T.: 1997, 'Vertical distribution of atmospheric particles and water vapor densities in the free troposphere: Lidar measurement in spring and summer in Nagoya, Japan', *Atmos. Environ.*, **31**, 1459-1465.
- Matsuki, A., Iwasaka, Y., Trochkin, D., Zhang, D., Osada, K. and Sakai, T.: 2002, 'Horizontal mass flux of mineral dust over east Asia in spring: aircraft-borne measurements over Japan', *J. Arid Land Studies*, **11**, 337-345.
- Matsuki, A., Iwasaka, Y., Osada, K., Matsunaga, K., Kido, M., Inomata, Y., Trochkin, D., Nishita, C., Nezuka, T., Sakai, T., Zhang, D. and Kwon, S.-A.: 2003, 'Seasonal dependence of the long-range transport and vertical distribution of free tropospheric aerosols over east Asia: On the basis of

- aircraft and lidar measurements and isentropic trajectory analysis', *J. Geophys. Res.*, **108**, Art. No. 8663.
- Merrill, J.T., Uematsu, M. and Bleck, R.: 1989, 'Meteorological analysis of long range transport of mineral aerosols over the north Pacific', *J. Geophys. Res.*, **94**, 8584-8598.
- Mori, I., Iwasaka, Y., Matsunaga, K., Hayashi, M. and Nishikawa, M.: 1999, 'Chemical characteristics of free tropospheric aerosols over the Japan Sea coast: aircraft-borne measurements', *Atmos. Environ.*, **33**, 601-609.
- Murayama, T., Sugimoto, N., Uno, I., Kinoshita, K., Aoki, K., Hagiwara, N., Liu, Z., Matsui, I., Sakai, T., Shibata, T., Arao, K., Sohn, B.-J., Won, J.-G., Yoon, S.-C., Li, T., Zhou, J., Hu, H., Abo, M., Iokibe, K., Koga, R. and Iwasaka Y.: 2001, 'Ground-based network observation of Asia dust events of April 1998 in East Asia', *J. Geophys. Res.*, **106**, 18345-18359.
- Okada, K. and Kai, K.: 1995, 'Features and elemental composition of mineral particles collected in Zhangye, China', *J. Meteorol. Soc. Japan*, **73**, 947-957.
- Sakai, T., Shibata, T., Kwon, S.-A., Kim, Y.-S., Tamura, K. and Iwasaka Y.: 2000, 'Free tropospheric aerosol backscatter, depolarization ratio, and relative humidity measured with the Raman lidar at Nagoya in 1994-1997: contribution of aerosols from the Asian Continent and the Pacific Ocean', *Atmos. Environ.*, **34**, 431-442.
- Sassen, K.: 2002, 'Indirect climate forcing over the western US from Asian dust storms', *Geophys. Res. Lett.*, **29**, Art. No. 1465.
- Sokolik, I.N. and Toon, O.B.: 1996, 'Direct radiative forcing by anthropogenic airborne mineral aerosols', *Nature*, **381**, 681-683.
- Sun, J., Zhang, M. and Liu, T.: 2001, 'Spatial and temporal characteristics of dust storms in China and its surrounding regions, 1960-1999: Relations to source area and climate', *J. Geophys. Res.*, **106**, 10325-10333.
- Tegen, I., Lacis, A. and Fung, I.: 1996, 'The influence on climate forcing of mineral aerosols from disturbed soils', *Nature*, **380**, 419-422.
- Trochkin, D., Iwasaka, Y., Matsuki, A., Zhang, D., and Osada, K.: 2002, 'Aircraft borne measurements of morphology, chemical elements, and number-size distributions of particles in the free troposphere in spring over Japan: estimation of particle mass concentrations', *J. Arid Land Studies*, **11**, 327-335.
- Trochkin, D., Iwasaka, Y., Matsuki, A., Yamada, M., Kim, Y.-S., Nagatani, T., Zhang, D., Shi, G.-Y., Shen, Z.: 2003a, 'Mineral aerosol particles collected in

- Dunhuang, China, and their comparison with chemically modified particles collected over Japan', *J. Geophys. Res.*, **108**, Art. No. 8642.
- Trochikine, D., Iwasaka, Y., Matsuki, A., Yamada, M., Kim, Y.-S., Zhang, D., Shi, G.-Y., Shen, Z. and Li, G.: 2003b, 'Comparison of the chemical composition of mineral particles collected in Dunhuang, China and those collected in the free troposphere over Japan: possible chemical modification during long-range transport, *Water, Air, and Soil Pollution: Focus*, **30**, 161-172.
- Yabuki, S., Okada, A., Ueda, A., Chang, Q. and Fan, Z.-L.: 1997, 'Sulfur isotope study of salt materials in saline lands and salt deposits around the desert areas in Xinjiang, China –Implications to the study of the source of the aeolian dust of inland Asia', *J. Arid Land Studies*, **11**, 127-138.
- Yabuki, S., Osamu, A., Mochizuki, S., Kanayama, K., Watanabe, K. and Xu, J.: 2003, 'Mineral identification of atmospheric microparticles collected at the mountainsides of Tianshan and Kunlun Mountains, NW China, *The second International Workshop on Sandstorms and Associated Dustfall abstracts*, Nagoya, Japan, 15 November 2003, pp. 50.
- Zhang, D. and Iwasaka, Y.: 2001, 'Chlorine deposition on dust particles in marine atmosphere', *Geophys. Res. Lett.*, **28**, 3313-3616.

Chapter 7

Effect of Air Pollutants on Microphysical Properties of Clouds

Masato NISHIZAWA and Yutaka ISHIZAKA
Hydrospheric Atmospheric Research Center
Nagoya University
Email: nishizawa.masato@jaea.go.jp
ishizaka@hyarc.nagoya-u.ac.jp

7.1 Introduction

It is known that the air pollutants emitted by industrial activities have caused the global environmental problems such as global warming, acid rain, and depletion of stratospheric ozone. Among them, the increase of anthropogenic hygroscopic aerosol like sulfate particles alters the microphysical properties and lifetime of clouds through the production of cloud condensation nuclei (CCN), and consequently affects radiation heat budget in the atmosphere. This is called indirect effect of aerosol in global warming. These particles also influence condensation and precipitation coefficients of lower stratiform clouds.

In this chapter, the changes of the microphysical properties of clouds resulting from the increase of hygroscopic aerosol particles are estimated by numerical experiments using a numerical meteorological model. In Section 7.2, the general characteristics of the model are described. In Section 7.3, the numerical experiments are outlined, and the results are shown in Section 7.4.

7.2 Numerical models of meteorological field and cloud physics

In general, numerical model of meteorological field is a tool that predicts or reproduces wind direction and speed, air temperature, air pressure, air humidity, amount of precipitation and others on the computer on the basis of the laws of

atmospheric physics and thermodynamics. There are various models according to one's problem to solve from general circulation model that calculates global climate change to cloud resolving model that calculates one cloud's life. In this chapter, the cloud-resolving model under development by authors is described briefly. In this model, processes of dynamics, eddy diffusion, planetary boundary layer, and radiation are calculated by PSU/NCAR MM5 (e.g. Duhdia, 1993), and cloud microphysics by HUCM (Hebrew University Cloud Model, e.g. Khain and Sednev, 1996). In HUCM, to deal with size distribution of cloud droplets explicitly, distribution function of cloud droplets is discriminated to finite bins, and microphysics of cloud droplets in each bin are calculated. Furthermore, activation processes of hygroscopic aerosol to CCN in supersaturation are included in HUCM, thus we can examine the effect of hygroscopic aerosol particles on microphysical properties of clouds. However, since this model deals with many prognostic variables, applicable horizontal spatial scale is usually limited to a few kilometers to a few ten kilometers.

7.3 Configuration of numerical experiment

The conditions of numerical experiments are shown in Table 1. The calculation domain is 2.5 km in east and west, 50 km in north and south, and top of domain is about 7 km (Fig.1). Initial wind velocities are set to zero in all three directions. Initial vertical profiles of temperature and relative humidity are obtained from result of aircraft observations. Thermal is located the center of domain to advance the production of cloud. Chemical composition of hygroscopic aerosol is assumed to be ammonium sulfate and three modal lognormal size distributions is assumed based on aircraft observations (Fig.2). In this experiment, initial number concentration of hygroscopic aerosol particles below 1 km is changed from 10 to 10^6 ($\#/cm^3$) to investigate changes of microphysical structure of clouds accompanied with the increase of hygroscopic aerosol. Above 1 km, initial number concentration of hygroscopic aerosol particles decreases exponentially with height. Cloud microphysical processes are assumed to be warm rain, so transformation of hygroscopic aerosol particles to cloud droplets by nucleation, condensational growth or evaporation of cloud droplet, and collision-coalescence processes is considered in this study.

Table 1. Calculation conditions

Number of grid points	6 x 51 x 45
Horizontal resolutions	500 m
Vertical resolution	70 m at the surface, 200 m at the top
Time step	1.5 sec
	0.5 sec for cloud microphysics
Calculation time	1 hour

7.4 Result and Discussion

Fig.3 shows snapshot of the calculated mixing ratio of water droplets (cloud and rain water) and their size distributions at several points at 6 min for hygroscopic aerosol particles of 10^3 ($\#/cm^3$). Symmetrical distributions of water droplets and updraft are produced by the thermal. Monomodal size distributions are obtained at the center of the cloud, but bimodal size distributions are obtained at the top and lateral boundaries. This bimodal size distribution is brought by entrainment of outside air of the clouds.

Fig.4 shows snapshots of the calculated mixing ratio of water droplets at 6 min for hygroscopic aerosol particles of 10 to 10^6 ($\#/cm^3$). The higher number concentration of hygroscopic aerosol particles is, the more water droplet is produced.

Fig.5 shows snapshots of the mean radius of water droplet at 6 min for hygroscopic aerosols of 10 to 10^6 ($\#/cm^3$). The higher number concentration of hygroscopic aerosol particles is, the smaller mean radius is. This is due to decrease of condensation water distributed on each CCN.

Fig.6 shows the relationship between initial number concentration of hygroscopic aerosol particles and hourly precipitation. Hourly precipitation has a peak at initial number concentration of hygroscopic aerosol particles of 2×10^3 ($\#/cm^3$). Smaller initial number concentration of hygroscopic aerosol particles produces less precipitation due to few cloud droplets. On the other hand, higher initial number concentration of hygroscopic aerosol produces less precipitation due to delay of growth rate of cloud droplets to rain drops.

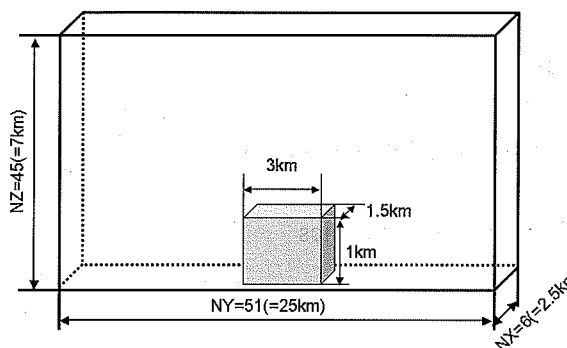


Figure 1. Calculation domain. Shaded zone denotes thermal.

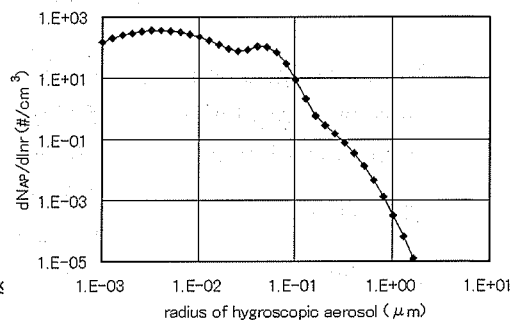


Figure 2. Initial size distribution of hygroscopic aerosol.

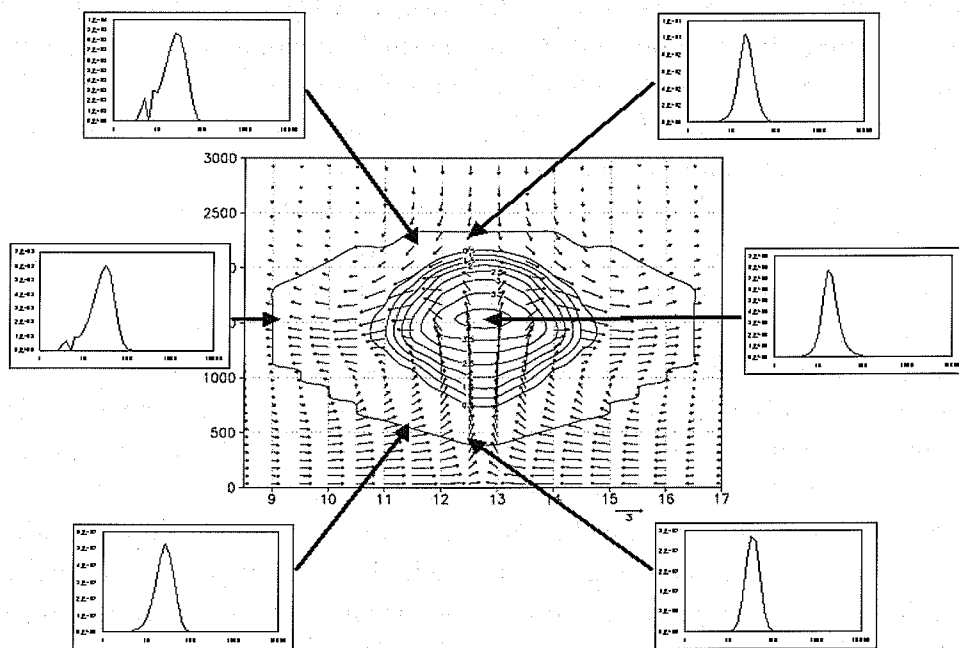


Figure 3. Mixing ratio and size distribution of water droplets at 6 minutes for initial number concentration of hygroscopic aerosol particles of 10^3 ($\#/\text{cm}^3$).

*NUMERICAL EXPERRIMENTS ON EFFECT OF AIR POLLUTANTS ON MICROPHYSICAL
PROPERTIES OF CLOUDS*

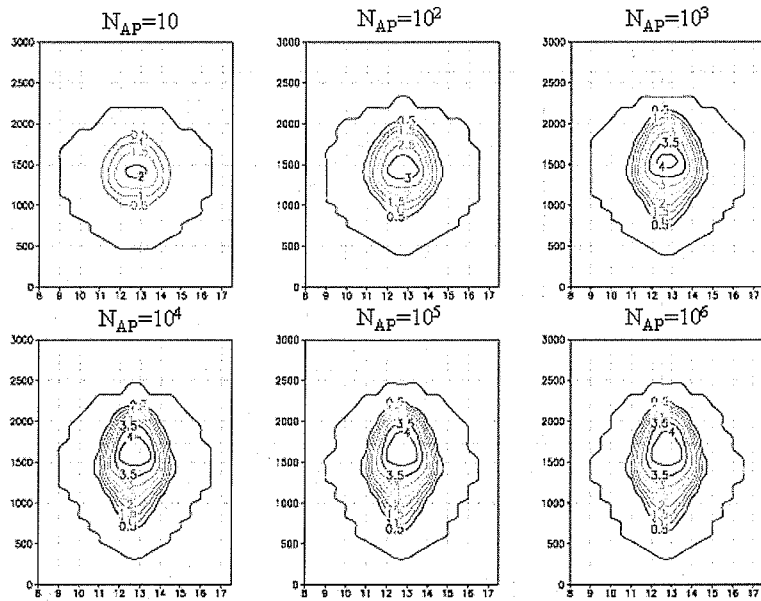


Figure 4. Mixing ratio of water droplet at 6 minutes for initial number concentration of hygroscopic aerosol of 10 to 10^6 ($\#/cm^3$).

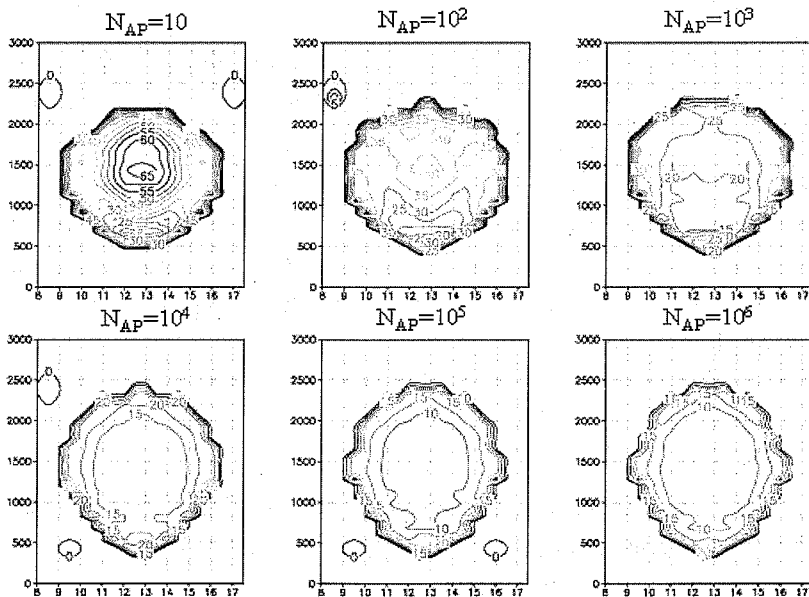


Figure 5. Mean radius of water droplet at 6 minutes for initial number concentration of hygroscopic aerosol of 10 to 10^6 ($\#/cm^3$).

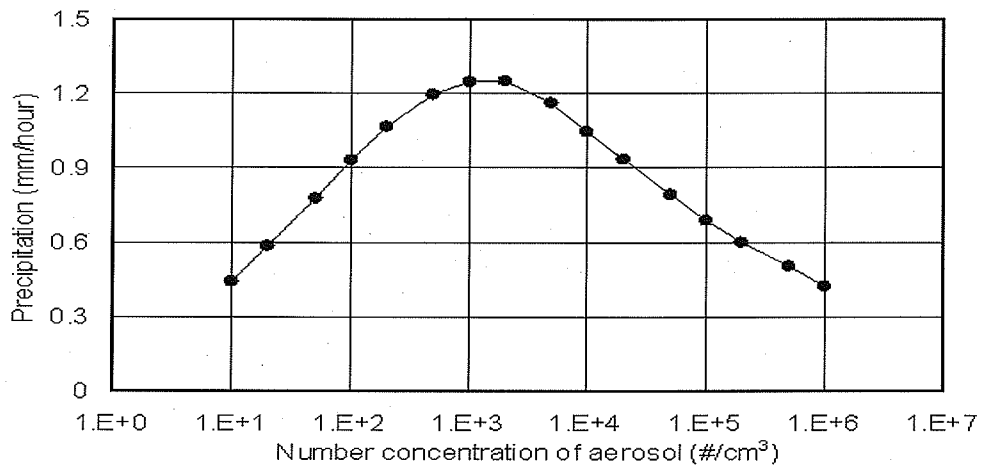


Figure 6. The relationship between initial number concentration of hygroscopic aerosol particles and hourly rainfall rate.

7.5 Summary

In this chapter, numerical experiments using cloud resolving model were introduced to investigate the effect of hygroscopic aerosol on microphysical properties of clouds. This model has a weak point that spatial range is limited due to many prognostic variables. However, this model could contribute to giving a sophisticated parameterization to general circulation model that can't treat cloud microphysics in detail. Moreover, if this model is calculated by a super computer with vector or parallel processors, it could be useful in analysis of actual meteorological phenomena.

References

- Dudhia, J., 1993. A nonhydrostatic version of the Penn State/NCAR mesoscale model: Validation tests and simulation of an Atlantic cyclone and cold front. *Mon. Wea. Rev.*, 121, 1493-1513.
- Khain, A. P., Sednev, I., 1996. Simulation of precipitation formation in the Eastern Mediterranean coastal zone using a spectral microphysics cloud ensemble model. *Atmos. Res.*, 43, 77-110.

Chapter 8

Numerical Models for Transport of Air-pollutants in the Atmosphere

Toshihiro KITADA
Faculty of Engineering,
Toyohashi University of Technology
Toyohashi, JAPAN
e-mail: kitada@earth.eco.tut.ac.jp

In this chapter numerical methods for the partial differential equation of atmospheric diffusion/chemistry/deposition are briefly discussed. Finite difference and finite element methods are mainly described.

8.1 Finite difference method

8.1.1 Basis

(1) Classification

The finite difference method can be classified in several ways.

They are:

- ① Explicit or implicit method; it depends on how time derivative is discretized. Explicit method does not require solution of the system of algebraic equations. Restriction for stable solution is usually severer in explicit methods than in implicit methods.
- ② Two-level, three-level, or higher level scheme; it depends on how many time points are involved in one discretized equation.
- ③ One step or multi-step method; it depends on how many steps are required to proceed calculation by one time step. Multi-step methods include “method of fractional steps” such as ADI (Alternating Direction Implicit), LOD (Locally One Dimensional method), and “predictor-corrector” method.

(2) Approximation of derivative with finite difference method

Basic difference approximation of the first order derivative of a function $\phi(x, t)$ at $X = i\Delta t$ can be derived as follows. Let Δx and Δt the step sizes on space and time, respectively. Thus, $(x, t) = (i\Delta x, n\Delta t)$.

$$\frac{\partial \phi}{\partial x} = (\phi_{i+1} - \phi_i) / \Delta x + O(\Delta x) \quad (1)$$

$$(\phi_{i+1} - \phi_{i-1}) / (2\Delta x) + O((\Delta x)^2) \quad (2)$$

$$\text{or } (\phi_{i+1/2} - \phi_{i-1/2}) / \Delta x + O((\Delta x)^2) \\ (\phi_i - \phi_{i-1}) / \Delta x + O(\Delta x) \quad (3)$$

where $\phi_i = \phi(i\Delta x)$. The following difference operators are usually used:

$$\text{Forward difference: } \Delta \phi_i = \phi_{i+1} - \phi_i$$

$$\text{Centered difference: } \delta \phi_i = \phi_{i+1} - \phi_{i-1} \text{ or } \delta \phi_i = \phi_{i+1/2} - \phi_{i-1/2}$$

$$\text{Backward difference: } \nabla \phi_i = \phi_i - \phi_{i-1}$$

Eqs. (1) - (3) can be derived by taking a Taylor series expansion of ϕ_{i+1} and ϕ_{i-1} .

$$\phi_{i+1} = \phi_i + \Delta x \left(\frac{\partial \phi}{\partial x} \right)_i + \frac{(\Delta x)^2}{2} \left(\frac{\partial^2 \phi}{\partial x^2} \right)_i + \frac{(\Delta x)^3}{6} \left(\frac{\partial^3 \phi}{\partial x^3} \right)_i + O((\Delta x)^4) \quad (4)$$

$$\phi_{i-1} = \phi_i - \Delta x \left(\frac{\partial \phi}{\partial x} \right)_i + \frac{(\Delta x)^2}{2} \left(\frac{\partial^2 \phi}{\partial x^2} \right)_i - \frac{(\Delta x)^3}{6} \left(\frac{\partial^3 \phi}{\partial x^3} \right)_i + O((\Delta x)^4) \quad (5)$$

By using similar procedure, higher order difference approximation can be derived. For example, Eq. (6) has its truncation error of the 4th order with respect to Δx .

$$\left(\frac{\partial \phi}{\partial x} \right)_i = \frac{4}{3} \left(\frac{\phi_{i+1} - \phi_{i-1}}{2\Delta x} \right) - \frac{1}{3} \left(\frac{\phi_{i+2} - \phi_{i-2}}{4\Delta x} \right) + O((\Delta x)^4) \quad (6)$$

In the same manner, the centered difference for the second order derivative, for example, can be obtained as in Eq. (7).

$$\left(\frac{\partial^2 \phi}{\partial x^2}\right)_i = \left(\frac{\phi_{i+1} - 2\phi_i + \phi_{i-1}}{\Delta x^2}\right) + O(\Delta x^2) \equiv \frac{\delta^2 \phi_i}{\Delta x^2} + O((\Delta x)^2) \quad (7)$$

Note. $O(\Delta x)$, $O((\Delta x)^2)$ etc. stand for the “truncation error” or “descretization error”.

The symbol $O(\)$ shows the order of the concerned term; for example, if $F = O(\Delta x)$,

$$|F| \leq A \cdot \Delta x \quad \text{for} \quad \Delta x \rightarrow 0$$

it means there exists a positive number “A” which satisfies the following relation.

8.1.2 Consistency, convergence, and stability

Criteria which assure solution of descretized difference equation is close to solution of the original differential equation are “consistency”, “convergence”, and “stability”. Let us consider the following equation as an example:

$$\frac{\partial \phi}{\partial t} = \frac{\partial^2 \phi}{\partial x^2} \quad (8)$$

If we apply forward difference to the time derivative and centered difference to the spatial derivative in Eq. (8), we obtain Eq. (9).

$$\Phi_i^{n+1} - (1 - 2r)\Phi_i^n - r(\Phi_{i+1}^n + \Phi_{i-1}^n) = 0 \quad (9)$$

where $r = \Delta t / (\Delta x)^2$, and Φ_i^n is solution of Eq. (9). We expect that Φ_i^n is an appropriate analog of the solution $\phi(i\Delta x, n\Delta t)$.

(1) Consistency

As $\Delta x, \Delta t \rightarrow 0$, if the difference equation (9) divided by Δt converges to the differential equation (8), Eq. (9) is said to satisfy the “consistency”. The consistency of a difference equation can be examined in the following manner. Let us use Eq.

(9) as an example. First, apply Taylor series expansion to the terms in Eq. (9) as follows.

$$\phi^{n+1}_i = \phi^n_i + \Delta t \left(\frac{\partial \phi}{\partial t} \right)_i^n + \frac{(\Delta t)^2}{2} \left(\frac{\partial^2 \phi}{\partial t^2} \right)_i^n + O(\Delta t^3) \quad (10)$$

$$\phi^{n+1}_{i+1} = \phi^n_{i+1} + \Delta x \left(\frac{\partial \phi}{\partial x} \right)_{i+1}^n + \frac{(\Delta x)^2}{2} \left(\frac{\partial^2 \phi}{\partial x^2} \right)_{i+1}^n + \frac{(\Delta x)^3}{6} \left(\frac{\partial^3 \phi}{\partial x^3} \right)_{i+1}^n + \frac{(\Delta x)^4}{24} \left(\frac{\partial^4 \phi}{\partial x^4} \right)_{i+1}^n + O(\Delta x^5) \quad (11)$$

$$\phi^{n+1}_{i-1} = \phi^n_{i-1} - \Delta x \left(\frac{\partial \phi}{\partial x} \right)_{i-1}^n + \frac{(\Delta x)^2}{2} \left(\frac{\partial^2 \phi}{\partial x^2} \right)_{i-1}^n - \frac{(\Delta x)^3}{6} \left(\frac{\partial^3 \phi}{\partial x^3} \right)_{i-1}^n + \frac{(\Delta x)^4}{24} \left(\frac{\partial^4 \phi}{\partial x^4} \right)_{i-1}^n + O(\Delta x^5) \quad (12)$$

Substitution of the Taylor series expansions of ϕ^{n+1}_i , ϕ^n_{i+1} , and ϕ^n_{i-1} in Eqs. (10), (11), and (12) into the corresponding terms on the lefthand side of Eq. (9), division by Δt , and rearrangement lead to the following equation.

$$\frac{1}{\Delta t} \left\{ \phi^{n+1}_i - (1-2r)\phi^n_i - r(\phi^n_{i+1} + \phi^n_{i-1}) \right\} - \left(\frac{\partial \phi}{\partial t} - \frac{\partial^2 \phi}{\partial x^2} \right)_i^n = \frac{\Delta t}{2} \left(\frac{\partial^2 \phi}{\partial t^2} - \frac{1}{6r} \frac{\partial^4 \phi}{\partial x^4} \right)_i^n + \quad (13)$$

The first term on the right hand side of Eq. (13) is called the principal part of the local truncation error of Eq. (9). Eq. (13) suggests that the right hand side converges to 0 when $\Delta t, \Delta x \rightarrow 0$; thus Eq. (9) converges to Eq. (8). In general, a difference equation is said to satisfy the “consistency” when its local truncation error becomes 0 for $\Delta t, \Delta x \rightarrow 0$.

(2) Convergence

Solution of a finite difference equation is called to have the nature of “convergence” when the following relation (14) is satisfied at any fixed point ($x=i\Delta x, t=n\Delta t$) in time-distance space for $\Delta t, \Delta x \rightarrow 0$ (that is, i and $n \rightarrow \infty$):

$$\left| \phi(i\Delta x, n\Delta t) - \Phi_i^n \right| \rightarrow 0 \quad (14)$$

(3) Stability

Solution of a finite difference equation is said to satisfy "stability" when the following quantity (15) is bounded for $n \rightarrow \infty$ with Δt , Δx being fixed:

$$\left| \phi(i\Delta x, n\Delta t) - \Phi_i^n \right| \quad (15)$$

The "convergence" is enough for a finite difference equation to give correct solution for the original differential equation. Verification on the nature of "convergence" of a finite difference equation is usually much more difficult than the other natures of "consistency" and "stability". Hence often the stability of a difference equation is examined as well as its consistency. Actually the Lax's equivalent theorem assures that for a class of linear partial differential equations both the consistency and stability of their finite difference analogs are the necessary and satisfactory condition for the convergence.

(4) The von Neumann's method for stability analysis

From Eqs. (9) and (13), it can be inferred that an error $Z_i^n = \phi(i\Delta x, n\Delta t) - \Phi_i^n$ also satisfies Eq. (9). Now, let us try to find a condition that Z_i^n is bounded for $t \rightarrow \infty$ by using von Neumann's method. It should be noted the following discussion is also applicable to the solution, Φ_i^n , itself. The error Z_i^n satisfies the following Eq. (16).

$$Z_i^{n+1} - (1-2r)Z_i^n - r(Z_{i+1}^n + Z_{i-1}^n) = 0 \quad (16)$$

Let us assume a component of the finite Fourier series solution of Eq. (16) with wave number k_x can be given as Eq. (17). (the wave number k_x denotes the number of waves accommodated within the length of 2π .)

$$Z_i^n = V^n e^{ik_x(i\Delta x)} = V^n e^{li\theta} \quad (17)$$

where $I = \sqrt{-1}$ is the imaginary unit, $\theta \equiv k_x \Delta x$ is phase angle, and V^n is amplitude at time $t = n\Delta t$. Other terms Z_i^{n+1} , Z_{i+1}^n , and Z_{i-1}^n in Eq. (16) can be expressed in a similar manner.

Substituting Z_i^n in Eq. (17) etc. into Eq. (16), dividing the resultant equation by $e^{in\theta}$, and rearranging it leads to an equation (18) on the amplitudes V^{n+1} and V^n . The von Neumann's stability analysis is to find a condition that the amplitude V^n does not diverge to infinity with time.

$$V^{n+1} = \{1 - 2r(1 - \cos \theta)\}V^n \quad (18)$$

If we define $G \equiv 1 - 2r(1 - \cos \theta)$, the following relation (19) has to be satisfied for that V^{n+1} in Eq. (18) is bounded for any $\theta = k_x \Delta x$ as $n \rightarrow \infty$.

$$|G| \leq 1 \quad \text{for all the } \theta = k_x \Delta x \quad (19)$$

On the von Neumann's method the followings may be noted:

- (1) Though the von Neumann's stability analysis is for linear differential equation with constant coefficients, the method is applicable locally also for the same equation with variable coefficients.
- (2) The von Neumann's method does not consider effect of boundary condition. It may be an important deficient.
- (3) Other methods for stability analysis are available.

8.1.3 Methods for solution of algebraic equations system

By applying any discretization method to partial differential equation a set of algebraic equations are obtained. In case of unsteady problem such a system has to be solved at every time steps.

For the solution of a linear system various direct and indirect/iterative methods are available (Togawa, 1972). For solution of nonlinear system Newton-Raphson

method and simple iterative methods can be applied (Wendorff, 1973).

8.1.4 Iterative method for linear algebraic equations system

Let us consider the following system.

$$\underline{A} \vec{x} = \vec{y} \quad (20)$$

where \underline{A} is a coefficient matrix, \vec{x} is a vector of unknown variables, and \vec{y} is a vector of known values. In iterative method the coefficient matrix \underline{A} in Eq. (20) is decomposed as Eq. (21).

$$\underline{A} = \underline{M} - \underline{N} \quad (21)$$

When \underline{A} in Eq. (21) is inserted into Eq. (20), the resultant equation can be converted to an iterative form Eq. (22).

$$\underline{M} \vec{x}^{(k+1)} = \underline{N} \vec{x}^{(k)} + \vec{y} \quad (k = 0, 1, 2, \dots) \quad (22)$$

When $\vec{x}^{(k+1)}$ in Eq. (22) converges, $\vec{x}^{(k+1)}$ at this stage apparently satisfies Eq. (20).

Depending on the methods of decomposition of matrix, \underline{A} , the following iterative methods can be derived.

(1) Gauss – Seidel method

The Gauss-Seidel method decomposes \underline{A} into three parts as Eq. (23).

$$\underline{A} = \underline{D} + \underline{E} + \underline{F} \quad (23)$$

where the matrices \underline{D} , \underline{E} , and \underline{F} are expressed as follows:

Diagonal matrix : $\underline{D} = (d_{ij}), \quad d_{ij} = \begin{cases} a_{ij} & (i = j) \\ 0 & (i \neq j) \end{cases} \quad (24)$

Lower triangle matrix (excluding diagonal part) :

$$\underline{E} = (e_{ij}), \quad e_{ij} = \begin{cases} 0 & (i \geq j) \\ a_{ij} & (i < j) \end{cases} \quad (25)$$

Upper triangle matrix (excluding diagonal part) :

$$\underline{F} = (f_{ij}), \quad f_{ij} = \begin{cases} a_{ij} & (i > j) \\ 0 & (i \leq j) \end{cases} \quad (26)$$

The Gauss-Seidel method forms an iteration scheme (27) based on the factorization (23).

$$(\underline{D} + \underline{E}) \vec{x}^{(k+1)} = -\underline{F} \vec{x}^{(k)} + \vec{y} \quad (k = 0, 1, 2, \dots) \quad (27)$$

(2) SOR (Successive Over Relaxation) method: point iterative SOR

SOR forms the matrices \underline{M} and \underline{N} in Eq. (21) by introducing an accerelation parameter α as:

$$\begin{aligned} \underline{M} &= \frac{1}{\alpha} (\underline{D} + \alpha \underline{E}) \\ \underline{N} &= \frac{1}{\alpha} ((1 - \alpha) \underline{D} - \alpha \underline{F}) \end{aligned} \quad (28)$$

By using Eq. (28), Eq. (22) can be written as:

$$\frac{1}{\alpha} (\underline{D} + \alpha \underline{E}) \vec{x}^{(k+1)} = \frac{1}{\alpha} \{ (1 - \alpha) \underline{D} - \alpha \underline{F} \} \vec{x}^{(k)} + \vec{y} \quad (29)$$

When $\alpha = 1$ is used, the SOR equals to the Gauss-Seidel method (27).

Necessary and satisfactory condition for convergence of Eq. (22) is that the spectral radius $\rho(\underline{H})$ of the matrix \underline{H} in Eq. (30) satisfies a condition (31).

$$\underline{H} \equiv \underline{M}^{-1} \underline{N} \quad (30)$$

$$\rho(\underline{H}) \leq 1 \quad (31)$$

where the spectral radius $\rho(\underline{H})$ means an eigen value of the matrix \underline{H} whose absolute value is the largest among the eigen values.

(3) Point Jacobi method

Point Jacobi method uses the following iteration:

$$\underline{D} \vec{x}^{(k+1)} = (\underline{D} - \underline{A}) \vec{x}^{(k)} + \vec{y} \quad (k = 0, 1, 2, \dots) \quad (32)$$

8.2 Numerical method for advection/diffusion equation

8.2.1 Definition of the equation and its boundary condition

Mass conservation of a chemical constituent in the atmosphere can be written with its dimensionless concentration ϕ' as:

$$\frac{\partial(\rho\phi')}{\partial t} + \nabla \cdot (\rho \vec{V} \phi') = \nabla \cdot (\rho \underline{K} \cdot \nabla \phi') + R + S \quad (33)$$

or

$$\rho \frac{\partial \phi'}{\partial t} + \rho (\vec{V} \cdot \nabla) \phi' = \nabla \cdot (\rho \underline{K} \cdot \nabla \phi') + R + S \quad (34)$$

where \vec{V} is wind vector, \underline{K} is a matrix of diffusivity, R is a chemical reaction term, and S is a source/sink term. When the air density ρ is assumed to be nearly constant, we may redefine concentration with dimension as $\phi \equiv \rho\phi'$. By using this definition, Eqs. (33) and (34) can be written as Eqs. (35) and (36).

$$\frac{\partial \phi}{\partial t} + \nabla \cdot (\vec{V} \phi) = \nabla \cdot (\underline{K} \cdot \nabla \phi) + R + S \quad (35)$$

or

$$\frac{\partial \phi}{\partial t} + (\vec{V} \cdot \nabla) \phi = \nabla \cdot (\underline{K} \cdot \nabla \phi) + R + S \quad (36)$$

Eqs. (33) and (35) are called “conservation” form, while Eqs. (34) and (36) are “advection” form. Both conservation and advection forms are mathematically equivalent through the continuity equation. However, these two forms sometimes lead to numerically different solution (Kitada, 1987).

Let us examine the following example (Kitada, 1987).

Eqs. (35) and (36) give different solution when flow field does not rigorously satisfy the equation of continuity. For example, the flow field is often prepared by interpolation and extrapolation of observed winds, and thus it does not necessarily satisfy the continuity equation.

Generally speaking, it is known that if flow field satisfies the continuity equation the conservation form such as (35) is better than the advection form of Eq. (36) since the conservation form equation discretized with centered-space difference preserves total mass in calculation domain (Roache, 1972). However, Kitada (1987) showed the conservation form equation introduces fictitious first order chemical reaction term into the calculation if the continuity equation is not satisfied, and thus violates mass balance within the calculation domain. This can be verified by rewriting Eq. (35) as Eq. (37). For simplicity, reaction term R and source/sink term S are removed from Eq. (35).

$$\frac{\partial \phi}{\partial t} + (\vec{V} \cdot \nabla) \phi + \underbrace{(\nabla \cdot \vec{V}) \phi}_{(*)} = \nabla \cdot (\underline{K} \cdot \nabla \phi) \quad (37)$$

The term $(*)$ in Eq. (37) should be zero when the continuity of the flow is satisfied.

However, if the divergence of the flow $(\nabla \cdot \vec{V})$ is not zero, then the term $(*)$ in Eq. (37) works as a false first order reaction. In the advection form (36) this term is forced to be zero under the assumption of the continuity of flow field. Based on these considerations, Kitada (1987) proposed a new equation form (38), that is the divergence-corrected form, which cancels the false chemical reaction effect in case of non zero divergence with preserving desirable nature of the conservation form when $\nabla \cdot \vec{V} = 0$.

$$\frac{\partial \phi}{\partial t} + \nabla \cdot (\vec{V} \phi) - \underbrace{(\nabla \cdot \vec{V}) \phi}_{(*)} = \nabla \cdot (\underline{K} \cdot \nabla \phi) \quad (38)$$

Let us think one dimensional flow field such as Fig. 1a which does not satisfies the continuity equation and its divergence field is given in Fig. 1b. Under this flow condition, we try to calculate pollutant advection problem with uniform initial concentration, boundary-concentrations fixed at initial concentration, and no real sink/source of pollutant. Formulations of this problem corresponding to Eqs. (35), (36), and (38) can be written as Eqs. (39), (40), and (41), respectively.

Expected correct solution of this problem is apparently the initial concentration to be always maintained everywhere. Fig. 2 shows results after 36 time steps (a) and 72 time step (b): dotted line by Eq. (39), solid line by Eq. (40), and dashed line by Eq. (41). As can be seen in Fig. 2, the conservation form (39) shows reduced or increased concentrations corresponding to positive or negative divergence shown in Fig. 1b, while the advection form (40) and the divergence-corrected form (41) give correct solution.

$$\frac{\partial \phi}{\partial t} + \frac{\partial(u\phi)}{\partial x} = 0 \quad (39)$$

$$\frac{\partial \phi}{\partial t} + u \frac{\partial \phi}{\partial x} = 0 \quad (40)$$

$$\frac{\partial \phi}{\partial t} + \frac{\partial(u\phi)}{\partial x} - \left(\frac{\partial u}{\partial x} \right) \phi = 0 \quad (41)$$

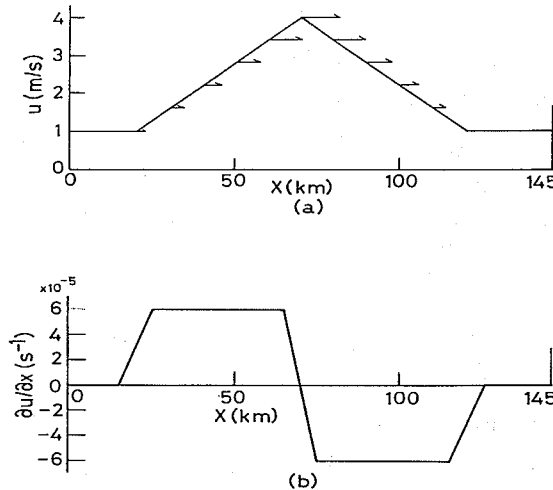


Figure 1. Wind (a) and its associated divergence (b) fields used in all simulations using Egs. (39,40, and 41).

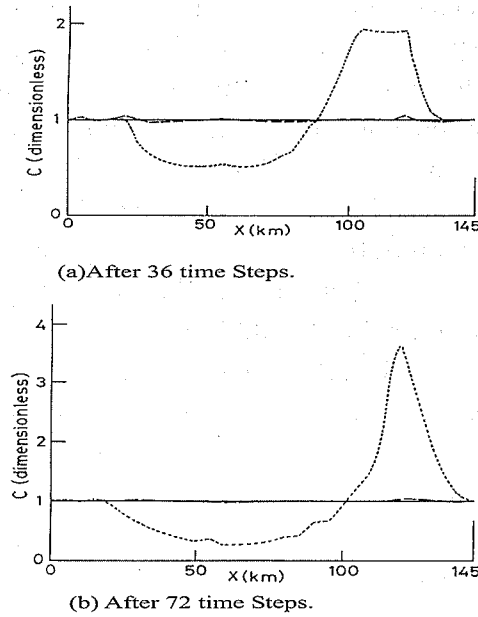


Figure 2. (a) Calculated concentration profiles after 36 time steps (=3h simulated time). Dotted line: by the conservation form, Equation (39), dashed line: by the divergence-corrected form, Equation (41), and solid line: by the advection form, Equation (40). (b) As in (a) except after 72 time steps. (Kitada, 1987).

In the later sections, we will use Eqs. (42), (43), and (44) for explanation of numerical methods; they are the simplified forms of Eq. (35).

$$\frac{\partial \phi}{\partial t} + \frac{\partial(u\phi)}{\partial x} = 0 \quad (42)$$

$$\frac{\partial \phi}{\partial t} - K \frac{\partial^2 \phi}{\partial x^2} = 0 \quad (43)$$

$$\frac{\partial \phi}{\partial t} + \frac{\partial(u\phi)}{\partial x} - K \frac{\partial^2 \phi}{\partial x^2} = 0 \quad (44)$$

where flow velocity u and diffusivity K are assumed constant.

Note. Eq. (42) (or its two dimensional form) is often used for the test of numerical methods for mass, momentum, or heat advection equation, because its analytical solution is expressed by simple parallel shift of initial distribution with a constant

velocity u , and thus numerical error associated with a particular numerical method can be clearly visualized.

8.2.2 Pressure equation for fluid dynamics calculation

(1) Historical review

To explain meaning of "pressure equation", let us think two-dimensional incompressible fluid dynamics equation. Momentum equation for this case can be written as Eqs. (45) - (48):

$$\left\{ \begin{array}{l} \frac{\partial u}{\partial t} + u \frac{\partial u}{\partial x} + v \frac{\partial u}{\partial y} = -\frac{\partial p}{\partial x} + \frac{1}{\text{Re}} \Delta u \\ \frac{\partial v}{\partial t} + u \frac{\partial v}{\partial x} + v \frac{\partial v}{\partial y} = -\frac{\partial p}{\partial y} + \frac{1}{\text{Re}} \Delta v \end{array} \right. \quad (45)$$

$$\left\{ \begin{array}{l} \frac{\partial u}{\partial t} + u \frac{\partial u}{\partial x} + v \frac{\partial u}{\partial y} = -\frac{\partial p}{\partial x} + \frac{1}{\text{Re}} \Delta u \\ \frac{\partial v}{\partial t} + u \frac{\partial v}{\partial x} + v \frac{\partial v}{\partial y} = -\frac{\partial p}{\partial y} + \frac{1}{\text{Re}} \Delta v \end{array} \right. \quad (46)$$

or

$$\left\{ \begin{array}{l} \frac{\partial u}{\partial t} + \frac{\partial u^2}{\partial x} + \frac{\partial uv}{\partial y} = -\frac{\partial p}{\partial x} + \frac{1}{\text{Re}} \Delta u \\ \frac{\partial v}{\partial t} + \frac{\partial uv}{\partial x} + \frac{\partial v^2}{\partial y} = -\frac{\partial p}{\partial y} + \frac{1}{\text{Re}} \Delta v \end{array} \right. \quad (47)$$

$$\left\{ \begin{array}{l} \frac{\partial u}{\partial t} + \frac{\partial u^2}{\partial x} + \frac{\partial uv}{\partial y} = -\frac{\partial p}{\partial x} + \frac{1}{\text{Re}} \Delta u \\ \frac{\partial v}{\partial t} + \frac{\partial uv}{\partial x} + \frac{\partial v^2}{\partial y} = -\frac{\partial p}{\partial y} + \frac{1}{\text{Re}} \Delta v \end{array} \right. \quad (48)$$

Furthermore, the equation of continuity is as follows.

$$\frac{\partial u}{\partial x} + \frac{\partial v}{\partial y} = 0 \quad (49)$$

In the early attempts to numerically calculate fluid dynamics, a set of Eq. (49) and either (45, 46) or (47, 48) was used. Those, however, all failed. By using so called pressure equation (50) instead of Eq. (49), the fluid dynamic equations (45, 46) were successfully solved (Harlow and Welch, 1965, and Hirt and Harlow 1967). The pressure equation (50) can be derived by differentiating Eq. (47) with respect to x and Eq. (48) with respect to y and then summing these two resultant equations.

$$\Delta p = -\frac{\partial^2 u^2}{\partial x^2} - 2 \frac{\partial^2 (uv)}{\partial x \partial y} - \frac{\partial^2 v^2}{\partial y^2} - \frac{\partial D}{\partial t} + \frac{1}{\text{Re}} \Delta D \quad (50)$$

where $D = \frac{\partial u}{\partial x} + \frac{\partial v}{\partial y}$ denotes divergence of flow. In the numerical calculation, the

divergence D at time $(n+1)$, which is a part of $\partial D / \partial t$, is set equal to zero

(2) HSMAC method (Highly Simplified MAC)—Hirt, C.W., Nichols, B.B., and Romers (1975) ; SOLA(Solution Algorithm)

The first successful method for computational fluid dynamics was the MAC method (Harlow and Welch, 1965). The method was further developed to be a simple form: Hily Simplified Marker and Cell Method (HSMAC).

Characteristics of HSMAC can be summarized as follows:

- (a) Discretize momentum equations in explicit manner.
- (b) Change flow velocity and pressure field iteratively so that they satisfy the forced condition such as the continuity equation or the pressure equation, and then advance time step.

Conceptual procedure for the solution:

- (a) Predict flow velocity: $\underline{\bar{v}}$
- (b) Then determine the velocity adjustment $\delta \underline{\bar{v}}$ so that residue $\varepsilon = \nabla \cdot \underline{\bar{v}} \rightarrow 0$.

$$\text{That is, } \nabla \cdot (\underline{\bar{v}} + \delta \underline{\bar{v}}) = 0 \quad (51)$$

The residue ε can be thought as a fuction of pressure. Thus if we assume that ε becomes zero when the pressure p will be modified as $p + \delta p$, the following expression can be written.

$$\varepsilon(p + \delta p) = 0$$

- (c) Apply Taylor series expansion. Then the following equation can be obtained.

$$\varepsilon(p) + \delta p \frac{\partial \varepsilon}{\partial p} + \frac{(\delta p)^2}{2} \frac{\partial^2 \varepsilon}{\partial p^2} + \dots = 0 \quad (52)$$

By truncating the series on the right hand side of Eq. (52) at the first order term with respect to δp , Eq. (53) can be obtained.

$$\delta p = -\frac{\varepsilon}{(\partial \varepsilon / \partial p)} \quad (53)$$

Real procedure for the solution:

- (i) Descretize momentum equations.

There can be several ways for it.

$$\vec{v}^{n+1} = \vec{v}^n + \Delta t f(p^n, \vec{v}^n) \quad (54)$$

$$\vec{v}^{n+1} = \vec{v}^n + \Delta t f(p^{n+1}, \vec{v}^n) \quad (55)$$

$$\vec{v}^{n+1} = \vec{v}^n + \Delta t f(p^{n+1}, \vec{v}^{n+1})$$

(ii) Let us set $\underline{\vec{v}}$ for the predicted \vec{v} by Eq. (54). At this stage, $\underline{\vec{v}}$ does not satisfy the equation of continuity since Eq. (54) is a fully explicit type and possibly includes large errors. Then try to obtain difference between $\underline{\vec{v}}$ and \vec{v}^{n+1} (that is, the correct flow velocity) by subtracting Eq. (54) from Eq. (55).

$$\vec{v}^{n+1} = \vec{v}^n + \Delta t f(p^{n+1}, \vec{v}^n) \quad (55)$$

$$- \underline{\vec{v}} = \vec{v}^n + \Delta t f(p^n, \vec{v}^n) \quad (54)$$

$$\vec{v}^{n+1} - \underline{\vec{v}} = \Delta t (f(p^{n+1}, \vec{v}^n) - f(p^n, \vec{v}^n)) \quad (56)$$

Since the principal part of the right hand side of Eq. (56) can be thought to be a function of pressure, the function f may be approximated with spacial gradient of pressure p and then the following equation can be obtained.

$$\vec{v}^{n+1} - \underline{\vec{v}} = -\Delta t (\nabla p^{n+1} - \nabla p^n) / \rho \quad (57)$$

where ρ is density of the fluid.

(iii) Take Laplacian of Eq. (57) and consider the relation $\nabla \cdot \vec{v}^{n+1} = 0$, then Eq. (58) can be obtained.

$$-\nabla \cdot \underline{\vec{v}} = -\frac{\Delta t}{\rho} \nabla^2 \delta p \quad (58)$$

where $\delta p = p^{n+1} - p^n$. By rewriting Eq. (58), Eq. (59) for δp can be derived.

$$\nabla^2 \delta p = \rho \nabla \cdot \underline{\vec{v}} / \Delta t \quad (59)$$

(iv) Apply centered difference for the left hand side of Eq. (59) and assume superiority of the diagonal terms in the resultant coefficient matrix, then the following equation can be obtained.

$$\delta p = - \frac{\rho \omega \varepsilon}{2\Delta t \left(\frac{1}{\Delta x^2} + \frac{1}{\Delta y^2} + \frac{1}{\Delta z^2} \right)} \quad (60)$$

where ω is a coefficient to accerelate convergence of the iterative procedure, and ranges $1 \leq \omega \leq 2$ where 1.7 is recommended. Again, note $\varepsilon = \nabla \cdot \underline{\vec{v}}$.

(v) Calculate velocity adjustment $\delta \underline{\vec{v}} (= \underline{\vec{v}}^{n+1} - \underline{\vec{v}}^n)$ by using Eq. (57) with δp of Eq. (60) being inserted into the right hand side.

$$\delta \underline{\vec{v}} = - \frac{\Delta t}{\rho} \nabla \delta p \quad (61)$$

Eq. (61) can be implemented on the MAC mesh as follows:

$$\begin{aligned} \delta u_{i+1/2,j,k} &= -\Delta t(\delta p_{i+1} - \delta p_i)/(\rho \Delta x), & \delta u_{i-1/2,j,k} &= -\Delta t(\delta p_i - \delta p_{i-1})/(\rho \Delta x) \\ \delta v_{i,j+1/2,k} &= -\Delta t(\delta p_{j+1} - \delta p_j)/(\rho \Delta y), & \delta v_{i,j-1/2,k} &= -\Delta t(\delta p_j - \delta p_{j-1})/(\rho \Delta y) \\ \delta w_{i,j,k+1/2} &= -\Delta t(\delta p_{k+1} - \delta p_k)/(\rho \Delta z), & \delta w_{i,j,k-1/2} &= -\Delta t(\delta p_k - \delta p_{k-1})/(\rho \Delta z) \end{aligned} \quad (62)$$

(vi) After the calculation of the velocity adjustment in Eq. (62), again calculate pressure adjustment δp by Eq. (60), and then recalculate $\delta \underline{\vec{v}}$. This procedure will be repeated until the continuity equation will be satisfied, that is, $\varepsilon = \nabla \cdot \underline{\vec{v}} = 0$ is attained.

8.2.3 Errors associated with numerical solution of advection/diffusion equation

Even if a finite difference analog of a partial differential equation satisfies condition for the solution's convergence or stability, the solution can not avoid some numerical errors since usually arbitrarily small Δt and Δx can not be chosen because of limited computer resources such as computation time and memory size.

There are several numerical errors as listed below:

(1) Damping or amplitude error

When the amplitude factor G in the von Neumann's stability analysis (see Eq. 19) satisfies the relation of $|G| < 1$, the amplitude of the corresponding Fourier component decreases without any physical reason.

(2) Phase or dispersion error

In case of exact solution of advection equation (for example, Eq. 42) all the Fourier components of the solution are transported with the same velocity, while in the solution of a finite difference analog its Fourier components are carried with different speed depending on its wave length; hence spatial segregation occurs among different Fourier components of the solution resulting in fictitious dispersion. The longest wave component is transported with the correct velocity u .

(3) Aliasing error

Aliasing error occurs associated with numerical solution of non-linear equations such as Eqs. (42) and (44) with $\phi \equiv u$. In the calculation of these equations, energy defined by ϕ^2 is transferred from longer wave to shorter one. However in the numerical calculation the energy transferred to the shortest wave which is defined with grid size, i.e. wave length $2\Delta x$, goes again to the longest wave, and destroys the solution. This error is called "Aliasing error". In the real world the energy transferred to very short wave is dissipated by molecular viscosity. Aliasing error becomes serious for long time simulation such as several months' global scale flow simulation.

(4) Transportive property

Pure advection equation (Eq. 42) should not transport characteristics of the solution to upwind direction. However some numerical schemes violate this rule, and they are called not to have "transportive property". For example, the popular FTCS (Forward Time Centered Space) method does not have this property, while upwind method retains this nature.

(5) Conservative property

Some numerical methods do not preserve total quantity (mass, energy etc.) in

calculation domain. For example, the FTCS does not preserve it when the method is applied to advection form equation such as Eq. (40). The scheme which preserves this quantity is called to have “conservative property”.

8.2.4 Explicit methods

When unsteady equations such as Eqs. (42), (43), and (44) are discretized, there are two types of methods, that is, explicit and implicit methods.

The largest advantage of explicit methods is that they do not require solution of a set of algebraic equations to advance calculation by one time step. In particular, they are very much useful when non-linear equation has to be numerically integrated for long time in a large calculation domain. Disadvantage of the method is that sometimes very severe condition is placed on time step and spatial grid size to obtain stable solution. Especially rapidly changing flow field, existence of locally strong emission source, and very fast chemical reaction tend to limit the use of explicit methods.

(1) Forward Time Centered Space method

This method discretizes unsteady partial differential equation using forward difference for time derivative and centered difference for spatial derivative which is evaluated at time t_n , and is one of the simplest methods. The truncation error is

$O(\Delta t, (\Delta x)^2)$. Eq. (42) can be approximated with FTCS as follows:

$$\Phi_i^{n+1} = \Phi_i^n - \frac{C}{2}(\Phi_{i+1}^n - \Phi_{i-1}^n) \quad (63)$$

where $C = u\Delta t / \Delta x$ is an important dimensionless number called as Courant number. It can be shown that Eq. (63) gives unconditionally unstable solution.

Similarly FTCS can be applied to Eq. (43) as:

$$\Phi_i^{n+1} = \Phi_i^n + d(\Phi_{i+1}^n - 2\Phi_i^n + \Phi_{i-1}^n) \quad (64)$$

where $d = K\Delta t / (\Delta x)^2$ is the “diffusion number” and another important dimensionless number. By the von Neumann’s method, an amplification factor G for Eq. (64) can be obtained as Eq. (65).

$$G = 1 - 2d(1 - \cos \theta) \quad (65)$$

For stability of the solution, $|G| \leq 1$ has to be held for any θ . Hence the following condition should be satisfied.

$$d \leq \frac{1}{2} \quad \text{or} \quad \Delta t \leq \frac{1}{2} \frac{\Delta x^2}{K} \quad (66)$$

Fig. 3 shows temporal change of the temperature, that is, solution of Eq. (64) for one dimensional heat conduction problem (ϕ as temperature in Eq. 43). Initial temperature distribution is given by a triangle with the highest temperature at the center of the region ($0 \leq x \leq \pi$), and temperatures are fixed at 0 at both ends of the region (that is, Dirichlet condition in Eq. 15 in chapter 1). Fig. 3a stands for the solution when the stability condition Eq. (66) is satisfied, while Figs. 3b, c, d are for the case that the condition is not satisfied. Fig. 3 clearly demonstrates that the solution with $d > 1/2$ diverges with time while it with $d < 1/2$ leads to correct solution.

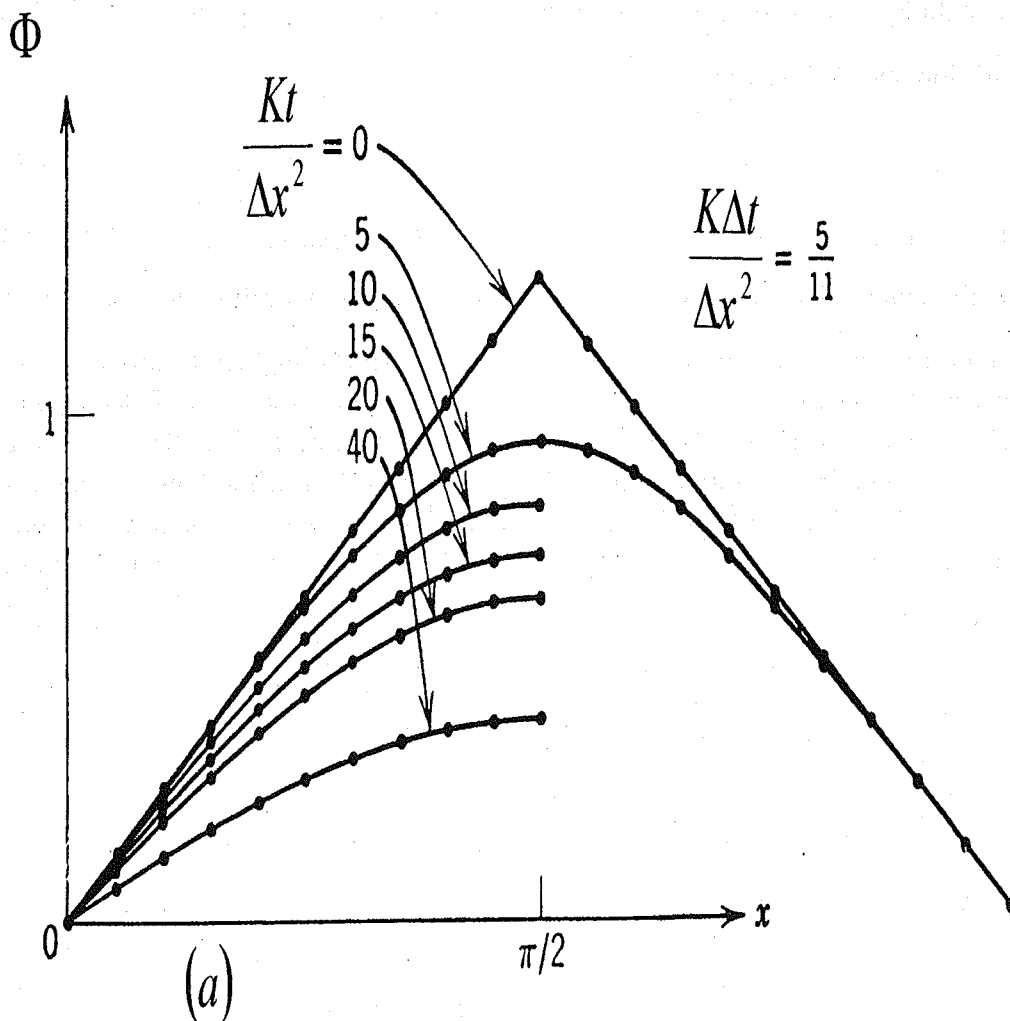


Figure 3(a). Temporal change of the solution of Eq. (64) with $d < 1.2$ being satisfied, that is $d = K\Delta t/\Delta x^2 = 5/11$.

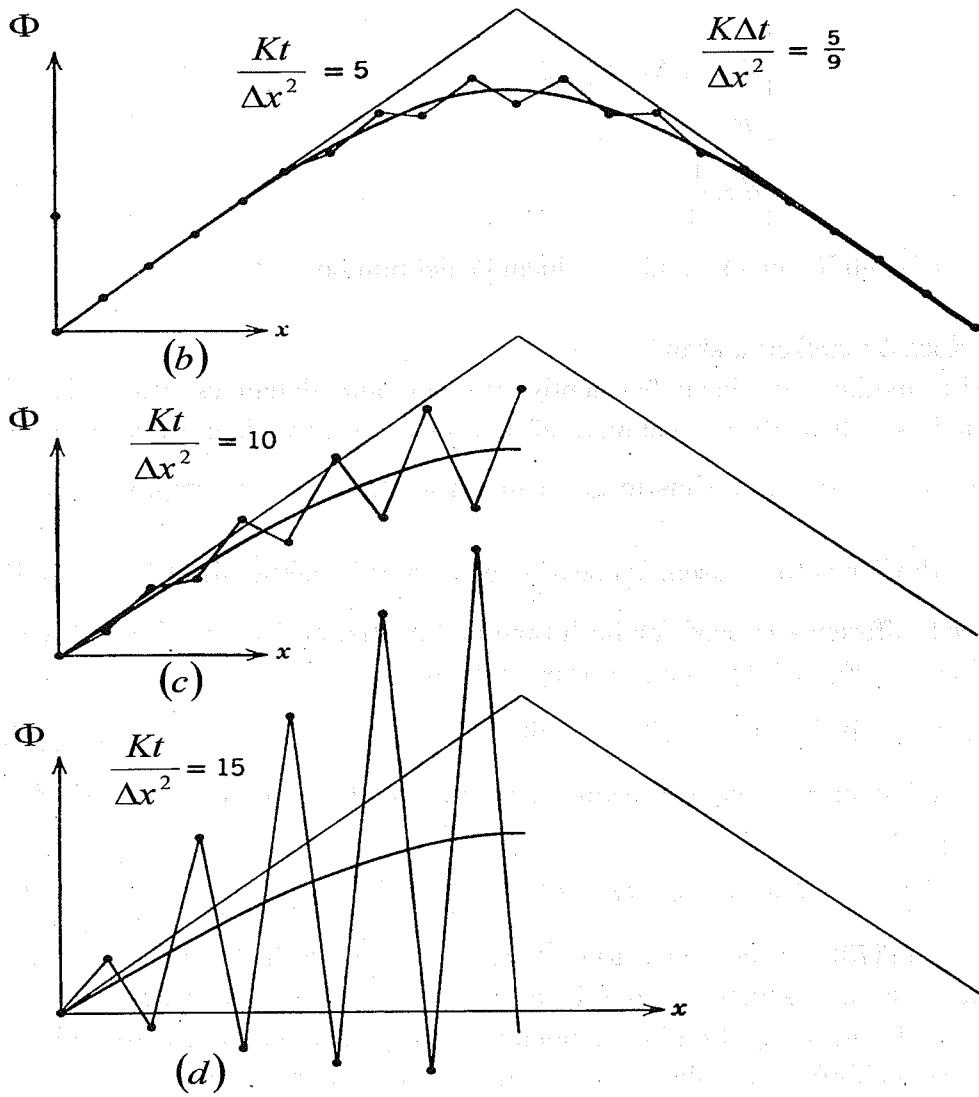


Figure 3(b), (c), (d). Same as in Fig. 3(a) but for $d > 1/2$, that is, $d = 5/9$.

FTCS scheme for Eq. (44) can be written as follows:

$$\Phi_i^{n+1} = \Phi_i^n + \left\{ -\frac{C}{2}(\Phi_{i+1}^n - \Phi_{i-1}^n) + d(\Phi_{i+1}^n - 2\Phi_i^n + \Phi_{i-1}^n) \right\} \quad (67)$$

Stability condition for Eq. (67) can be derived as Eq. (68) by following to the von Neumann's analysis.

$$\left\{ \begin{array}{l} R_c = |u\Delta x / K| \leq 2 \\ \text{and} \\ d \leq \frac{1}{2} \end{array} \right. \quad (68)$$

where R_c is cell Reynolds number or local Peclet number.

(2) Midpoint leapfrog method

This method has been frequently used in fluid dynamics calculation. The scheme is so called "three level method" and includes variable at three time points such as t_{n-1}, t_n , and t_{n+1} . Thus to get solution at the first time step, another "two level method" has to be used. Truncation error of this method is $O((\Delta t)^2, (\Delta x)^2)$. Centered difference is used for both time and spatial derivatives. Eq. (42) can be discretized as Eq. (69) by using leapfrog method.

$$\Phi_i^{n+1} = \Phi_i^{n-1} - C(\Phi_{i+1}^n - \Phi_{i-1}^n) \quad (69)$$

From stability analysis using the von Neumann's method, the solution of Eq. (69) is stable only for

$$\text{Courant number } |C| \leq 1 \quad (70)$$

The relation (70) is often said as the CFL (Courant-Friedrichs-Lewy) condition.

The scheme which is obtained by applying the leapfrog method to advection-diffusion equation (44) is unconditionally unstable. Hence, to avoid this a method called "DuFort-Frankel Leapfrog" has been invented as Eq. (71).

$$\Phi_i^{n+1} = \Phi_i^{n-1} - C(\Phi_{i+1}^n - \Phi_{i-1}^n) + 2d \left\{ \Phi_{i+1}^n - \underbrace{(\Phi_i^{n+1} + \Phi_i^{n-1})}_* + \Phi_{i-1}^n \right\} \quad (71)$$

Eq. (71) can be regarded as a scheme in which a part of diffusion term discretized with centered difference, $2\Phi_i^n$, is replaced with $\Phi_i^{n+1} + \Phi_i^{n-1}$. By this treatment, the scheme becomes conditionally stable, and the condition to be satisfied is Courant number $|C| \leq 1$.

(3) Up-wind method

As already described, FTCS analog, Eq. (67), of advection-diffusion equation (44) is required for its stable solution to satisfy the condition of $|u\Delta x/K| \leq 2$ (see Eq. 68). This constraint can be severe limitation for implementation of the solution; for example, in case of fast flow situation. Up-wind scheme was invented to avoid this limitation. One deficit of this method is that the method tends to introduce "false diffusion" called "artificial viscosity" into its solution when Courant number $|C| < 1$. Truncation error of this method is $O(\Delta t, \Delta x)$.

Up-wind scheme for pure advection equation Eq. (42) can be written as follows:

$$\Phi_i^{n+1} = \begin{cases} \Phi_i^n - C(\Phi_i^n - \Phi_{i-1}^n) & \text{for } u \geq 0 \\ \Phi_i^n - C(\Phi_{i+1}^n - \Phi_i^n) & \text{for } u < 0 \end{cases} \quad (72)$$

where $C \equiv u\Delta t / \Delta x$.

Artificial viscosity of Eq. (72) can be verified by taking Taylor series expansion of Φ_i^{n+1} and $\Phi_{i\pm 1}^n$ around Φ_i^n and substituting them into Eq. (72). The method is called Hirt's analysis. Now, let us think the case of $u \geq 0$. Substituting Taylor series expansion of Φ_i^{n+1} and Φ_{i-1}^n into Eq. (72) for $u \geq 0$ and rearranging the resultant equation leads to Eq. (73).

$$\frac{\partial \phi}{\partial t} = -u \frac{\partial \phi}{\partial x} + \frac{u\Delta x}{2} \frac{\partial^2 \phi}{\partial x^2} - \frac{\Delta t}{2} \frac{\partial^2 \phi}{\partial t^2} + \text{higher order terms} \quad (73)$$

Taking the relation $\frac{\partial^2 \phi}{\partial t^2} = u^2 \frac{\partial^2 \phi}{\partial x^2}$ into account, Eq. (73) can be rewritten as follows:

$$\frac{\partial \phi}{\partial t} = -u \frac{\partial \phi}{\partial x} + K_e \frac{\partial^2 \phi}{\partial x^2} + \text{higher order terms} \quad (74)$$

$$K_e \equiv u\Delta x(1 - C)/2 \quad (75)$$

where K_e is called “artificial viscosity”. This means that the up-wind scheme Eq. (72) actually solves Eq. (74), which is an advection-diffusion equation with artificial viscosity K_e , instead of pure advection equation, Eq. (42). Eq. (75) suggests Eq. (72) can give exact solution when Courant number $C=1$.

(4) Leith method

This method with its truncation error $O(\Delta t^2, \Delta x^2)$ does not have artificial viscosity when applied to Eq. (42). It can be regarded as a method into which an artificial diffusion term is added so that it cancels the “artificial viscosity”. This method equals to Lax-Wendorff method for constant u . For Eq. (42), Leith method gives following scheme.

$$\Phi_i^{n+1} = \Phi_i^n - \frac{C}{2}(\Phi_{i+1}^n - \Phi_{i-1}^n) + \underbrace{\frac{C^2}{2}(\Phi_{i+1}^n - 2\Phi_i^n + \Phi_{i-1}^n)}_{(*)} \quad (76)$$

Eq. (76) can be obtained as follows. First, take Taylor series expansion of Φ_i^{n+1} as Eq. (77).

$$\phi_i^{n+1} = \phi_i^n + \Delta t \left(\frac{\partial \phi}{\partial t} \right)_i^n + \frac{1}{2} \Delta t^2 \left(\frac{\partial^2 \phi}{\partial t^2} \right)_i^n + O(\Delta t^3) \quad (77)$$

Then, replace $\frac{\partial \phi}{\partial t}$ and $\frac{\partial^2 \phi}{\partial t^2}$ in Eq. (77) with Eq. (42) and Eq. (78) which can be derived from Eq. (42).

$$\frac{\partial^2 \phi}{\partial t^2} = -u \frac{\partial^2 \phi}{\partial t \partial x} = -u \frac{\partial}{\partial x} \left(\frac{\partial \phi}{\partial t} \right) = u^2 \frac{\partial^2 \phi}{\partial x^2} \quad (u = \text{constant}) \quad (78)$$

Thus, the following equation can be obtained.

$$\phi_i^{n+1} = \phi_i^n - u \Delta t \left(\frac{\partial \phi}{\partial x} \right)_i^n + \frac{1}{2} u^2 \Delta t^2 \left(\frac{\partial^2 \phi}{\partial x^2} \right)_i^n + O(\Delta t^3) \quad (79)$$

Finally, applying centered difference to the 2nd and 3rd terms on the right hand side in Eq. (79) results in Eq. (76). The stability condition for Eq. (76) is the same to

up-wind scheme (72), that is, $|C| \leq 1$.

Hirt's analysis can show Eq. (76) is analog of the original advection equation Eq. (42).

Leith method can be applied to two (and three) dimensional problem by using a concept of "fractional time steps". Let us think the following two-dimensional equation.

$$\frac{\partial \phi}{\partial t} = -u \frac{\partial \phi}{\partial x} - v \frac{\partial \phi}{\partial y} \quad (80)$$

Leith used Eq. (81) for x and (82) for y direction. To advance calculation by one time step, first solve Eq. (81) to cover whole domain, and then Eq. (82) based on the solution by Eq. (81).

$$\Phi_{ij}^{n+1/2} = \Phi_{ij}^n - \frac{1}{2} C_x \delta_x \Phi_{ij}^n + \frac{1}{2} C_x^2 \delta_x^2 \Phi_{ij}^n \quad (81)$$

$$\Phi_{ij}^{n+1} = \Phi_{ij}^{n+1/2} - \frac{1}{2} C_y \delta_y \Phi_{ij}^{n+1/2} + \frac{1}{2} C_y^2 \delta_y^2 \Phi_{ij}^{n+1/2} \quad (82)$$

Conditions for stability are $|C_x| \leq 1$ for Eq. (81) and $|C_y| \leq 1$ for Eq. (82).

(5) Fromm method: zero average phase error method

From combined schemes of leading phase error and lagging phase error to give a method which has zero average phase error. For Eq. (42), Fromm method gives Eq. (83) with its truncation error $O(\Delta t^2, \Delta x^2)$. Condition for stability of this scheme is $|C| \leq 1$.

$$\begin{aligned} \Phi_i^{n+1} = \Phi_i^n + \frac{C}{4} (\Phi_{i-1}^n - \Phi_{i+1}^n + \Phi_{i-2}^n - \Phi_i^n) + \frac{C^2}{4} (\Phi_{i-1}^n - 2\Phi_i^n + \Phi_{i+1}^n) \\ + \frac{C^2 - 2C}{4} (\Phi_{i-2}^n - 2\Phi_{i-1}^n + \Phi_i^n) \end{aligned} \quad (83)$$

Eq. (83) can be derived as follows. First, form a leading phase error scheme by using Leith method.

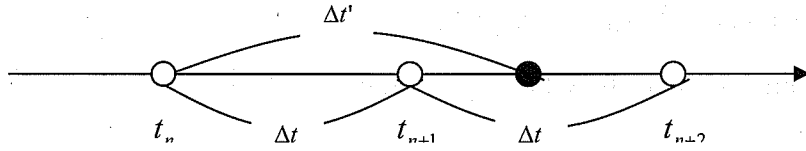


Figure 4. Time points used for derivation of a leading phase error scheme. Black circle denotes a hypothetical time point at which $u\Delta t'/\Delta x = 1$ is satisfied starting from time point t_n .

In Fig. 4, let Δt be a real time step, and let $\Delta t'$ be a hypothetical time step to satisfy $u\Delta t'/\Delta x = 1$. Take Taylor series expansion of $\phi_i^{t_n+\Delta t}$ around $\phi_i^{t_n+\Delta t'}$.

$$\phi_i^{t_n+\Delta t} = \phi_i^{t_n+\Delta t'} + (\Delta t - \Delta t') \left(\frac{\partial \phi}{\partial t} \right)_i^{t_n+\Delta t'} + \frac{(\Delta t - \Delta t')^2}{2} \left(\frac{\partial^2 \phi}{\partial t^2} \right)_i^{t_n+\Delta t'} + O((\Delta t - \Delta t')^3) \quad (84)$$

Rewrite Eq. (84) by using the following relations:

$$\left(\frac{\partial \phi}{\partial t} \right)_i^{t_n+\Delta t'} = \left(-u \frac{\partial \phi}{\partial x} \right)_i^{t_n+\Delta t'} \left(\frac{\partial^2 \phi}{\partial t^2} \right)_i^{t_n+\Delta t'} = \left(u^2 \frac{\partial^2 \phi}{\partial x^2} \right)_i^{t_n+\Delta t'}$$

Then apply centered difference for $\frac{\partial \phi}{\partial x}$ and $\frac{\partial^2 \phi}{\partial x^2}$ in the resultant equation. Finally,

Eq. (3-85) can be obtained by considering $u\Delta t'/\Delta x = 1$ and $C \equiv u\Delta t/\Delta x$.

$$\Phi_i^{t_n+\Delta t} = \Phi_i^{t_n+\Delta t'} - \frac{(C-1)}{2} (\Phi_{i+1}^{t_n+\Delta t'} - \Phi_{i-1}^{t_n+\Delta t'}) + \frac{(C-1)^2}{2} (\Phi_{i+1}^{t_n+\Delta t'} - 2\Phi_i^{t_n+\Delta t'} + \Phi_{i-1}^{t_n+\Delta t'}) \quad (85)$$

Here we consider $\phi_{i+1}^{t_n+\Delta t'} = \phi_i^n$ and $\phi_{i-1}^{t_n+\Delta t'} = \phi_{i-2}^n$. Then Eq. (85) can be written as

$$\Phi_i^{n+1} = \Phi_{i-1}^n - \frac{(C-1)}{2} (\Phi_i^n - \Phi_{i-2}^n) + \frac{(C-1)^2}{2} (\Phi_i^n - 2\Phi_{i-1}^n + \Phi_{i-2}^n) \quad (86)$$

Eq. (86) has leading phase error, while the original Leith scheme (76) has lagging phase error. Fromm's scheme (83) is formed by averaging Eq. (85) and (86).

Fig. 5 schematically shows leading and lagging phase errors.

Fromm method can be extended to multi-dimensional case in a manner similar to Leith method, that is, fractional time steps.

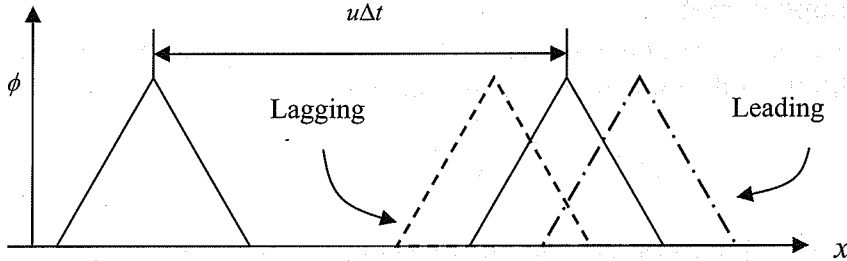


Figure 5. Schematic explanation of leading and lagging phase errors.

8.2.5 Implicit method

Let us explain explicit and implicit methods by using Eq. (43) as an example.

$$\frac{\partial \phi}{\partial t} + \frac{\partial(u\phi)}{\partial x} - K \frac{\partial^2 \phi}{\partial x^2} = 0 \quad (43)$$

Let time derivative in Eq. (43) discretize with forward time difference. Then, difference analog of Eq. (43) can be classified into explicit or implicit method depending on the time point for evaluation of the other spatial derivatives. Both explicit and implicit methods may be expressed in one equation as follows:

$$\frac{\phi_i^{n+1} - \phi_i^n}{\Delta t} = \alpha \left[-\frac{\partial(u\phi)}{\partial x} + K \frac{\partial^2 \phi}{\partial x^2} \right]_i^n + (1 - \alpha) \left[-\frac{\partial(u\phi)}{\partial x} + K \frac{\partial^2 \phi}{\partial x^2} \right]_i^{n+1} \quad (87)$$

Eq. (87) becomes explicit method when $\alpha=1$ and implicit method when $0 \leq \alpha < 1$. As can be seen in this equation, implicit method must solve a set of algebraic equations to advance calculation by one time step, suggesting larger computation load. Implicit method usually gives stable solution; there are no conditions placed for the solution's stability if effect of boundary condition is negligible; even if there is influence of boundary condition, restrictions to be satisfied for the stable solution are generally not severe. Theoretical deficit of the implicit method is that it transfers any change occurred at one place throughout the whole calculation domain with infinite speed. This is incorrect in the real world since the media such as atmosphere, ocean, and earth's solid shell do not allow such a phenomenon.

Practically, however, this is often not the problem since the change transferred far from the original place with short time such as one time step is usually negligibly small.

(1) Fully implicit method

This method corresponds to Eq. (87) with $\alpha=0$. For example, Eq. (40) can be written with the fully implicit method as follows:

$$\Phi_i^{n+1} = \Phi_i^n - u\Delta t \frac{(\delta\Phi)_i^{n+1}}{2\Delta x} \quad (88)$$

where centered difference (see Eq. 2) is used for spatial derivative. Eq. (88) can be expressed as follows:

$$-\frac{C}{2}\Phi_{i-1}^{n+1} + \Phi_i^{n+1} + \frac{C}{2}\Phi_{i+1}^{n+1} = \Phi_i^n \quad (89)$$

The von Neumann's method gives the amplification factor G of Eq. (89) as Eq. (90), thus indicating Eq. (89) is unconditionally stable.

$$|G|^2 = \frac{1}{1 + C^2 \sin^2 \theta} \leq 1 \quad (\theta = k_x \Delta x) \quad (90)$$

Similarly, fully implicit difference analog of the diffusion equation (43) is given by Eq. (91).

$$\Phi_i^{n+1} = \Phi_i^n + K\Delta t \frac{(\delta^2\Phi)_i^{n+1}}{(\Delta x)^2} \quad (91)$$

The amplification factor G of Eq. (91) is written as Eq. (92), and again Eq. (91) is unconditionally stable.

$$G = \frac{1}{1 + 2d(1 - \cos \theta)} \leq 1 \quad (92)$$

(2) Crank-Nicolson method

The well-known Crank-Nicolson method is derived by specifying $\alpha = 1/2$ in Eq. (87), and the resultant scheme has a truncation error of $O((\Delta x)^2, (\Delta t)^2)$. When the method is applied to Eq. (40), the following Eq. (93) is obtained.

$$\Phi_i^{n+1} = \Phi_i^n - \frac{u\Delta t}{2} \left[\frac{(\delta\Phi)_i^n}{2\Delta x} + \frac{(\delta\Phi)_i^{n+1}}{2\Delta x} \right] \quad (93)$$

Eq. (93) can be rewritten as Eq. (94).

$$-\frac{C}{4}\Phi_{i-1}^{n+1} + \Phi_i^{n+1} + \frac{C}{4}\Phi_{i+1}^{n+1} = \frac{C}{4}\Phi_{i-1}^n + \Phi_i^n - \frac{C}{4}\Phi_{i+1}^n \quad (94)$$

The amplification factor G of this scheme is derived by the von Neumann's method as Eq. (95).

$$G = \frac{1 - \frac{C^2}{4}\sin^2\theta - C\sin\theta \cdot I}{1 + \frac{C^2}{4}\sin^2\theta} \quad (I = \sqrt{-1}) \quad (95)$$

where Courant number is $C = u\Delta t/\Delta x$. From Eq. (95), the relation of $|G|^2 = 1$ can be derived, and thus Eq. (95) is unconditionally stable.

The Crank-Nicolson analog of Eq. (43) can similarly be derived as Eq. (96).

$$-\frac{d}{2}\Phi_{i-1}^{n+1} + (1+d)\Phi_i^{n+1} - \frac{d}{2}\Phi_{i+1}^{n+1} = \frac{d}{2}\Phi_{i-1}^n + (1-d)\Phi_i^n + \frac{d}{2}\Phi_{i+1}^n \quad (96)$$

The von Neumann's stability analysis gives the following amplification factor G for Eq. (96).

$$G = \frac{1 - d(1 - \cos\theta)}{1 + d(1 - \cos\theta)} \quad (97)$$

From this equation, we can see unconditionally stable nature of Eq. (96) since the relation $|G| \leq 1$ holds. However, in case of large Δt some Fourier components

possibly overshoot and then oscillate. For example, when $d(= K\Delta t/(\Delta x)^2) \leq \frac{1}{2}$ is

not satisfied, it can be known by eye-inspection that the smallest wave length component (wave length, $\Lambda = 2\Delta x$) overshoots. For the wave length of $\Lambda = 2\Delta x$,

its wave number is $k_x = \frac{2\pi}{2\Delta x}$, and then $\cos\theta = -1$ since $\theta = k_x\Delta x = \pi$. Thus the

numerator is $1 - 2d$, and G in Eq. (97) is negative for $d > \frac{1}{2}$.

(3) A combined expression of fully implicit, Crank-Nicolson, and FTCS for a diffusion equation Eq. (43)

Similar to Eq. (87), fully implicit, Crank-Nicolson, explicit methods applied to Eq. (43) give the following equation.

$$\frac{\phi_i^{n+1} - \phi_i^n}{\Delta t} = (1 - \alpha) \left[K \frac{(\delta^2 \phi)_i^n}{(\Delta x)^2} \right] + \alpha \left[K \frac{(\delta^2 \phi)_i^{n+1}}{(\Delta x)^2} \right] \quad (98)$$

where $\alpha = 0$ for FTCS, $\alpha = 1/2$ for Crank-Nicolson, and $\alpha = 1$ for fully implicit.

Characteristics of these three methods can be illustrated as in Fig. 6 where solutions by these methods are schematically shown for $t_n \sim t_{n+1}$.

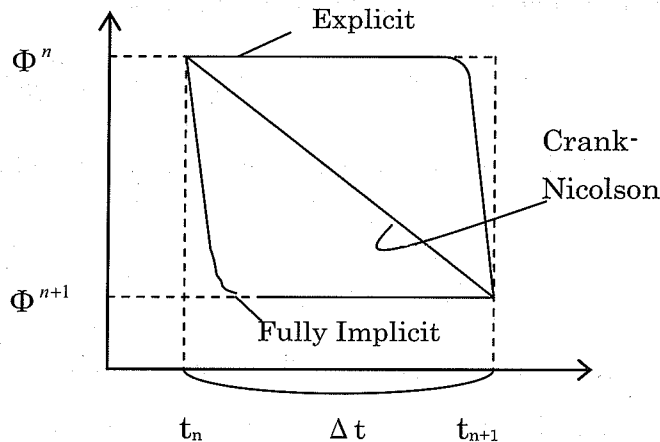


Figure 6. Schematic illustration on the characteristics of explicit, Crank-Nicolson, and fully implicit.

Let us assume Φ as temperature, and Eq. (43) represents one dimensional heat conduction problem. If we think time-varying heat conduction phenomenon, it is usually observed that the temperature changes rapidly at first and then gradually. This indicates that temporal change of the variable calculated with "Fully Implicit

Method" shown in Fig. 6 is closer to the observation, and thus more appropriate, suggesting the order of truncation is not necessarily dominant factor for selection of numerical method (Patankar, 1980); for example, note that the truncation error of the Crank-Nicolson method, Eq. (98) with $\alpha = 1/2$, is $O((\Delta x)^2, (\Delta t)^2)$, while that of fully implicit, Eq. (98) with $\alpha = 1$, is $O((\Delta x)^2, \Delta t)$.

(4) Multi-step method for implicit scheme – Predictor-corrector method

A class of methods to avoid the difficulty that a set of algebraic equations has to be solved simultaneously with keeping some advantages of implicit method is used.

(a) Matsuno's method or Euler-backward scheme

The Matsuno's method approximates fully implicit method with following two steps: each step is calculated explicitly. For example, Eq. (88) is implemented with the Matsuno's treatment as follows:

$$\left. \begin{aligned} \Phi_i^{n+1*} &= \Phi_i^n - (u \Delta t) \frac{(\delta \Phi)_i^n}{2 \Delta x} \\ \Phi_i^{n+1} &= \Phi_i^n - (u \Delta t) \frac{(\delta \Phi)_i^{n+1*}}{2 \Delta x} \end{aligned} \right\} \quad (99)$$

If variables at extra time point $(n+1^*)$ are eliminated from Eq. (99), the following equation can be derived.

$$\Phi_i^{n+1} = \Phi_i^n - \frac{C}{2} (\Phi_{i+1}^n - \Phi_{i-1}^n) + \left(\frac{C}{2} \right)^2 (\Phi_{i+2}^n + \Phi_{i-2}^n - 2\Phi_i^n) \quad (100)$$

The von Neumann stability analysis requires the same condition for both Eqs. (99) and (100), that is, $|C| \leq 1$. One advantage of Eq. (99) is that it can be applied at grid points by one grid inside the domain, while Eq. (100) is not. This method is also known to suppress temporal development of high frequency noise and is often used for long term integration of meteorological dynamics. The method's truncation error is $O(\Delta t, \Delta x^2)$. As can be seen in the third term on the right hand side in Eq.

(100), the method also has artificial viscosity $(C/2)^2$ which is a function of Δt and tends to be small with decreased time step. This method is also expanded to advection-diffusion equation (44) as follows:

$$\left. \begin{aligned} \Phi_i^{n+1*} &= \Phi_i^n - \frac{C}{2}(\Phi_{i+1}^n - \Phi_{i-1}^n) + d(\Phi_{i+1}^n + \Phi_{i-1}^n - 2\Phi_i^{n+1*}) \\ \Phi_i^{n+1} &= \Phi_i^n - \frac{C}{2}(\Phi_{i+1}^{n+1*} - \Phi_{i-1}^{n+1*}) + d(\Phi_{i+1}^{n+1*} + \Phi_{i-1}^{n+1*} - 2\Phi_i^{n+1}) \end{aligned} \right\} \quad (101)$$

(b) 2nd order Runge Kutta scheme

This method can be applied to Eq. (40) as follows.

$$\left. \begin{aligned} \Phi_i^{n+1*} &= \Phi_i^n - (u \Delta t) \frac{(\delta \Phi)_i^n}{2 \Delta x} \\ \Phi_i^{n+1} &= \Phi_i^n - \frac{(u \Delta t)}{\alpha + \beta} \left\{ \alpha \frac{(\delta \Phi)_i^n}{2 \Delta x} + \beta \frac{(\delta \Phi)_i^{n+1*}}{2 \Delta x} \right\} \end{aligned} \right\} \quad (102)$$

where $\alpha + \beta = 1$. When $\alpha = \beta = \frac{1}{2}$, Eq. (102) is called as a simplified Runge Kutta method or Heun method, which shows weakly unstable nature with an amplification factor $G = 1 + O(\Delta t^2)$.

8.2.5 Fractional Steps Method or Alternative Direction Method

A class of fractional-steps' methods has been developed to efficiently calculate multi-dimensional problems. The fractional steps' methods are multi-steps method, and usually consist of many one-dimensional equations which are obtained by decomposition of the original equation.

ADI (Alternating Direction Implicit), LOD (Locally One Dimensional), and component-by-component splitting method are prominent in this group.

(1) ADI methods

Since a paper by Peaceman & Rachford (1955), several methods are proposed on ADI methods. It is expected that they have two advantages of (1) unconditionally stable nature of implicit method and (2) reduction in computation time due to decomposition of the problem to one-dimensional equations. Let us take the following multi-dimensional diffusion equations as examples.

$$\frac{\partial \phi}{\partial t} = \frac{\partial^2 \phi}{\partial x^2} + \frac{\partial^2 \phi}{\partial y^2} \quad (103)$$

$$\frac{\partial \phi}{\partial t} = \frac{\partial^2 \phi}{\partial x^2} + \frac{\partial^2 \phi}{\partial y^2} + \frac{\partial^2 \phi}{\partial z^2} \quad (104)$$

Before discussing ADI methods, let us take a look at one-dimensional but general linear partial differential equation as Eq. (105).

$$\frac{\partial \phi}{\partial t} = L(x, t, D, D^2)\phi \quad (105)$$

where L denotes linear operator, and $D \equiv \partial/\partial x$. Now take a Taylor series expansion

of ϕ_i^{n+1} , use Eq. (105) with centered space difference approximation of partial derivatives with respect to x such as $D = \frac{2}{\Delta x} \sinh^{-1} \frac{\delta_x}{2}$ (Hildebrand, 1974), and then Eq. (106) can be obtained. Eq. (106) is a general form of two-level scheme.

$$\begin{aligned} \phi_i^{n+1} &= \left(1 + \Delta t \frac{\partial}{\partial t} + \frac{1}{2} (\Delta t)^2 \frac{\partial^2}{\partial t^2} + \dots\right) \phi_i^n \\ &= \exp\left(\Delta t \frac{\partial}{\partial t}\right) \phi_i^n \\ &= \exp(\Delta t L) \phi_i^n \\ &= \exp\left[\Delta t L \left(i\Delta x, n\Delta t, \frac{2}{\Delta x} \sinh^{-1} \frac{\delta_x}{2}, \left(\frac{2}{\Delta x} \sinh^{-1} \frac{\delta_x}{2}\right)^2\right)\right] \phi_i^n \end{aligned} \quad (106)$$

Furthermore, it should be noted the following relations hold (Hildebrand, 1974):

$$D = \frac{2}{\Delta x} \sinh^{-1} \frac{\delta_x}{2} = \frac{1}{\Delta x} \left(\delta - \frac{1^2}{2^2 3} \delta^3 + \frac{1^2 3^2}{2^4 5} \delta^5 - \dots \right) \approx \frac{\delta}{\Delta x} \quad (107)$$

$$D^2 = \left(\frac{2}{\Delta x} \sinh^{-1} \frac{\delta_x}{2} \right)^2 = \frac{1}{(\Delta x)^2} \left(\delta - \frac{1^2}{2^2 3} \delta^3 + \frac{1^2 3^2}{2^4 5} \delta^5 - \dots \right)^2 \approx \frac{\delta^2}{(\Delta x)^2} \quad (108)$$

where δ denotes centered difference operator (see Eq. 2).

(a) Derivation of ADI scheme

Following to Eq. (106), Eq. (103) can be rewritten as Eq. (109).

$$\phi_{i,j}^{n+1} = \exp(\Delta t (D_x^2 + D_y^2)) \phi_{i,j}^n \quad (109)$$

where $D_x \equiv \frac{\partial}{\partial x}$ and $D_y \equiv \frac{\partial}{\partial y}$. By taking exponential function in Eq. (109) as a usual one, Eq. (109) can be rewritten as Eq. (110).

$$\exp\left(-\frac{\Delta t}{2}(D_x^2 + D_y^2)\right)\phi_{i,j}^{n+1} = \exp\left(\frac{\Delta t}{2}(D_x^2 + D_y^2)\right)\phi_{i,j}^n \quad (110)$$

Now, rewrite differential operator D_x^2 etc. as $D_x^2 \cong \frac{1}{\Delta x^2} \delta_x^2$ etc. by using Eq. (108),

and then Eq. (110) can be written as Eq. (111) or (112).

$$\exp\left(-\left(\frac{\Delta t}{2(\Delta x)^2} \delta_x^2 + \frac{\Delta t}{2(\Delta y)^2} \delta_y^2\right)\right)\Phi_{i,j}^{n+1} = \exp\left(\frac{\Delta t}{2(\Delta x)^2} \delta_x^2 + \frac{\Delta t}{2(\Delta y)^2} \delta_y^2\right)\Phi_{i,j}^n \quad (111)$$

$$\exp\left(-\frac{\Delta t}{2(\Delta x)^2} \delta_x^2\right)\exp\left(-\frac{\Delta t}{2(\Delta y)^2} \delta_y^2\right)\Phi_{i,j}^{n+1} = \exp\left(\frac{\Delta t}{2(\Delta x)^2} \delta_x^2\right)\exp\left(\frac{\Delta t}{2(\Delta y)^2} \delta_y^2\right)\Phi_{i,j}^n \quad (112)$$

Take a Talyor series expansion of exponential functions in Eq. (112), and truncate the series after the 3rd term, and Eq. (113) can be obtained.

$$\left(1 - \frac{\Delta t}{2(\Delta x)^2} \delta_x^2\right)\left(1 - \frac{\Delta t}{2(\Delta y)^2} \delta_y^2\right)\Phi_{i,j}^{n+1} = \left(1 + \frac{\Delta t}{2(\Delta x)^2} \delta_x^2\right)\left(1 + \frac{\Delta t}{2(\Delta y)^2} \delta_y^2\right)\Phi_{i,j}^n \quad (113)$$

From Eq. (113), a typical ADI scheme can be deduced.

(b) Peaceman-Rachford scheme

By introducing hypothetical time point $n+1^*$, Peaceman-Rachford scheme can be obtained from Eq. (113).

$$\left(1 - \frac{1}{2} \frac{\Delta t}{(\Delta x)^2} \delta_x^2\right)\Phi_{ij}^{n+1^*} = \left(1 + \frac{1}{2} \frac{\Delta t}{(\Delta y)^2} \delta_y^2\right)\Phi_{ij}^n \quad (114a)$$

$$\left(1 - \frac{1}{2} \frac{\Delta t}{(\Delta y)^2} \delta_y^2\right)\Phi_{ij}^{n+1} = \left(1 + \frac{1}{2} \frac{\Delta t}{(\Delta x)^2} \delta_x^2\right)\Phi_{ij}^{n+1^*} \quad (114b)$$

Usually, $n+1^*$ is taken as $n + \frac{1}{2}$. The truncation error of this equation is

$$O(\Delta t^2, \Delta x^2).$$

Fig. 7 shows conceptual schematic for the calculation procedure by Eqs. (114a) and (114b).

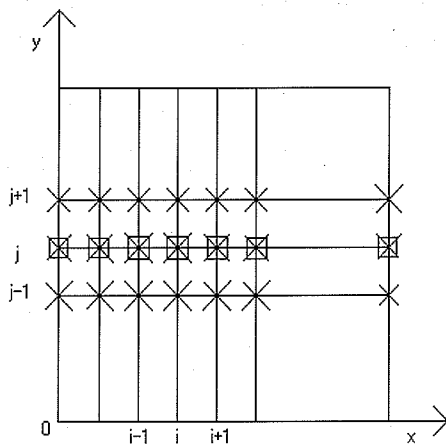


Figure 7a. One-dimensional calculation with Eq. (114a) for $t_n \leq t \leq t_{n+1/2}$. “ \square ” denotes unknown variable at $t_{n+1/2}$, and “ x ” known variable at t_n .

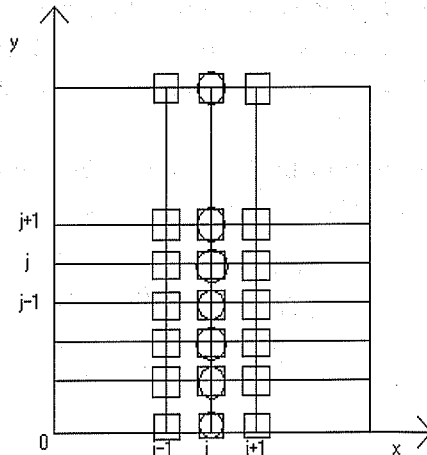


Figure 7b. Same as Fig. 3.7a but for Eq. (114b) for $t_{n+1/2} \leq t \leq t_{n+1}$. “ \circ ” denotes unknown variable at t_{n+1} , and “ \square ” known variable at $t_{n+1/2}$.

Peaceman and Rachford (1955) converted multi-dimensional problem into “multi” one dimensional problems, and by doing so they could successfully avoid large computational burden to solve a huge system of linear algebraic equations simultaneously with keeping desirable nature of unconditional stability of implicit method. Implicit treatment of one dimensional equation leads to a set of linear algebraic equations with a tri-diagonal matrix which can be quite easily solved. A computer code for the tri-diagonal matrix is added in the appendix.

Many other ADI methods such as D’Yakonov (1963), Douglas-Rachford (1956), etc. are prosed (Mitchell and Griffiths, 1980).

(2) LOD (locally One Dimensional) method or Component by component splitting-up method

This method splits any partial differential equation (PDE) in multi-dimensional space into several one dimensional equations, and then approximates them with finite difference analog etc. The procedure of derivation may look different from ADI methods. In reality, that these two groups of fractional steps methods, ADI and LOD, have very close relation will be shown here.

Formulation by LOD starts from splitting of original PDE into one-dimensional equations. For example, Eq. (103) is divided to two equations as follows:

$$\begin{cases} \frac{\partial \phi}{\partial t} = \frac{\partial^2 \phi}{\partial x^2} & \text{for } t_n \leq t \leq t_{n+1*} \\ \frac{\partial \phi}{\partial t} = \frac{\partial^2 \phi}{\partial y^2} & \text{for } t_{n+1*} \leq t \leq t_{n+1} \end{cases} \quad (115)$$

where $t_{n+1*} - t_n = t_{n+1} - t_{n+1*} = \Delta t$. When we discretizes Eq. (115) with Crank-Nicolson procedure, the following equations are obtained:

$$\left\{ \begin{aligned} \left(1 - \frac{1}{2} \frac{\Delta t}{(\Delta x)^2} \delta_x^2\right) \phi_{ij}^{n+1*} &= \left(1 + \frac{1}{2} \frac{\Delta t}{(\Delta x)^2} \delta_x^2\right) \phi_{ij}^n & \text{for } t_n \leq t \leq t_{n+1*} \\ \left(1 - \frac{1}{2} \frac{\Delta t}{(\Delta y)^2} \delta_y^2\right) \phi_{ij}^{n+1} &= \left(1 + \frac{1}{2} \frac{\Delta t}{(\Delta y)^2} \delta_y^2\right) \phi_{ij}^{n+1*} & \text{for } t_{n+1*} \leq t \leq t_{n+1} \end{aligned} \right. \quad (116a)$$

$$\left\{ \begin{aligned} \left(1 - \frac{1}{2} \frac{\Delta t}{(\Delta y)^2} \delta_y^2\right) \phi_{ij}^{n+1} &= \left(1 + \frac{1}{2} \frac{\Delta t}{(\Delta y)^2} \delta_y^2\right) \phi_{ij}^{n+1*} & \text{for } t_{n+1*} \leq t \leq t_{n+1} \end{aligned} \right. \quad (116b)$$

It should be noted that Eq. (116) can be derived from Eq. (113), as the ADI method Eq. (114), by introducing an intermediate time point t_{n+1*} though Eq. (116) was derived as the Crank-Nicolson analogs of the splitted equations Eq. (115). (When Eq. (116) is derived from Eq. (113), that the order of the operators δ_x^2 and δ_y^2 can be changed is assumed.) Eq. (116) is easier in calculation than Eq. (114), since each equation of Eq. (116) includes only one space variable operator and thus is purely one dimensional while Eq. (114) is not.

Similar to Fig. 7, the computation procedure of Eq. (116) can be illustrated as Fig. 8.

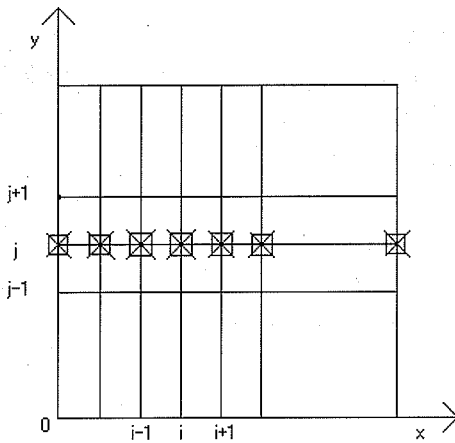


Figure 8a. One-dimensional calculation with Eq. (116a) for $t_n \leq t \leq t_{n+1*}$. “□” denotes unknown variable at t_{n+1*} , and “x” known variable at t_n .

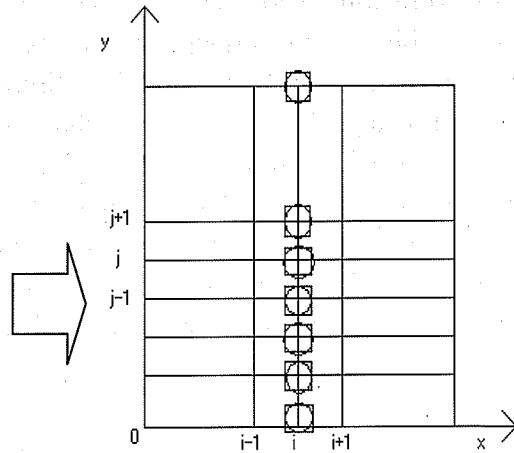


Figure 8b. Same as Fig. 8a but for Eq. (116b) for $t_{n+1*} \leq t \leq t_{n+1}$. “○” denotes unknown variable at t_{n+1} , and “□” known variable at t_{n+1*} .

By inspection of Figs. 7 and 8, difference between Eqs. (114) and (116) in their implementation is apparent.

8.2.7 Comparison of various numerical schemes

Various numerical methods for partial differential equations have been proposed, and numerical errors associated with them were discussed in 3.1.2 of this text. Yet it is still uncertain what kinds of deformation the errors introduce into a correct solution. Here we will visualize numerical solutions obtained with some numerical schemes. For the purpose, simple advection equation in one dimensional space, Eq. (40), will be used since its correct solution is simple and clear, that is, migration of initial distribution with constant flow velocity is the expected answer.

$$\frac{\partial \phi}{\partial t} + u \frac{\partial \phi}{\partial x} = 0 \quad (40)$$

Fig. 9a illustrates performance of 15 different numerical methods for the “sine” curve as its initial distribution and therefore correct solution (Carmichael, et al., 1980). In the experiment, Courant number was set at 0.5. The figure tells us the

order of truncation error is not necessarily only decisive factor, and also the scheme's stability is not enough for correct solution. In Fig. 9, CNG-L and CNG-C are not finite difference method but finite element method with the Galerkin method of linear (-L) and cubic (-C) shape functions and the Crank-Nicolson type treatment for time. Fromm, Egan & Mahony, and CNG-L and -C appear as desirable methods. (It may be noted that when the noted that the 1st upwind difference should give exact solution if the Courant number is 1.) Fig. 9b shows results of the same test as Fig. 9a but for initial distribution of square wave. The square wave test is more severe than the sine wave. However, performance of each method is quite similar to Fig. 9a.

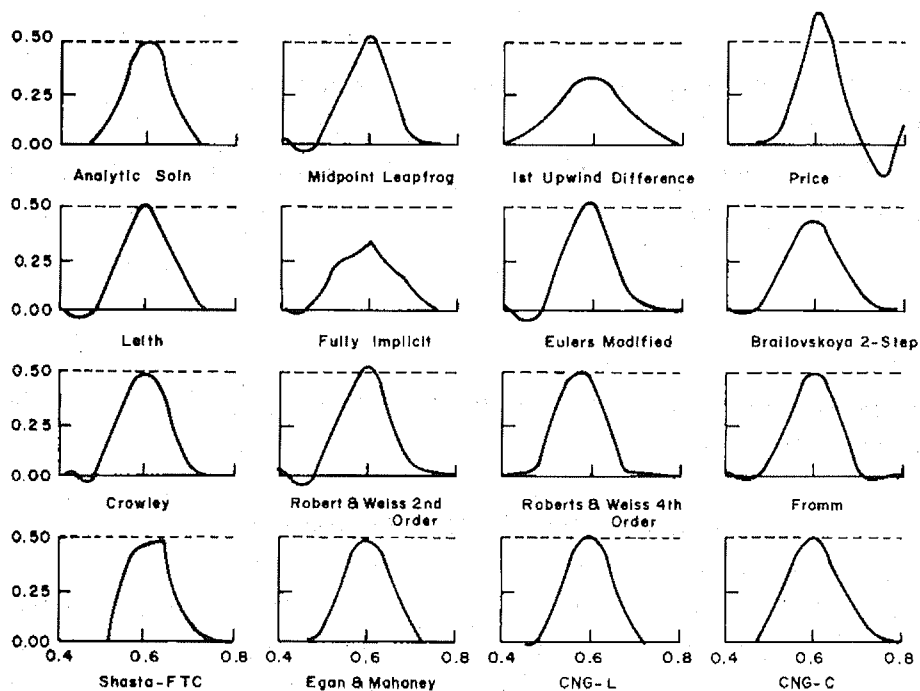


Figure 9a. Comparison of numerical methods for one-dimensional sine wave test.

Solutions shown after 100 time steps and $u\Delta t / \Delta x = 0.5$ (Carmichael, et al., 1980).

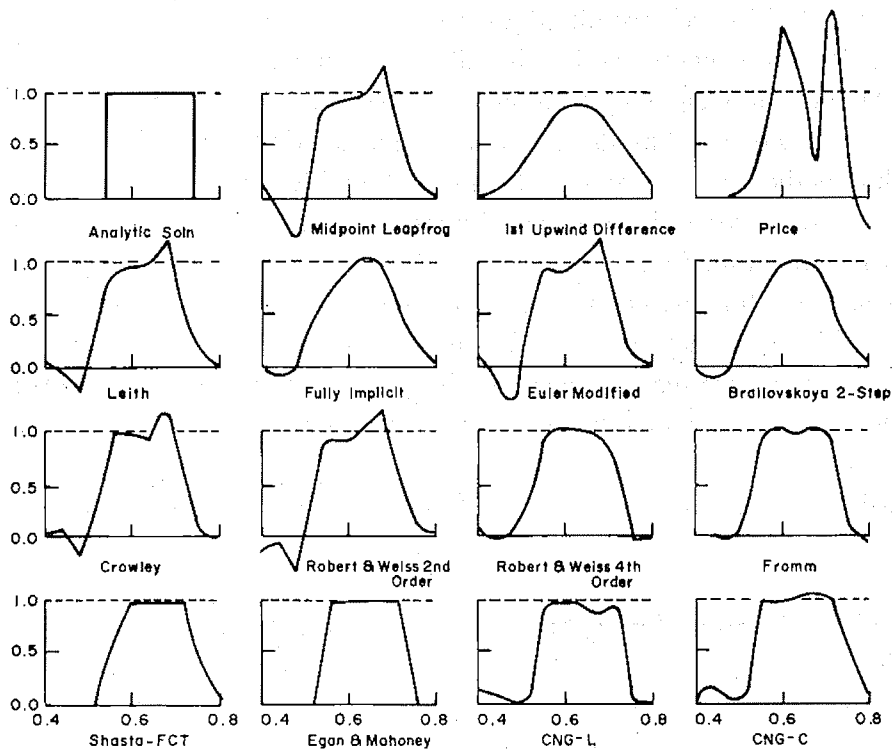


Figure 9b. Comparison of numerical methods for the one-dimensional square wave test. Solutions shown after 200 time steps and $u\Delta t / \Delta x = 0.25$ (Carmichael, et al.1980).

8.3 Finite element method

8.3.1 Basis

(1) Classification

Two concepts are used to formulate finite element analog of differential equation. One is variational principle and the other is method of weighted residuals. Formulation based on the variational principle is made on the basis of existence of variational principle which gives a given differential equation to be solved as its stationary condition. Therefore this method can not be applied if the given differential equation does not have its variational principle. On the other hand, the formulation by the method of weighted residuals is based on the “weak” solution of the given equation in a finite dimensional approximate solution function space. Thus this formulation can be applied to the differential equation for transport

phenomena in fluid which usually does not have the variational principle. In this note, the method of weighted residuals will be described.

The Method of Weighted Residuals (MWR) is further classified into several groups depending on what kinds of test or weight functions are chosen:

- (a) Galerkin method which uses trial (basis or shape) function as test function.
- (b) Least-square method which uses a function generated by applying differential operator to test function.
- (c) Collocation method uses delta function as test function.
- (d) The other moment methods use other functions.

Finite element formulation based on the method of weighted residuals is made by using local function, which has non zero value for only limited area, for test and trial functions.

See Mitchell and Wait (1977), Chung (1978), etc. for detail of the finite element methods.

8.3.2 Finite element formulation based on the method of weighted residuals

(1) Procedure of formulation

Let us take the following equation as an example.

$$Au = f \quad (117)$$

where $u = u(\mathbf{x})$ is the solution function, f is a given function, $\mathbf{x} \in \mathbf{R}$,

and $A \equiv -\frac{\partial^2}{\partial x^2} - \frac{\partial^2}{\partial y^2}$ is differential operator.

(a) Step 1:

Look for weak solution instead of exact (classical) solution for Eq. (117). The weak solution satisfies the following equation:

$$(Au, v) = (f, v) \quad \text{for all } v \in H \quad (118a)$$

or

$$(u, A^* v) = (f, v) \quad \text{for all } v \in H_1 \quad (118b)$$

where (\cdot, \cdot) denotes the inner product and, for example,

$$(Au, v) \equiv - \iint_R \left(\frac{\partial^2 u}{\partial x^2} + \frac{\partial^2 u}{\partial y^2} \right) v dx dy \quad (118c)$$

Furthermore, A^* is the adjoint operator of A which satisfies $(Au, v) = (u, A^* v)$. H is the Hilbert space which includes all the measurable functions that become zero on the boundary of the domain, ∂R . H_1 is a function space which includes the function v , $A^* v$ of which is measurable, and $H_1 \subset H$ holds. v is called test function.

(b) Step 2:

Now, from Eq. (117) the order of the operator A is 2. Eq. (118a) requires the function u has measurable 2nd order derivative, $u \in H_2^{(2)}(R)$, while Eq. (118b) needs that the function u is simply measurable, $u \in L_2(R)$, and the function v has measurable 2nd order derivative and is zero on the boundary, $v \in {}^\circ H_2^{(2)}(R)$.

By applying partial integration to Eq. (118a) or (118b), the above-described constraints on u and v , that is, $u \in H_2^{(2)}(R)$ and $v \in {}^\circ H_2^{(2)}(R)$, can be relaxed. (The partial integration, the Green-Gauss's theorem, is described below as Eq. (123).)

$$a(u, v) = (f, v) \quad \text{for all } v \in H_2 \quad (118d)$$

$$\text{where } a(u, v) = \iint_R \left[\left(\frac{\partial u}{\partial x} \right) \left(\frac{\partial v}{\partial y} \right) + \left(\frac{\partial u}{\partial y} \right) \left(\frac{\partial v}{\partial x} \right) \right] dx dy.$$

(c) Step 3:

For Eq. (118a) or (118d), try to obtain approximate solution U in N dimensional space. The equation to give U can be written as follows:

$$(AU, V) = (f, V) \quad \text{for all } V \in K_N \quad (119a)$$

or

$$a(U, V) = (f, V) \quad \text{for all } V \in K_N \quad (119b)$$

Let us assume that function W_i ($i = 1, 2, \dots, N$) forms the space K_N . Then, Eqs.

(119a, b) can be rewritten by using W_i as Eqs. (120a, b):

$$(AU, W_i) = (f, W_i) \quad i = 1, 2, \dots, N \quad (120a)$$

$$a(U, W_i) = (f, W_i) \quad i = 1, 2, \dots, N \quad (120b)$$

where W_i is called test or weight function.

(d) Step 4:

Express approximate solution function U with the functions φ_i ($i = 1, 2, \dots, N$) which form space K_N .

$$U = \sum_{i=1}^N C_i \varphi_i \quad (121)$$

where C_i denotes coefficient, and φ_i is called trial (basis or shape) function. By substituting Eq. (121) into Eq. (120), the following equations can be obtained:

$$\left(\sum_{j=1}^N C_j (A\varphi_j), W_i \right) = (f, W_i) \quad i = 1, 2, \dots, N \quad (122a)$$

or

$$a\left(\sum_{j=1}^N C_j \varphi_j, W_i \right) = (f, W_i) \quad i = 1, 2, \dots, N \quad (122b)$$

Eqs. (122a, b) are algebraic equations for unknown C_j since φ_j and W_i are known functions. By solving these equations, C_j can be obtained, and these C_j are substituted into Eq. (121) to obtain U . When local functions, which have non zero values in the limited area, are used for φ_j and W_i , the finite element formulation is derived.

Note: Definition of words and theorems used in this sub-section is briefly described as follows.

- (i) H, H_1, H_2 : Hilbert space which can be regarded as infinite-dimensional Euclid space and is a complete inner product space.
- (ii) Measurable: If an inner product of $f(x)$ such as $\int_a^b f(x)^2 dx$ is bounded, $f(x)$ is called "measurable".
- (iii) $L_2(R)$: a Hilbert space where the inner product is defined by $(u, v) = \int_a^b u \cdot v dx$ and $\int_a^b u^2 dx$ is bounded.
- (iv) Gauss's divergence theorem: $\int_V \nabla \cdot \mathbf{A} dV = \int_S \mathbf{A} \cdot \mathbf{n} dS$
- (v) Green-Gauss's theorem: $\int_V \phi \nabla^2 \psi dV = - \int_V \nabla \phi \cdot \nabla \psi dV + \int_S \phi \nabla \psi \cdot \mathbf{n} dS$ (123)

where ϕ and ψ are the functions which are defined in V and on S , and differentiable. \mathbf{n} is an outward unit vector normal to the surface S of the region V .

(2) Formulation with various MWD (Methods of Weighted Residuals)

Various MWD formulations can be derived by specifying different functions for W_i in Eq. (122a, b). They may be summarized as follows:

Method	Test function W_i
Galerkin	ϕ_i
Least square	$A \phi_i$
Collocation	$\delta(\mathbf{X} - \mathbf{X}_i)$
The others	Other functions, W_i

where φ_i is trial function in Eq. (121), and A is differential operator defining original PDE such as $A \equiv -\frac{\partial^2}{\partial x^2} - \frac{\partial^2}{\partial y^2}$ in Eq. (117). Eq. (117) can be rewritten as follows;

$$\frac{\partial^2 u}{\partial x^2} + \frac{\partial^2 u}{\partial y^2} = -f(x, y) \quad (117)$$

For Eq. (117), Eqs. (120a, b) of the above MWDs can be written as follows:
For Galerkin method:

$$\int_{\Omega} \left(\frac{\partial^2 U}{\partial x^2} + \frac{\partial^2 U}{\partial y^2} + f(x, y) \right) \varphi_i dx dy = 0 \quad (124a)$$

By applying the partial integration, Eq. (123), Eq. (124a) can be rewritten as:

$$-\int_{\Omega} \left(\frac{\partial U}{\partial x} \frac{\partial \varphi_i}{\partial x} + \frac{\partial U}{\partial y} \frac{\partial \varphi_i}{\partial y} - f \varphi_i \right) dx dy + \int_{\partial \Omega} \varphi_i \nabla U \cdot \mathbf{n} dl = 0 \quad (124b)$$

For least square method:

$$\int_{\Omega} \left(\frac{\partial^2 U}{\partial x^2} + \frac{\partial^2 U}{\partial y^2} + f \right) \left(\frac{\partial^2 \varphi_i}{\partial x^2} + \frac{\partial^2 \varphi_i}{\partial y^2} \right) dx dy = 0 \quad (125)$$

For collocation method:

$$\int_{\Omega} \left(\frac{\partial^2 U}{\partial x^2} + \frac{\partial^2 U}{\partial y^2} + f \right) \delta(x - x_i) \delta(y - y_i) dx dy = 0 \quad (126)$$

For other MWDs:

$$-\int_{\Omega} \left(\frac{\partial U}{\partial x} \frac{\partial W_i}{\partial x} + \frac{\partial U}{\partial y} \frac{\partial W_i}{\partial y} - f W_i \right) dx dy + \int_{\partial \Omega} W_i \nabla U \cdot \mathbf{n} dl = 0 \quad (127)$$

8.3.3 FEM (Finite Element Method) equation

Finite element methods can be formulated by using local functions, which have non-zero values only at limited parts of the calculation domain, for the trial (or shape) function φ_i and the test (or weight) function W_i . An example of FEM equations, boundary condition, and treatment of time derivative will be discussed

below based on the Galerkin method.

(1) FEM equations by the Galerkin method

Let us consider the following one dimensional equation.

$$\frac{\partial u}{\partial t} + \frac{\partial^2 u}{\partial x^2} - \alpha^2 u - f(x) = 0 \quad (0 \leq x \leq 1) \quad (128)$$

Taking inner product of Eq. (128) and trial function ϕ_i to obtain the “weak” solution of Eq. (128) leads to the following equations.

$$\int_0^1 \left(\frac{\partial U}{\partial t} + \frac{\partial^2 U}{\partial x^2} - \alpha^2 U - f(x) \right) \phi_i dx = 0 \quad (i = 1, 2, \dots, N) \quad (129a)$$

Note that the exact solution “ u ” in Eq. (128) is already replaced by a finite-dimensional approximation function “ U ” in Eq. (129a).

Then, by applying partial integration to the product of 2nd derivative term and ϕ_i , the following equations can be obtained.

$$-\int_0^1 \left(-\frac{\partial U}{\partial t} + \frac{\partial U}{\partial x} \frac{\partial \phi_i}{\partial x} + \alpha^2 U \phi_i + f \phi_i \right) dx + \left(\frac{\partial U}{\partial x} \phi_i^* \right)_0^1 = 0 \quad (i = 1, 2, \dots, N) \quad (129b)$$

where the 2nd term on the right hand side is called “natural boundary condition”.

The function ϕ_i^* presents variation of $\partial U / \partial n$ along the boundary; in this example,

ϕ_i^* is equal to either 1 or 0, since the problem is now one dimensional in space.

Substituting the approximation function $U(x) = \sum_{j=1}^N C_j \phi_j$ (Eq. 121) into Eq. (129b) and rearranging it give the following equations.

$$\sum_{j=1}^N (\varphi_i \varphi_j) \frac{\partial C_j}{\partial t} - \sum_{j=1}^N \left(\int_0^1 \frac{\partial \varphi_i}{\partial x} \frac{\partial \varphi_j}{\partial x} dx + \int_0^1 \alpha^2 \varphi_i \varphi_j dx \right) C_j = \int_0^1 f \varphi_i dx - \left(\frac{\partial U}{\partial x} \phi_i^* \right)_0^1 \quad (i=1,2,\dots,N) \quad (130)$$

Eq. (130) gives a set of linear ordinary differential equations on C_j ($j=1,2,\dots,N$).

Since the functions φ_i (or φ_j) (i or $j=1,2,3,\dots,N$) are "local" functions, integrals in Eq. (130) can be performed locally and thus each Eq. (130) includes only limited number of unknown variables C_j . Let us take piecewise linear "local" functions for

φ_i to explain how the integrals are performed locally. The function φ_i corresponding to the node "i" is defined as a linear function which is non zero only for $x_{i-1} \leq x \leq x_i$ and $x_i \leq x \leq x_{i+1}$ as shown in Fig. 10. The "global" trial function φ_i is given by the sum of the "local" functions $\varphi_2^{(I)}$ at the element (I) and $\varphi_1^{(I+1)}$ at the element (I+1) as $\varphi_i \equiv \varphi_2^{(I)} + \varphi_1^{(I+1)}$ (see Fig. 10), and φ_i is always zero at the other elements. Thus the integral in Eq. (130) can be performed also as the sum of the local integrals as follows:

$$\int_0^1 g \varphi_i dx = \int_0^{L_I} g \varphi_2^{(I)} dx + \int_0^{L_{I+1}} g \varphi_1^{(I+1)} dx \quad (131)$$

where "g" is arbitrary function, L_I is the length of the element (I), $\varphi_2^{(I)}$ is the local linear function at the element (I), etc.

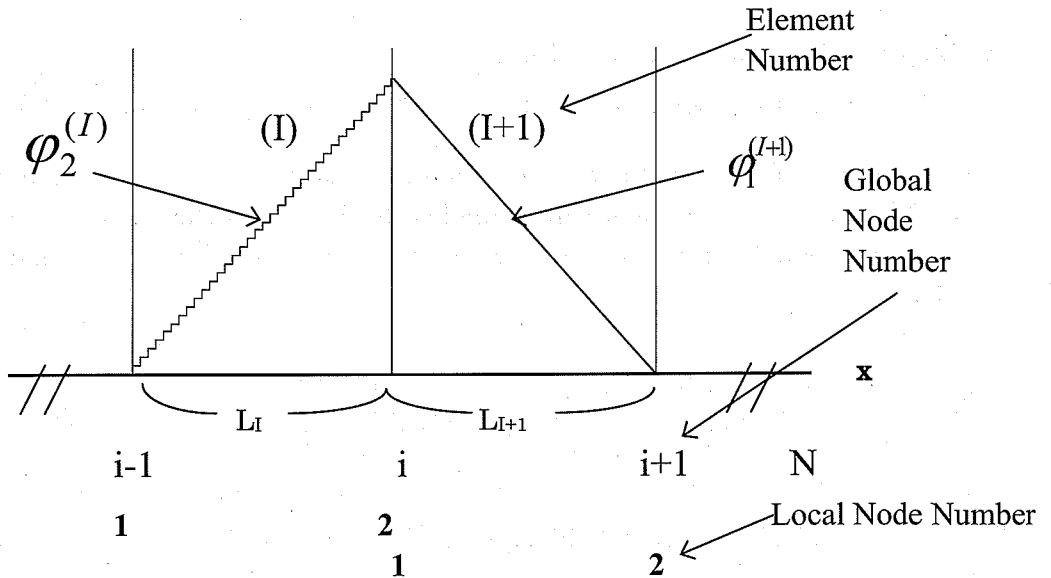


Figure 10. Schematics of a FEM element in one dimension; “i” stands for the “global node” number, “(I)” is the “element” number, and “1” or “2” is the “local node” number. The global node “i” corresponds to the local nodes “2” of the element “(I)” and “1” of the element “(I+1)”. Global trial function ϕ_i associated with the global node “i” is given by the sum of the local trial functions $\phi_2^{(I)}$ at element (I) and $\phi_1^{(I+1)}$ at element (I+1): $\phi_i = \phi_2^{(I)} + \phi_1^{(I+1)}$; ϕ_i is zero in the region outside the elements (I) and (I+1).

(2) Boundary condition

Gradient type boundary conditions such as Neumann (Eq. 16 in chap. 1) and Robin (Eq. 17 in chap. 1) can be incorporated into calculation through the natural boundary condition, that is, the 2nd term on the right hand side in Eq. (130), while the Dirichlet type condition (Eq. 15 in chap. 1) is taken into account by replacing Eq.

(130) at the end nodes of $i=1$ or N with, for example, $C_{1 \text{ or } N}^{n+1} = C_b$ (a fixed boundary value).

(3) Treatment of time derivative term

Time derivative term $\partial C_j / \partial t$ in Eq. (130) can be approximated with any difference method such as forward, centered, backward, etc., and furthermore the Crank-Nicolson type treatment can be applied to the rest of the terms in Eq. (130). Eq. (132) presents the FEM equations when the Crank-Nicolson formula is used for Eq. (130).

$$\sum_{j=1}^N (\varphi_i, \varphi_j) \frac{C_j^{n+1} - C_j^n}{\Delta t} - \sum_{j=1}^N \left(\int_0^1 \frac{\partial \varphi_i}{\partial x} \frac{\partial \varphi_j}{\partial x} dx + \int_0^1 \alpha^2 \varphi_i \varphi_j dx \right) \frac{C_j^{n+1} + C_j^n}{2} = \int_0^1 \frac{f^{n+1} + f^n}{2} \varphi_i dx - \left(\frac{\partial U}{\partial x} \phi_i^* \right)_0^1$$

(132)

($i=1, 2, \dots, N$)

The results indicated with "CNG-L" and "CNG-C" in Fig. 9 were obtained by Eq. (132) with use of linear and cubic functions for φ_i .

References

- Carmichael, G.R., T. Kitada, and L.K. Peters (1980) Application of a Galerkin finite element method to atmospheric transport problems, *Computers & Fluids*, **8**, 155-176.
- Chung, T.J. (1978) *Finite Element Analysis in Fluid Dynamics*, McGraw Hill.
- Kitada, T. (1987) Effect of non-zero divergence wind fields on atmospheric transport calculations, *Atmos. Environ.*, **21**, 785-788.
- Douglas, J. and H.H. Rachford (1956) On the numerical solution of heat conduction problems in two and three space variables, *Trans. Amer. Math. Soc.*, **82**, 421-439.
- D'Yakonov, Ye G. (1963) Referred in *Mitchell and Griffiths* (1980).
- Harlow, F.H. and J.E. Welch (1965) Numerical calculation of time-dependent viscous incompressible flow of fluid with free surface, *Physics of Fluids*, **8**, 2182-2189.
- Hirt, C. W. and F. H. Harlow (1967) A general corrective procedure for the numerical solution of initial-value problems, *J. of computational physics*, **2**, 114-119.
- Mitchell, A.R. and D.R.Griffiths (1980) *The Finite Difference Methods in Partial Differential Equations*, John Wiley & Sons.
- Mitchell, A.R. and R. Wait (1977) *The Finite Element Method in Partial Differential Equations*, John Wiley & Sons.
- Patankar, S.V. (1989) *Numerical Heat Transfer and Fluid Flow*, Hemisphere.
- Peaceman, D.W. and H.H. Rachford (1955) The numerical solution of parabolic and elliptic differential equations, *J. Soc. Indust. Appl. Math.*, **3**, 28-42.
- Richtmyer, R.D. and K.W.Morton (1967) *Difference Methods for Initial - Value Problems*, Wiley (1967)
- Roache, P.J. (1972) *Computational Fluid Dynamics*, Hermosa Publishers, Albuquerque, N.M., USA.
- Togawa, H. (1976) *Matrix no Suuchi Keisan (Numerical Calculation of Matrix)*, OHM Sha Shoten, Tokyo, Japan (in Japanese).
- Wendorff, B. (1966) *Theoretical Numerical Analysis*, Academic Press.

8.5 Appendix

Solver for tri-diagonal matrix.

```
*****
```

```
***
```

```
***
```

```
***      PROGRAM TRISOLVER BY KITADA
```

```
***
```

```
***
```

```
***
```

```
*****
```

```
* NDAM: ORDER OF LINEAR ALGEBRAIC EQUATION SYSTEM; MUST BE  
GIVEN BY
```

```
*      USERS; NDAM=21 IS JUST AN EXAMPLE/
```

```
* SEE COMMENTS IN SUBROUTINE SOLV FOR ARRAYS A, B, C, F, AND X
```

```
*
```

```
      PARAMETER (NDAM=21)
```

```
*
```

```
      REAL      XOUT (NDAM),AIN(NDAM), BIN(NDAM), CIN(NDAM),  
FIN(DAM)
```

```
*
```

```
      OPEN                                (50,FILE='.....',  
STATUS='UNKNOWN',FORM='UNFORMATTED')
```

```
      N=NDAM
```

```
      AIN(1)= .....
```

```
      AIN(2)=.....
```

```
      .....
```

```
      AIN(N)=.....
```

```
      BIN(2)=.....
```

```
      BIN(3)=.....
```

```
      .....
```

```
      BIN(N)=.....
```

```
      CIN(1)=.....
```

```
      CIN(2)=.....
```

```
      .....
```

```
      CIN(N-1)=.....
```

```
      FIN(1)=.....
```

```
      FIN(2)=.....
```

```
      .....
```

```
      FIN(N)=.....
```

```

*
      CALL SOLV(N, AIN, BIN, CIN, FIN, XOUT)
*
      WRITE(6,1000) (XOUT(K),K=1,N)
1000 FORMAT(' XOUT(K)=',5X, 10E10.3)
      WRITE(50) (XOUT(K),K=1,N)
      CLOSE(50)
      STOP
      END
*****
***                                     ***
***          SUBROUTINE SOLV          ***
***                                     ***
*****

      SUBROUTINE SOLV(N,A,B,C,F,X)
*****
* N: ORDER OF LINEAR ALGERAIC EQUATION SYSTEM; NUMBER OF
VARIABLES *
*A(K): ONE DIMENSIONAL ARRAY TO STORE DIAGONAL COMPONENT
      OF
      TRI-DIGONAL COEFFICIENT MATRIX, K=1 TO N --- INPUT
*
* B(K): ONE DIMENSIONAL ARRAY TO STORE LOWER-DIAGONAL
COMPONENT OF
*      TRI-DIGONAL COEFFICIENT MATRIX; ONLY K=2 TO N IS
EFFECTIVE
*                                     ----- INPUT
*
* C(K): ONE DIMENSIONAL ARRAY TO STORE UPPER-DIAGONAL
COMPONENT OF
*      TRI-DIGONAL COEFFICIENT MATRIX; ONL K=1 TO N-1 IS
EFFECTIVE *
*                                     ----- INPUT
*
* F(K): ONE DIMENSIONAL ARRAY TO STORE RIGHT-HAND SIDE IN
LINEAR
*      ALGEBRAIC EQUATION SYSTEM; K=1 TO N ----- INPUT

```

```

*
* X(K): ONE DIMENSIONAL ARRAY TO STORE SOLUTION OF LINEAR
ALGEBRAIC
*
* EQUATION SYSTEM ----- OUTPUT
*
*****
*
* | A(1) C(1) | | X(1) | | F(1) |
* | B(2) A(2) C(2) | | X(2) | | F(2) |
* | B(3) A(3) C(3) | | X(3) | | F(3) |
* | * * * | | * | | * |
* | B(K) A(K) C(K) | | X(K) | = | F(K) |
* |
* | * * * | | * | | * |
* | B(N-1) A(N-1) C (N-1) | | X (N-1) |
| F(N-1) |
* | B(N) A(N) | | X(N) |
| F(N) |
*
*****
*
REAL A(N),B(N),C(N),F(N),X(N),A1(N),C1(N),Y(N),Z
N1=N-1
N2=N-2
A1(1)=A(1)
C1(1)=C(1)/A1(1)
DO 10 I=2,N1
A1(I)=A(I)-B(I)*C1(I-1)
10 C1(I)=C(I)/A1(I)
A1(N)=A(N)-B(N)*C1(N1)
Y(1)=F(1)/A1(1)
DO 20 I=2,N
20 Y(I)=(F(I)-B(I)*Y(I-1))/A1(I)
X(N)=Y(N)
DO 30 J=1,N1
30 X(N-J)=Y(N-J)-C1(N-J)*X(N-J+1)
RETURN

```

END

Chapter 9

Climate Change

Akimasa SUMI
Center for Climate System Research
University of Tokyo
Tokyo, JAPAN
e-mail: sumi@ccsr.u-tokyo.ac.jp

9.1 Introduction

Due to recent expansion of human-being's activity, a human-being can start to interfere our planet, the Earth. For example, huge increase of our energy consumption has increased CO₂ concentration in the atmosphere, which has an impact on the radiational energy budget over the Earth surface. This has a huge impact to the future of our life. It is said that there exist potential danger to future human life.

However, it should be noted that climate or environment of the Earth surface is not the same all the time. Rather, a change is a peculiar characteristic of our environment. In other word, climate is always changing. For example, the change of the Earth climate is demonstrated in Fig.1. It can be well noted that warm and cold periods are occurring repeatedly. It should be also noted that the Earth itself has been changing. The life of the Earth is 46 Billion years and the Earth environment has been evolving to the present situation. Through the evolution of the Earth, the composition of the atmosphere had changed. CO₂ contained in the early sage of the earth was filtered into the ocean floor. The ozone layer and biosphere was generated and ore climate is based on the interaction between the physical climate system and the biosphere.

Weather and climate have a profound influence on life on the Earth. They are part of the daily experience of human beings and are essential for health, food production and well-being. Many people consider the prospect of human-induced climate change as a matter of concern. If we wish to understand, detect and

eventually predict the human influence on climate, we need to understand the behavior of the climate system of the Earth and the processes that lead to climate change.

The “weather”, as we experience it, is the fluctuating state of the atmosphere around us, characterized by temperature, wind, precipitation, clouds and other weather elements. This weather is the result of rapidly developing and decaying weather systems such as mid-latitude cyclone and anti-cyclone systems associated with fronts, showers and tropical cyclones.

The “Climate” refers to the average weather in terms of the mean and its variability over a certain time-span and a certain area. Classical climatology provides a classification and description of the various climate regimes on the Earth. Climate varies from place to place, depending on latitude, distance to the sea, vegetation, presence or absence of mountains or other geographical factors. Climate also changes from season to season, year to year, decade to decade or on much longer time-scales, such as the geological time scale. An interesting example is the Ice Ages. Statistically significant variations of the mean state of the climate or of its variability, typically persisting for decades or longer, are referred to as “climate change”.

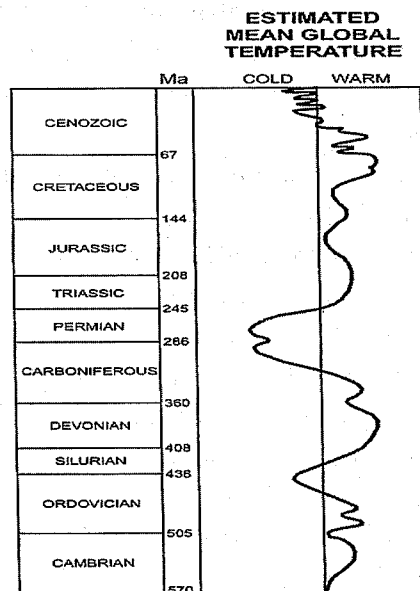


Figure 1. Generalized temperature history of the Earth plotted as relative departures from the present global mean (Frakes et al, 1992).

9.2 Climate system and its variability

9.2.1 Climate system

The climate system consists of many sub systems, which are interacting each other and forced by various external and internal forcing. They are the atmosphere, the hydrosphere, the cryosphere, the land surface, the biosphere and the human-sphere. It should be noted that the climate system behaves as an integrated system. The Earth has three major forcings, that is, solar radiation, heating by radioactivity, and heat from the interior of the Earth. The most important of three forcing for the climate system is the solar radiation (see, Fig.2). Which is the external forcing depends on definition. For example, heating due to the ozone is considered as the external forcing when we considered the ozone distribution is not changing. But when we consider that the impact of the ozone depletion on the climate, it should be considered as an internal forcing. The direct effect of human activities on the climate system is considered an external forcing.

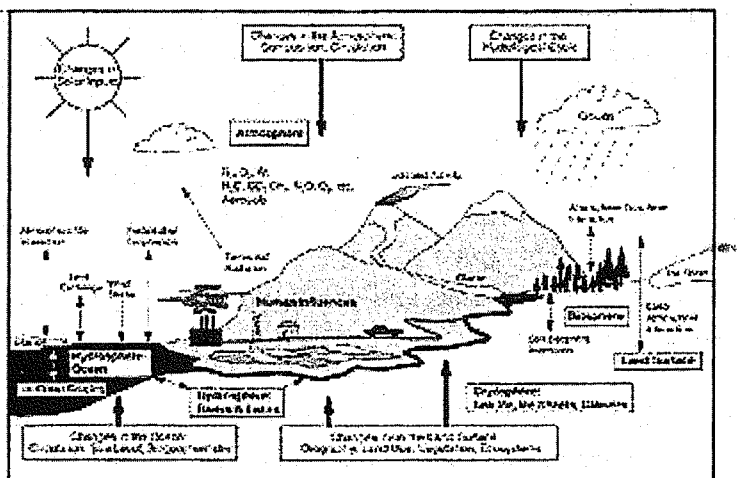


Figure 2. Schematic view of the components of the global climate system (bold), their processes and interactions (thin arrows) and some aspects that may change (bold arrows).

The atmosphere is the fastest part of the system. As stated in the

Introduction, atmospheric composition has changed with the evolution of the Earth. The dry atmosphere composition at the present is nitrogen (N_2 , 78.1% volume mixing ratio), oxygen (O_2 , 20.9% volume mixing ratio, and argon (Ar, 0.93% volume mixing ratio). These gases have only limited interaction with the incoming solar radiation and they do not interact with the infrared radiation emitted by the Earth. However there are a number of trace gases, such as carbon dioxide (CO_2), methane (CH_4), nitrous oxide (N_2O) and ozone (O_3), which do absorb and emit infrared radiation. These gases are called to be greenhouse gases, which plays an essential role in the Earth's radiation energy budget. Moreover it should be noted that the atmosphere contains water vapor (H_2O), which is also a natural greenhouse gas. A water cycle is the most important element of the Earth climate system. In other words, solid, liquid and gas state of water can be possible in the atmosphere. These three states are the reason why we have a variety of weather and climate. Besides, the atmosphere also contains solid and liquid particles (aerosols) and clouds, which interact with the incoming and outgoing radiation in a complex and spatially very variable manner.

The atmospheric distribution of ozone and its role in the Earth climate is important. Ozone in the troposphere and lower stratosphere acts as a greenhouse gas. High ozone concentration in the stratosphere absorbs solar ultra-violet radiation. This prohibits damaging form of radiation to the human-beings and the biosphere.

The hydrosphere consists of rivers, lakes and aquifers, and saline water of the oceans and seas. Fresh water runoff from the land returns to the oceans in rivers. It influences the ocean's salinity and circulation. The oceans cover approximately 70% of the Earth's surface. They store and transport a large amount of energy and dissolve and store great quantities of carbon dioxide. Their circulation, driven by the wind and by density contrasts caused by salinity and thermal gradients (the thermohaline circulation), is much slower than the atmospheric circulation. Mainly due to the large thermal inertia of the oceans, they damp vast and strong temperature changes and function as a regulator of the Earth's climate and as a source of natural climate variability, in particular on the longer time-scales.

The cryosphere, including the ice sheets of Greenland and Antarctica, continental glaciers and snow fields, sea ice and permafrost, is important to the climate system from its high reflectivity (albedo) for solar radiation, its low thermal conductivity, its large thermal inertia and, especially, its critical role in driving deep ocean water circulation. Because the ice sheets store a large amount of water, variations in their volume are a potential source of sea level variations.

Vegetation and soils at the land surface control the reflection of the solar radiation to the atmosphere. Some is returned as long-wave (infrared) radiation, heating the atmosphere as the land surface warms. Some serves to evaporate water, either in the soil or in the leaves of plants, bringing water back into the atmosphere. Because the evaporation of soil moisture requires energy, soil moisture has a strong influence on the surface temperature. The texture of the land surface (its roughness) influences the atmosphere dynamically as winds blow over the land's surface. Roughness is determined by both topography and vegetation. Wind also blows dust from the surface into the atmosphere, which interacts with the atmospheric radiation.

The marine and terrestrial biospheres have a major impact on the atmosphere's composition. The biota influence the uptake and release of greenhouse gases. Through the photosynthetic process, both marine and terrestrial plants (especially forests) store significant amounts of carbon from carbon dioxide. Thus, the biosphere plays a central role in the carbon cycle, as well as in the budgets of many other gases, such as methane and nitrous oxide. Other biospheric emissions are the so-called volatile organic compounds (VOC) which may have important effects on atmospheric chemistry, on aerosol formation and therefore on climate. Because the storage of carbon and the exchange of trace gases are influenced by climate, feedbacks between climate change and atmospheric concentrations of trace gases can occur. The influence of climate on the biosphere is preserved as fossils, tree rings, pollen and other records, so that much of what is known of past climates comes from such biotic indicators.

These sub-systems of the climate system are interacting each other on a wide range of space and time scales, making the system extremely complex. These interactions consist of exchange of energy, water, and substances through fluxes of mass, heat and momentum.

As an example, the atmosphere and the oceans are strongly coupled and exchange water vapor and heat through evaporation and precipitation. The precipitation has an influence on salinity, its distribution and the thermohaline circulation. Atmosphere and oceans also exchange carbon dioxide among other gases.

Some other examples: sea ice hinders the exchanges between atmosphere and oceans; the biosphere influences the carbon dioxide concentration by photosynthesis and respiration, which in turn is influenced by climate change. The biosphere also affects the input of water in the atmosphere through evapotranspiration, and the atmosphere's radiative balance through the albedo

effect of plants.

It should be noted that any change in the components of the climate system and their interactions, or in the external forcing, may result in climate variations. We will explain these climate variations in the following sections.

9.2.2 Forcing and response

(1) External forcing and internal forcing

Climate system can be considered to be a forced-response system. Forcing can be classified to be an external forcing and an internal forcing. External forcing is an energy originated outside the system and an internal forcing is an energy originated inside the system. For climate, a solar radiation is a major forcing, which can be classified to be an external forcing. Solar radiation is not constant. It is fluctuated. In Fig.3, recent observation by satellites is shown. 1-2 W/m² fluctuation in 10 year time scale is noted. The solar radiation is changing in much longer time scale. In Fig.4, reconstruction of the total solar radiance is shown. From 1600, there exists a large fluctuation. The minimum around 1800 is considered to correspond to the little Ice Age. In a geological time-scale, an orbital change of the Earth has a large impact on the solar radiation. Due to the change of orbital parameter, solar radiation input to the earth can be changed. These changes are known as a Milankovitch cycle.

Another example of an external forcing is a sphericity and rotation of the Earth. The sphericity defines the largest scale of the atmospheric response. In other words, there exists no phenomenon whose horizontal scale is larger than the 40000km. The Earth rotation has a large impact on the atmospheric circulation. One example is a geostrophic flow, which can be explained by a balance between pressure gradient force and the Coriolis force. The land-ocean contrast and the large-scale mountain can be considered to be an external forcing. Monsoon flow is a typical example forced by the land-ocean contrast.

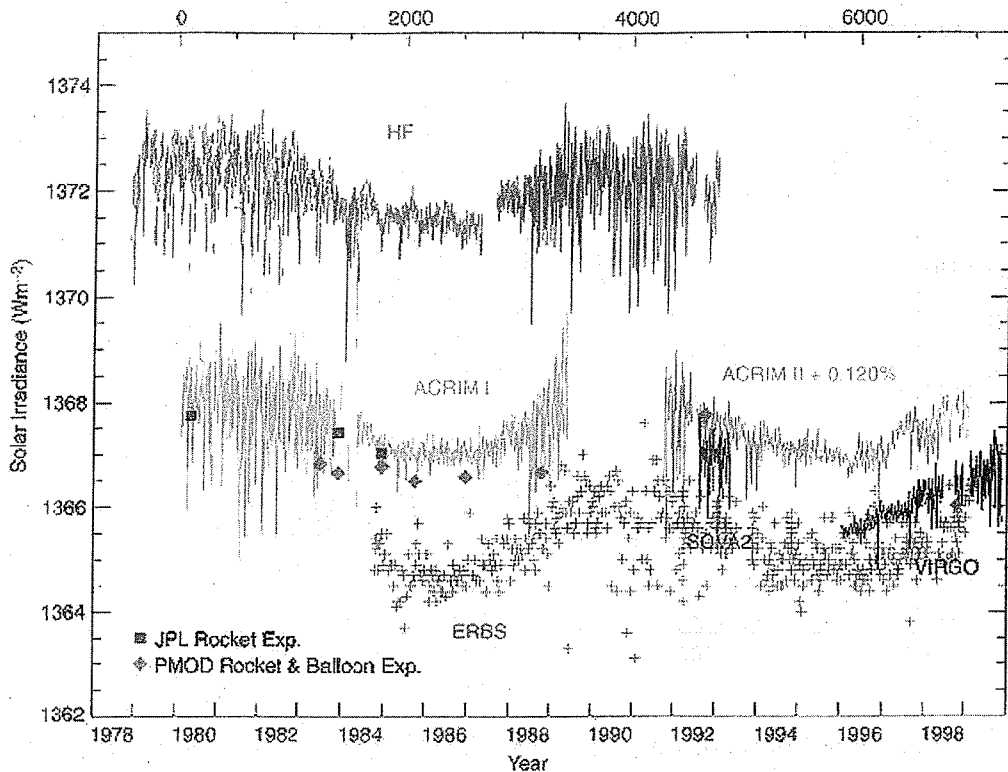


Figure 3. Change of solar constant observed by satellite.

Another example is gravity. Due to the gravity, atmosphere is stratified, in other words, atmosphere is classified into a sphere. From the surface, it is divided into the troposphere, the stratosphere, and the mesosphere. Also, convection can be possible due to the gravity. Besides convection, many phenomena are originated to the buoyancy forcing.

An example of an internal forcing is heat released in the convection. The heat makes air parcel warmer, which is going upward. In other word, convective heating drives the atmospheric circulation. Another example is an ice-sheet. Once the ice-sheet covers the Earth, it reflects the sun light. It may affect the Earth climate. Most famous example is the Ice age.

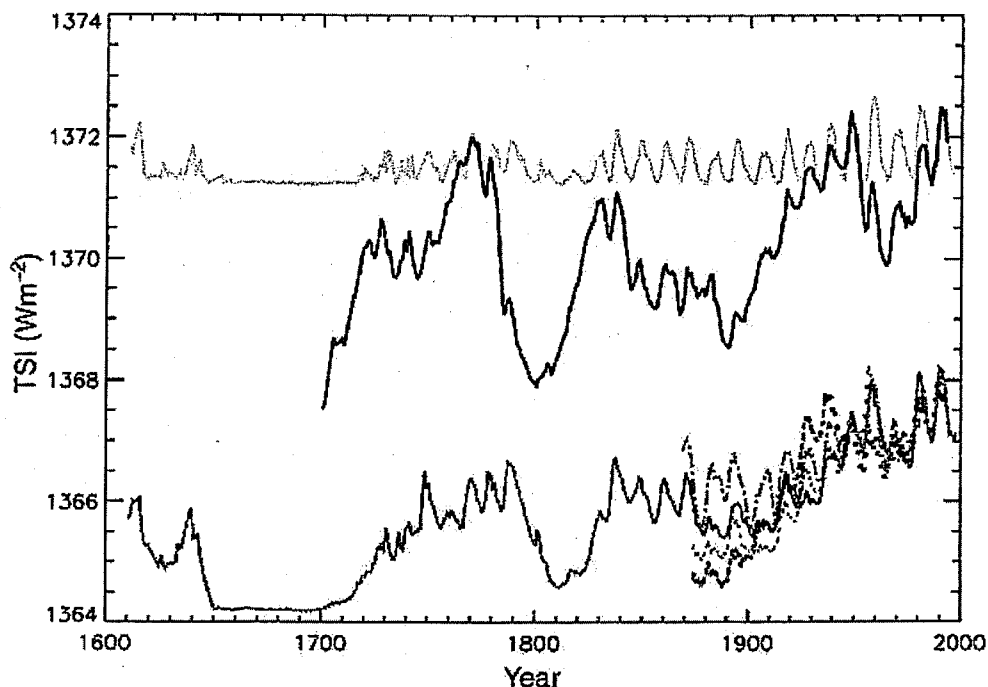


Figure 4. Reconstructions of total solar irradiance (TSI) by Lean et al. (1995, solid red curve), Hoyt and Schatten (1993, data updated by the authors to 1999, solid black curve), Solanki and Fligge (1998, dotted blue curves), and Lockwood and Stamper (1999, heavy dash-dot green curve); the gray curve shows group sunspot numbers (Hoyt and Schatten, 1998) scaled to Nimbus-7 observations for 1979 to 1993.

Change of atmospheric composition is considered to be another example of an internal forcing. For example, an increase of CO_2 from the Earth can warm the Earth climate through greenhouse effect. However, it should be noted that a distinction between an internal forcing and an external forcing is dependent on the time scale of the issue. If time-scale of the internal forcing is longer than the time scale of the problem, the internal forcing can be considered to be an external forcing and given.

(2) Response of the climate system to the forcings

The Earth climate can be summarized in Fig.5. Basically, the tonal symmetric features are dominated, which is based on the sphericity and rotation of the earth.

For, example, the easterly in the lower equatorial atmosphere is explained by the angular momentum conservation; and the westerly in the mid latitude can be explained by the geostrophic balance and thermal wind balance.

The land-ocean contrast have a huge impact on the mid-latitude climate. There exist a strong warm ocean current and a permanent trough in the upper atmosphere in the western part of the ocean, which favors cyclone genesis. Developed cyclone hits the western part of the continent. Thus, climate in the mid-latitude can be considered to result in the cyclone activity and the land-ocean contrast.

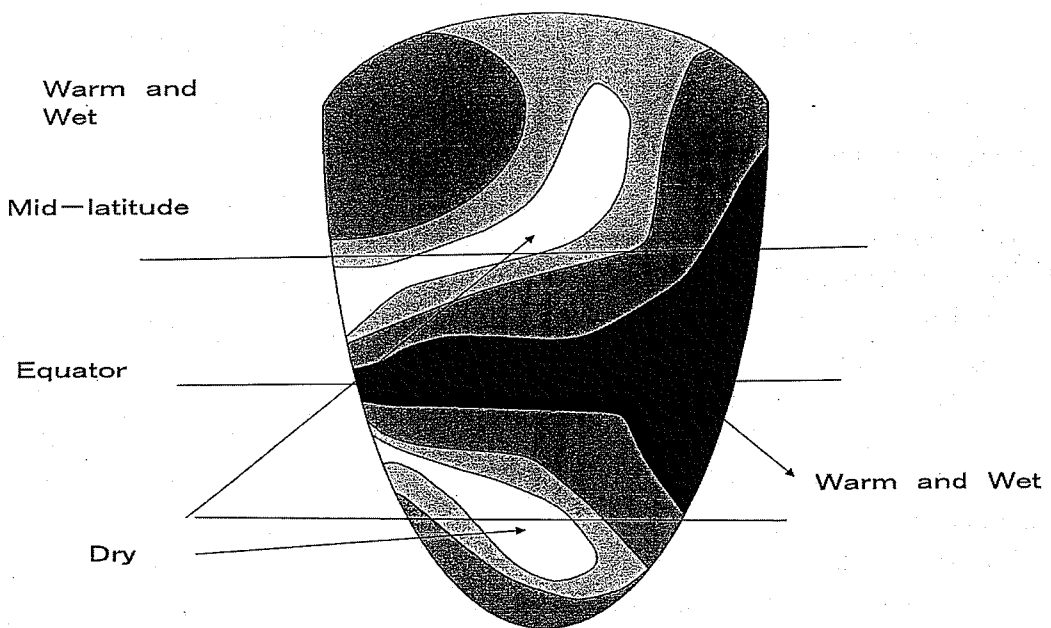


Figure 5. Ideal distribution of climate on the continent(Trewartha,1986)

In the tropics, the land-ocean contrast causes a monsoon flow. The monsoon westerly is the prominent westerly found in the tropics. In general, westerly is associated with a large convection. A dynamical response of atmosphere in the tropics to convective heating is well known as a Matsuno-Gill pattern(see, Fig.6). This response pattern is a key to consider climate system.

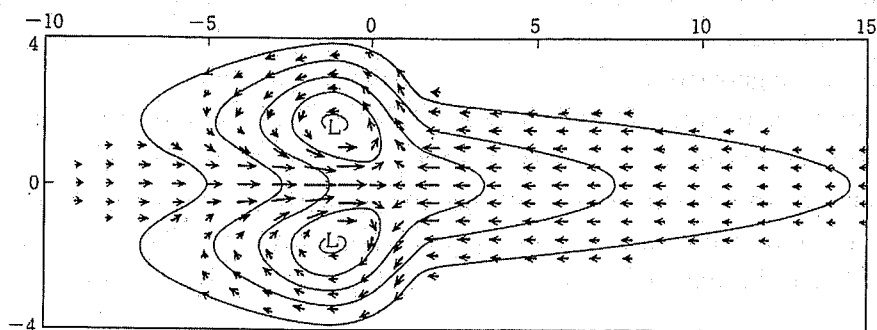


Figure 6. Matsuno- Gill Pattern(see to Matsuno(1968) and Gill(1980))

9.2.3 Variability

There exists a wide range of variabilities in the climate system. It consists of short time scale and longer time scales. It should be noted that each time-scale has its own mechanism. In other words, it is one of the objectives to understand the mechanism of each time-scale phenomena.

(1) Diurnal variation

This is 24 hour time-scale phenomena. Land-ocean breeze is one example. The diurnal phenomena is, in a sense, forced by diurnal change of the solar radiation. Another example is a tide. Semi-diurnal phenomena are also included in the diurnal phenomena.

(2) Weekly variability

Most typical phenomena in a week time scale are a baroclinic wave or a cyclone and anti-cyclone pair. Its generation is controlled by instability in the atmospheric basic state and propagation speed is controlled by the mean flow.

(3) Monthly time-scale

It is well known that there exist phenomena of monthly time scale. Madden-Julian phenomena in the tropics are one example of these phenomena. Others are active-break cycle of the monsoon system, and index cycle of the jet stream in the mid-latitude. Blocking phenomena is considered to be related to this category.

(4) Annual cycle

Annual cycle is strongly related to the movement of the Earth around the Sun. Seasonal change is one of the strongest forcing to the Earth climate, which characterizes the climate of the Earth. Even in the tropics, the monsoon is forced

by the annual cycle.

(4) Yearly time-scale

ENSO is the typical phenomena belonging to this category. ENSO is determined by the air-sea interaction in the tropics and the annual cycle.

(6) Decadal time-scale

Recently, it becomes well known that there exist phenomena much longer than 10 years. This phenomenon is defined to be a decadal phenomenon. For example, a number of typhoons in the western Pacific are not the same. It varies in about 20 year time scale. However, the mechanism is now being investigated. .

(7) Much longer time-scale

There exist many time-scales in the geological time scale. One example is the Ice Age cycle, which is considered to be forced by the Milankovitch cycle, but the interaction between an ice-sheet and an atmosphere is also important. It is a hot topic in the Earth system science.

9.2.4 Global Warming

It is a main concern of our society whether the Earth climate is and will be heated up by a human activity. This is called as a Global warming issue and as it is urgent concern, it is widely investigated by many researchers. These activities are summarized in many IPCC reports.

In Fig.8, the time sequence of the globally averaged surface temperature from 1861 to 2000 is displayed (Jones et al., 2001). It is noted that the surface temperature is increasing, especially in 90s. There is no doubt that recent climate becomes warmer. However, this does not directly mean that this warming is a result of human activities. As is explained in the previous sections, there exist many natural fluctuations based on natural forcing. For example, a temperature increase between 1920 and 1940 is clearly noted. This is apparently independent of CO₂ in the atmosphere. In other words, due to natural reason, this amount of warming becomes possible.

In order to confirm that the Earth climate is influenced by human activity, an intensive effort is being conducted. This is called as a "detection study". The popular method we are applying is a "fingerprint" method, where we are trying to find out the fingerprint which is predicted by the model simulation. Another method is to simulate the time sequence of the past temperature from 1860 to present by applying various forcing, including natural and anthropogenic forcing. Anyhow, a climate model plays a key role in the global warming issues.

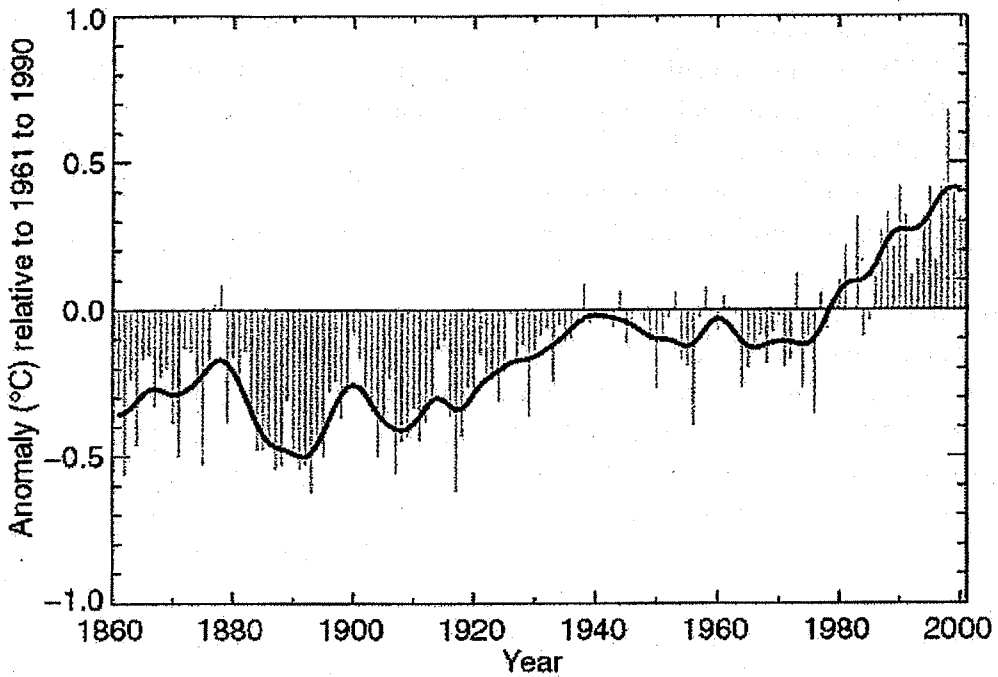


Figure 7. Annual anomalies of globally average land surface air temperature(°C) from 1961 to 1990.

9.3 Climate models

9.3.1 Energy Balance Model (EBM)

The most important principle of the response is the energy conservation. For example, if the Earth climate is steady, the input and output of energy is balanced. Let us assume a globally averaged temperature of the Earth. Here, a is the Earth radius, and S_0 is a solar constant of the earth surface. Planetary albedo is α , then, the solar input of the earth is $\pi a^2 \times S_0 \times (1 - \alpha)$. Output from the Earth is considered to be thermal radiation from the Earth surface corresponding to the Earth surface temperature, T_e . That is $4\pi a^2 \sigma T_e^4$. These terms are balanced;

$$\pi a^2 S_0 (1 - \alpha) = 4\pi a^2 \sigma T_e^4$$

This temperature is defined to be a radiative equilibrium temperature.

The earth is covered by the atmosphere, whose greenhouse effect altered the atmospheric temperature. Followings are a simple explanation of the greenhouse effect. Let us assume the one layer of the atmosphere, whose temperature is T_a . Atmosphere is assumed to be transparent to the solar radiation, but the earth radiation from the surface is completely absorbed by the atmosphere. Then, the energy conservation can be described in the following equations:

$$I_E + \delta T_a^4 - \delta T_g^4 = 0$$

$$-2\delta T_a^4 + \delta T_g^4 = 0$$

$$\delta T_a^4 = I_E$$

$$\text{here } I_E = \pi \frac{S_0}{4} (1 - \alpha)$$

Then, $T_g = 2^{1/4} T_a$.

Compared with the radiative equivalent temperature, the equivalent temperature is increased.

This is due to the greenhouse effect.

When we want the radiational process properly, we have to use a radiative transfer model. At the same time, convective process should be incorporated. This model is called as a radiative convective model. In Fig.8, the results from Manabe and Strickler(1964) are displayed. Temperature profile is well simulated.

9.3.2 AGCM and NWP

It is our dream that based on the physical laws we would like to predict the future weather. This is the first motivation to start the Numerical Weather Prediction (NWP) by Richardson (1922). Although his attempt could not be realized, his dream excited enthusiasm of many followers. After the World War II, an electronic computer became available. Then, the NWP model was developed at many meteorological centers in the world. From the beginning, it is well known that a model for the weather prediction can be used to simulate the atmospheric circulation and climate of the Earth. The model for this purpose is called to be an

Atmospheric General Circulation Model (AGCM). In other words, NWP is an initial value problem and GCM simulation is a boundary value problem. However, there was a slightly difference between these two. In general, NWP model is designed to achieve a good skill of weather forecasting and AGCM tends to be tuned to achieve a radiational balance. Recently, it is said that both model should be the same (a unified model). In other word, a model which can be used for climate simulation should be validated through day-by-day weather fluctuations.

9.3.3 OGCM

Similar efforts to AGCM has been paid to simulate ocean circulation. However, this is not an easy task compared to the atmosphere, because there are many unknown processes and data in the ocean. Besides those, there exists the difference of characteristics between atmosphere and ocean. Eddies in the atmosphere are cyclone and anti-cyclone, which are thousands km. But eddies in the ocean is several ten km and characteristic speed of the ocean is slower than that of the atmosphere. This means that a huge computer resource to simulate ocean eddies. However, recent development in the ocean observation and super computer, we could step in another stage in ocean model development.

9.3.4 Coupled models

Atmospheric climate state is mainly determined by SST. Once SST is given, we can easily simulate the atmospheric state by using AGCM. However, SST is not an external factor but it is an internal factor. In other words, SST is also determined by the atmosphere. Atmosphere is influenced by the ocean through SST and the ocean circulation is controlled by the wind. Therefore, it is necessary to combine the atmosphere and the, ocean together to simulate the climate correctly. This work was first succeeded in the ENSO simulation, because both time scales is similar. However, the difference of the time scale in the atmosphere and the ocean is problem. For example, time integration of several months is sufficient for the atmospheric model, but it takes more than several hundred years to get a balanced state in the ocean. Intensive efforts are being done and these results are summarized in IPCC reports.

9.4 Global warming issue

9.4.1 Detection

The response to anthropogenic changes in climate forcing is main topic of the

global warming. Recent surface temperature increase is clearly demonstrated in the observation (Fig.7). However, natural internal and externally forced climate variability can occur on similar temporal and spatial scales. Slow climate components, such as the ocean, have particularly important roles on decadal and century time-scales and interact with faster components. Externally forced climate variations such as solar radiation or volcanic aerosols may change the climate. Increasing concentrations of greenhouse gases or sulphate aerosols are, of course, the most important factor to determine the future climate. Therefore it is very difficult to detect a signal of "global warming due to anthropogenic forcing".

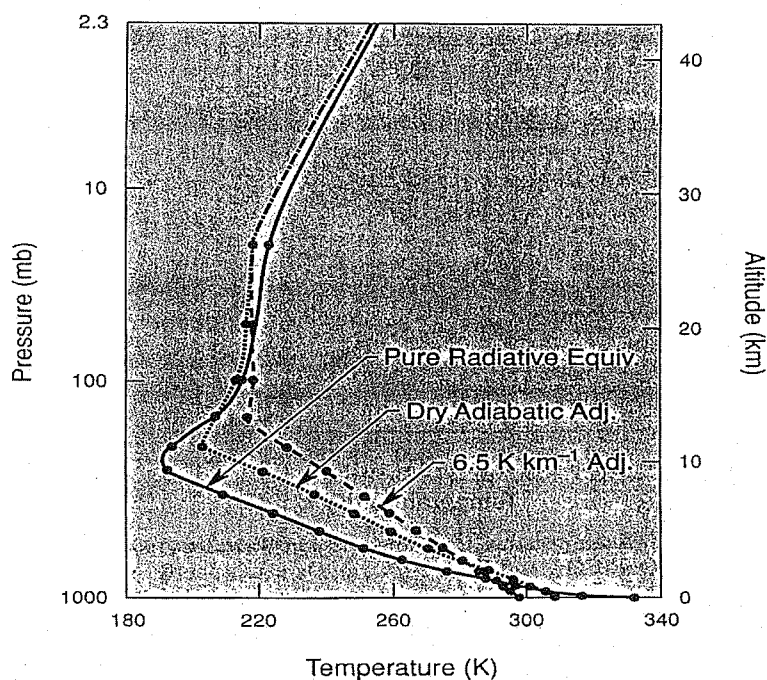


Figure 8. Vertical temperature profile obtained from the one-dimensional radiative-convective model of Manabe and Strickler (1964). Shown are temperature profiles for the pure radiative equilibrium case, convectively adjusting to a dry adiabat and a lapse rate of 6.5 K km^{-1} .

9.4.2 Prediction

In order to predict the future climate change associated with an anthropogenic forcing, prediction by using a climate model can be used in many research centers. These results are summarized in IPCC Tar. Fig.9 is one example of the prediction of

the globally averaged surface temperature. It can be noted that results are consistent each other, although there exists a

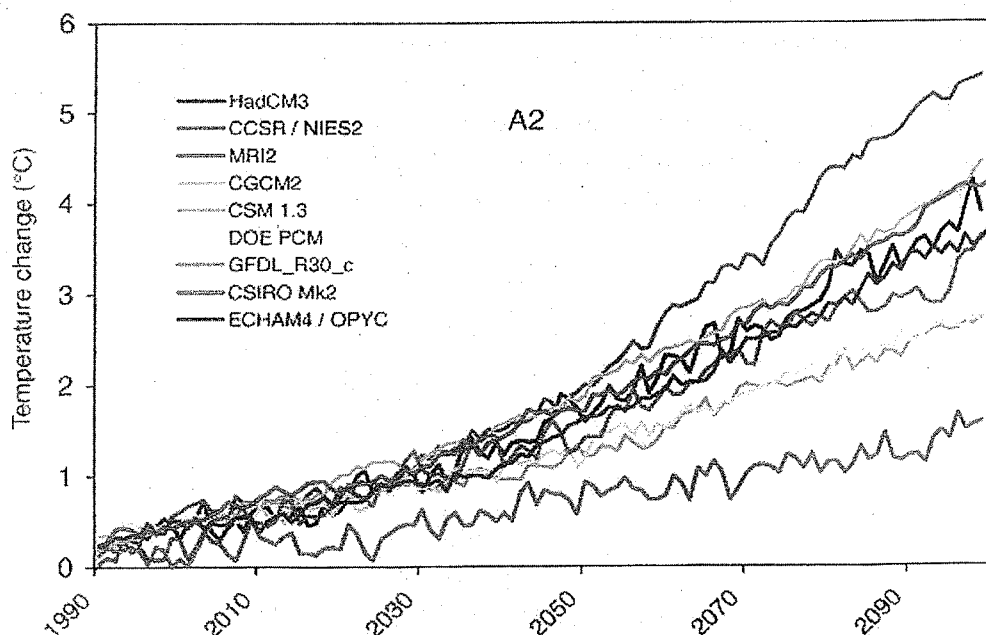


Figure 9. The time evolution of the globally averaged temperature change relative to the years (1961 to 1990) of the SRES simulations A2 (Unit: °C).

9.4.3 Attribution

Attribution is a most difficult task, because we have to find out whether a human impact is going to change the climate or not. As our knowledge and data is limited, it is impossible to prove it at present. We can guess what is going on. In Fig.10, the results are displayed. When we want to simulate a time sequence of the globally averaged surface temperature by using the climate model, it is impossible to simulate it only by using the natural forcing. However, when we use only anthropologic forcing, the simulation becomes better, and when we use both forcing, the correspondence between the simulation and the observation is the best. Based on these results, we concluded that it is difficult to explain the present warming without human impact.

Comparison between modeled and observations of temperature rise since the year 1860

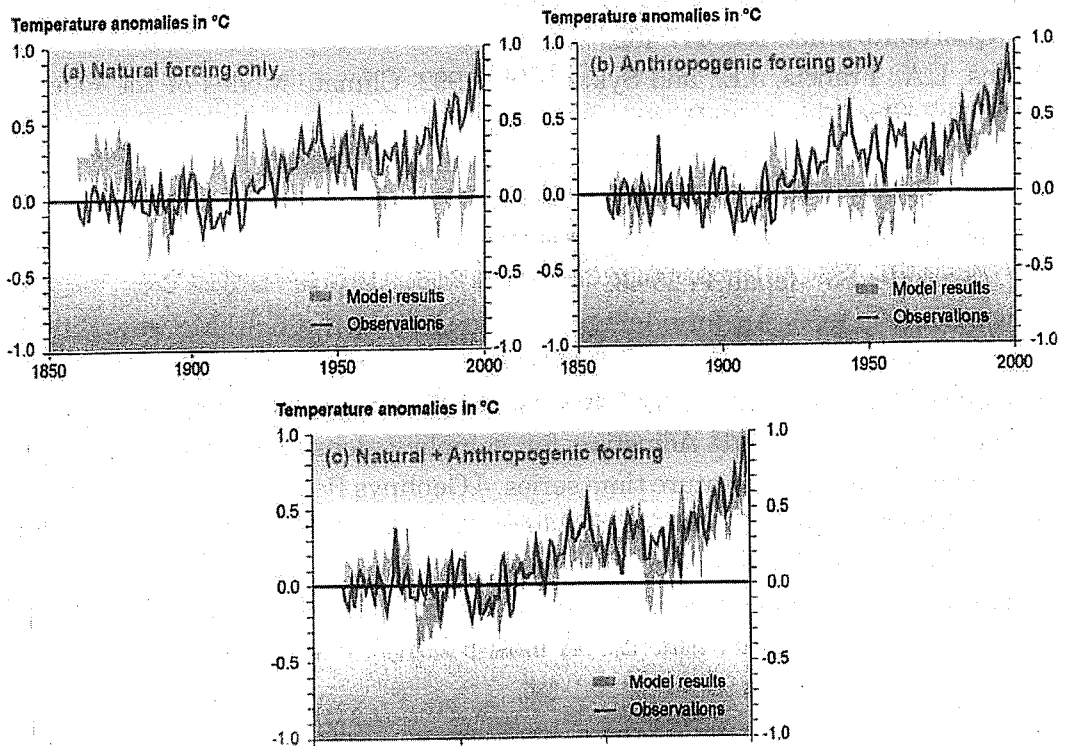


Figure 10. Temperature anomalies with natural forcing (top left), anthropogenic forcing (top right) and both (bottom). Unit is $^{\circ}\text{C}$.

9.5 Summary

Research on Climate Change is a new science. It is very interesting and important topic. However, it is related to a wide variety of disciplines in the Earth Science and it takes a huge effort to master it. However, integration of various disciplines is the future direction of the research and we should work harder to achieve this goal.

References

- Gill, A.E., 1980: Some simple solutions for heat-induced tropical circulation, *Quart.J.Roy.Met.* 106, 447-462.
- Frakes, L.A., Francis, J.E., and Syktus, J.L, 1992: *Climate Modes of the Paleozoic*. Cambridge University Press.
- IPCC, 2001: *Climate Change 2001, The Scientific Basis*, Cambridge University Press, 881pp.
- Matsuno, T., 1968: Quasi-geostrophic motions in the equatorial area, *J.Met.Soc.Japan*, 44, 25-43.
- Trewartha, G.T., 1986: *An Introduction to Climate* (4-th Edition), McGraw-Hill Book Co.
- Jones, P.D., T.J.Osborn, K.R.Briffa, C.K.Folland, E.B.Horton, L.V.Alexander, D.E.packer, and N.A.Rayner, 2001: Adjusting for sampling density in grid box land and ocean surface temperature time series, *J.Geohpys.Res.*, 106, 3371-3380.
- Lean, J., A.Sumanitch and O.White, 1992: Estimating the Sun's radiative output during the Maunder Minimum, *Geophys.Res.Lett.*, 19, 1591-1594.
- Manabe, S. and R.F.Strickler, 1964: On the thermal equilibrium of the atmosphere with a convective adjustment, *J. Atmos. Sci.*, 21, 361-385.

PRACTICE

Computer Simulation of Transport of Pollutants in the Atmosphere

Gakuji KURATA
Graduate School of Engineering,
Toyohashi University of Technology
Toyohashi, JAPAN
e-mail: kurata@eco.tut.ac.jp

In the chapter 1 and 8, the basics on transport process of air-pollutant and their modeling in the atmosphere were discussed. This chapter will deal with the practice about the modeling and numerical simulation of the advection and diffusion process of the pollutants in the atmosphere.

In order to obtain the solution of an advection-diffusion equation, strategies can be classified into two large groups. One group is the method to use mathematically solved equation, such as Gaussian-Puff or Gaussian-Plume model. Practice 1, 2 and 3 treats these analytical methods. Another method is numerical simulation. Practice 4 and 5 treats the one and two dimensional calculation by the simplest finite difference method.

The following software is used in this chapter.

- FORTRAN 77 or 90 Compiler
- GrADS (Visualization) <http://grads.iges.org/grads/>
(You can use any software which can draw a contour figure.)

1. Calculation of the concentration distribution using an analytical solution

Practice 1 Gaussian Puff Model

In the case of the instantaneous point source, emitted pollutants are diffused by the turbulence within the atmosphere. If the diffusivity is uniform and independent of direction (isotropic), then the solution is expressed as the following equation.

$$C = \frac{Q}{8(\pi K t)^{3/2}} \exp\left(-\frac{x^2 + y^2 + z^2}{4 K t}\right) \quad (1)$$

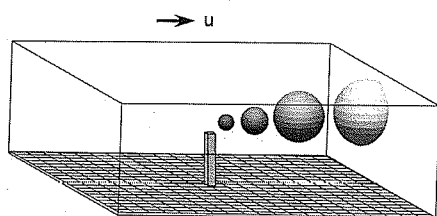
K : turbulent diffusivity (isotropic case)

Q : source intensity

When the source of emission is at (x_0, y_0, z_0) instead of $(0, 0, 0)$, and the discharged time is $t=t_0$, the concentration $C(x, y, z, t)$ at the time t in place (x, y, z) is expressed with the following formulas. Here, the wind speed (u, v, w) is uniform.

$$C(x, y, z, t) = \frac{Q}{8\{\pi^3(t-t_0)^3 K_x K_y K_z\}^{1/2}} \times \exp\left\{-\frac{1}{4(t-t_0)} \left[\frac{(x-x_0-ut)^2}{K_x} + \frac{(y-y_0-vt)^2}{K_y} + \frac{(z-z_0-wt)^2}{K_z} \right]\right\} \quad (2)$$

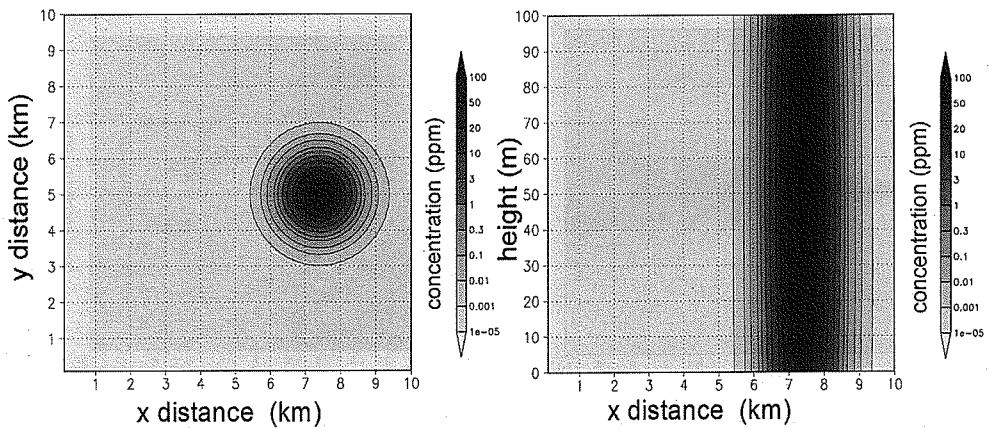
Here, calculate the concentration distribution ($\text{ppb} = 1.0 \times 10^{-9} \times \text{m}^3/\text{m}^3$) at t (sec), when the substance of $1.0 \text{ (m}^3\text{)}$ is instantaneously emitted at time $t=0$ from a chimney of height $H=50\text{m}$. Here, set a calculation domain to $10\text{km} \times 10\text{km} \times 100\text{m}$. A source is assumed to be at the center of the domain. Diffusion coefficient is assumed to be $50.0 \text{ (m}^2\text{/s)}$ for horizontal direction and $1.0 \text{ (m}^2\text{/s)}$ for vertical direction. Moreover, horizontal wind velocity is set to 1.0 (m/s) only for x direction. (Sample Program source code is Program-1 in Appendix of this chapter)



```
dset ^prog-1.dat
title TEST
undef 1e+20
xdef 100 linear 100 100
ydef 100 linear 100 100
zdef 11 linear 0 10
tdef 20 linear 0Z1JAN2004 1mn
vars 1
  c 11 99 c [ppbv]
endvars
```

List 1. A sample of GrADS control file

Since the outputted file (prog-1.dat) is 4-dimensional data containing three spatial and one temporal dimension, it can be visualized on any cross-section, using GrADS. A control file for GrADS is as List. 1. For example, concentration distribution at time $t=20(\text{min})$ is shown in Fig. 1.



Practice 2 Gaussian Plume Model

(a) Horizontal plot at $z=50(\text{m})$, $t=20(\text{min})$

(b) Vertical plot at $y=5000(\text{m})$, $t=20(\text{min})$

Figure 1 Example of GrADS output for Practice 1

If the pollutants are emitted continuously from point source, the concentration field becomes steady-state (not varying with time). So, the analytical solution is independent from time and is expressed as following.

$$C = \frac{Q}{2\pi u \sigma_y \sigma_z} \exp \left[-\frac{1}{2} \left(\frac{y^2}{\sigma_y^2} + \frac{(z-H)^2}{\sigma_z^2} \right) \right] \quad (3)$$

where, σ_y and σ_z are standard deviation in y and z direction as $\sigma_y(x) = \gamma_y \cdot x^{a_y}$, $\sigma_z(x) = \gamma_z \cdot x^{a_z}$. $\gamma_y, \gamma_z, a_y, a_z$ are listed in Table 2.1 in chapter 1.

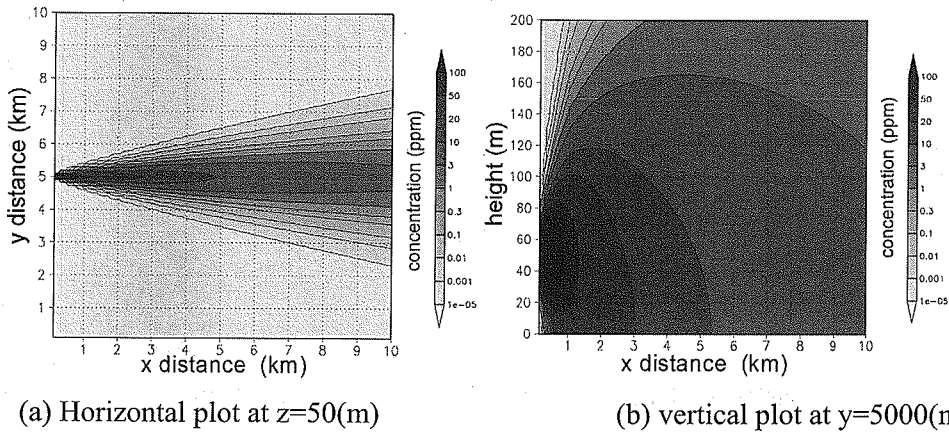


Figure 2. Example of GrADS Output for Practice 2

In the case that the stability condition of Pasquill-Gifford is “A”, and the substance of $1.0 (\text{m}^3/\text{s})$ is continuously emitted from the chimney of 50m height, visualize the concentration distribution under the steady state.

Sample program of this practice is listed as Program 2 in Appendix. In this program, steady-state solution is obtained after enough time steps.

Figure 2 (a) and (b) are visualized like Practice1.

Practice 3 Gaussian Plume Model (with ground reflection, Line source)

In the case of continuous line source, the concentration becomes uniform on the direction parallel to the source. So, only the vertical cross-section which intersected perpendicularly with the line source is considered. The steady-state analytical solution becomes following.

$$C = \frac{Q}{(2\pi)^{1/2} u \sigma_z} \exp\left[-\frac{z^2}{2\sigma_z^2}\right] \quad (4)$$

σ_z is calculated by $\sigma_z(x) = \gamma_z \cdot x^{az}$ as well as the case of point source.

Here, when the substance of $1.0 (\text{m}^3)$ is emitted per 1 m segment of the line source with a height of 50m , calculate the concentration distribution at the steady state. Wind velocity is assumed to be $5 (\text{m/s})$. Also, calculate under the condition where a lid is at 200m height.

Sample program is listed as Program 3 in Appendix. An example of a calculation result is shown in Figure 3.

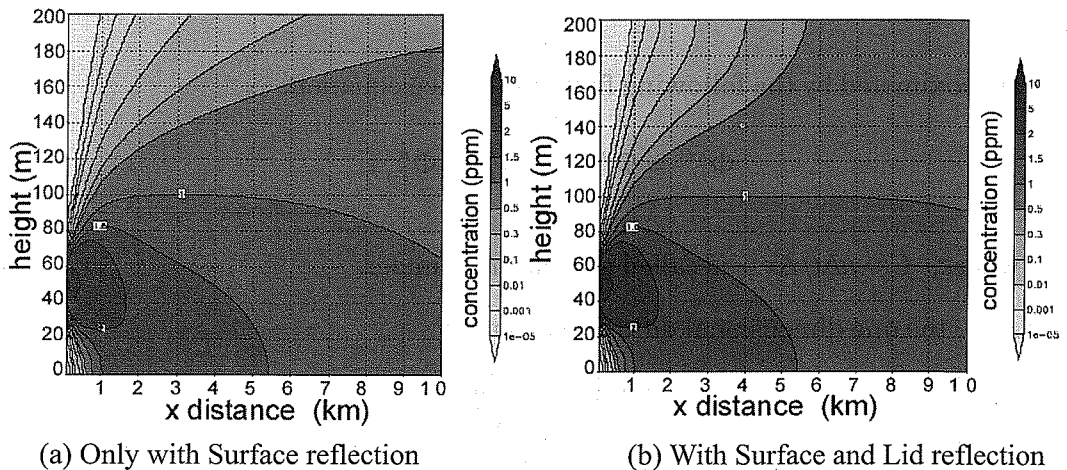


Figure 3. Examples of GrADS output for Practice 1.3

2. Numerical Simulation of 1-dimensional and 2-dimensional Advection and Diffusion by FTCS Method

In this section, 1-dimensional and 2-dimensional advection and diffusion equation are solved with the finite difference equation by FTCS (Forward Time Center Spatial) method.

Superscript index of arbitrary scalar variable, Φ , denotes the time, and subscript index denotes space, as shown in Figure 4.

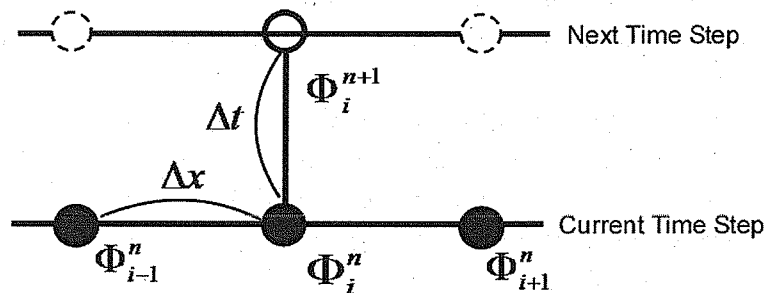


Figure 4. Grid definition of the variables, and the rule of the index.

Practice 4 One-dimensional advection diffusion equations.

One-dimensional advection equation

$$\frac{\partial \Phi}{\partial t} = -u \frac{\partial \Phi}{\partial x} \quad (4)$$

is approximated by the following finite difference equation.

$$\Phi_i^{n+1} = \Phi_i^n - \frac{C}{2} (\Phi_{i+1}^n - \Phi_{i-1}^n) \quad (4')$$

where, $C = u\Delta t/\Delta x$ is called as Courant number.

Also, the one dimensional diffusion equation

$$\frac{\partial \Phi}{\partial t} = K \frac{\partial^2 \Phi}{\partial x^2} \quad (5)$$

is approximated by the following finite difference equation.

$$\Phi_i^{n+1} = \Phi_i^n + d(\Phi_{i+1}^n - 2\Phi_i^n + \Phi_{i-1}^n) \quad (5')$$

where $d = K\Delta t/(\Delta x)^2$ is called as diffusion number.

Visualize the time variation of concentration distribution in case that the initial concentration ($C=100\text{ppm}$) exists between $x=50(\text{m})$ and $x=60(\text{m})$ on the one-dimensional space of length 1000 (m) using the difference equation by the FTCS method. Here, $dx=10$ (m), $K=5$ (m^2/s), $U=1.0(\text{m/s})$.

Sample program is listed as Program 4 in Appendix.

Concentration distribution at $t=1(\text{s})$, $t=100$ (s), $t=200$ (s), $t=400(\text{s})$, $t=600(\text{s})$, become like Figure 5.

Generally, the advection equation by FTCS method is unstable. In the above calculation, since the diffusion term weakened instability, calculation did not diverge. If the source code corresponding to the diffusion term is commented out in the above program, the solution will diverge. So, in order to stabilize an advection term, an upwind difference scheme is usually used.

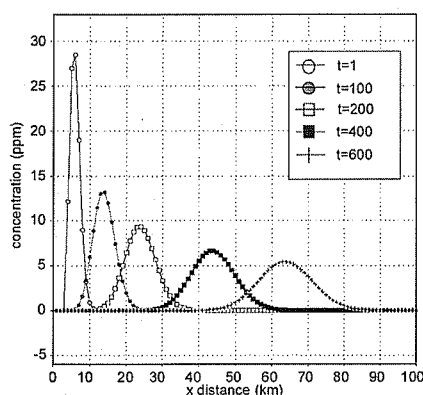


Figure 5. Concentration distribution with time by the FTCS method

The finite difference equation of an advection term becomes as follows.
(Substitute the line 24 of Program 4)

$\& \quad -U*(C(IX)-C(IX-1))/1.0/DX*DT \quad \leftarrow \text{Advection term}$
--

However, in this case, pseudo-diffusion of $Ke = \frac{1}{2}u\Delta x(1 - \frac{u\Delta t}{\Delta x})$ is generated.

When $u=1.0$ (m/s) and $\Delta t/\Delta x=1.0$, Ke become 0, so, pseudo-diffusion does not occur, and the original shape is maintained during advection.

However, for example, when $\Delta x=10.0$ (m) and $\Delta t=1.0$ (s), Ke become 4.5 (m^2/s). This is almost equal to an original diffusion coefficient and becomes the cause of a large error.

If a source code corresponding to the advection term in program 4 is commented out, examination of the stability about diffusion term can be done. Figure 6 is the sample result of the stability test. Here, the position of initial distribution was moved in the center of the domain. And, only Δt is varied.

If Δt satisfies the conditions acquired from the stability analysis of Von Neumann to a diffusion term as below, a solution is stabilized like Figure 6(a), but when not satisfying, a solution oscillates like Figure 6 (b).

$$\Delta t \leq \frac{1}{2} \frac{\Delta x^2}{K} \quad (= 10.0 \dots \text{in this condition})$$

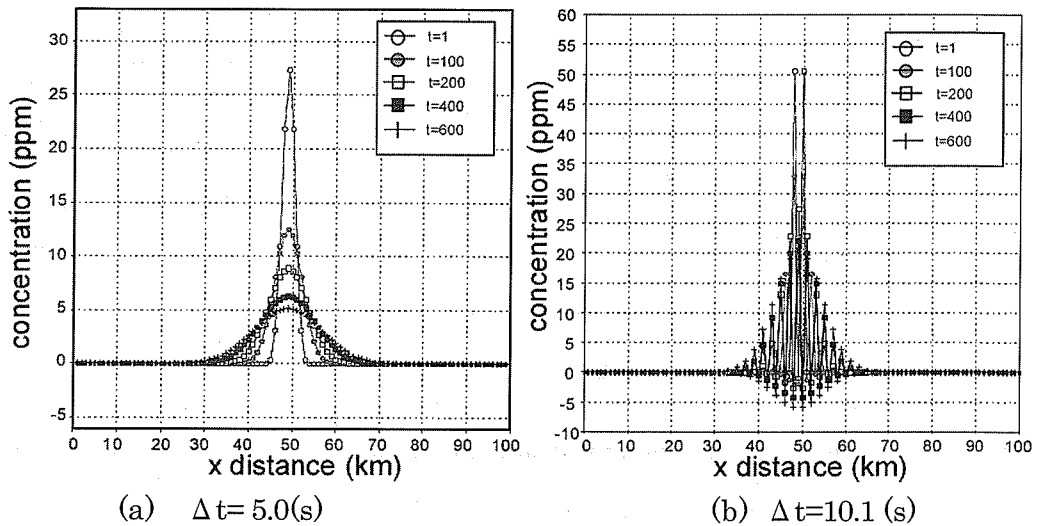


Figure 6. Results of stability test for FTCS diffusion equation.

Practice 5 Two-dimensional advection diffusion equations (Line source)

Calculate the concentration distribution, when pollutants of $1 \text{ (m}^3/\text{s)}$ per 1m segment of line source are discharged at the height of 50m . Wind velocity is 5 (m/s) for x direction, and diffusion coefficient is $3.0 \text{ (m}^2/\text{s)}$ for vertical and $5.0 \text{ (m}^2/\text{s)}$ for horizontal.

Sample program is listed as Program 5 in Appendix.

This program can output the concentration distribution for every minute of the unsteady state started from the clean condition. The concentration distribution after enough time (in this case, after 200 minutes) becomes almost steady, and can be compared with the result of the Plume model of Practice-3. Although some difference can be seen by the difference between the definition of the diffusion width of a Plume model, and the uniform diffusion coefficient used here, however it is clear that the tendency is well in agreement.

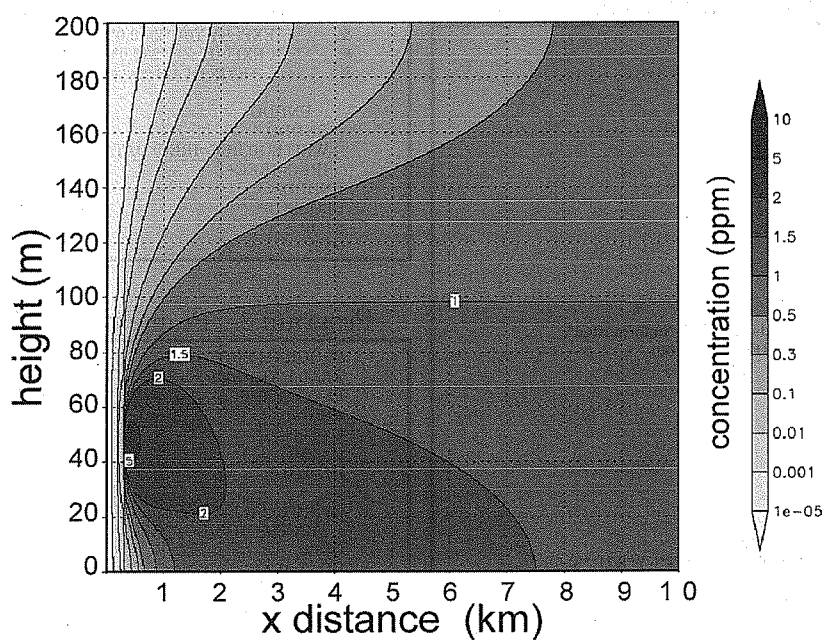


Figure 7. Result from 2D FTCS advection-diffusion Model.

Appendix 1. Program Source Sample (P. 232–233)

PRACTICE

Program 1 3D Puff model calculation

```

PROGRAM PROG1
REAL DATA(100,100)
PI=3.1415926
IREC=1
U=1
V=0
W=0
KX=50.0
KY=50.0
KZ=1.0
X0=5000.0
Y0=5000.0
Z0=50.0
T0=0.0

OPEN(10,FILE="prog-1.dat",FORM="unformatted",
& ACCESS="DIRECT",RECL=100*100)
Q=1.0
DO IT=1,20
  DO IZ=1,11
    DO IX=1,100
      DO IY=1,100
        T=IT*60.0
        X=IX*100.0
        Y=IY*100.0
        Z=IZ*10.0
        DATA(IX,IY)= 1.0E9 *
& Q/(8.0*((PI**3)*((T-T0)**3)*KX*KY*KZ)**(0.5))
& *EXP(-(X-X0-U*T)**2/KX
& + (Y-Y0-V*T)**2/KY
& + (Z-Z0-W*T)**2/KZ )
& /(4.0*(T-T0)))
      ENDDO
    ENDDO
    WRITE(10,REC=IREC) DATA
    IREC=IREC+1
  ENDDO
ENDDO
CLOSE(10)
STOP
END

```

Program 2 3D Plume model (point source)

```

PROGRAM PROG2
REAL DATA(100,100)
PI=3.1415926
IREC=1
U=1.0
H=50.0
Y0=5000.0

OPEN(10,FILE="prog-2.dat",FORM="unformatted",
& ACCESS="DIRECT",RECL=100*100)
Q=1.0
DO IZ=0,20
  Z=IZ*10.0
  DO IX=1,100
    X=IX*100.0
    DO IY=1,100
      Y=IY*100.0
CCCC---- Parameters are Stability class A
      IF(X.LT.1000.0) THEN
        SIGY=0.1107*X**0.929
      ELSE
        SIGY=0.1467*X**0.889
      ENDIF
      IF(X.LT.1000) THEN
        SIGZ=0.1046*X**0.826
      ELSE IF(X.LT.10000) THEN
        SIGZ=0.400*X**0.632
      ELSE
        SIGZ=0.811*X**0.555
      ENDIF

```

```

& DATA(IX,IY)= 1.0E6 *
& Q/(2.0*PI*U*SIGZ*SIGY)
& *EXP(-(Y-Y0)**2/(2.0*SIGY**2))
& *(EXP(-(H-Z)**2/(2.0*SIGZ**2))
& +EXP(-(H+Z)**2/(2.0*SIGZ**2)))

ENDDO
ENDDO
WRITE(10,REC=IREC) DATA
IREC=IREC+1
ENDDO
CLOSE(10)
STOP
END

```

Program 3 Plume model (Line source)

```

PROGRAM PROG3
REAL DATA(100)
PI=3.1415926
IREC=1
U=5.0
H=50.0
HL=200.0

OPEN(10,FILE="prog-3.dat",FORM="unformatted",
& ACCESS="DIRECT",RECL=100)
Q=1.0
DO IZ=0,20
  Z=IZ*10.0
  DO IX=1,100
    X=IX*100.0
CCC -----Stability Class D
    IF(X<1000) THEN
      SIGZ=0.1046*X**0.826
    ELSE IF(X<10000) THEN
      SIGZ=0.400*X**0.632
    ELSE
      SIGZ=0.811*X**0.555
    ENDIF
    DATA(IX)=1.0E3 * Q/((2.0*PI)**0.5*U*SIGZ)
    & *
    & EXP(-(H-Z)**2/(2.0*SIGZ**2))
    & +EXP(-(H+Z)**2/(2.0*SIGZ**2))
    & +EXP(-(HL+(HL-H)-Z)**2/(2.0*SIGZ**2)) ←
    & ) Remove 'C', if Lid case

    ENDDO
    WRITE(10,REC=IREC) DATA
    IREC=IREC+1
  ENDDO
ENDDO
CLOSE(10)
STOP
END

```

Program 4 1-D FTCS advection-diffusion Model

```

PROGRAM PROG4
REAL C(101),C1(101), KX

OPEN(10,FILE="prog-4.dat",FORM="UNFORMATTED"
& ACCESS="DIRECT",RECL=101)

U=1.0
DT=1.0
DX=10.0
KX=5.0
IREC=1
NSTEP=2000.0/DT
NOUT=20.0/DT ← Output Interval (sec)

DO IX=1,101

```

COMPUTER SIMULATION OF TRANSPORT OF POLLUTANTS IN THE ATMOSPHERE

```

C(IX)=0.0
ENDDO

C(5)=100.0

DO IT=1,NSTEP
DO IX=2,100
C1(IX)=C(IX)
&      -U*(C(IX+1)-C(IX-1))/2.0/DX*DT      <- Advection term
&      +KX*(C(IX+1)-2.0*C(IX)+C(IX-1))      <- Diffusion term
&      /DX**2 * DT      <- (diffusion)

ENDDO

C1(1)=0.0
C1(101)=C1(100)

DO IX=1,101
C(IX)=C1(IX)
ENDDO
IF(MOD(IT,NOUT).eq.0)THEN
WRITE(10,REC=IREC) C
IREC=IREC+1
ENDIF

ENDDO

CLOSE(10)

STOP
END

```

```

&      /DZ**2 * DT
& ENDDO
ENDDO

DO IX=1,101
C1(IX,1)=C(IX,1)+
&      -U*(C(IX,1)-C(IX-1,1))/1.0/DX*DT
&      +ALPHAX*(C(IX+1,1)-2.0*C(IX,1)+C(IX-1,1))
&      /DX**2 * DT
&      +ALPHAZ*(C(IX,2)-2.0*C(IX,1)+C(IX,1))
&      /DZ**2 * DT
C1(IX,81)=C(IX,81)+
&      -U*(C(IX,81)-C(IX-1,81))/1.0/DX*DT
&      +ALPHAX*(C(IX+1,81)-2.0*C(IX,81)+C(IX-1,81))
&      /DX**2 * DT
&      +ALPHAZ*(C(IX,81)-2.0*C(IX,81)+C(IX,80))
&      /DZ**2 * DT
& ENDDO

DO IZ=1,81
C1(1,IZ)=0.0
C1(101,IZ)=C1(100,IZ)
ENDDO

DO IX=1,101
DO IZ=1,81
C(IX,IZ)=C1(IX,IZ)
ENDDO
ENDDO
IF(MOD(IT,NOUT).eq.0)THEN
WRITE(10,REC=IREC) C
IREC=IREC+1
ENDIF

ENDDO

CLOSE(10)

STOP
END

```

Program-5 2-D FTCS advection-diffusion
Model (Line source)

```

PROGRAM PROG5
REAL C(101,81),C1(101,81)

OPEN(10,FILE="prog-5.dat",FORM="UNFORMATTED"
& ,ACCESS="DIRECT",RECL=101*81)

U=5.0
DT=0.5
DX=100.0
DZ=2.5
ALPHAX=5.0
ALPHAZ=3.0
IREC=1
NSTEP=12000.0/DT
NOUT=60.0/DT

DO IX=1,101
DO IZ=1,81
C(IX,IZ)=0.0
ENDDO
ENDDO
C(5,20)=100.0

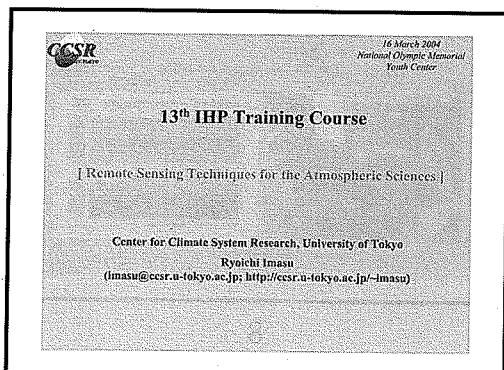
DO IT=1,NSTEP
C(5,20)=C(5,20)+(1.0E3*DT/DX/DZ)
DO IX=2,100
DO IZ=2,80
C1(IX,IZ)=C(IX,IZ)
&      -U*(C(IX+1,IZ)-C(IX-1,IZ))/2.0/DX*DT
&      -U*(C(IX,IZ)-C(IX-1,IZ))/1.0/DX*DT
&      +ALPHAX*(C(IX+1,IZ)-2.0*C(IX,IZ)+C(IX-1,IZ))
&      /DX**2 * DT
&      +ALPHAZ*(C(IX,IZ+1)-2.0*C(IX,IZ)+C(IX,IZ-1))

```

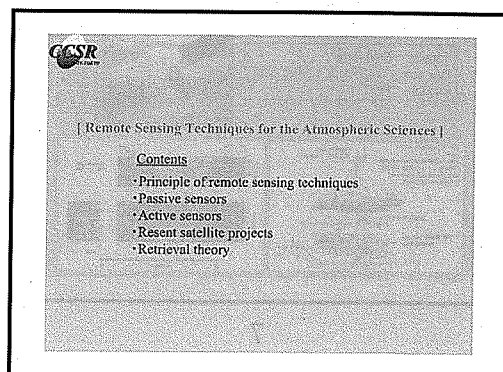
Technical Tours (Selected Presentation Slides):

- (1) R. Imasu: Remote Sensing Technologies for the Atmospheric Sciences
- (2) A. Abe-Ouchi: Climate in the Past
- (3) The Earth Simulator Center, JAMSTEC

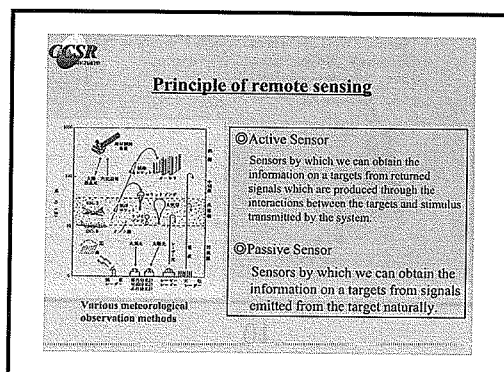
(1) R. Imasu: Remote Sensing Technologies for the Atmospheric Sciences



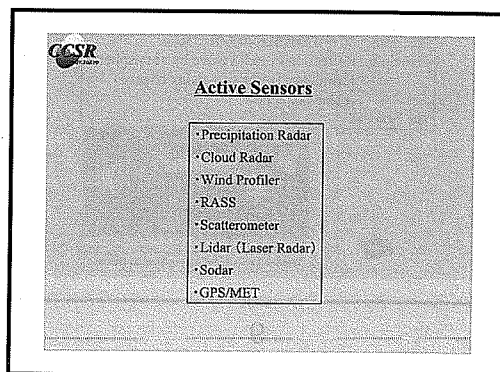
1



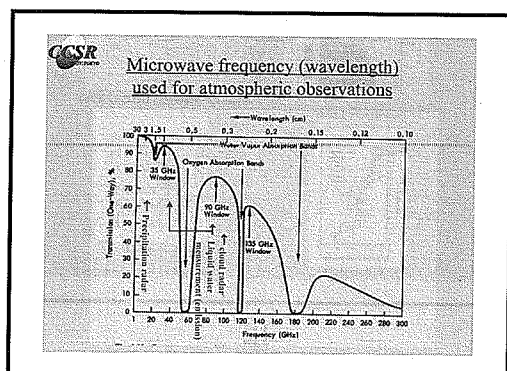
2



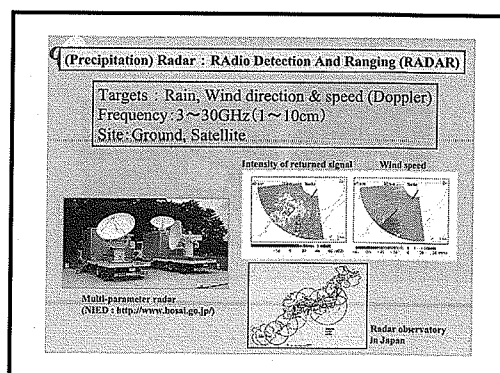
3



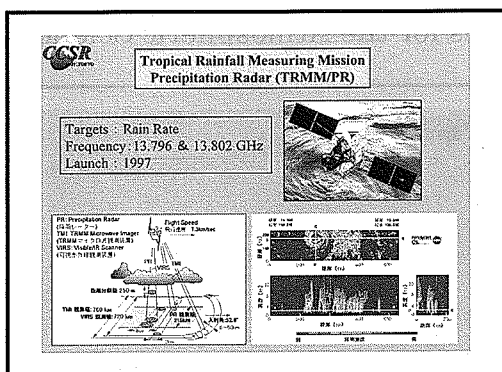
4



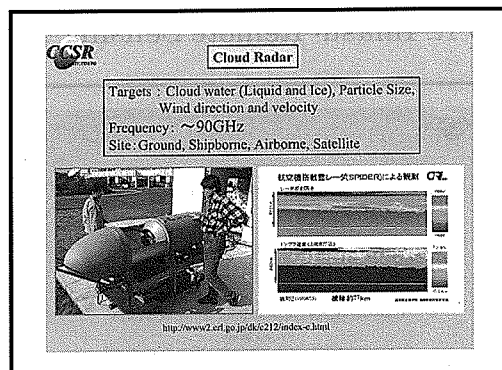
5



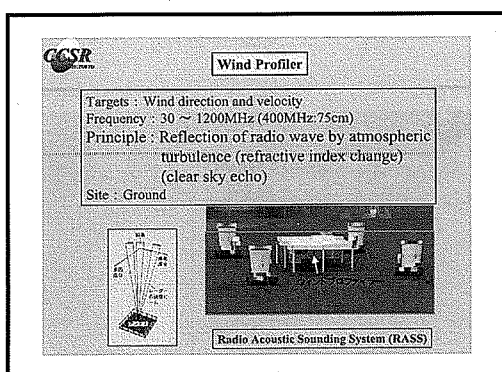
6



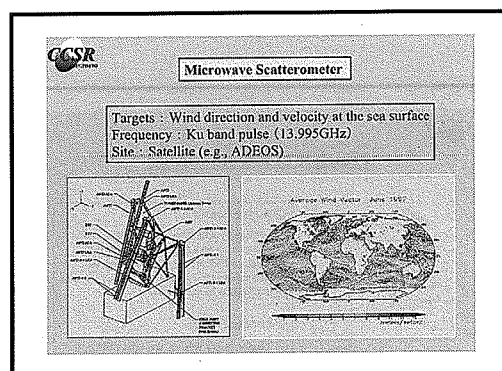
7



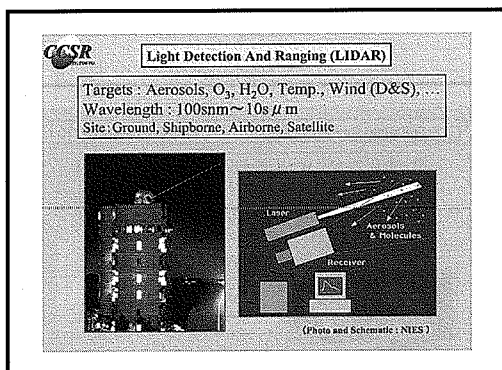
8



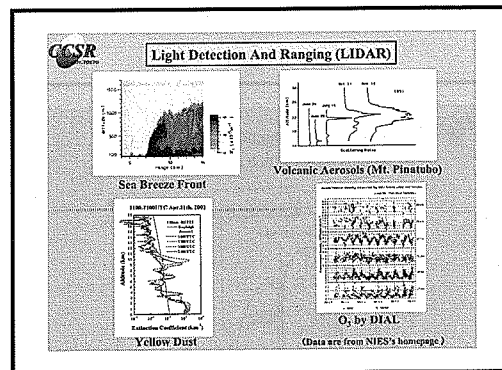
9



10



11



12

CCSR

Light Detection And Ranging (LIDAR)

[Lidar Type]	[Targets]
Mie Scattering Lidar	: Aerosols, Clouds
Rayleigh Scattering Lidar	: Temperature (Pressure)
Raman Scattering Lidar	: Temperature, Water vapor
Resonance Scattering/Fluorescence Lidar	: Sporadic E, Na, Fe, Ca layer
Doppler Lidar	: Wind direction and speed
Differential Absorption Lidar (DIAL)	: H ₂ O, O ₃ , SO ₂ , NO ₂ , ...

Details : <http://info.nies.go.jp/8094/-cm/Japanese/LidarText/LidarInt.htm>

13




CCSR

Sonic Detection And Ranging (SODAR)

Targets : Wind direction and velocity (Doppler)

Principle : Temperature (air density) dependency of the speed of sound

Site : Ground

(Photo : Univ. Kyushu)

14

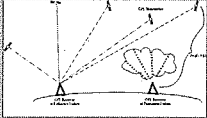
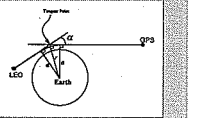
CCSR

Global Positioning System / Meteorology (GPS/MET)

Targets : Temperature, Water vapor (Perceptible water)

Principle : Refractive index change due to the fluctuation of temperature and water vapor in the path

Site : Ground

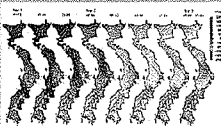
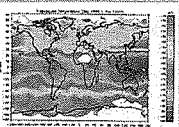



(Kursinski et al., 2000)

15

CCSR

Global Positioning System / Meteorology (GPS/MET)

(Iwabuchi, 1996) (Nakada et al., 2000: JMSJ, 691-700)

16

CCSR

Passive Sensors

- Satellite Imagery (VIS, NIR, TIR: Temp. & H₂O)
- Sounding Sensors (Temp., Gases)
- Dobson spectrometer (O₃)
- Microwave radiometer

[Satellite sensors] (for minor constituents)

- Emission (Microwave) measurement sensors
- Solar occultation sensors
- Solar Scattering-Absorption sensors
- Emission (Infrared) measurement sensors

17

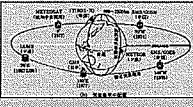

CCSR

Meteorological Satellite (Imagery)

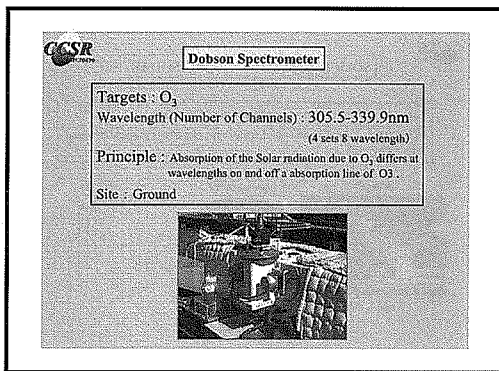
Targets : Clouds, Water vapor, Sea Surface Temperature, ...

Wavelength (Number of Channels) : 0.5-12 μ m (2-5Ch)

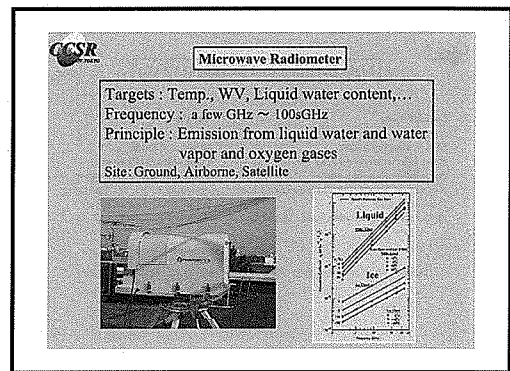
Orbit : Geostationary, Polar orbit (geosynchronous, non-sync.)

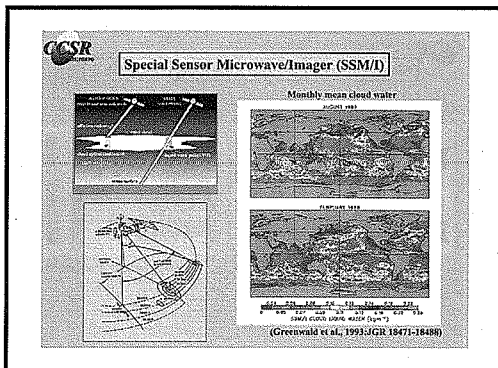
18



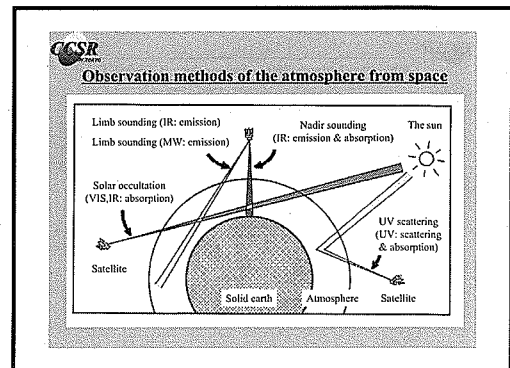
19



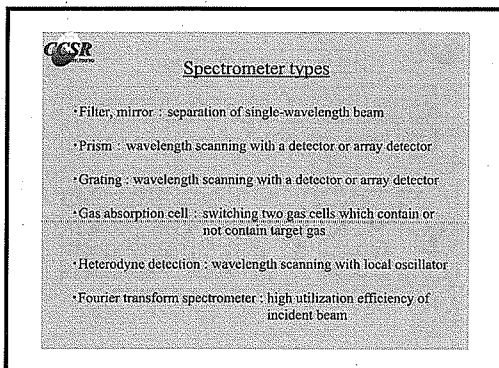
20



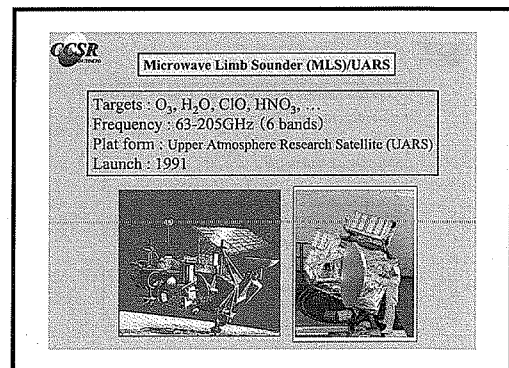
21



22



23



24

JCSF

Superconducting subMillimeter-wave Limb-Emission Sounder (SMILES)

Targets : O₃, ClO, HCl, HOCl, HNO₃, SO₂, ...
 Frequency : 624.32-650.32GHz (3バンド)
 Plat form : JEM/ISS
 Launch : 2005(?)

JEM/ISS
 International Space Station
 Limb Sounding

SMILES CUTAWAY VIEW
 (Schematic View)

[illegible]

Stratospheric Aerosol and Gas Experiment (SAGE) I, II, III


Targets : Aerosols, O_3 , NO_2 , H_2O , $OClO_2$...

Wavelength (resolution) : 280-1030nm (~1nm)

Plat form : METEOR-3M, Space Station

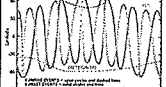
Launch : 2001, 2004 (?)

SAGE III Instrument



1. Primary Instrument
 2. Secondary Instrument
 3. Tertiary Instrument
 4. Quaternary Instrument
 5. Quinary Instrument
 6. Senary Instrument
 7. Septenary Instrument
 8. Octenary Instrument
 9. Nonary Instrument
 10. Decenary Instrument
 11. Undecenary Instrument
 12. Duodecenary Instrument

SAGE III SOLAR OCCULTATION COVERAGE



SAGE I (1980-1989) - solid line
 SAGE II (1990-1999) - dashed line
 SAGE III (2000-2009) - dotted line

Stratospheric Aerosol Measurement I, II (SAM)

October 1978 - December 1992

Optical Depth

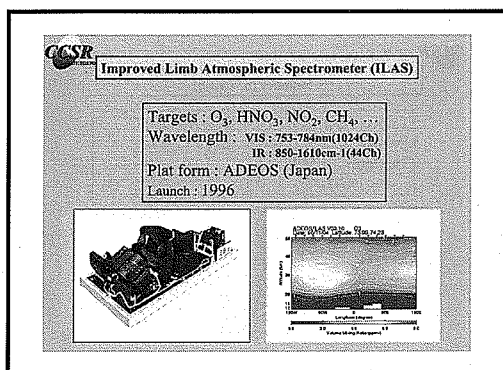
10¹
10⁰
10⁻¹
10⁻²

1979 1981 1983 1985 1987 1989 1991

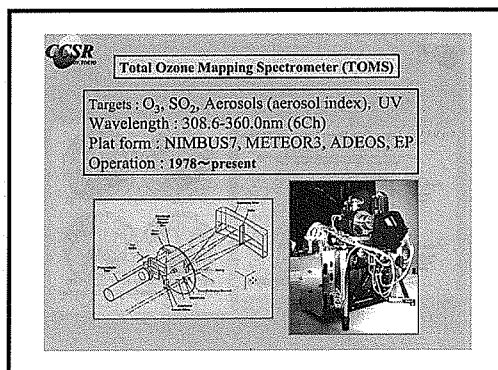
Auror
Atlantic

Date	Location
1979-10-10	Atlantic
1980-01-10	Atlantic
1980-04-10	Atlantic
1980-07-10	Atlantic
1980-10-10	Atlantic
1981-01-10	Atlantic
1981-04-10	Atlantic
1981-07-10	Atlantic
1981-10-10	Atlantic
1982-01-10	Atlantic
1982-04-10	Atlantic
1982-07-10	Atlantic
1982-10-10	Atlantic
1983-01-10	Atlantic
1983-04-10	Atlantic
1983-07-10	Atlantic
1983-10-10	Atlantic
1984-01-10	Atlantic
1984-04-10	Atlantic
1984-07-10	Atlantic
1984-10-10	Atlantic
1985-01-10	Atlantic
1985-04-10	Atlantic
1985-07-10	Atlantic
1985-10-10	Atlantic
1986-01-10	Atlantic
1986-04-10	Atlantic
1986-07-10	Atlantic
1986-10-10	Atlantic
1987-01-10	Atlantic
1987-04-10	Atlantic
1987-07-10	Atlantic
1987-10-10	Atlantic
1988-01-10	Atlantic
1988-04-10	Atlantic
1988-07-10	Atlantic
1988-10-10	Atlantic
1989-01-10	Atlantic
1989-04-10	Atlantic
1989-07-10	Atlantic
1989-10-10	Atlantic
1990-01-10	Atlantic
1990-04-10	Atlantic
1990-07-10	Atlantic
1990-10-10	Atlantic
1991-01-10	Atlantic
1991-04-10	Atlantic
1991-07-10	Atlantic
1991-10-10	Atlantic

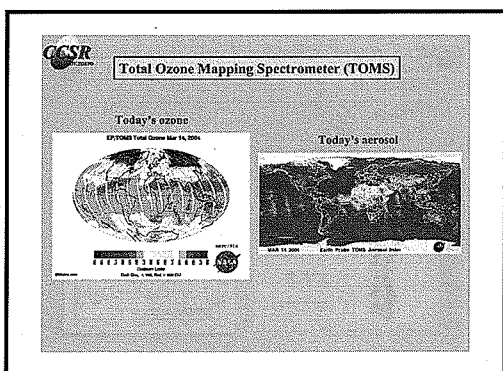
239



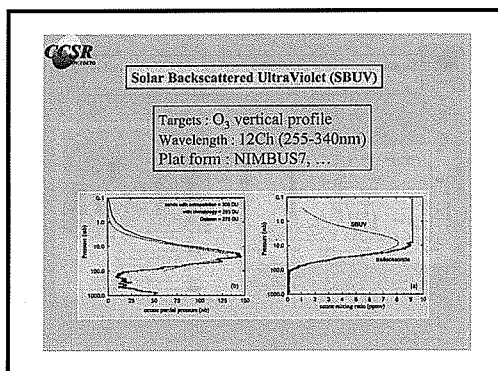
31



32



33



34

CCSR

Infrared sensors (launched)

Sensor	Satellite	Channel	Target
SIRS	Nimbus 3 (1969)	8Ch 5cm ⁻¹	T, H ₂ O
IRIS	Nimbus 4 (1970)	5-25 cm ⁻¹ (5,2.8cm ⁻¹)	T, H ₂ O
SCR	Nimbus 4, 5 (1970, 1972)		T, H ₂ O
ITPR	Nimbus 5 (1972)	7Ch	T, H ₂ O
VTPR	NOAA 2-5 (1972-1976)		T, H ₂ O
PMR	Nimbus 6 (1975)		T (>50km)
LRJR	Nimbus 6 (1975)	Limb T, H ₂ O, O ₃	
LIMS	Nimbus 7 (1978)	Limb T, H ₂ O, O ₃ , NO ₂ , HNO ₃	
HIRS	TIROS-N (1978)	20Ch	T, H ₂ O; O ₃
	NOAA 6 (1979)		
VISSR	GOAS 4 (1980)	12Ch	T, H ₂ O
ISAMS	UARS (1991)	4.6-16.6 μm	CO, CH ₄ , ...
HALOE	UARS (1991)	2.43-10.25 μm	HCl, HF, ...

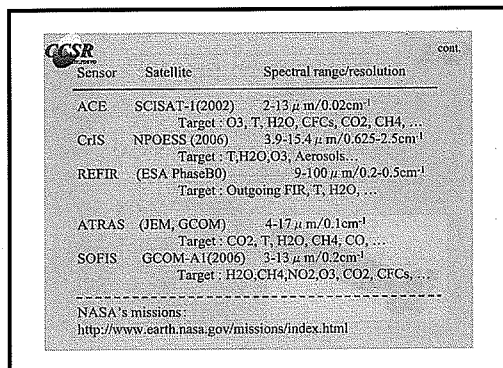
35

CCSR

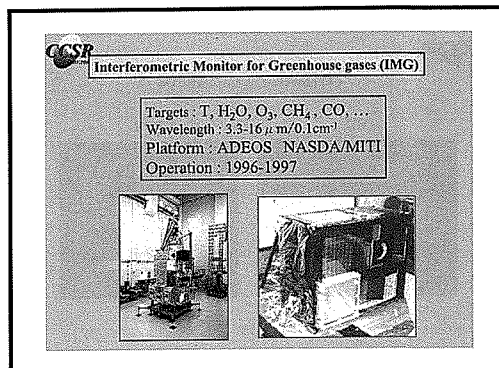
Infrared sensors (planned or proposed)

Sensor	Satellite	Spectral range/resolution
IMG	ADEOS (1996)	3.3-15.4 μm/0.1cm ⁻¹ Target : T, H ₂ O, CH ₄ , CO, O ₃ , ...
MOPITT	EOS-AMT (1999)	3Ch Target : CO, CH ₄
AIRS	EOS-PM (2002)	3.74-15.4 μm (2400Ch)/1200(I/DI) Target : T, H ₂ O
MIPAS	ENVISAT-1 (2002)	4.15-14.6 μm/0.035cm ⁻¹ Target : Stratospheric minor constituents
TES	EOS-Chem (2004)	3.2-15.4 μm/0.1(0.025)cm ⁻¹ Target : O ₃ (Tropo.), CO, CH ₄ , ...
IASI	METOP-1 (2004)	3.4-15.5 μm/0.25cm ⁻¹ Target : T, H ₂ O, O ₃ , CH ₄ , CO, ...

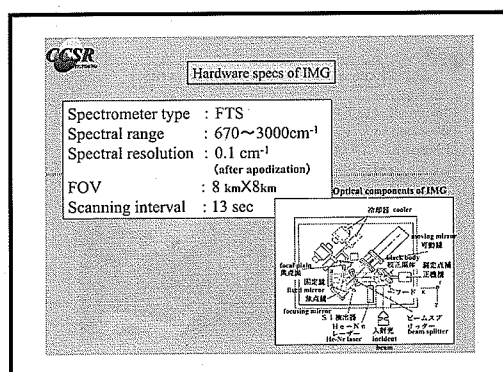
36



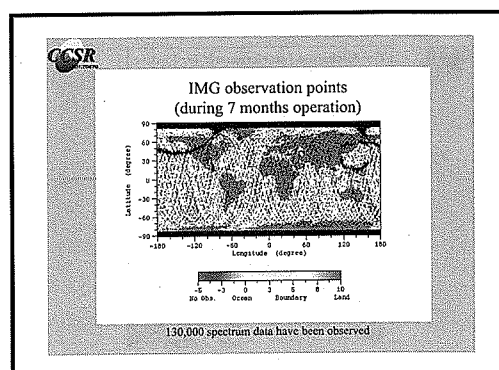
37



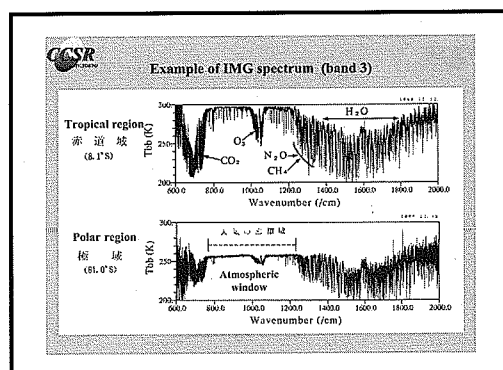
38



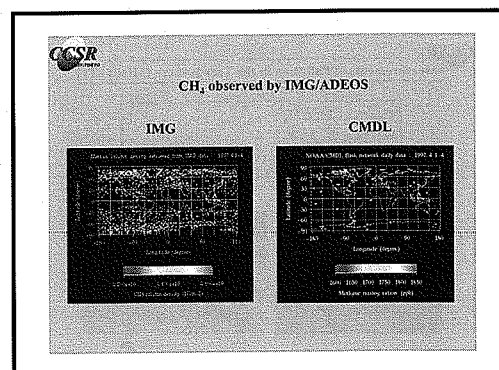
39



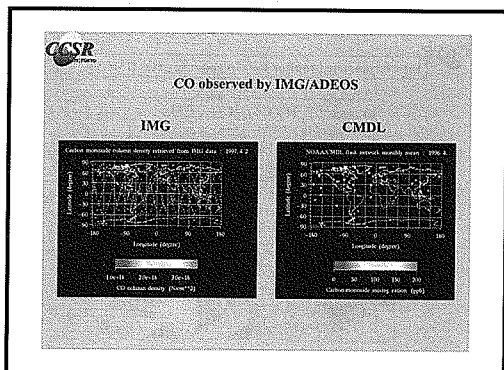
40



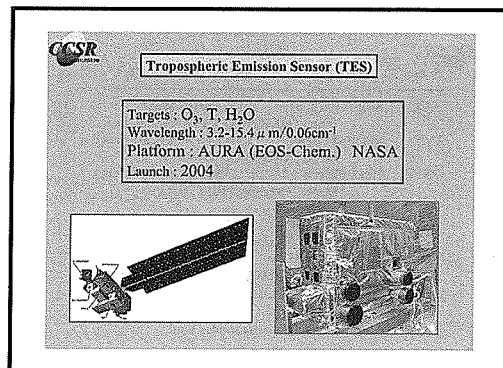
41



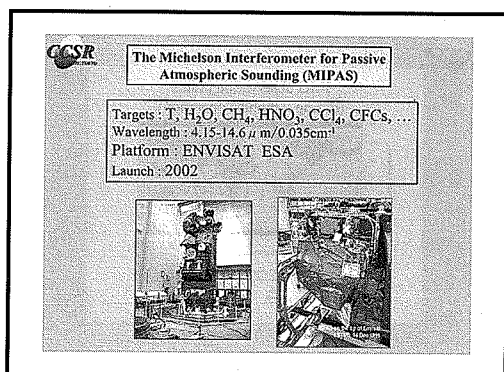
42



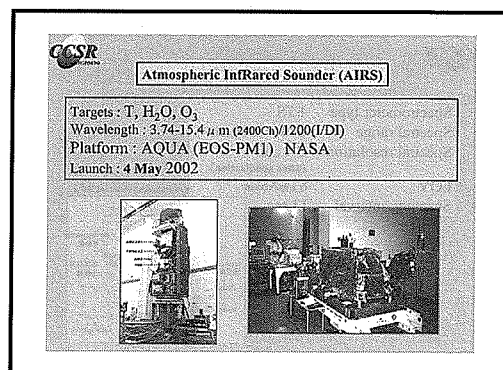
43



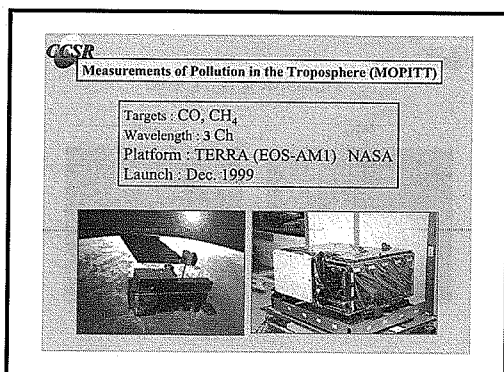
44



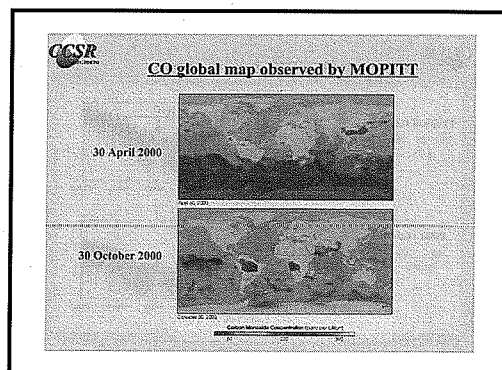
45



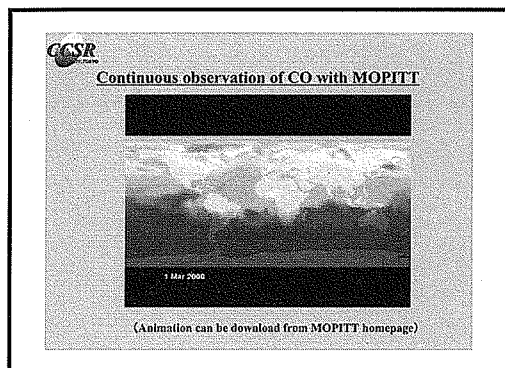
46



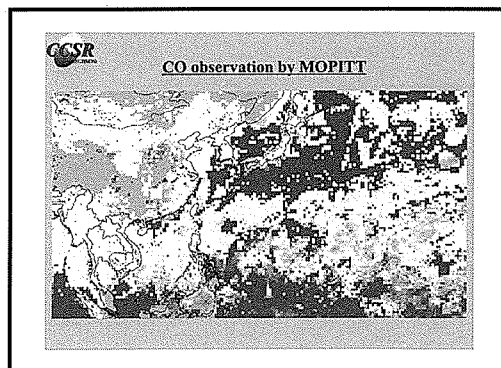
47



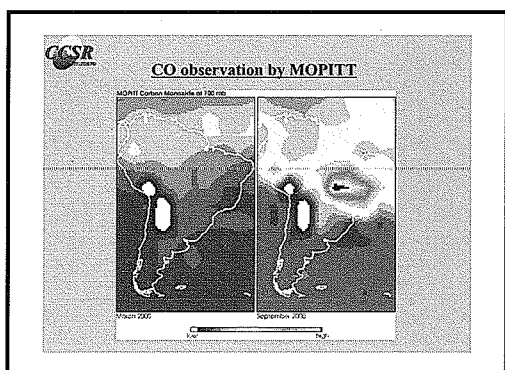
48



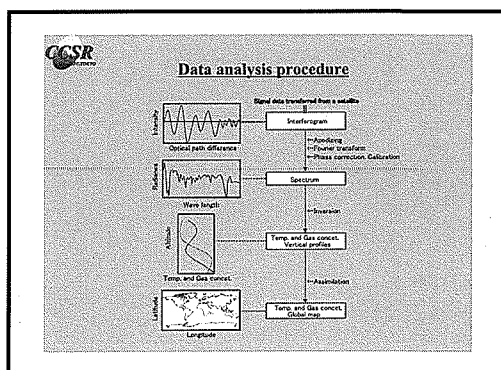
49



50



51



52

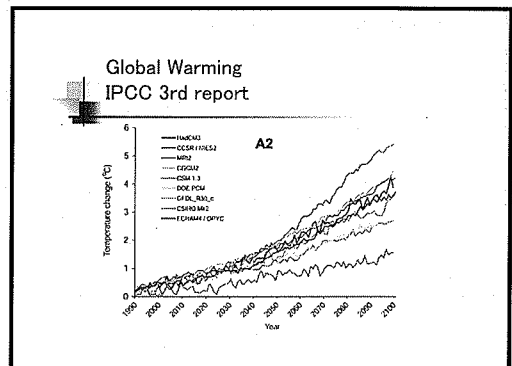
(2) A. Abe-Ouchi: Climate in the Past

13 th IHP Training Course
 <Climate in the Past>

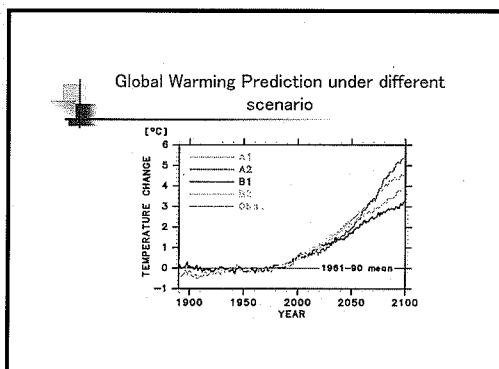
Ayako Abe-Ouchi
 (CCSR, Univ. of Tokyo)
 abeouchi@ccsr.u-tokyo.ac.jp

- How was the Climate in the Past?
- Climate Modelling

1



2



3

Mountain Glacier

■ More than 80 % of Mountain Glacier will melt down by the end of 21 Century

4

Ice Sheet:
 Antarctica and Greenland

Ice Sheet volume*
 Converted to Sea level change

- Antarctica ~ sea level 70 meter
- Greenland ~ Sea level 7 meter

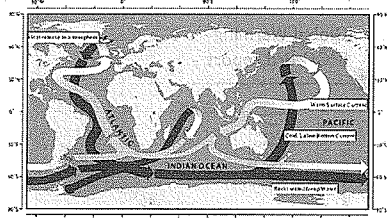
5

IPCC(2001) Sea level change 1990→2100
 by IS92a+AOGCMs

Components	Sea level change(m)		
Thermal expansion	0.11	—	0.43
Glaciers	0.01	—	0.23
Greenland ice sheet	-0.02	—	0.09
Antarctic ice sheet	-0.17	—	0.02
...
Total			0.77

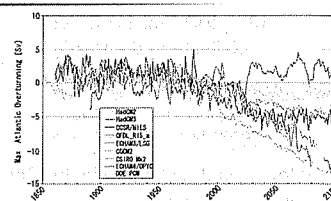
6

Ocean Current (Thermohaline Circulation)



7

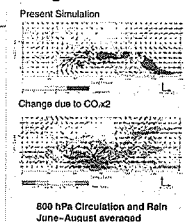
Change of Meridional Circulation (North Atlantic)



8

Summer Monsoon Change due to Global Warming

- Monsoon is regionally intensified due to Glob. Warming.
- Water vapour transport increases due to Glob. Warming.



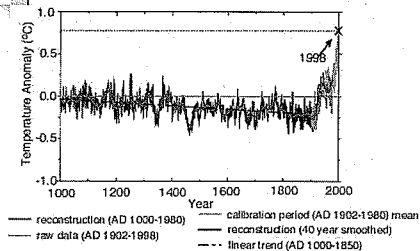
9

Climate Change in the Past ?

- Did the climate in the past change?
- The mechanism of the climate change in the past?

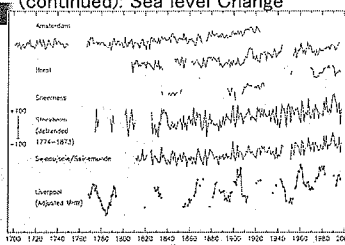
10

Temperature change in the past 1000 Years

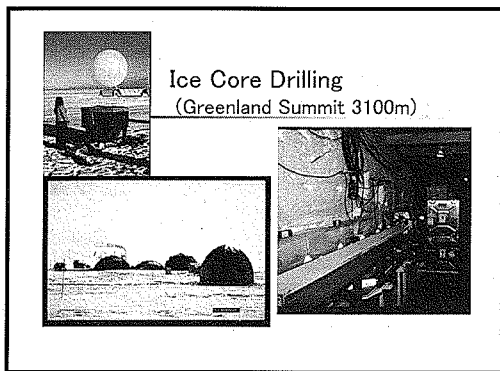


11

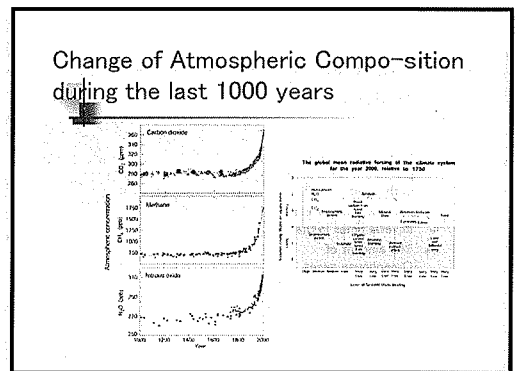
Climate in the past 1000 years (continued): Sea level Change



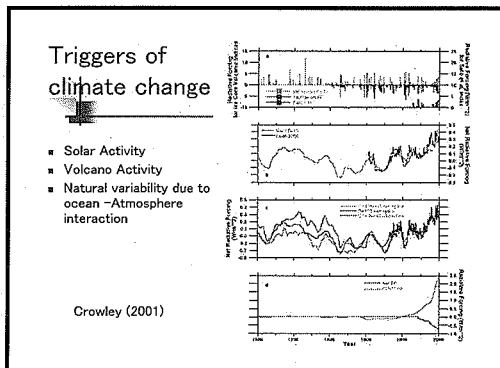
12



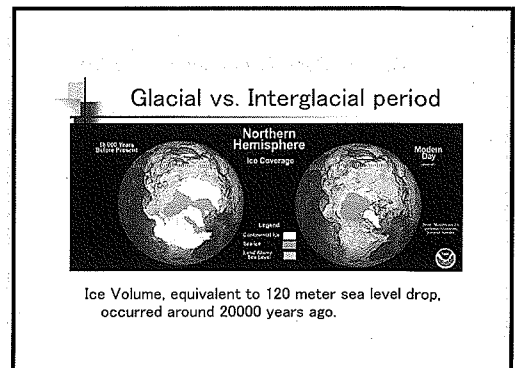
13



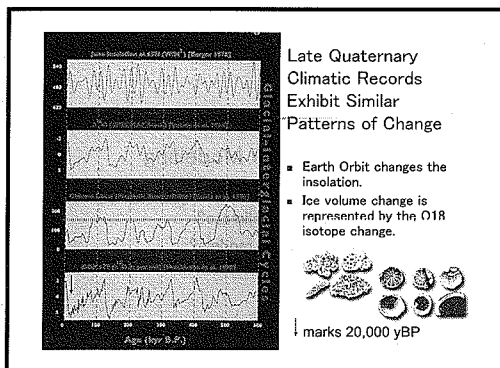
14



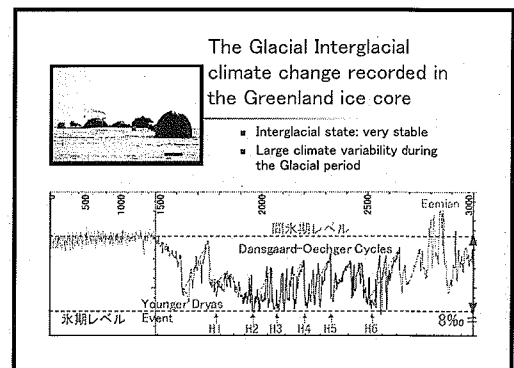
15



16



17



18

The climate change in the Earth history

- It was even warmer than present in some periods in the past
- Earth was covered by ice several times in the past.
- The amount of Greenhouse gases changed due to the Solid earth activity.

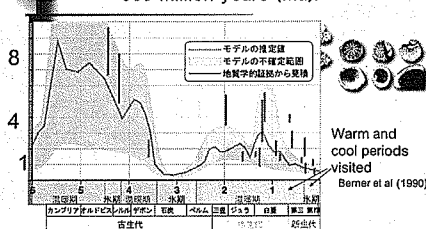


SeismoSaurus

—Jura

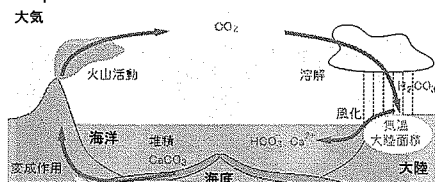
19

Atmospheric CO2 change in the last 600 Million years (Ma).



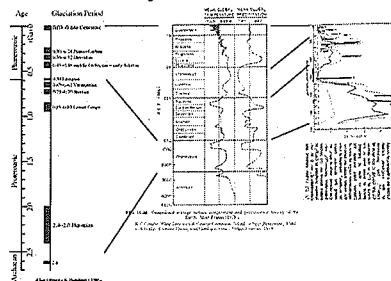
20

Carbon Cycle (Geochemical cycle)



21

Earth history and Climate



22

Summary

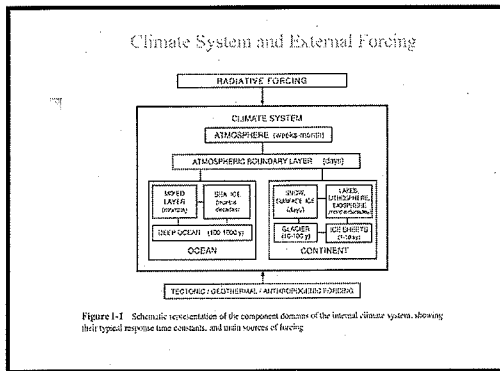
- The warming in the 19- 20 Century is above the significant level in the last 1000 years.
- Climate changes larger than the anticipated global warming occurred in the past many times.
- The climate change for the society and for the earth have different problems.
- Modelling the earth climate is useful for both predicting and understanding the climate in the past.

23

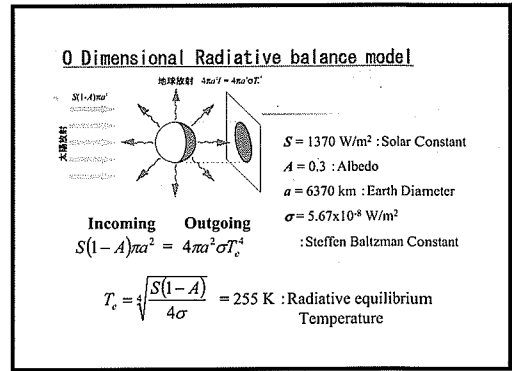
Climate Modelling

- Can we model the climate?
- How do we use the models?

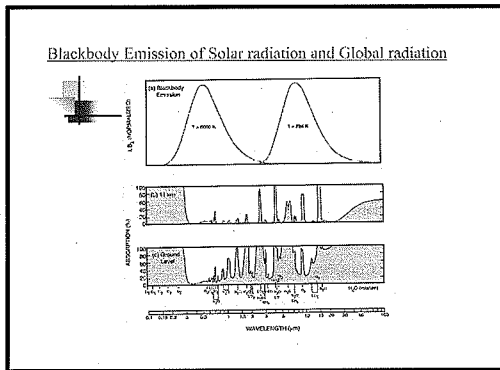
24



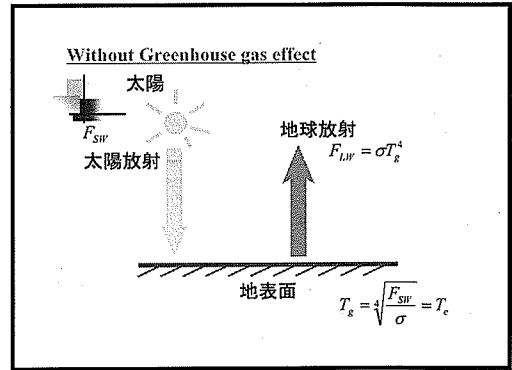
25



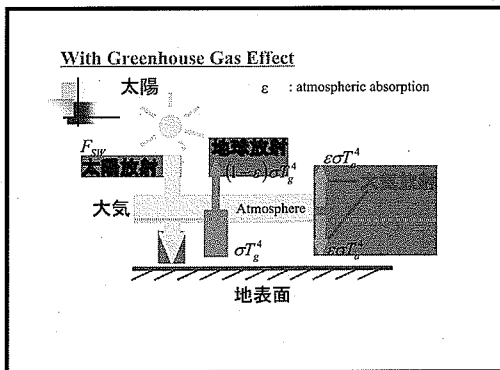
26



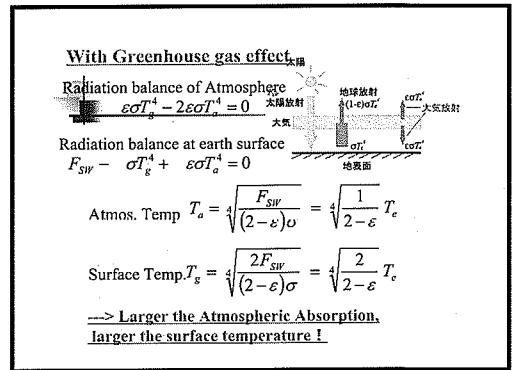
27



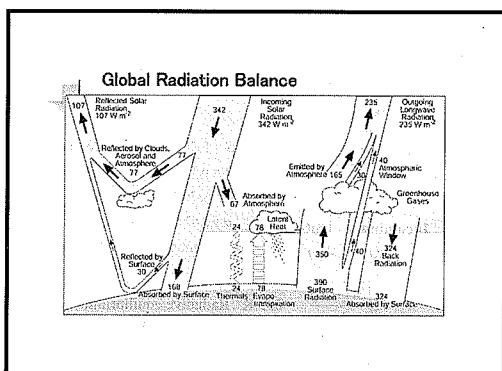
28



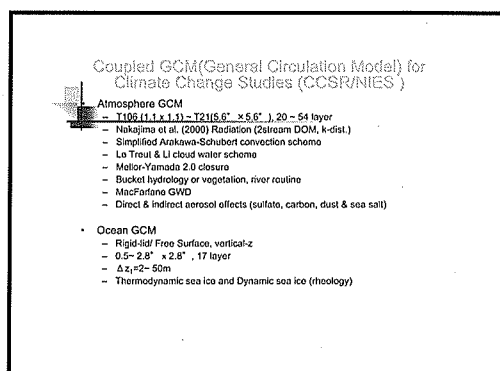
29



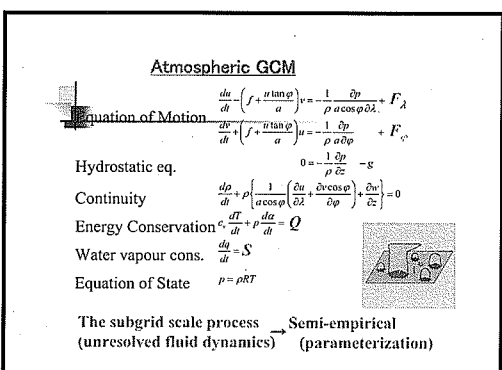
30



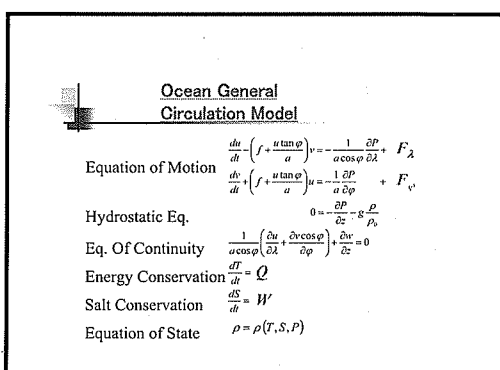
31



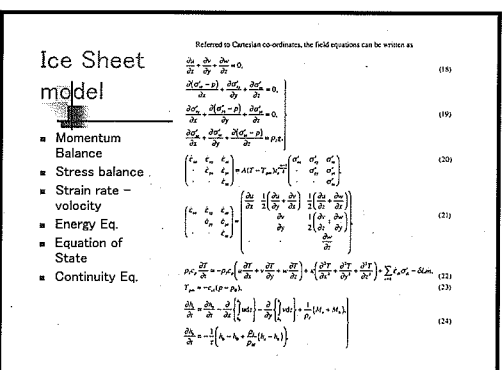
32



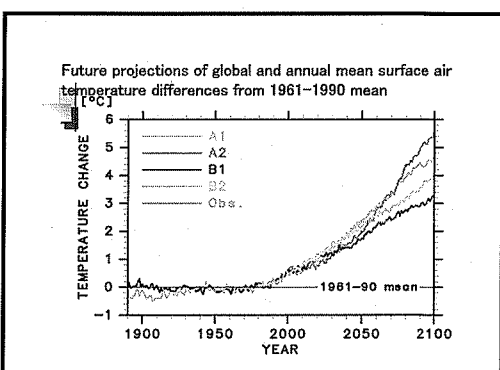
33



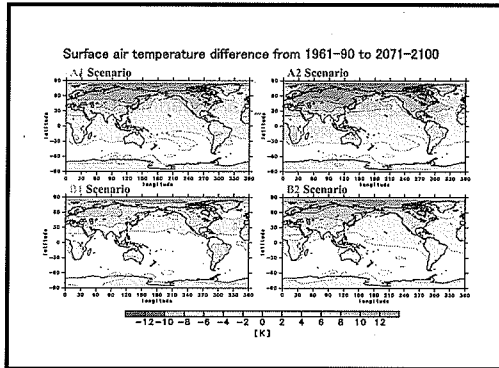
34



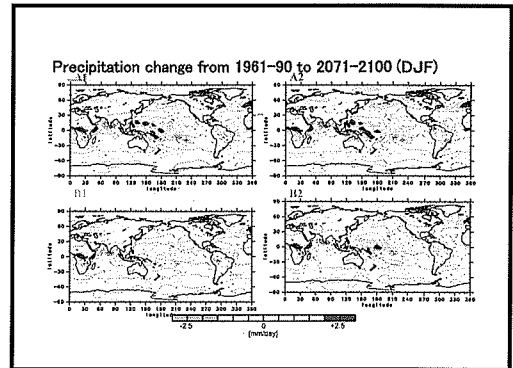
35



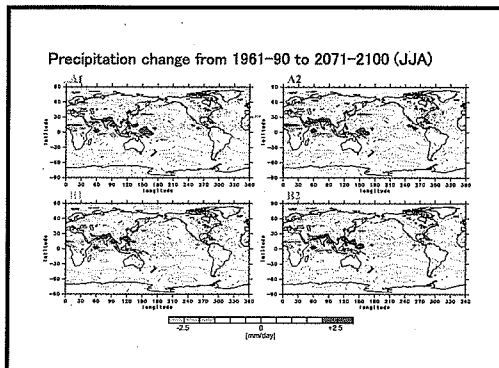
36



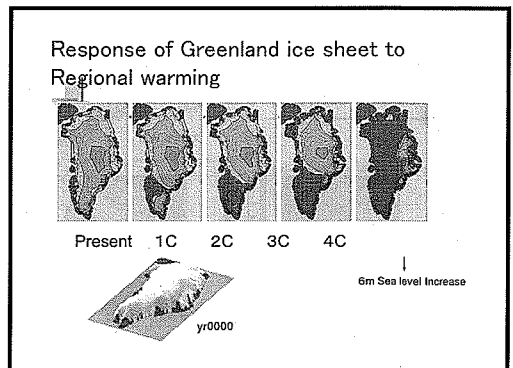
37



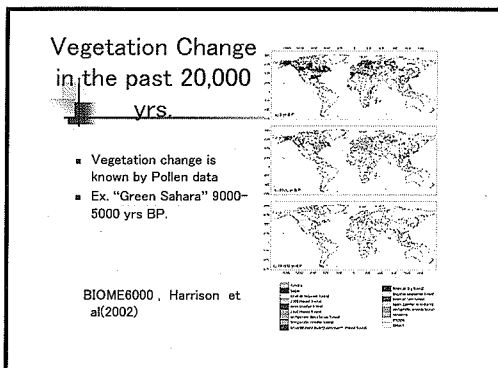
38



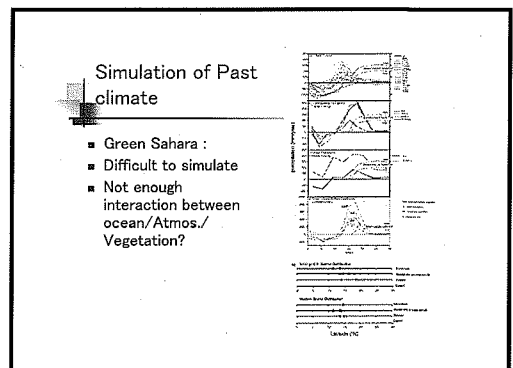
39



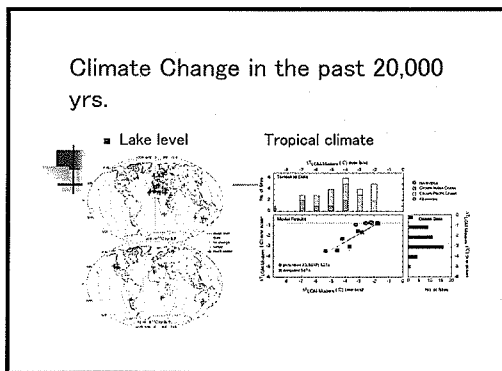
40



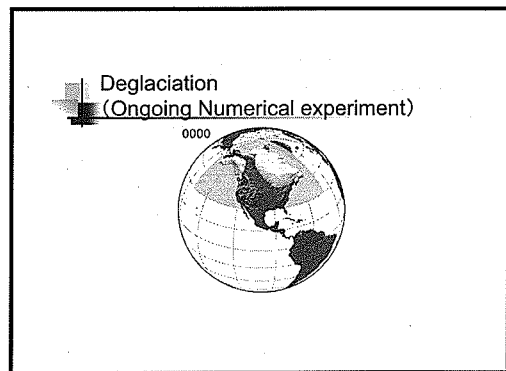
41



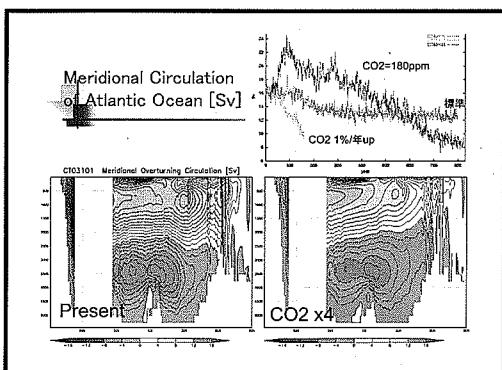
42



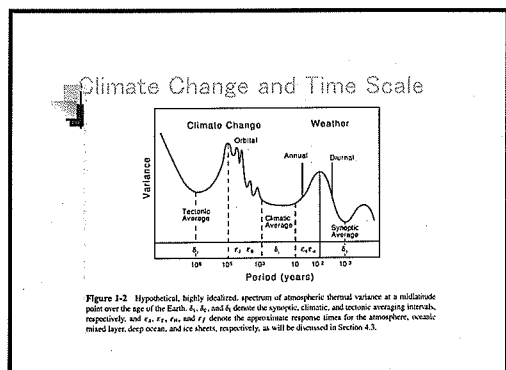
43



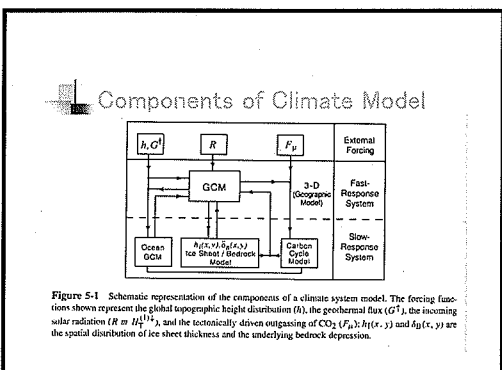
44



45

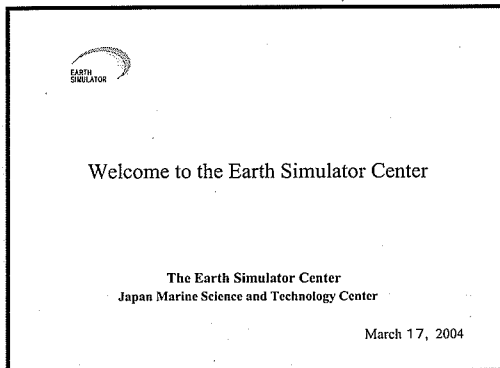


46

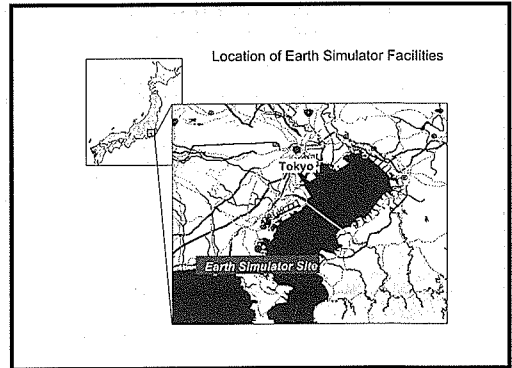


47

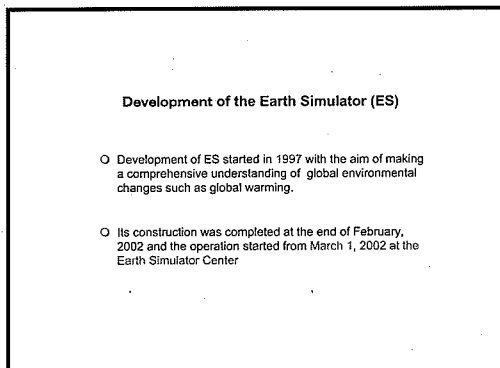
(3) The Earth Simulator Center, JAMSTEC



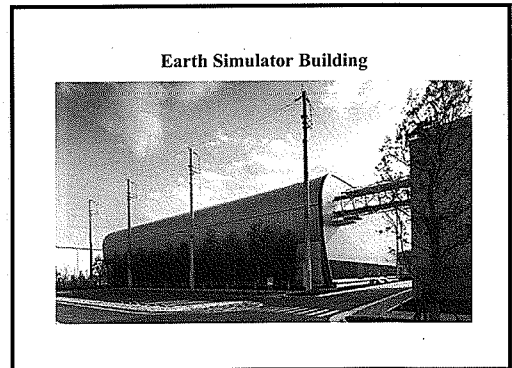
1



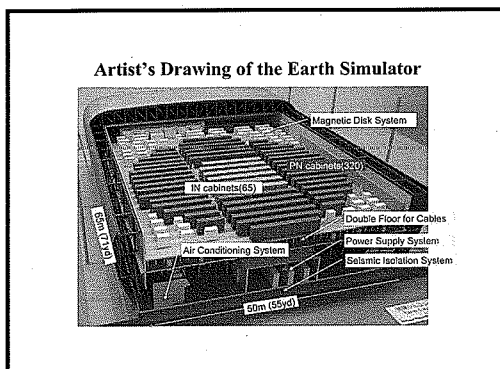
2



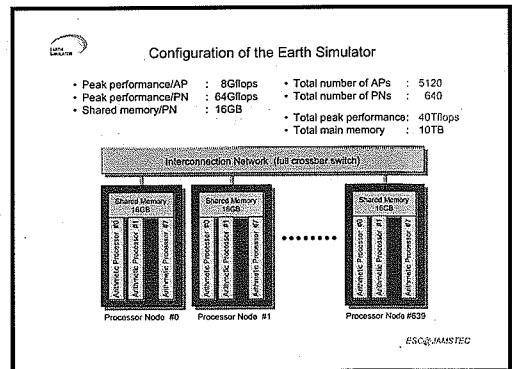
3



4



5



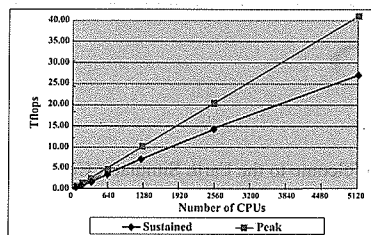
6

Ultra high performance of the Vector-based Parallel Earth Simulator

- ★ 35.86 Teraflops (about 90% of the peak value for the Linpack benchmark test in April, 2002)
- ★ 26.58 Teraflops (about 65% of the peak value for the global atmospheric circulation code (AFES) in May, 2002)

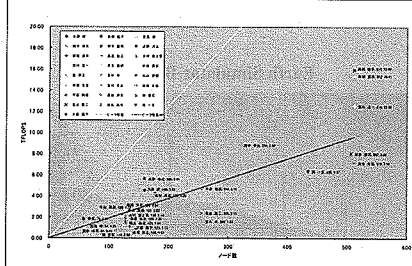
7

Sustained Performance



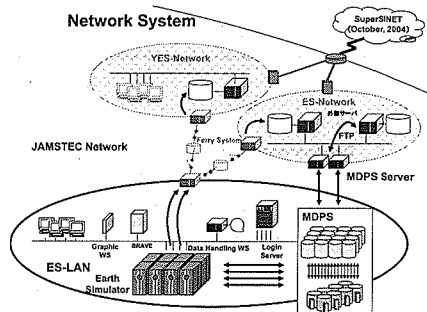
8

Average Performance of Running Projects for 2003



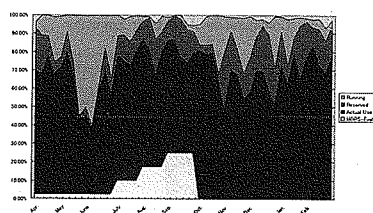
9

Network System



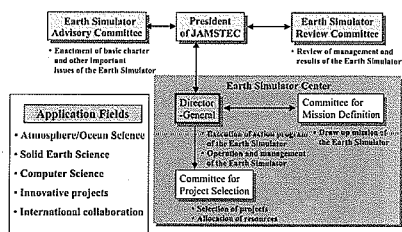
10

Running Status of ES (April 7, 2003 – March 7, 2004)



11

Management of the Earth Simulator



12

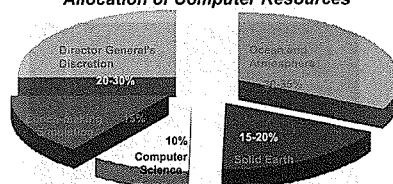
Roles of the Earth Simulator Center

- Produce reliable and sound prediction data of global environmental changes
- Promote a big leap in high performance computing science and technology
- Take the initiative and leadership in opening up the 21st Century Science apart from the 20th century reductionism
- Become the Center of Excellence of simulation Science

13



Allocation of Computer Resources



Selected Projects		
Research fields	at present in 2002	at future in 2005
Ocean and Atmosphere	17	12
Solid Earth	8	9
Computer Science	4	2
Epoch-Making Simulation	11	11

14

34 projects are accepted in
FY2003

- 12: Climate Science
- 9: Solid Earth Science
- 2: Computer Science
- 11: Innovative Projects

15

International Collaboration

- Hadley Center/CGAM (UK)
- Scripps Institute of Oceanography (USA)
- CIRA (Italy)
- Canada Met Office (Canada)
- NERSC (USA)
- CNRS/IFREMER (France)
- Texas Univ.(USA)
- Minnesota Univ. (USA)

16

The real value of Simulator is
determined not only by its speed
but also by its main memory

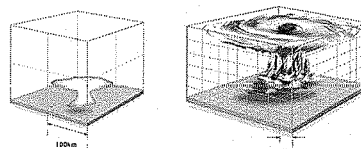
The Earth Simulator makes it possible to
simulate with such a high resolution as a
couple of thousands grid points on one
spatial direction, in contrast to the
conventional several hundreds grid points



This opens a new era in Simulation Science !

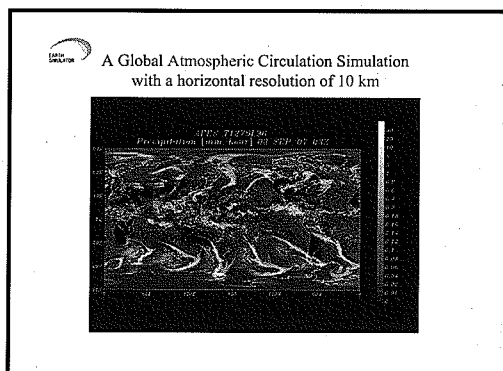
17

Quantitative and qualitative difference between the conventional simulation and the Earth Simulator[®] simulation

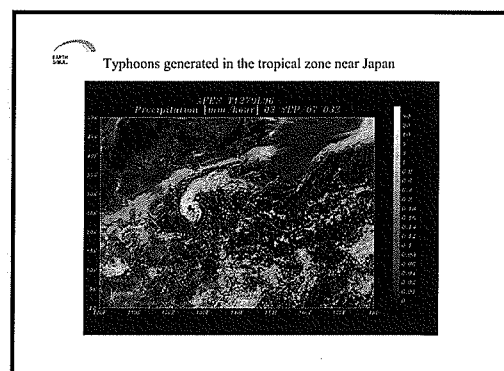


The Earth Simulator can deal with the cyclone (typhoon) in
a self-consistent way, while the conventional simulation cannot.

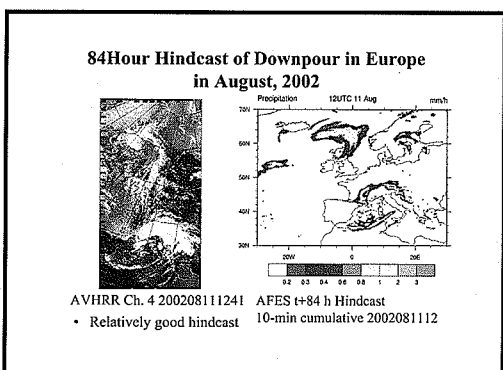
18



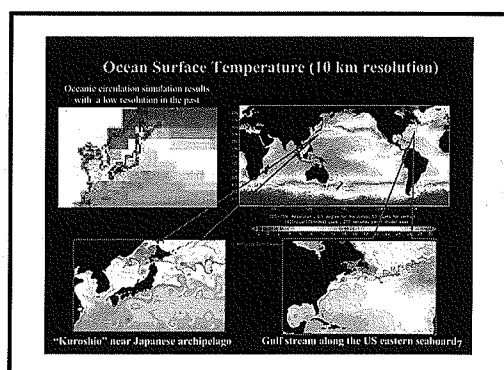
19



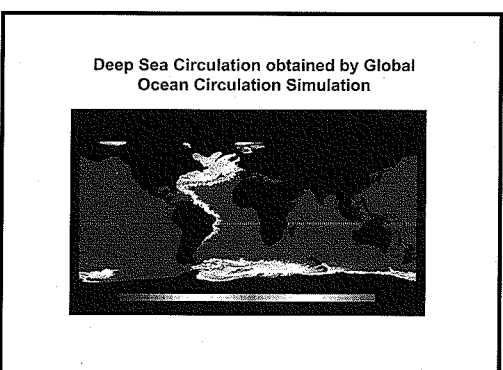
20



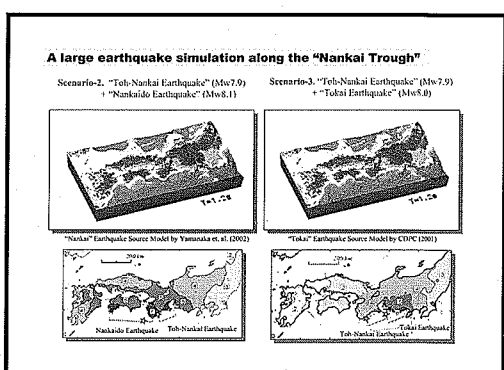
21



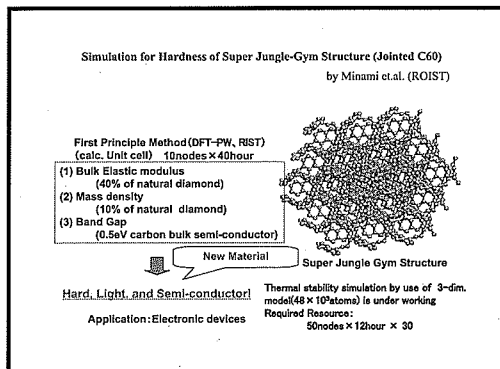
22



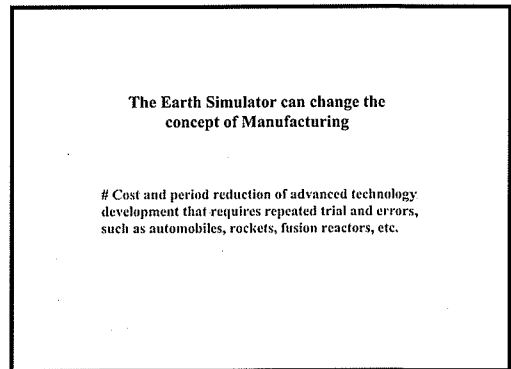
23



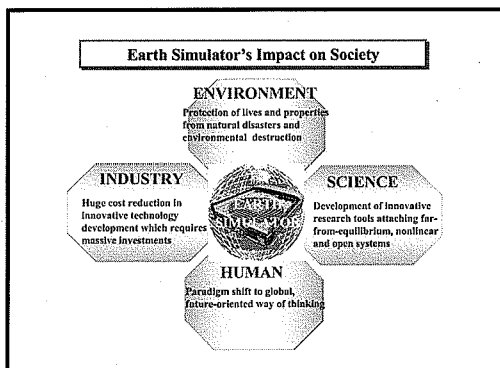
24



25



26



27

Part II

Outline of the Training Course in 2004

1111

Collection of the
University of Toronto
Library

Outline

As a part of the Japanese contribution to the International Hydrological Programme (IHP), a short course for participants from the Asia-Pacific region is conducted on Effects of Pollutants on Atmospheric Environment, from 7 to 20 March, 2004, at Hydrospheric Atmospheric Research Center and Graduate School of Environmental Studies, Nagoya University, Nagoya, Japan. The course includes a series of lectures in English, practice sessions and technical tours to Department of Ecological Engineering, Toyohashi University of Technology, Center for Climate System Research, University of Tokyo, the Earth Simulator Center, Japan Marine Science and Technology Center (JAMSTEC), the Earth Observation Research Center, National Space Development Agency of Japan (NASDA) and Atmospheric Environmental Division, National Institute for Environmental Studies concerned with atmospheric environmental studies.

Objectives

The general aim of the 13th IHP short course is to help participants to develop their basic knowledge of the effect of air-pollutants on the atmospheric environments and climate changes and to contribute to solve current global environmental problems. Anthropogenic pollutants affect atmospheric environment such as the formation of clouds and precipitation, the Earth's radiative balance, the quality of precipitation water and the ecosystem. In the East Asia region, international projects of Asian Pacific Regional Aerosol Characterization Experiment (ACE-Asia) and Asian Atmospheric Particle Environment Change Studies (APEX) are now being put into practice to understand the multiphase atmospheric chemical system and to solve radiative forcing due to anthropogenic aerosols over the Asian Pacific regions. To cope with the atmospheric environmental problem, basic understanding of physical and chemical nature of gases and aerosol particles, and their effect on microphysical, chemical and optical properties of clouds are required.

The course is focused to two major subjects. First is to examine gases, aerosol particles and clouds with direct aircraft/ground observations and lidar/satellite observations. Second is to study the effect of anthropogenic pollutants on atmospheric environments with mathematical modeling and simulation. The lectures and practices were conducted in Nagoya University and Toyohashi University of Technology.

List of Participants

- Mr. Sofyan Asep (Indonesia), Tempaku-cho, Hibarigaoka 1-1, Toyohashi 441-8580, Aichi, Japan
- Mr. Suharguniyawan Eka (Indonesia), Jl. Angkasa I No. 2 Kemayoran Jakarta 10720
- Mr. Vithaya Somphanh (Lao Pdr), P.O. Box 811 Vientiane Lao P.D.R
- Mr. Duong Hong Son (Vietnam), 5/62 Nguyen Chi Thanh, Dong Da, Hanoi, Vietnam
- Ms. De Sales Louernie-Fernandez (Philippines), Room 317 National Engineering Center, University of the Philippines

- Ms. Jitkornkitsil Narumol (Thailand), 3/12 Utongnok Rd., Wachira, Dusit District, Bangkok, 10300, Thailand
Ms. Zangmo Dawa (Bhutan), P.O. Box 674 Thimphu, Bhutan
Ms. Aberkane Teresa (New Zealand), 58 Kilmore Street, P.O. BOX 345, Christchurch, New Zealand
Mr. Khatri Pradeep (Nepal), Graduate School of Environmental Studies, Nagoya University, Japan

Course Contents (conveners: Y. Ishizaka and T. Kitada)

Lecturers

- H. Fukushima (School of High-Technology for Human Welfare, Tokai University)
S. Hatakeyama (Atmospheric Environmental Division, National Institute for Environmental Studies)
Y. Ishizaka (Hydrospheric Atmospheric Research Center, Nagoya University)
Y. Iwasaka (Graduate School of Environmental Studies, Nagoya University)
T. Kitada (Department of Ecological Engineering, Toyohashi University of Technology)
N. Sugimoto (Atmospheric Environmental Division, National Institute for Environmental Studies)
A. Sumi (Center for Climate System Research, University of Tokyo)

Lectures

L1 Basics on Transport Processes of Air-Pollutant and their Modeling in the Atmosphere.....

T. Kitada

Basic equations of advection/diffusion/deposition of air-pollutants in the atmosphere
Gaussian plume/puff models, and numerical models for transport of air-pollutants in the atmosphere

L2 Basics of Gases, Aerosol Particles and CCN

Y. Ishizaka

Basic knowledge of gases and aerosol particles
Physical properties of aerosol particles
Activation of aerosol particles as CCN
Observation of Aerosol particles and CCN over the East China Sea

L3 Long-range Transport of Air-pollutants in the East Asian Pacific Rim Region.....

S. Hatakeyama

Aircraft observation of gases in the East Asia
Trajectory analysis
Long-range transport of air-pollutants in the East Asia

L4 Observation of Aerosol Particles in the East Asia using Lidars.....

N. Sugimoto

Principles of lidar remote sensing
Observation of aerosol particles with lidars
Network monitoring of aerosol particles in the East Asia

L5 Observation of Aerosol Particles in the East Asia using Satellites.....

H. Fukushima

Principles of satellite remote sensing
Satellite sensors for aerosol observation
Observation of aerosol particles in the East Asia

L6 Nature and Behaviors of Aerosol Particles in the Atmosphere

Y. Iwasaka

Nature of aerosol particles in the atmosphere
Vertical and horizontal distribution of aerosol particles
Emission and transport of yellow dusts
Optical properties of aerosol particles in the atmosphere
Atmospheric aerosols and global material cycles

L7 Effect of Air-Pollutants on Microphysical Properties of Clouds

M. Nishizawa and Y. Ishizaka

Numerical model of meteorological field
Cloud physical model
Effect of CCN on microphysical properties of clouds

L8 Numerical Models for Transport of Air-Pollutants in the Atmosphere.....

T. Kitada

Finite difference method
Numerical method for advection/diffusion equation
Finite element method

L9 Human Activity and Climate Change.....

A. Sumi

Introduction: History of Numerical Weather Prediction (NWP) and General Circulation Model (GCM)
Dynamics for NWP and GCM
Numerical Methods for NWP and GCM
Application of Models: Global warming and seasonal forecasting

Practices

P1 Measurement and Analysis of Gases and Aerosol Particles.....

Y. Iwasaka

OUTLINE OF THE TRAINING CORUSE IN 2004

**P2 Visitation of field observation site on gases, aerosol particles and Cloud
Condensation Nuclei.....**
Y. Ishizaka

P3 Computer Simulation of Transport of Pollutants in the Atmosphere.....
G. Kurata

Technical Tours

T1 Center for Climate System Research, University of Tokyo
M. Endoh, R. Imasu and A. Abe-Ouchi

**T2 The Earth Simulator Center, JAMSTEC
Earth Observation Research Center, NASDA.....**
T. Y. Nakajima

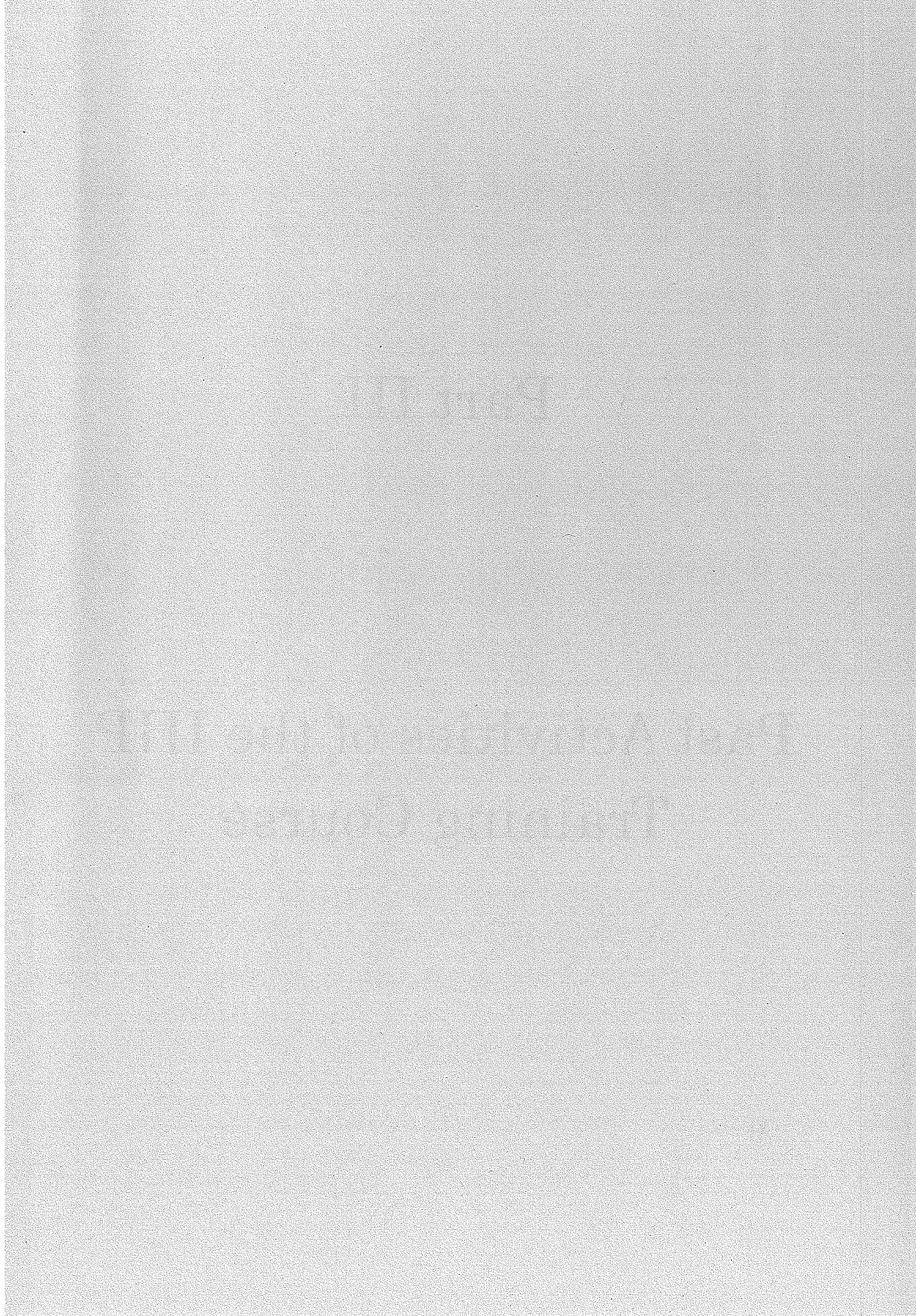
**T3 Atmospheric Environmental Division, National Institute for Environmental
Studies**
S. Hatakeyama and N. Sugimoto

Schedule (7 - 20 March, 2004)

07 (Sunday) Mar., 2004	Arrival at Nagoya	Stay in Nagoya
08 (Monday)	Guidance, Lecture 1 and Reception at Nagoya University	Stay in Nagoya
09 (Tuesday)	Lectures 2 & 3	Stay in Nagoya
10 (Wednesday)	Lectures 4 & 5	Stay in Nagoya
11 (Thursday)	Lecture 6 and Practice 1	Stay in Nagoya
12 (Friday)	Lectures 7 & 9	Stay in Nagoya
13 (Saturday)	Lecture 8 and Practice 2	Stay in Nagoya
14 (Sunday)	Japanese Culture Introduction and Free Time	Stay in Nagoya
15 (Monday)	Practice 3	Stay in Toyohashi
16 (Tuesday)	Technical Tour 1	Stay in Tokyo
17 (Wednesday)	Technical Tour 2	Stay in Tokyo
18 (Thursday)	Technical Tour 3	Stay in Tsukuba
19 (Friday)	Technical Tour 3 and Closing Ceremony	Stay in Tokyo
20 (Saturday)	Departure from Narita Airport	

Part III

Past Activities of the IHP Training Course



Past activities of the IHP Training Course (1991- 2003)

The IHP Training Course in Asia and the Pacific Region has been executed since 1991 by the Working Group for IHP Training Course, under the direction of the Sub-Committee for IHP, Japanese National Commission for UNESCO. The Training Course was aimed at giving participants an opportunity to learn observation technology of hydrology and to have practical experience in hydrological observation in the field.

In the First to Sixth-sessions of the Training Course, the training began with two or three preliminary lectures to introduce the subjects to be studied throughout the remainder of the course schedule. After this introduction, students have been taken around to several specialized institutes in the days following, to hear about what was actually done there, and to see modern instrumentation in general hydrology. It has been found, however, that this training approach possibly encourages passiveness on a part of the students because they spend an inordinate amount of time traveling daily to the host institutions where they can only listen and observe rather than participate actively.

Some innovations, therefore, were made at the Seventh-session, both in the educational content and in the schedule. Firstly, we decided to focus the training course on more clearly denned targets, and the first Year's programme concentrated on Snow Hydrology. Secondly, we decided to include practice sessions such as a field programme to allow the students, themselves, the opportunity to carry out experiments and make relevant observations/analyses. Finally, we decided to prepare a newly edited textbook for the participants in the training course.

1. The First IHP Training Course, 1991

1.1 Participants

Ms. Zhao Ling (China), Student of the Special Program of Sciences of Atmosphere and Hydrosphere, Graduate School of Science, Nagoya Univ., Japan

Mr. Zhao Jing (China), *ibid.*

Ms. Hidayat Bernadia Irawati Tjandradewi (Indonesia), *ibid.*

Mr. Geng Biao (China), Student of Sciences of Atmosphere and Hydrosphere, Graduate School of Science, Nagoya Univ., Japan

Ms. Sri Mulat Yuningsih (Indonesia), Res. Inst. for Water

Mr. Roslan BinSahat (Malaysia), Resources Development, Dept. of Public Works Hydrology Branch, Dept. of Drainage and Irrigation

1.2 Schedule and Lectures

Mar. 2-3 Water Res. Inst., Nagoya Univ. (Nagoya)

- Lecture on runoff processes in river watersheds (Prof. F. Takagi, Water Res. Inst., Nagoya Univ.)
- Lecture and practice session on precipitation and water resources in Asia (Assoc. Prof. Y. Fujiyoshi, Asst. Prof. K. Kato, Assoc. Prof. Y. Ishizaka, Water Res. Inst. Nagoya Univ.)
- Lecture and practice session on the matter cycle and water quality in the hydrosphere (Prof. M. Sakamoto, Prof. N. Handa, Assoc. Prof. K. Ohta, Water Res. Inst., Nagoya Univ.)

Mar. 4-6 Chubu Regional Construction Bureau, Min. of Construction (Chubu Region)

- Technical tour of hydrological facilities for river control

Mar. 7-8 (Sat - Sun): holidays

Mar. 9 Water Resources Res. Center, Disaster Prevention Res. Inst., Kyoto Univ.

- Laboratory experiment on evaporation from bare soil

- Mar. 10 Kiryu Experimental catchment, Faculty of Agriculture, Kyoto Univ.
- Meteorological and hydrological observations at a small catchment in hilly terrain
- Mar. 11 (Kyoto to Tsukuba)
- Mar. 12 Forestry & Forest Products Res. Inst., Min. of Agriculture, Forestry & Fisheries (Hitachi-Ohta)
- Training on evaporation and soil moisture measurements, and hydrological observation
- Mar. 13 National Inst. for Environmental Studies, Environment Agency (Tsukuba)
- Technical tour of research facilities for water quality conservation
- Mar. 14-15 (Sat-Sun) : holidays
- Mar. 16-17 Public Works Res. Inst., Min. of Construction (Tsukuba)
- Lectures on hydrological observations and models of water discharge
- Mar. 18 Forecast Dept. & Observation Dept., Japan Meteorological Agency (Tokyo)
- Lecture and technical tour concerning Short-range precipitation forecasting using radar and the AMeDAS (automated meteorological data acquisition system)
- Mar. 19 Meteorological Satellite Center, Japan Meteorological Agency (Kiyose)
- Technical tour of Meteorological Satellite Center

2. The Second IHP Training Course, 1992

2.1 Participants

Ms. Zhao Ling (China), Student of the Special Program of Sciences of Atmosphere and Hydrosphere, Graduate School of Science, Nagoya Univ., Japan

Ms. Thapa, Arati (Nepal), Student of Special Program of Sciences of Atmosphere and Hydrosphere, Graduate School of Science, Nagoya Univ.,

Japan

Mr. Kayastha, Rijan Bhakta (Nepal), *ibid.*

Mr. Sarwono, Pitoyo Sudibyo (Indonesia), *ibid.*

Mr. Le Cong Thanh (Vietnam), *ibid.*

Mr. Xu Guangxiang (China), *ibid.*

Mr. Adisak, Suriyavanagul (Thailand), Electricity Generating Authority

Mr. Pham Van Tan (Vietnam), Network Operation Dept., Hydrometeorological Service

Mr. Ekanayaka M. Wimalasena (Sri Lanka), Investigation Section, National Water Supply and Drainage Board

Mr. S. Mahmoud Borghei (Iran), Asst. Prof., Dept. of Civil Engineering Sharif Univ. of Technology

2.2 Schedule and Lectures

Mar.1-2 Water Res. Inst., Nagoya Univ. (Nagoya)

- Lecture and practice session on precipitation and water resources in Asia (Asst. Prof. T. Ohta, Asst. Prof. K. Kato, Assoc. Prof. Y. Ishizaka, Water Res. Inst., Nagoya Univ.)
- Lecture and practice session on the material cycle and
- water quality in the hydrosphere (Assoc. Prof. H. Terai, Water Res. Inst., Nagoya Univ.)
- Technical tour

Mar. 3-5 Kanto Regional Construction Bureau, Min. of Construction (Nagoya to Tokyo, Kanto Region)

- Technical tour of hydrological facilities for river control

Mar. 6-7 (Sat-Sun): holidays

Mar. 8-9 Environmental Res. Center, Univ. of Tsukuba (Tsukuba)
Observation and data analysis of evapotranspiration

Mar. 10-11 National Res. Inst. for Earth Science & Disaster Prevention,
Science & Technology Agency (Tsukuba-Ichihara, Chiba)
Laboratory experiment of rainfall

- Technical tour of an experimental hydrological catchment

Mar. 12-14 (Fri-Sun): holidays

Mar. 15-16 National Res. Inst. of Agricultural Engineering, Min. of Agriculture,
Forestry & Fisheries (Tsukuba) Analysis of irrigation and
drainage Study of experimental ground water facilities

- Mar. 17 Forecast Dept. & Observation Dept., Japan Meteorological Agency (Tokyo)
- Lecture and technical tour for short-range Precipitation for casting using radar and the AMeDAS
- Mar. 18 Meteorological Satellite Center, Japan Meteorological Agency (Kiyose)
- Technical tour of Meteorological Satellite Center

3. The Third IHP Training Course, 1993

3.1 Participants

- Mr. Kamal, Md. Syeeduzzaman (Bangladesh), Student of the Special Program of Sciences of Atmosphere and Hydrosphere, Graduate School of Science, Nagoya Univ., Japan
- Ms. Sipayung, SintaBerliana (Indonesia), *ibid.*
- Ms. HeKaiqing (China), *ibid.*
- Mr. ZhuYan (China), Dept. of Hydrology, Hohai Univ.
- Mr. Wu Yongxiang (China), Nanjing Inst. of Hydrology & Water Resources, Min. of Water Resources
- Ms. Suva, Imelda Manalastas (Philippines), Bureau of Res. & Standards, Dept. of Public Works & Highways
- Mr. Dwivedi, Ashok Kumar (India), Hydrological investigations Division, National Inst. of Hydrology, Roorkee
- Mr. Ahmad, Bashir (Pakistan), Centre of Excellence in Water Resources Engineering, Univ. of Engineering & Technology, Lahore

3.2 Schedule and Lectures

- Aug.16-17 Institute for Hydrospheric-Atmospheric Sciences (IHAS), Nagoya Univ.(Nagoya)
- Lectures on multi-scale cloud distributions in monsoon regions of Asia (Asst. Prof. K. Kato)
 - Lectures on cloud physics and chemistry in Climate studies (Prof. H. Tanaka)

OUTLINE OF THE TRAINING COURSE IN 2004

- Lectures on Asian cryosphere and changes in water Resources (Prof. Y. Ageta)
- Lectures on water cycle and stable isotopes (Assoc. Prof. M. Nakawo)
- Aug. 18-20 Chubu Regional Construction Bureau, Min. of Construction (Chubu Region)
 - Technical tour of hydrological facilities for river control
- Aug. 21-22 (Sat-Sun): holidays
- Aug. 23 Water Resources Res. Center, Disaster Prevention Res. Inst., Kyoto Univ.
 - Lecture on control of run-off water
- Aug. 24 Kiryu Experimental Catchment, Faculty of Agriculture, Kyoto Univ.
 - Meteorological and hydrological observations at a small (Kyoto to Tsukuba)
- Aug. 25 Forestry & Forest Products Res. Inst., Min. of Agriculture, Forestry & Fisheries (Hitachi-Ohta)
- Aug. 26 Training on evaporation and soil moisture measurements, and hydrological observation
- Aug. 27 Public Works Res. Inst., Min. of Construction (Tsukuba)
 - Lectures on hydrological observations and models of water discharge
- Aug. 28-29 (Sat-Sun): holidays
- Aug. 30 Public Works Res. Inst., Min. of Construction (Tsukuba)
 - Lectures on hydrological observations and models of water discharge
- Aug. 31 National Inst. for Environmental Studies, Environment Agency (Tsukuba)
 - Technical tour of research facilities for water quality conservation
- Sep. 1 Meteorological Satellite Center, Japan Meteorological Agency (Kiyose)
Technical tour of Meteorological Satellite Center
- Sep. 2 Forecast Dept. & observation Dept., Japan Meteorological Agency (Tokyo)
 - Lecture and technical tour concerning short-range

precipitation forecasting using radar and the AMeDAS

4. The Fourth IHP Training Course, 1994

4.1 Participants

- Mr. Sunil Adhikary (Nepal), Student of the Special Program of Sciences of Atmosphere and Hydrosphere, Graduate School of Science, Nagoya Univ., Japan
- Mr. Zhang Wan Chang (China), *ibid.*
- Mr. Mohammad Rezwanul Islam (Bangladesh), *ibid.*
- Mr. Birbal Rana (Nepal), Student of Stiences of Atmosphere and Hydrosphere, Graduate School of Science, Nagoya Univ., Japan
- Ms. Y. K. Handapangoda (SriLanka), Teaching Asst.. in Civil Engineering, Univ. of Peradenlya, Peradenlya
- Ms. Byambaagiin Oyunchimeg (Mongolia), Min. of Nature and Environment, Inst. of Water Problems, Ulaan Baatar
- Mr. M. Fakhruddin (Indonesia), Puslitbang Limnology, LIPI, Bogor
- Ms. Gadis Sri Haryani Bengen (Indonesia), Res. and Development Center for Limnology, Indonesian Inst. of Sciences, Bogor

4.2 Schedule and Lectures

- Aug. 15-16 IHAS, Nagoya Univ. (Nagoya)
- Lecture on Asian monsoon and water cycle (Asst. Prf. K. Kato)
 - Lecture on carbon cycling with water cycle (Prof. N. Handa)
 - Lecture on aquatic micro-organisms and water quality (Assoc. Prof. H. Terai)
- Aug. 17-19 Kanto Regional Construction Bureau, Min. of Construction (Nagoya to Tokyo, Kanto Region)
- Technical tour of hydrological facilities for river control
- Aug. 20-21 (Sat-Sun) : holidays
- Aug. 22-23 Environmental Res. Center, Univ. of Tsukuba (Tsukuba)
- Observation and data analysis of evapotranspiration
- Aug. 24-25 National Res. Inst. of Agricultural Engineering, Min. of

- Agriculture, Forestry & Fisheries (Tsukuba)
 - Analysis of irrigation and drainage
 - Study of experimental facilities for ground water
- Aug. 26 National Inst. for Environmental Studies, Environment Agency (Tsukuba)
 - Technical tour of Res. facilities for water quality conservation
- Aug. 27-28 (Sat-Sun): holidays
- Aug. 29-30 National Res. Inst. for Earth Science & Disaster Prevention, Science & Technology Agency (Tsukuba-Chiba Pref.)
 - Large scale rainfall experiment
 - Technical tour of an experimental hydrological catchment
- Aug. 31 Forecast Dept. & observation Dept., Japan Meteorological Agency (Tokyo)
 - Lecture and technical tour concerning short-range Precipitation forecasting using radar and the AMeDAS
- Sep. 1 Meteorological Satellite Center, Japan Meteorological Agency (Kiyose)
 - Technical tour of Meteorological Satellite Center

5. The Fifth IHP Training Course, 1995

5.1 Participants

- Ms. Meng Xiao (China), Student of the Special Program of Sciences of Atmosphere and Hydrosphere, Graduate School of Sciences, Nagoya Univ., Japan
- Mr. Talukder Abul Bashar MD. Alauddin (Bangladesh), *ibid.*
- Mr. Liu Jing Shi (China), *ibid.*
- Mr. Begkhutod Perapol (Thailand), *ibid.*
- Mr. Bhatt Maya Prakash (Nepal), *ibid.*
- Mr. Ma Xieyao (China), Student of Sciences of Atmosphere and Hydrosphere, Graduate School of Science, Nagoya Univ., Japan

5.2 Schedule and Lectures

<Part 1 : Chubu Region>

Dec. 13-15 Chubu Regional Construction Bureau, Min. of Construction
(Aichi and Gifu)

- Technical tour of hydrological facilities for river control

<Part 2 : Kinki Region>

Feb. 13 Lake Biwa Res. Inst., Shiga Pref. (Otsu)

- Lecture and technical tour for Lake Biwa

Feb. 14 Branch Office of Kinki District of Public Works, Min. of
Construction (Otsu)

- Lecture and technical tour for mountain conservation
Dept. of Forestry, Kyoto Univ. (Otsu)

- Lecture and technical tour of an experimental basin

Feb. 15 Disaster Prevention Res. Inst., Kyoto Univ. (Uji)

- Lecture and technical tour on disaster prevention
Hirakata Operation Center, Min. of Construction (Hirakata)

- Lecture on river water control

Feb. 16 Section of River Management, Kyoto Pref. (Kyoto)

- Technical tour concerning river management

<Part3 : Kanto Region>

Mar. 11 Inst. for Forestry and Forest Products, Min. of Agriculture, Forestry
and Fisheries (Hitachi-Ohta)

- Training on evaporation and soil moisture measurement,
and on making hydrological observation

Mar. 12 National Inst. for Environmental Studies, Environment
Agency (Tsukuba)

- Technical tour of research facilities for water quality
conservation

Mar.13 Public Works Res. Inst., Min. of Construction (Tsukuba)

- Lecture on hydrological observation and models of water
discharge

Mar.14 Forecast Dept. & observation Dept., Japan Meteorological
Agency (Tokyo)

- Lecture and technical tour concerning Short-range

- Precipitation forecasting using radar and the AMeDAS
- Mar. 15 Meteorological Satellite Center, Japan Meteorological Agency (Kiyose)
- Technical tour of Meteorological Satellite Center

6. The Sixth IHP Training Course

6.1 Participants

- Mr. Zulkefle bin Ghazali (Malaysia), Hydrology Division, Dept. of Irrigation and Drainage
- Mr. Rhoel C. Villa (Philippines), National Hydraulic Res. Center, U. P. College of Engineering
- Mr. Luong Tuan Anh (Vietnam), Inst. of Meteorology and Hydrology, Hanoi Hydrometeorological Service of Vietnam
- Mr. Atthaporn Buddhapolit (Thailand), Hydrology Division, Royal Irrigation Dept.
- Ms. Rungkarn Krishnamra (Thailand), Soil and Water Conservation Division, Land Development Dept.

6.2 Schedule and Lectures

- Aug. 19-20 IHAS, Nagoya Univ. (Nagoya)
- Lecture on hydrological characteristics of tropical forests (Prof. K. Kuraji, Univ. of Tokyo)
 - Lecture on remote sensing from space (Prof. K. Nakamura, IHAS, Nagoya Univ.)
 - Lecture on development of distributed rainfall-runoff model by using digital elevation models (Prof. Y. Tachikawa, Kyoto Univ.)
 - Lecture on the new thrust of IHP activities in Southeast Asia and Pacific, Asian/Pacific FRIEND (Flow Regimes from International Experimental and Network Data) (Prof. K. Takeuchi, Yamanashi Univ.)
- Aug. 21-23 Kanto Regional Construction Bureau, Min. of Construction (Kanto Region)
- Technical tour of hydrological facilities for river control

Aug. 24-25 (Sat-Sun): holidays

Aug. 26-27 Environmental Res. Center, Tsukuba Univ. (Tsukuba)

- Lecture and practice session on evapotranspiration measurements
- Lecture on the role of the biosphere for climate systems

Aug. 28-29 National Res. Inst. of Agricultural Engineering, Min. of Agriculture, Forestry & Fisheries (Tsukuba)

- Analysis of irrigation and drainage
- Technical tour to an irrigated paddy field

Aug. 30 Public Works Res. Inst., Min. of Construction (Tsukuba)

- Technical tour of research facilities for water quality conservation

Aug. 31-Sep. 1 (Sat-Sun): holidays

Sep. 2-3 National Res. Inst. for Earth Science & Disaster Prevention Environment Agency (Chiba Pref.)

- Large-scale rainfall experiment
- Technical tour to the hydrological catchment basin

Sep. 4 Forecast Dept. & Observation Dept., Japan Meteorological Agency (Tokyo)

Lecture and technical tour concerning short-range Precipitation forecasting using radar and the AMeDAS

Sep. 5 Meteorological Satellite Center, Japan Meteorological Agency (Kiyose)

- Technical tour of Meteorological Satellite Center

7. The Seventh IHP Training Course on “Snow Hydrology”, 1998

The general aim of the IHP short course is to help participants develop their basic knowledge of hydrological systems and of their sensitivity to climate changes as well as to contribute to solving current global environmental problems. The cryosphere is most vulnerable to the projected global warming trend that has recently become a major concern in many countries. The seventh training course focuses on snow hydrology.

The topics covered range from basic knowledge of the role of the cryosphere in the global environment to technical applications, including observations and measurements in snow packs.

7.1 participants

Mr. D. B. Chettri (Bhutan), Executive Engineer, Meteorology Unit, Div.
Power, Min. of Trade and Industry

Mr. Liang, Zhongmin (China), Teacher, Dept. Hydrology, Hohai Univ.

Mr. Om Ratna Bajracharya (Nepal), Senior Hydrologist, Dept. Hydrology
and Meteorology, Min. of Science and Technology

Mr. Shiva Bhakta Prajapati (Nepal), Hydrologist, Dept. Hydrology and
Meteorology, Min. of Science and Technology

Mr. Aurangzeb Khattak (Pakistan), Asst. Director, WRRRC

Mr. Edwin Aldrian (Indonesia), M2, IHP Student, IHAS, Nagoya Univ.

Mr. Dang Xuan Phong (Vietnam), M2, IHP Student, IHAS, Nagoya Univ.,
Japan

Mr. Li, Jianjun (China), M2, IHP Student, IHAS, Nagoya Univ., Japan

Mr. Yudi Iman Tauhid (Indonesia), M2, IHP Student, IHAS, Nagoya Univ.,
Japan

Mr. Bhuwan Chandra Bhatt (Nepal), M1, IHP Student, IHAS, Nagoya Univ.,
Japan

Mr. Zhou Shiqiao (China), M1, IHP Student, IHAS, Nagoya Univ., Japan

Mr. Kayastha Rijan Bhakta (Nepal), Res. Fellow, IHAS, Nagoya Univ.,
Japan

Mr. Suresh Chandra Pradhan (Nepal), Hydrological Asst., Dept.
Hydrology and Meteorology, Min. of Science and Technology

Mr. Keshav Raj Sharma (Nepal), Hydrological Asst., Dept. Hydrology and
Meteorology, Min. of Science and Technology

Mr. Chok Bahadur Gurung (Nepal), Hydrological Asst., Dept. Hydrology
and Meteorology, Min. of Science and Technology

Dr. Dodi Wangdu, Head (Bhutan), Division of Geology and Mines

Ms. Diraagiin Erdenetsetseg (Mongolia), Expert, Centre for Climate and
Environmental Change, Inst. of Meteorology and Hydrology

Mr. Nozomu Naito (Japan), D3, Graduate Student, IHAS, Nagoya Univ.

Mr. Fumio Nakazawa (Japan), M1, Graduate Student IHAS, Nagoya Univ.

Mr. Yoshihiro Yoshioka(Japan), M2, Graduate Student, Nagaoka Univ. of Technology

7.2 Schedule and Lectures

Lecturers

- Y. Ageta, IHAS, Nagoya Univ.
T. Aoki, Meteorological Res. Inst.
K. Goto-Azuma, Nagaoka Inst. of Snow and Ice Studies, National Res. Inst. for Earth Science and Disaster Prevention
N. Hayakawa, Dept. of Civil and Environmental Engineering, Nagaoka Univ. of Technology
H. Iida, Sediment Control Division, Dept. of Civil Engineering, Toyama Prefectural Government
I. Kamiishi, Centre of Snow and Ice Technology, ARGOS Co. Ltd.
S. Kobayashi, Res. Inst. for Hazards in Snowy Areas, Niigata Univ.
M. Lu, Dept. of Civil and Environmental Engineering, Nagaoka Univ. of Technology
H. Mizuno, Meteorological College
M. Nakawo, IHAS, Nagoya Univ.
H. Ohno, Japan International Res. Centre for Agricultural Sciences
K. Satow, Civil Engineering, Nagaoka National College of Technology
T. Takeda, IHAS, Nagoya Univ.
Y. Takeuchi, Nagaoka Inst. of Snow and Ice Studies, National Res. Inst. for Earth Sciences and Disaster Prevention
K. Yokoyama, Hokuriku National Agricultural Experiment Station

Schedule (9 March, 1998-22 March,1998)

- Mar. 9 Arrival at Nagoya, Japan
Mar. 10 (IHAS, Nagoya Univ.)
 ▪ Guidance
 ▪ Lecture on glaciers and the water cycle
 ▪ Lecture on precipitation process
 ▪ Lecture on synoptic conditions and snowfall precipitation

OUTLINE OF THE TRAINING COURSE IN 2004

- process
- Ice breaker reception in the evening
- Mar. 11 (IHAS, Nagoya Univ.)
- Technical tour
- Move from Nagoya to Myoko (4 hour train ride)
- Mar. 12
- Lecture on water circulation over the earth : the roles of snow and ice
- Radiation processes and remote sensing of snow
- Practice session for spectral albedo observations on a snow field
- Mar. 13
- Lecture on snowmelt hydrology
 - Practice session for hydrographical observations
 - Fabrication of the Endo-type snow-water content meter(1)
- Mar. 14
- Lecture on metamorphism of deposited snow
 - Lecture on snow changes in snow pack and melt water chemistry during snowmelt
 - Lecture on heat budget of a snow pack
- Mar. 15
- Technical bus tour to
- Niigata Experiment Laboratory, Public Works Res. Inst.,
Tohkamachi Experiment Station, Forestry and Forest
Products Res. Inst., Nagaoka Inst. of Snow and Ice Studies,
National Res. Inst. for Earth Science and Disaster
Prevention(Stay overnight at a spa, Yomogihira Hot
Spring, in the snow region)
- Mar. 16
- Technical bus tour continues to Myoken Weir, Shinano
River
- Facilities for snow removal by melting in Nagaoka City
 - Shinano River Work office, Hokuriku Regional
Construction Bureau
 - Oukouzu Division Work, Shinano River and the Division
Work Museum
 - Arai Weir, Shinano River
 - Fabrication of the Endo-type snow-water content meter(2)
- Mar. 17 Practice session for heat exchange over a snow surface
- Mar. 18 Practice session for snow pit observations
- Mar. 19 Data handling exercise(reception in the evening)
- Mar. 20 Report preparation

Move from Myoko to Nagoya(train ride)

Mar. 21 Closing ceremony

Mar. 22 Departure from Nagoya

8. The Eighth IHP Training Course on “Remote Sensing”, 1999

Recently, the environmental problems attracts strong attentions. The spatial scales of the problems range from very local one to global one. Environmental problems have close connection to atmospheric and hydrospheric phenomena. For the atmospheric and hydrospheric sciences, satellite remote sensing is very useful and essential because of its capability to observe the atmosphere and hydrosphere in a big scale. For example, recently launched TRMM (Tropical Rainfall Measuring Mission) is providing us a unique three-dimensional rain structures regardless of the location over tropical and a part of mid latitude regions. ADEOS (Advanced Earth Observing Satellite) gave us beautiful images of global phytoplankton distribution over global ocean.

Ground-based remote sensing Which includes radars and lidars is also useful for the atmospheric observation.

The lectures give the basic theory of remote sensing, technology and applications, and current Earth observation satellites, etc.

8.1 Participants

Mr. Limsakul Atsamon(Thailand), IHAS, Nagoya Univ., Japan

Ms. Jiang Cuiling(China), IHAS, Nagoya Univ., Japan

Mr. Aryal Deepak(Nepal), IHAS, Nagoya Univ., Japan

Ms. Aranya Fuangswasdi(Thailand), Ground Water Division, Dept. of Mineral Resources

Ms. Zainab Hashim(Malaysia), Hydrology Division, Dept. of Irrigation and Drainage

Mr. Wibowo Hendro(Indonesia), Puslitbang Limnologi-LIPI

Dr. Cheng Ming(China), Nanjing Inst. of Hydrology and Water Resources,

Min. of Water Resources

Mr. Te Navuth(Cambodia), Min. of Water Resources and Meteorology

Ms. Yuko Ogawa(Japan), Global Information and Early Warning Service,
Food and Agriculture Organization of the United Nations, Italy

Mr. Thongdum Pengyai(Thailand), Hydrometeorology Division,
Meteorological Dept.

Mr. Chhetri B. Tek(Nepal), IHAS, Nagoya Univ., Japan

Mr. Haryoko Urip(Indonesia), Meteorological and Geophysical Agency

Ms. Li Zhuxiao(China), IHAS, Nagoya Univ., Japan

8.2 Schedule and Lectures

Lecturers and lecture titles

Y. Honda, Chiba Univ. : Global vegetation observation II

T. Iguchi, Communications Res. Laboratory(CRL), Min. of Posts and
Telecommunications : Active microwave measurement of rain and
clouds from space I

T. Itabe, Communications Res. Laboratory, Min. of Posts and
Telecommunications : Lidar proving of the atmosphere

K. Kajiwara, Chiba Univ. : Global vegetation observationI

T. Koike, Nagaoka Univ. of Technology : soil wetness measurement from
satellite micro wave remote sensing

T. Kozu, Communications Res. Laboratory, Min. of Posts and
Telecommunications : Active microwave measurement of rain and
Clouds from space II

K. Nakamura, IHAS, Nagoya Univ. : Observation of atmosphere by radar

T. Saino, IHAS, Nagoya Univ.: Ocean color observation by satellite

H. Shimoda, Tokai Univ.: Current remote sensing technology for global
warming monitoring

D. Short, IHAS, Nagoya Univ.: The Tropical Rainfall Measuring Mission

K. Tsuboki, IHAS, Nagoya Univ.: Radar measurement of precipitation
processes

S. Uratsuka, Communications Res. Laboratory, Min. of Post and
Telecommunications: Synthetic aperture radar and its applications

Schedule

Mar. 8	Arrival at Nagoya, Japan
Mar. 9	Guidance, lectures and reception at IHAS, Nagoya Univ.
Mar. 10	Lectures and technical tour in IHAS, Nagoya Univ.
Mar. 11	Lecture and guidance of data analysis training
Mar. 12	Data analysis training
Mar. 13	Data analysis training (continued)
Mar. 14	Move to CRL at Koganei, Tokyo
Mar. 15	Lectures
Mar. 16	Lectures and technical tour at CRL
Mar. 17	Move to Tokai Univ. and lectures / move to Chiba Univ.
Mar. 18	Lectures
Mar. 19	Lectures and move to Nagoya
Mar. 20	Free day
Mar. 21	Departure from Nagoya

9. The Ninth IHP Training Course on “Limnology”

1999 summer

Limnology is a field of study on terrestrial water ecosystems such as lakes, rivers, reservoirs, ground waters and wetland. Human activities have been linked very closely to those water ecosystems and changed them directly or indirectly through global environmental changes. We have to learn basic limnological processes and how to manage and conserve those water ecosystems with sustainable development through the next century.

Limnological studies in Japan only began in 1899 and we are celebrating their centennial history. The following Programs have been prepared to welcome trainees of the IHP training course in limnology in the summer of 1999.

9.1 Participants

Mr. Abung Rachmann (Indonesia), Res. Inst. for Water Resources

Development

Dr. Arveti Nagaraju (India), Dept. of Geology, Sri Venkateswara Univ.

Dr. Chen Yuaufang (China), College of Water Resources and
Environment, Hohai Univ.

Ms. Daram S. Enkhsetseg (Mongolia), Inst. of Meteorology and
Hydrology

Mr. Hossain Md Anawar (Bangladesh), IHP student in IHAS, Nagoya
Univ., Japan

Ms. Lythi M. Hai (Vietnam), Dept. of Water Resources and Environment,
Inst. of Geography

Mr. Mohd. Talha Mohd. Zaharon (Malaysia), Environmental Health
Section, Engineering Services Division, Min. of Health

Ms. Sirisampan Satiraporn (Thailand), IHP student in IHAS, Nagoya
Univ., Japan

9.2 Schedule and Lectures

Lecturers and lecture titles

H. Terai, IHAS, Nagoya Univ.: Material cycling in deep and shallow water
ecosystems

K. Ichino, Faculty of International Communication, Aichi Univ.: Low-cost water
treatment systems using constructed wetlands

T. Yoshioka, IHAS, Nagoya Univ. Current technology in
limnology (1) Stable isotope ecology

T. Okino, Faculty of Sciences, Shinshu Univ.: A historical review of
limnology in Japan and a case study on Lake Suwa

K. Kato, School of Allied Medical Sciences, Shinshu Univ.: Current
technology in limnology (2) Microbial ecology

T. Hanazato, Suwa Hydrobiological Station, Shinshu Univ.: global environment
and lake ecosystems

H. Fushimi, School of Environmental Sciences, The Univ. of Shiga Pref.:
water resources and environmental problems of Lake Biwa

M. Sakamoto, School of Environmental Sciences, The Univ. of Shiga
Pref.: Eutrophication and management of freshwater environments

M. Nakamura, Lake Biwa Res. Inst. Shiga Pref. Lake Biwa-Yodo River

water systems: Evolving issues on integrated management of water quality

M. Kumagai, Lake Biwa Res. Inst., Shiga Pref.: Ecological inhomogeneity due to dynamic variability in Lake Biwa

T. Nakajima, Lake Biwa Museum, Shiga Pref.: Evolution and distribution of cyprinid fish in East Asia during Neogene, and formation of the cyprinid fauna in Lake Biwa

R. F. Walker, Lake Biwa Res. Inst., Shiga Pref.: Current technology in limnology (3) Algal species classification by image processing

N. Nakamoto, Faculty of Textile Science and Technology, Shinshu Univ.: Misunderstanding of slow sand filtration in Japan and the biological mechanism of its system

M. Overmars, UNESCO, Jakarta Office: Special Lecture Current IHP activities in Asia Pacific Region

Schedule

- | | |
|---------|---|
| Jul. 26 | Arrival at Nagoya, Japan |
| Jul. 27 | Guidance and lectures at IHAS (icebreaker reception in the evening) |
| Jul. 28 | Move to Suwa Hydrobiological Laboratory, guidance and lecture |
| Jul. 29 | Field trip on Lake Suwa, observation and sampling |
| Jul. 30 | Chemical and biological analysis of water and sediment samples |
| Jul. 31 | Field trip to Lake Shirakoma, observation and sampling (reception in the evening) |
| Aug. 1 | Technical bus tour to Kurobe Reservoir and Nishina subalpine lakes |
| Aug. 2 | Lake Kizaki Laboratory, travel to Hikone by train |
| Aug. 3 | Lecture at the Univ. of Shiga Pref., Visit Limnological Laboratory, move to Otsu |
| Aug. 4 | Lecture and technical tour at Lake Biwa Res. Inst. |
| Aug. 5 | Field trip to Lake Biwa on their search vessel "Hakken" |
| Aug. 6 | Technical tour to Lake Biwa Museum, back to Nagoya |
| Aug. 7 | Closing Ceremony and reception |
| Aug. 8 | Departure from Nagoya |

10. The Tenth IHP Training Course on “Hydrology related to Head Water Management” 2000 summer

“Head Water Area” is understood as both supplying a source of clean water and assisting in the prevention of flood/sediment disasters for living people downstream. Over-cutting of trees or industrial pollution sometimes damages to the surrounding environment of “Head Water”. Japan has experiences such failures 100 years ago. In this training course, we would like to focus on hydrological impacts of non-vegetation, and on the effects of both reforestation in steep slope and erosion control works in river-bed. The watersheds, we focus on, are damaged in the past with sulphurous acid gas caused by the refining factory of copper. Lectures are provided as the Faculty of Technology, Gunma University, Kiryu-city, Gunma Prefecture, and field training is to be done in the basin of the Watarase River, a tributary of the Tone River which is very important for Tokyo Metropolitan.

10.1 Participants

Mr. Evandri Ahmad (Indonesia): R & D Center for Informatic and Computer Science

Mr. Yuebo Xi (P. R. China): Hohai Univ.

Mr. Suy Sovann (Cambodia): Min. of Water Resources and Meteorology

Mr. Monoloth Soukhanouvong (Laos PDR): Dept. of Meteorology and Hydrology (DMH) Min. of Agriculture and Forestry (MAF)

Ms. Stephanie Bowis (New Zealand): West Coast Regional Council

Ms. Ubolwan Jenphanitsub (Thailand): Office of the National Water Resources Committee

Mr. Nguyen Kim Tuyen (Vietnam): Hydrometeorological Service of Vietnam

Mr. Birendra Raj Adhikari (Nepal): M1, IHP Student, IHAS Nagoya Univ.

Mr. Karma(Bhutan): M1, IHP Student, IHAS Nagoya Univ.

10.2 Schedule and Lectures

Lecturers and lecture titles

- T. Ohta, Graduate School of life and Agriculture, Univ. of Tokyo, : Typology of erosion processes and watershed management, Effect of human activities on head water
- S. Kobatake, Gunma Univ.,: History of mountain devastation in the Watarase River, Runoff analysis of head water
- Y. Fukushima, Nagoya Univ.,: Hydrological processes in headwater
- Y. Kawano, Min. of Agriculture, Forest conservation project in headwater areas
- Y. Nakamura, Min. of Construction, : Sediment disaster preventive works in Japan
- K. Honda, Asian Inst. of Technology, Thailand, : Evaluation of Erosion Control Work using Remote Sensing and GIS
- T. Tsujimoto, Nagoya Univ.,: Sediment Transport and River Management
- H. Tanji, Min. of Agriculture, Irrigation system and watershed management
- H. Kawashima, Graduate School of life and Agriculture, Univ. of Tokyo, : River basin management and water quantity
- G. Takahashi, Toyama Prefectural Univ. of Agriculture, Watershed management and conservation of ecosystem

Schedule

- | | |
|---------|---|
| Jul. 24 | Arrival at Narita Airport and move to Kiryu-city by limousine |
| Jul. 25 | Guidance and lecture at the campus of Gunma Univ. |
| Jul. 26 | Lecture |
| Jul. 27 | Lecture |
| Jul. 28 | Technical tour to Ashio |
| Jul. 29 | Technical tour to Mt. Nsntai |
| Jul. 30 | Inspect sights of Nikko |
| Jul. 31 | Lecture and Practice |

- Aug. 1 Lecture and Practice
- Aug. 2 Technical tour to the integrated Dam Control Office
- Aug. 3 Lecture
- Aug. 4 Technical tour to the Watarase Retarding Basin and Tone-Oozeki Barrage
- Aug. 5 Move to Tokyo
- Aug. 6 Departure from Narita

11. The Eleventh IHP Training Course on “Hydrogen and Oxygen Isotopes in Hydrology” 2001 summer

Stable isotopes of hydrogen and oxygen, and tritium of hydrological waters, have been used to trace water circulation in various scale in time and space. They have been revealed to be good parameters for understanding the hydrological systems and solving the hydrological problems. Fundamentals for sampling, determination, data analysis, and transport models of water isotopes will be briefly lectured about seawater, water vapor, precipitation water, snow, ice, surface water, soil water, ground water, and volcanic and hydrothermal water. Participants can get comprehensive idea of the application of hydrogen and oxygen isotopes in hydrology by practice to collect various kinds of hydrological samples, determine their isotope ratios, and analyze their data by themselves.

11.1 Participants

Dr. Chague-Goff, Catherine (New Zealand): National Inst. of Water & Atmospheric Research (NIWA)

Mr. Deris, Mohammad (Malaysia): Hydrology and Water Resources Division, Dept. of Irrigation and Drainage Malaysia

Ms. Kemanuntagosorn, Naowarat (Thailand): Applied Hydrology Section
Water Resources Management Dept. Hydro Power Survey and Land Division

Ms. Ngo, Van Anh Thi (Vietnam): Water and Air Environmental Research Center,

- Inst. of Meteorology and Hydrology
Ms. Po, Salina (Cambodia): Water Quality Analysis in Department of Hydrology and Riverworks of Min. of Water Resources and Meteorology
Mr. Putuhena, William Marcus (Indonesia): Research Institute for Water Resources, Min. of Settlement and Regional Infrastructure
Mr. Hankin, Stuart Ian (Australia): Australian Nuclear Science and Technology Organisation
Dr. Hughes, Catherine Emily (Australia): Australian Nuclear Science and Technology Organisation
Mr. Raju, Aryal (Nepal): Graduate student of IHP special course at Nagoya Univ.
Mr. Zhu, Xuesong (China): Graduate student of IHP special course at Nagoya Univ.
Mr. Hashimoto, Shigemasa (Japan): Graduate student of Science, Nagoya Univ.
Mr. Uemura, Ryu (Japan): Graduate student of Environmental Science and Technology, Tokyo Inst. of Technology

11.2 Schedule and Lectures

Lecturers and lecture titles

- N. Yoshida, Tokyo Inst. of Technology: Fundamentals of hydrogen and oxygen isotopes in hydrology
O. Matsubara, Akita Univ.: General feature on the hydrogen and oxygen isotopes ratios of natural water
A. Numaguti, Hokkaido Univ.: Large-scale transport of water vapor and isotope variability
A. Sugimoto, Kyoto Univ.: Water circulation in regional scale
M. Nakawo, Nagoya Univ.: Isotopes in snow and ice
H. Satake, Toyama Univ.: Tritium in precipitation and surface waters
M. Tsujimura, Tsukuba Univ.: Stable isotopic composition in soil water
M. Yasuhara, Geological Survey of Japan: Environmental isotopes in groundwaters
J. Shimada, Kumamoto Univ.: Use of Environmental isotope tracers to reveal groundwater flow system
H. Wushiki, Japan International Cooperation Agency: Water in arid lands
M. Kusakabe, Okayama Univ.: Volcanic and hydrothermal waters

Schedule

Sep. 9	Arrival at Nagoya
Sep. 10	Guidance and lectures at Nagoya Univ. (icebreaker reception in the evening)
Sep. 11	Lecture and laboratory tour at IHAS, Nagoya Univ.
Sep. 12	Move to Volcanic Fluid Research Center, Tokyo Institute of Technology at Kusatsu-Shirane
Sep. 13	Lecture and Practical, Sampling of Hydrothermal water etc. and laboratory tour at the center
Sep. 14	Move to Tokyo
Sep. 15	Lectures at National Olympic Memorial Youth Center
Sep. 16	Lectures and practice
Sep. 17	Move to Chiba Experimental Forest, University of Tokyo, Lecture and practice, sampling of stream water etc.
Sep. 18	Move to Tokyo, lecture and practice
Sep. 19	Lecture and practice, Measurement of samples at Yokohama Campus of Tokyo Institute of Technology
Sep. 20	Lecture and practice, Simulation training, and Discussion
Sep. 21	Closing ceremony, Free time
Sep. 22	Departure from Narita Air Port

12. The twelfth IHP Training Course on

“Precipitation and Water Resources” 2003 winter

The twelfth short course focuses on understanding mechanism and prediction of heavy rainfall and flood runoff including river basin management. The topic on draught in senses of phenomena and management will be included as a typical topic of water resources. The problems of water resources and ways of solving them depend much on features of nature and human activity in the field people are living. In this sense, participants can get essential and comprehensive idea of ways of planning, managing and monitoring problems on water resources of their own

countries including precipitation.

12.1 Participants

- Mr. Bunthon DAUK (Kingdom of Cambodia): Provincial Service of Water Resources and Meteorology
- Ms. Eulis RETNOWATI (Republic of Indonesia): Forest and Nature Conservation Research and Development Centre
- Mr. Sengsoulianh INTACHACK (Lao People's Democratic Republic): Ministry of Agriculture and Forestry, Department of Meteorology and Hydrology
- Ms. Huong T. T. NGUYEN (Socialist Republic of Viet Nam): Department of Water Resources and Environment Institute of Geography
National Centre for Natural Science and Technology of Viet Nam Institute of Geography Hoang
- Ms. Michelle A. WILD (New Zealand): National Institute of Water and Atmospheric Research Ltd.
- Ms. Panporn SUWAN (Kingdom of Thailand): Department of Water Resources
- Mr. Asnor Muizan Bin ISHAK (Malaysia): Hydrology and Water Resources Division, Department of Irrigation and Drainage Malaysia
- Mr. Haytham M. AWAD (Arab Republic of Egypt): Institute of Environmental Systems, Kyushu University
- Mr. Sameh A. KANTOUSH (Arab Republic of Egypt): Department of Civil Engineering, Faculty of Science and Engineering, Saga University
- Mr. Andrés CALIZAYA T. (Republic of Bolivia): Institute of Hydraulic and Hydrology (IHH) of Major University San Andres La Paz.
- Mr. Shafi M. TAREQ (People's Republic of Bangladesh): Hydrospheric Atmospheric Research Center, Nagoya University
- Mr. Khatri, PRADEEP (Kingdom of Nepal): Hydrospheric Atmospheric Research Center, Nagoya University
- Ms. Prasamsa, SINGH (Kingdom of Nepal): Hydrospheric Atmospheric Research Center, Nagoya University

12.2 Schedule and Lectures

Lecturers and lecture titles

T. Hori, Kyoto Univ.: Water Resources planning and Management
Y. Ichikawa, Kyoto Univ.: Distributed Runoff Modeling
E. Nakakita, Kyoto Univ.: Radar Hydrology, Short-term Rainfall Prediction Using Radar
K. Nakamura, Nagoya Univ.: Rain Observation from Satellites
T. Shinodara, Nagoya Univ.: Cloud Resolving Model
Y. Tachikawa, Kyoto Univ.: Catchment Hydrology, Flood Runoff Prediction
I. Tamagawa, Gifu Univ.: Boundary Layer
K. Tanaka, Kyoto Univ.: land Surface Processes
K. Tsuboki, Nagoya Univ.: Basics on Numerical Simulation
H. Uyeda, Nagoya Univ.: Basics of Meteorology on Precipitation, Basics on Mesoscale Meteorology and Radar Meteorology

Schedule

Feb.23	Arrival at Nagoya
Feb.24	Guidance, Lectures 1 & 2, Reception at Nagoya University
Feb.25	Lectures 3 & 4,
Feb.26	Lecture 5 and Practice 1
Feb.27	Practice 1 (cont'd) and Technical Tour 1
Feb.28	Writing report and Lecture 6
Mar.1	Technical Tour 2 on the way to Kyoto
Mar.2	Japanese culture introduction and Free time
Mar.3	Lectures 7 & 8
Mar.4	Practice 2
Mar.5	Lectures 9 & 10
Mar.6	Practice 3
Mar.7	Technical Tour 3 and Closing ceremony
Mar.8	Departure from Kansai (Osaka) Air Port